Title
Hanging Tether Management for Unmanned Air - Surface Vehicle Teams

Author
Talke, Kurt Arthur

Publication Date
2021

UNIVERSITY OF CALIFORNIA SAN DIEGO

Hanging Tether Management for Unmanned Air - Surface Vehicle Teams

A dissertation submitted in partial satisfaction of the
requirements for the degree
Doctor of Philosophy

in

Engineering Sciences (Mechanical Engineering)

by

Kurt Arthur Talke

Committee in charge:

Professor Thomas Bewley, Chair
Professor Maurício de Oliveira
Professor James Friend
Professor Falko Kuester
Professor Melvin Leok

2021

The dissertation of Kurt Arthur Talke is approved, and it is acceptable in quality and form for publication on microfilm and electronically.

University of California San Diego

2021

DEDICATION

For Jacob, Leila, and Baby Baboo

TABLE OF CONTENTS

LIST OF FIGURES

LIST OF TABLES

LIST OF SUPPLEMENTAL VIDEOS

Autonomous Hanging Tether Management and Experimentation for a UAV-USV Team.mp4

ACKNOWLEDGEMENTS

The work in this dissertation was only possible through the help of numerous individuals. Thank you to my PhD advisor, Professor Thomas Bewley for always lending an ear, guiding me through challenges, helping me to see a different perspective, and always finding the important pieces. I would also like to thank Professor Maurício de Oliveira for his genuine interest, vigor, passion, and always having an open door to discuss the latest happenings. Professor James Friend's guidance, time and enthusiasm contributed to a large fundamental part of Chapter 7. He is one of the best instructors I have come across, relatable and truly cares about his students. Thank you to my fellow lab colleagues, Daniel Yang, Eric Sihite, Ricardo Gorinstein, James Strawson, Dylan Drotman, and Joon Jang, for all the help, guidance, and technical prowess.

The biggest thank you goes out to my father, Professor Frank Talke, for always supporting me through thick and thin, providing life guidance, good genes, perspective, patience, instilling the best engineering fundamentals, drive to succeed, and encouragement to always do the right thing. Thank you to my sister, Kristen Hamilton, for being my sounding board and emotional guidance. Thank you to my mother, Kathryn Talke, for your endless love and support.

Most important, my wife, the love of my life, Sophie Talke, has been by my side throughout this entire endeavor, and deserves everything she has ever wanted. Thank you for your patience, support, love, friendship, kindness, tears, and our children, Jacob, Leila, and Baby Baboo on the way.

Support for this work was provided by Naval Information Warfare Center Pacific under the Naval Innovative Science and Engineering program and the Department of Defense SMART Scholarship for Service program. A special thank you goes out to the engineers who lent their time and expertise on this effort: Aaron Burmeister, Frederick Birchmore, Nick Stroumtsos, and Dan Jennings.

Chapter 2 in full, is a reprint of the material as it appears in IEEE International Conference on Robotics and Automation (ICRA) 2019, K. Talke, D. Drotman, N. Stroumtsos,M. Oliveira, and T. Bewley, “Design and parameter optimization of a 3-$\underline{\text{P}}$SR parallel mechanism for replicating wave and boat motion”. The dissertation author was the primary investigator and author of these pages.

Chapter 3 in full, is a reprint of the material as it appears in IEEE International Conference on Intelligent Robots and Systems (IROS) 2018, K. Talke, M Oliveira, and T. Bewley, “Tether shape analysis for a UAV - USV team”. The dissertation author was the primary investigator and author of these pages.

Chapters 4-6, in full, have been submitted for publication as it may appear in Field Robotics 2021, K. Talke, F. Birchmore, T. Bewley, “Autonomous Hanging Tether Management and Experimentation for a UAV-USV Team”. The dissertation author was the primary investigator and author of these pages.

Chapter 7, in part is currently being prepared for submission for publication of the material, K. Talke, J. Friend, T. Bewley. The dissertation author was the primary investigator and author of these pages.

Chapters 8-9, in full are currently being prepared for submission for publication of the material, K. Talke, J. Friend, T. Bewley. The dissertation author was the primary investigator and author of these pages.

VITA

2006	B. S. in Mechanical Engineering, University of California Berkeley
2006	B. S. in Material Science & Engineering, University of California Berkeley
2007-2010	Mechanical Engineer, Delta Design
2010-2011	Graduate Teaching Assistant, University of California San Diego
2011	M. S. in Engineering Sciences (Mechanical Engineering), University of California San Diego
2011 - Current	Mechanical Engineer, Naval Information Warfare Center Pacific
2013-2015	Instructor, University of California San Diego
2020-2021	Graduate Teaching Assistant, University of California San Diego
2021	Ph. D. in Engineering Sciences (Mechanical Engineering), University of California San Diego

PUBLICATIONS

V. Lubarda and K. Talke, "Analysis of the equilibrium droplet shape based on an ellipsoidal droplet model," Langmuir, vol. 27, pp. 10705–10713, 09 2011.

V. Lubarda and K. Talke, "Configurational forces and shape of a sessile droplet on a rotating solid substrate.," Theoretical & Applied Mechanics, vol. 39, no. 1, 2012.

A. Burmeister, N. Pezeshkian, K. Talke, A. Hart, and G. GilBreath, "Design of a multi-segmented robot for hull climbing," tech. rep., Space and Naval Warfare System Center Pacific, San Diego Ca., 2013.

A. Burmeister, N. Pezeshkian, K. Talke, S. Ostovari, H. Everett, A. Hart, G. Gilbreath, and H. Nguyen, "Design of a multi-segmented magnetic robot for hull inspection," tech. rep., Space and Naval Warfare System Center Pacific, San Diego Ca., 2014.

K. Talke, L. Kelley, P. Longhini, and G. Catron, "Tip-over prevention through heuristic reactive behaviors for unmanned ground vehicles," in Unmanned Systems Technology XVI, vol. 9084, p. 90840L, International Society for Optics and Photonics, 2014.

L. Kelley, S. Ostovari, A. Burmeister, K. Talke, N. Pezeshkian, A. Rahimi, A. Hart, and H. Nguyen, "Design and experimental validation of a simple controller for a multi-segment magnetic crawler robot," in Unmanned Systems Technology XVII, vol. 9468, p. 94680N, International Society for Optics and Photonics, 2015.

L. Kelley, K. Talke, P. Longhini, and G. Catron, “Tip-over prevention: Adaptive control development and experimentation,” in 2015 IEEE International Conference on Robotics and Automation (ICRA), pp. 4367–4372, IEEE, 2015.

H. Nguyen, A. Nans, K. Talke, P. Candela, and H. Everett, “Automatic behavior sensing for a bomb-detecting dog,” in Unmanned Systems Technology XVII, vol. 9468, p. 94680K, International Society for Optics and Photonics, 2015.

A. Burmeister, K. Talke, A. Hart, N. Pezeshkian, S. Ostovari, and L. Kelley, “Multi-segmented magnetic robot,” Mar. 7 2017. US Patent 9,586,636.

K. Talke, A. Burmeister, and A. Jones, “Track kit for two wheeled balancing ground vehicle,” Nov. 7 2017. US Patent 9,809,264.

K. Talke, M. De Oliveira, and T. Bewley, “Catenary tether shape analysis for a uav-usv team,” in 2018 IEEE/RSJ International Conference on Intelligent Robots and Systems (IROS), pp. 7803–7809, IEEE, 2018.

K. Talke, D. Drotman, N. Stroumtsos, M. Oliveira, and T. Bewley, “Design and parameter optimization of a 3-PSR parallel mechanism for replicating wave and boat motion,” in 2019 IEEE International Conference on Robotics and Automation (ICRA), May 2019.

K. Talke, A. Burmeister, D. Leung, M. Baker Jr, and M. Jones, “Stowable payload carrier,” July 30 2019. US Patent 10,363,856.

A. Burmeister, K. Talke, D. Leung, M. Baker Jr, and M. Jones, “Explosive initiation safety and handling system for explosive ordnance disposal robots,” Apr. 2 2019. US Patent 10,247,526.

A. Burmeister, K. Talke, D. Leung, M. Baker Jr, and M. Jones, “Explosive initiation safety and handling method for explosive ordnance disposal robots,” Aug. 27 2019. US Patent 10,393,489.

K. A. Talke, “Tether management system for a tethered uav,” June 14 2020. US Patent Pending, App # 16874026.

K. A. Talke, N. Stroumtsos, and D. Drotman, “Device and method for replicating wave motion,” June 29 2021. US Patent 11,049,410.

ABSTRACT OF THE DISSERTATION

Hanging Tether Management
for Unmanned Air - Surface Vehicle Teams

by

Kurt Arthur Talke

Doctor of Philosophy in Engineering Sciences (Mechanical Engineering)

University of California San Diego, 2021

Professor Thomas Bewley, Chair

The mission of an unmanned air vehicle (UAV) tethered to a small unmanned surface vehicle (USV) is considered. The tether doubles as a power umbilical and communications link, providing unlimited flight duration and secure data transfer while limiting mobility. Contrary to the majority of existing tethered UAV work which assumes a taut tether for dynamic stability, this dissertation addresses the challenge of tether management for a slack, hanging tether in a dynamic ocean environment up to sea state 4 on the Douglas scale. For controlled laboratory experimentation, a novel wave and boat motion replication mechanism is developed capable of replicating motion up to 2.2 m heave, 32° roll, and

35° pitch. A reference hanging tether model maximizes heave robustness, providing a target tether length, departure angle, and tension. An effective estimation and control strategy is presented and validated indoor through motion capture experimentation and outdoor using a differential global positioning system (GPS) solution. The foundation of a simulation model for the complete tethered UAV - USV team is developed. The dynamic partial differential equations of motion are derived by treating the tether as a continuous body using Hamilton's principle of least action. A simulation model is then developed, discretizing the elastic tether with linear and quadratic shape functions. Finally, the simulation results are experimentally validated.

The primary contributions of this dissertation include:

1. A novel 3-$\underline{\text{P}}$SR mechanism capable of replicating the pitch, roll, and heave motion of a boat in sea state 4 (see Chapter 2),
2. A catenary hanging cable theory-based model to determine a reference tether length, angle, or tension for maximum heave robustness (see Chapter 3),
3. A relative velocity-based gain scheduled tether management controller (see Chapter 4.2),
4. A Kalman filter model to estimate relative altitude, fusing a slow, relative altitude differential GPS measurement with fast inertial measurements (see Chapter 4.4),
5. The experimental validation of the heave robustness model, filter and controller (see Chapter 6),
6. The derivation of the partial differential equations of motion of a continuous three dimensional elastic string pendulum and UAV-USV team (see Chapter 7), and
7. The development and experimental validation of a quadratic shape function simulation model (see Chapter 8 and Chapter 9).

Chapter 1

Introduction

Lightweight, agile, low cost, unmanned air vehicles (UAV) provide numerous capabilities for a variety of missions and tasks. However, a significant limitation is short mission duration due to battery life, weight and payload capacity, often limited to less than 30 minutes flight time [1]. This compounds when trying to use the UAV to perform any task involving a payload such as cameras or radios. The more payload, the greater thrust required, and the shorter the mission. To overcome short duration flight, similar to the approach of pumping fuel up to a rotorcraft [2], a recent trend has been to provide a power umbilical tether with the power source on the ground or base station, providing for unlimited flight duration [3–5]. Such a persistence of flight capability can greatly benefit emergency and disaster response efforts by providing a secure communication network node or video surveillance in the sky [6], as well as military Intelligence, Surveillance, and Reconnaissance (ISR) missions such as presented here. However, a tether limits the mobility of the UAV and introduces the problem of tether management due to the dynamics and control of the tether. Taut tether flight may also be undesirable since it introduces downward forces on the UAV due to tether tension. These forces must be overcome by increasing UAV thrust, ultimately reducing the overall payload capacity and total power budget.

Most published works in the field of tethered flight are restricted to the taut tether case. Taut tether flight can be used to avoid dealing with tether oscillations [2], improve flight stability [7–11] or enhance landing capability [12–14]. Such systems neglect the reduced payload capacity and increased UAV thrust requirement. They employ either no tether management while the UAV maintains tension with novel linear and nonlinear flight controllers [8, 15], or a tension monitoring winch mechanism that continuously reels in any slack tether length [16]. Station keeping, where the UAV remains stationary, is not possible for systems where the UAV controls tension. Advanced tethered flight challenges have been undertaken, such as landing on an inclined surface [17], coordinated load carrying [18] [19], or using two unmanned ground vehicles (UGV) to control the flying height of a UAV [20]. However, all of the above examples operate with a taut tether, and are not applicable to the present study.

Other systems have considered non-taut tethered flight using a reactive tether management approach [21]. The addition of a tether to a UAV gives an additional measurable feature to develop non-GPS based UAV position estimation techniques. Primarily, the tether arrival angle at the UAV is measured [22], or the tension at the UAV [23], and incorporated into the state estimation algorithm. Another work used the measured tether length, tension, and departure angle as a means for non-GPS position estimation of the UAV based off a catenary cable model [6, 24]. However, the work relies on a clutch-driven winch mechanism and on the UAV for tension control with no consideration of total power budget. These tethered systems consider only a scenario where the base station is stationary, not undergoing any dynamic motion. Other work has considered tethered UAVs with moving platforms, but only under taut conditions with no experimental validation [25]. The above examples do not consider the mission presented here involving a highly dynamic moving base and do not consider any tether management

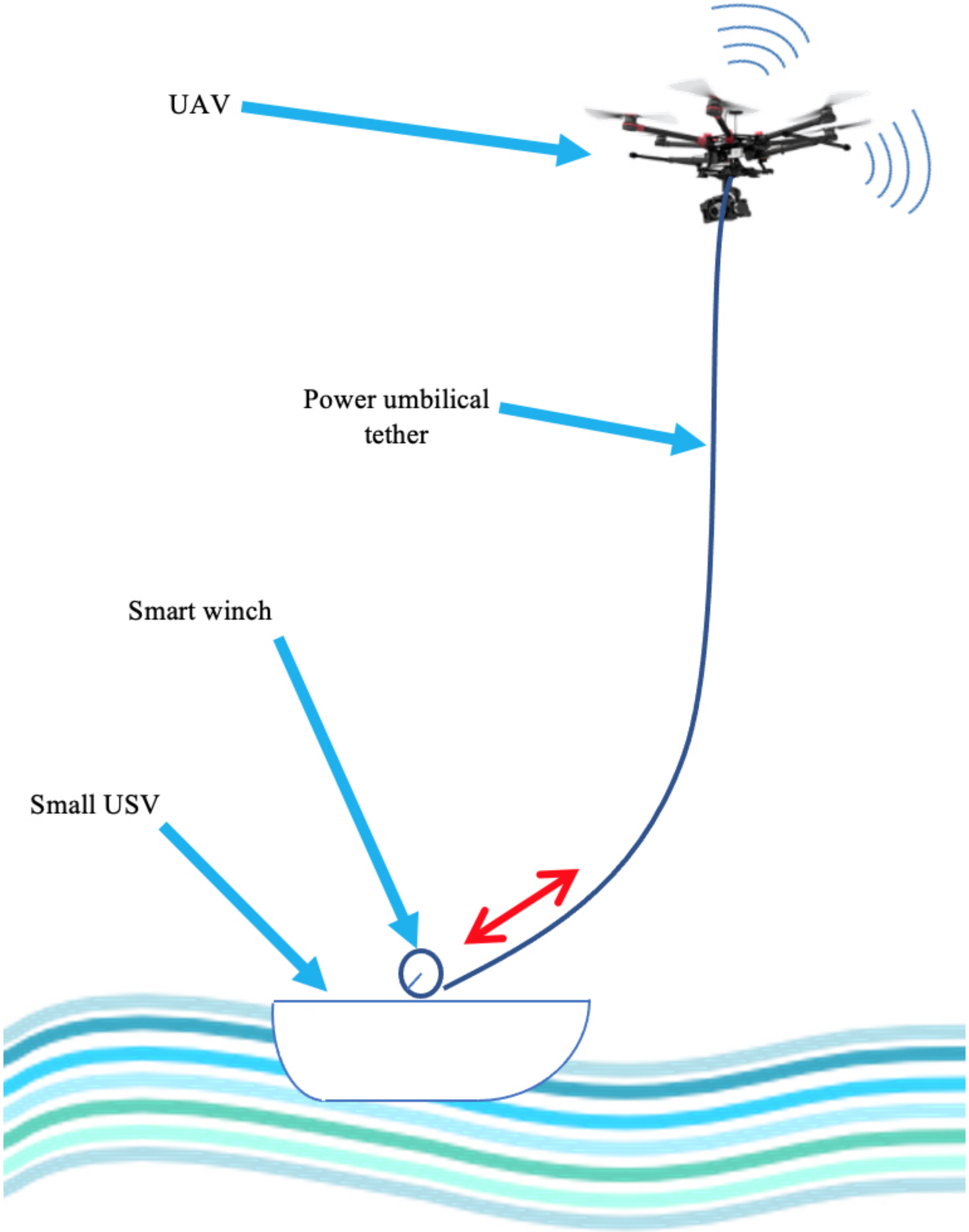

Figure 1.1: Schematic of a tethered UAV USV team in up to sea state 4. The winch system controls tether length to account for the dynamic motion of the small USV, leaving the tether in a hanging, semi-slack state at all time.

The mission schematic for a tethered UAV system considered here is shown in Fig. 1.1. The UAV, flying at up to 50 meters altitude must maintain position, orientation, and altitude for communication or ISR missions. The UAV is tethered to a small, 3 to 7 m length unmanned surface vehicle (USV) subject to a dynamic ocean environment. The power umbilical tether enables long duration UAV flight over 22 hours [26]. However, the total system power budget is limited for small USVs on long duration missions. A reasonable hypothesis is that compared to taut tether flight, a hanging tether can minimize the counteracting tether tension forces, ultimately decreasing power consumption and the required thrust safety margins of the UAV. The fast acting dynamics of an ocean environment are inherently compensated for through the varying sag of the tether. Flying on a non-taut, or hanging tether can decouple the motion of the UAV and USV, but introduces two potential failure mechanisms solved by tether management: preventing the tether going taut affecting UAV flight, or fouling with the USV during a large heave event.

In order to effectively develop, validate, and analyze any prototype and control approach, a repeatable testing environment is needed for replicating open water dynamics and boat motion. A testing platform capable of replicating wave and boat motion allows for land-based testing, reducing costs and the design iteration cycle time. The alternative, of relying on weather conditions to test in specific sea states is too costly, time limiting, and dangerous. Chapter 2, presents the design of a novel, low-cost, 3-$\underline{P}$SR parallel mechanism capable of replicating the full scale range of boat motion up to sea state 4: up to 2.2 m heave, 32° roll, and 35° pitch. A design parameter optimization is presented to maximize the roll-pitch workspace. A three-axis interpolation approach is presented to accurately generate a desired path through the roll-pitch workspace. The 3-$\underline{P}$SR parallel mechanism was fabricated and experimentally validated using an inertial measurement unit (IMU).

For semi-slack hanging tether control, a reference model is necessary. Chapter 3 analyzes the static catenary hanging cable problem and develops a model-based approach for tether management driven by relative position and tether length. A recommended relative flying position is presented considering robustness to vertical motion of the USV. An approximate model is presented in the form of a low order polynomial. This provides a computationally inexpensive approach for determining a reference tether length, angle, or tension. The proposed model allows for a large range of flying positions while lowering overall power consumption. Experimental testing confirms the validity of the proposed catenary tether model.

Chapter 4 develops a tether management prototype design, relative position estimator, and control system for autonomous tether management. The prototype is capable of measuring tether length, departure angle, and tension. With the goal of outdoor operation, a Kalman filter model is developed to fuse a slow, 4 Hertz Real-Time Kinetic differential GPS (RTK dGPS) based relative position measurement with fast, 100 Hertz inertial measurements, to output a fast, 100 Hertz estimate of the relative position, relative velocity, and inertial sensor bias. A relative velocity-based gain scheduled controller was developed to smooth out any errors and discontinuities seen in the Kalman filter at low relative velocities. Chapter 5 describes the phased testing procedure. The experimental approach is split into three stages UAV surrogate, indoor flight, and outdoor flight testing in order to first validate the controller and mechanical prototype, tune and validate the estimation filter, and then evaluate the RTK dGPS solution. Chapter 6 presents the results from experimental testing. The system is experimentally validated through indoor motion capture based experimentation and outdoor RTK dGPS-based experimentation. Indoor experimentation, using a UAV surrogate for a perfectly known, controlled environment, demonstrated the developed estimator and controller greatly reduce tether tension and forces on the UAV compared to taut tether control. Indoor flight testing successfully showed decoupling of USV heave motion from UAV altitude and position, while also demonstrating a similar UAV altitude and position range compared to un-tethered flight. Finally, outdoor flight testing using a dGPS and an IMU-based Kalman filter solution to measure relative position showed the feasibility in an unknown dynamic environment. A hanging tether management system can extend longevity, decrease power consumption, extend mission duration, increase flight altitude, and decrease the required thrust safety margins of the UAV.

In order to eventually develop more capable control methodologies, a complete dynamic model and simulation environment are required. Chapter 7 presents a complete Hamilton's principle derivation of the equations of motion for an elastic string pendulum. In Chapter 8, the continuous body is discretized via the Galerkin finite element method, developing a formulation for one dimensional linear, and quadratic shape functions. Chapter 9 discusses the simulation results, and compares them to experimental three dimensional pendulum motion capture experiment performed to validate the developed numerical model.

This dissertation is outlined as follows. Chapter 2 details the 3-$\underline{\text{P}}$SR wave and boat motion replication parallel mechanism. Chapter 3 derives the heave robustness catenary tether model. Chapter 4 describes the prototype winch, controller and estimator developed. Chapter 5 details the experimental test setup. Chapter 6 presents the experimental validation results. Chapter 7 presents the dynamic derivations of the three dimensional elastic string pendulum dynamics and UAV-USV dynamic equations of motion. Chapter 8 presents the development of linear and quadratic shape function finite element formulations for simulation. Chapter 9 presents the simulation results and validates them with experimental testing. Chapter 10 presents the continued and future work. Finally, Chapter 11 summarizes the key conclusions of this dissertation.

Chapter 2

Design and Parameter Optimization of a 3-$\underline{\text{P}}$SR Parallel Mechanism for Replicating Wave and Boat Motion

This chapter presents the design of a novel, low-cost, 3-$\underline{\text{P}}$SR parallel mechanism capable of replicating the full scale range of boat heave up to sea state 4. A design parameter optimization maximized the roll-pitch workspace. A three-axis interpolation approach is presented to accurately generate a desired path through the roll-pitch workspace. The 3-$\underline{\text{P}}$SR parallel mechanism was fabricated and experimentally validated using an IMU.

The remainder of the chapter is organized as follows. Section 2.1 discusses the relevant mechanism background. Section 2.2 details the design and hardware selection. Section 2.3 derives the relevant geometric constraints to develop the kinematic lookup table. Section 2.4 details and discusses the roll-pitch workspace. Section 2.5 discusses the design parameter optimization approach and results. Section 2.6 discusses the interpolation of the lookup table. Section 2.7 investigates the generation of motion profiles and discusses the experimental results. Section 2.8 details recent improvements. Section 2.9 summarizes the key conclusions.

2.1 Background

The development of the parallel six degree of freedom (6-DOF) Gough-Stewart platform in the 1960s sparked a wealth of research into wave and boat motion simulation and replication. Originally developed for simulating flight [27] and tire testing [28], the platform has been used in a variety of applications, including telescope positioning [29], cnc machining [30], precision surgery [31], wave compensation [32], wave energy conversion [33,34], and floating platform replication for UAV landing [35]. To carry heavy loads, the designs often use a hydraulic piston, which have limited range of extension. The high cost and limited motion from hydraulic pistons limits the capabilities of existing systems, usually resulting in mechanisms that are scaled down. This can be problematic if trying to capture the full heave, or vertical translation displacement of boat motion in large waves. Some 6-DOF and 4-DOF prismatic-spherical-spherical (6-$\underline{\text{P}}$SS, 4-$\underline{\text{P}}$SS) mechanisms on parallel linear rails have been proposed to achieve larger displacements, but not for wave replication [36–38]. Other ship motion replication mechanisms decouple heave from orientation, using lifts to capture the full scale range of vertical motion, but are large and costly [39]. Man made wave pools, like Naval Surface Warfare Center (NSWC) Carderock's Maneuvering and Sea-keeping (MASK) basin have been used for replicating waves [40,41]. These wave replication systems are very expensive to build and use. Often, they are specifically built for recreation and limited to less than 1.25 m waves [42]. There is no existing low-cost system that can capture the full scale range of heave for moderate to high sea states.

For the coordinated UAV-USV scenario, USV motion can be characterized by three orientation DOFs {roll, pitch, yaw} and three translation DOFs {heave, surge, sway}. The dominant DOFs of the USV induced by sea waves are roll, pitch, heave. The other three DOFs {surge, sway, yaw} change at a slower rate, are an order of magnitude smaller, and are often induced by propellers, wind, and currents [43]. Any drift of the minor DOFs motion are more easily gradually corrected by the UAV-USV system. Thus, a reduced 3-DOF mechanism, which has control in the primary DOFs {roll, pitch, heave} is sufficient to capture the major motions of the USV in high sea states. That motion can be accounted for via feedback control applied to the winch system for reliable operation.

Many 3-DOF prismatic-revolute-spherical (3-PRS) and revolute-prismatic-spherical (3-RPS) parallel mechanisms have been proposed and thoroughly analyzed [44–51]. However, these mechanisms don't provide the desired control in the primary DOFs for wave replication {roll, pitch, heave}, with minimal coupling of the minor DOFs {surge, sway, yaw}. By switching the location of the joints, thus creating a 3-DOF prismatic-spherical-revolute (3-$\underline{\text{P}}$SR) parallel mechanism, the desired mobility and control can be achieved. Specifically, the 3-$\underline{\text{P}}$SR design allows for large displacement heave and precise control of 2 orientation DOFs {roll, pitch}.

2.2 Design

A 3-$\underline{\text{P}}$SR parallel mechanism is proposed to replicate the primary DOFs {roll, pitch, heave} for wave replication, similar to one developed for a shipboard stabilization platform [52]. The proposed design, as shown in Fig. 2.1 does not require a redundant fourth link which differentiate it from previous work. The proposed design uses linear guides to achieve the required heave range for sea state 4.

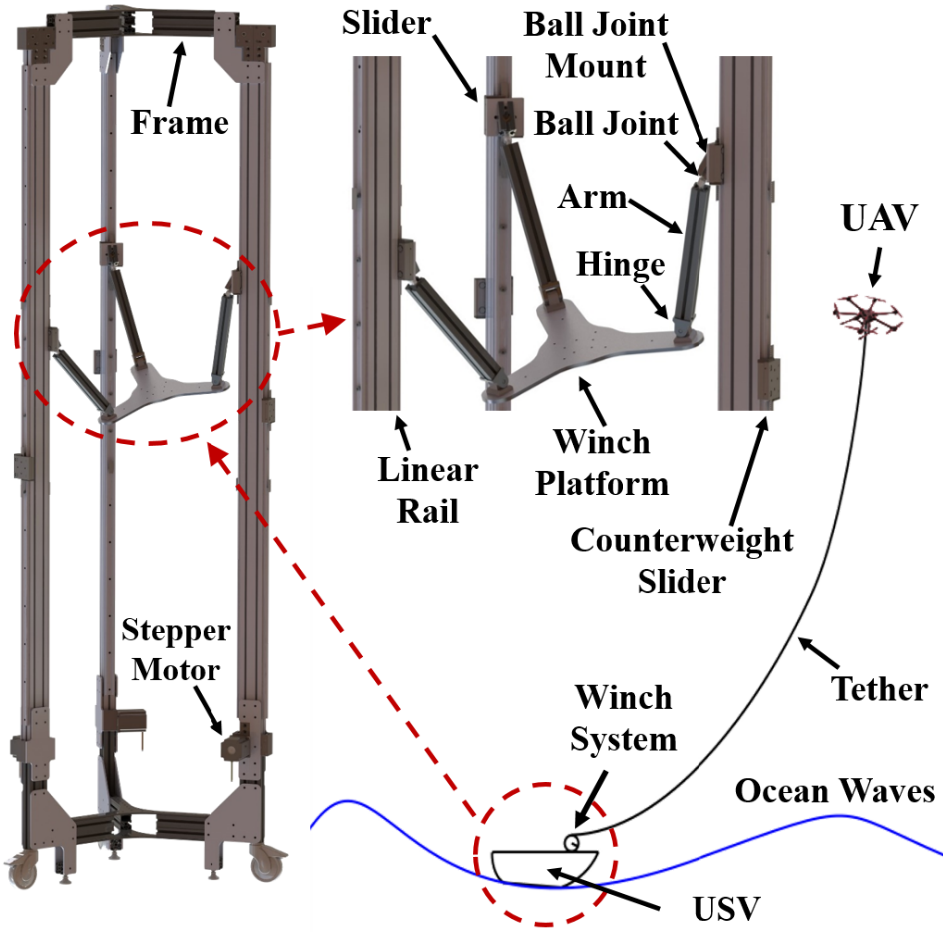

Figure 2.1: Conceptual 3-PSR parallel mechanism for wave and boat motion replication. The sliders on the vertical rails are kinematically linked to the platform, and actuated to replicate the roll, pitch and heave motion experienced by an USV. This specific mechanism is designed for testing a winch controller for a tethered UAV-USV system.

2.2.1 Mechanical Design

To accommodate the large displacement required in the vertical direction, three rails with belt driven actuated sliders are used as prismatic joints. The sliders are attached to three arms through spherical ball joints. The arms then connect to a platform through revolute hinge joints. The platform is large enough to carry the winch system, and can roll and pitch at any height along the vertical rails by changing the relative slider heights according to the workspace lookup table derived in Section 2.4. The radially symmetric

Table 2.1: 3-PSR Prototype Hardware

Hardware	Supplier	Part Number
T-slotted frame	MiniTec	Profile 45x90 F
Linear rail + slide	MiniTec	LR6S + LR6
Timing belt pulley	MiniTec	28.0510/1
Stepper motor	Anaheim Automation	34Y214S-LW8
Motor driver	Anaheim Automation	MBC10641
Micro-controller	Azteeg	X3
Power supply	B&K Precision	9117
Ball joint	Mcmaster	8412K120
Hinge	MiniTec	21.2020
Firmware	Custom	-

equilateral design limits an UAV to 120° of operating space. Similar to an elevator, a secondary slider system acts as a counterweight to ease the static torque requirements of the actuators and prevent catastrophic damage in the event of a failed motor. Low-cost stepper motors allow for a motion profile to be commanded in open loop.

A primary benefit of this design and the following analysis is the ability to scale the design for larger wave heights. By extending the vertical rails, the heave range can be increased. Larger payloads can be achieved by increasing the radius, arm length, and platform size. A higher torque motor can be easily integrated to account for a heavier payload. This design works well in applications where heave is a major component of the required motion, an order or two greater. The platform can be oriented up from the sliders instead of down, which would be beneficial for perfecting the automated landing of an UAV.

2.2.2 Hardware

An experimental prototype was developed using T-slotted extruded aluminum for the frame, fabricated large enough to replicate wave conditions up to 2.5 m heave (sea state

4), with a 5 to 15 second period [53]. A geared belt system was used driven by NEMA 34 stepper motors with a maximum torque of 8.5 N-m, enough to carry a 15 kg payload on the platform. Stepper motor drivers capable of 10 A at 80 V were required to fully use the torque range of the motors. A 3D printer micro-controller based off the Arduino ATMEGA 2560 communicates with the stepper motor drivers. Custom firmware was developed to command motor steps per clock tick, running at 10 Hertz. Table 2.1 lists the specific hardware used. All hardware was purchased for under $6k USD.

2.3 Kinematics

The kinematic derivations in the literature on 3-$\underline{\text{P}}$SR parallel mechanisms are limited, primarily due to the challenge of determining coupling DOFs of the platform for typical inverse kinematic approaches. A previous 3-$\underline{\text{P}}$SR mechanism derived an inverse mapping between the platform and sliders under the assumption that the platform location and orientation are known [52]. They first determined the coupling of the translation DOFs {surge, sway} to determine the platform location when orientation DOFs {roll, pitch} are independently specified. They then use screw theory to solve for the required slider heights. However, they neglect the induced coupling of the orientation DOF {yaw} when two orientation DOFs {roll, pitch} are specified jointly. To reiterate, knowing two orientation DOFs {roll, pitch} does not immediately give the position of corners of the platform for typical inverse kinematic approaches. Because the third orientation DOF {yaw} coupling can not be solved analytically when two orientation DOFs {roll, pitch} are specified, a forward kinematic numerical procedure to develop a lookup table is considered here.

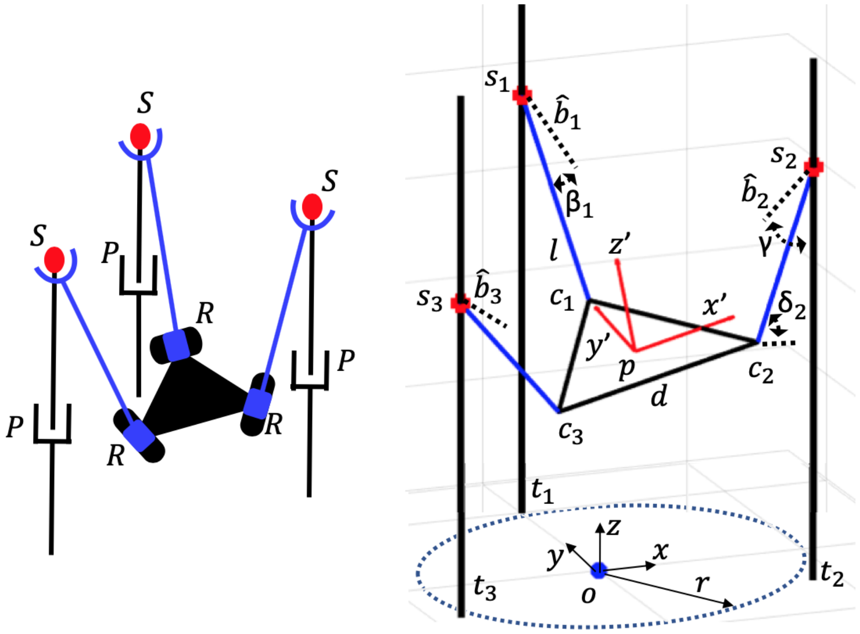

a) b)

Figure 2.2: 3-<u>P</u>SR mechanism schematic. a) Diagram of the linkage structure. b) Design parameters for solving kinematics.

2.3.1 Geometric and Hinge Constraints

Given slider heights for the schematic shown in Fig. 2.2, the spatial coordinates of the corners of the platform can be solved using geometric constraints and hinge constraints for each of the three towers. The distance between the platform corner and slider is defined as:

$$||s_i - c_i|| = l \tag{2.1}$$

where s_i are the coordinates of the slider for the i'th tower, c_i are the coordinates of the i'th corner of the platform, and l is the constant length of the arm. A similar geometric constraint equation specifies the size of the platform:

$$||c_i - c_j|| = d \tag{2.2}$$

where c_j are the coordinates of the j'th corner and d is the edge length of the equilateral shaped platform. The hinge joint constrains the arm to be perpendicular to the back edge of the platform. When perpendicular, the inner product of the vector from the slider to the corner of the platform and the back edge is zero:

$$\langle s_i - c_i, c_j - c_k \rangle = 0 \tag{2.3}$$

where c_k are the coordinates of the k'th corner of the platform.

Combining Eq. 2.1, Eq. 2.2, and Eq. 2.3 for each of the three towers leads to a system of 9 equations with 9 unknowns. The nine unknowns are the x, y, and z coordinates of the three platform corners. This set of equations can be solved with a numerical solver such as the Newton-Raphson (NR) method for any given set of slider heights [54].

2.3.2 Platform Pose

The location of point p, roll, pitch, yaw, hinge, and ball joint angles can be determined knowing the x, y, and z locations of the three corners of the platform. Point p, defined as the center of mass (COM) of the platform, is found from the mean of the x, y, and z coordinates of the corners. The coupled surge, sway, and heave of the platform correspond to the translation of point p. The body coordinate vectors, x', y', and z' define an affine rotation matrix from a unit length coordinate system centered at the origin of the world frame, o. The platform normal vector is found from the normalized cross product of two of the edges.

$$z' = \frac{(c_1 - c_3) \times (c_1 - c_2)}{||\,(c_1 - c_3) \times (c_1 - c_2)\,||} \tag{2.4}$$

The remaining platform body coordinate vectors are found from the normalized vector between corner 1 and point p,

$$y' = \frac{(c_1 - p)}{||\,(c_1 - p)\,||} \tag{2.5}$$

and the cross product of y' and z'.

$$x' = y' \times z' \tag{2.6}$$

The roll, pitch, and yaw angles can be backed out from three separate entries of the 1-2-3 Tait Bryan rotation matrix [55]:

$$\phi = \arcsin {z'}^{(1)} \tag{2.7}$$

$$\theta = -\arcsin \frac{{z'}^{(2)}}{\cos\phi} \tag{2.8}$$

$$\psi = -\arcsin(\frac{{y'}^{(1)}}{\cos\phi}) \tag{2.9}$$

where ϕ is roll, θ is pitch, ψ is yaw, and the 1 and 2 superscripts correspond with the first and second entry of the respective vector. The i'th hinge angle, δ_i, is found from the normalized inner product of the arm vector with the vector from the respective corner to point p:

$$\delta_i = \arccos \frac{\langle c_i - p, s_i - c_i \rangle}{||c_i - p|| l} \tag{2.10}$$

The i'th ball joint angle, β_i, is found from the normalized inner product between the arm vector and the mounting axis as:

$$\beta_i = \arccos \frac{\langle s_i - c_i, \hat{b}_i \rangle}{l} \tag{2.11}$$

where $\hat{b}_i$ is the unit length mounting axis of the ball joint defined by:

$$\hat{b}_i = R\left(\gamma\right)\hat{t}_i \tag{2.12}$$

where γ is the ball joint mounting angle and $\hat{t}_i$ is the unit length vector from the origin to the base of the tower. $R\left(\gamma\right)$ is a rotation matrix to rotate the vector by the ball joint mounting axis angle:

$$R\left(\gamma\right) = \begin{bmatrix} 1 & 0 & 0 \\ 0 & \cos\gamma & -\sin\gamma \\ 0 & \sin\gamma & \cos\gamma \end{bmatrix} \tag{2.13}$$

The equations defined here provide the precise platform pose required to define the workspace for parameter optimization.

2.4 Workspace

The workspace for nominal, nondimensional length parameters is first investigated, i.e., the tower radius, $r = 1$, arm length, $l = 1$, and platform edge length $d = 1$, and then the results are used to optimize these design parameters in Section 2.5. All possible combinations of relative slider heights were simulated apriori to develop a lookup table relating platform pose to slider heights. To capture the entire workspace, the first slider was kept at a height of $2.5r$, and the other two ranged from 0 to $5r$ in 200 increments. For each combination of slider heights, the geometric constraints were solved numerically from Eq. 2.1, Eq. 2.2, and Eq. 2.3 using the tower base coordinates as initial guesses for the NR method. When a numerical solution was found, the roll and pitch angles were calculated using Eq. 2.7 and Eq. 2.8.

2.4.1 Physical Constraints

Two physical constraints are applied to avoid mechanical singularities. First, the platform must physically stay within the towers. The arm vectors must never be parallel with the towers, imposed by only keeping solutions where the inner product between the arm vector and tower vector is greater than 0.

$$\langle s_i - c_i, \hat{t}_i \rangle \geq 0 \tag{2.14}$$

Secondly, the arm can not rotate through the platform, limiting the hinge range from 0° to 180°. This is imposed by only keeping solutions where the inner product between the arm vector and platform normal are greater than 0.

$$\langle s_i - c_i, z' \rangle \geq 0 \tag{2.15}$$

2.4.2 Workspace Results

The workspace for the nominal parameters are shown in Fig. 2.3a. As the design is symmetric across the y-z plane, the workspace is symmetric across the $\phi = 0$ axis. The slider curves, defining the movements of the three sliders, wrap back in on themselves in the regions near the boundaries and corners of the workspace. These regions of kinematic lock corresponds to an extreme platform orientation that can only be achieved after a specified set of slider movements. More specifically, after the platform moves to the boundary of the workspace, it can move back away from the boundary by yawing. The curves stop when the physical constraints are applied, where the mechanism would become singular.

The yaw coupling, as shown in Fig. 2.3b for sub-optimal design parameters, is largest at the extreme roll and pitch angles and regions near the edge of the boundary. The coupling is different for the same roll and pitch combinations in these regions as seen

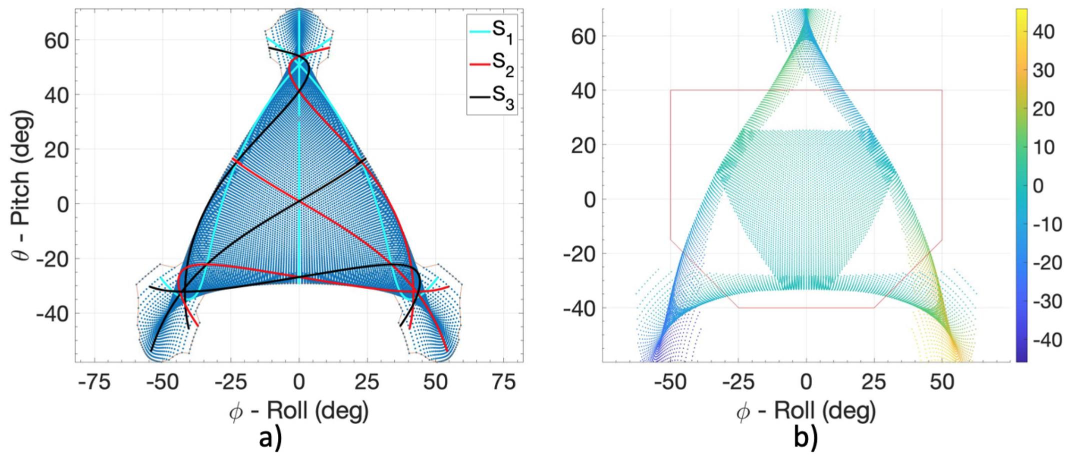

Figure 2.3: Roll - pitch workspace for: a) Nominal design parameters $r = l = d = 1$. The S_1, S_2, and S_3 curves correspond to the path through the space by changing one of the slider heights while keeping the other two constant. The three curves for each slider path correspond to different relative slider heights of the other two sliders. b) Sub-optimal design parameters $r = 1$, $l = 1.1$, and $d = 1.15$. Yaw coupling is shown by the color intensity map. The missing area results from imposing the physical constraints. The roll - pitch workspace inside the polygon was maximized in the parameter optimization.

by the overlapping color intensities. Imposing the physical constraints can potentially leave holes, or disjoint regions in the workspace. These regions represent where the platform would have to travel outside the towers, or the hinge would rotate past 180°, through a mechanical singularity, and potentially invert the platform.

The coupling of the two uncontrollable translation degrees of freedom have similar results, but are not shown. Surge is symmetric across the $\phi = 0$ axis, while sway is inversely symmetric across the same axis. The maximum translation coupling is ∼50% of the nominal scale. For this application, where heave motion is significantly greater than the nominal scale, the yaw, surge and sway coupling are within an acceptable negligible range.

2.5 Design Parameter Optimization

An engineering objective is to find the design parameters which maximize the workspace given the geometric and physical constraints. A parameter study was performed varying l and d relative to r from 50% to 150% in 2.5% increments. For each parameter combination, the area of the boundary of the workspace was calculated. The parameter sets with disjointed workspace were discarded. The regions of kinematic lock at the corners of the workspace were reduced by limiting the hinge angle range from 26° to 180°. This was enforced by normalizing Eq. 2.15 and keeping solutions greater than or equal to .45:

$$\frac{\langle s_i - c_i, z' \rangle}{||\langle s_i - c_i, z' \rangle||} \geq .45 \approx \cos(90^\circ - \delta_i) \tag{2.16}$$

To further remove the regions of kinematic lock from the optimization, the boundary of the workspace was intersected with the polygon shown in Fig. 2.3b. The area of the intersection was then calculated for all parameter combinations and the maximum found.

2.5.1 Ball Joint Mounting Angle

The ball joint used in the prototype is capable of 30° rotation in all directions. For each design parameter set in the nominal optimization, the ball joint axis angle was varied from 20° to 45° in 1° increments. The area of the resulting workspace was calculated such that all ball joint angles within the workspace were less than the physical limit.

2.5.2 Parameter Optimization Results

The scale of this optimization resulted in ~70 million numerical solves of the system of nine equations, which proved computationally intensive. To speed up the process, the optimization was performed on a supercomputer, running all 41 possible combinations

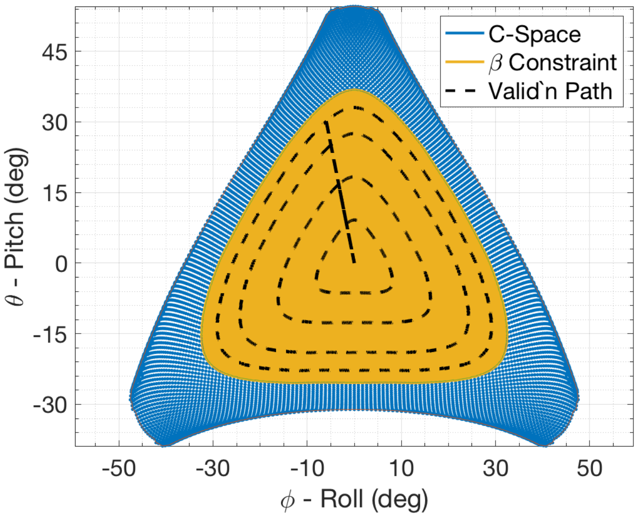

Figure 2.4: Optimized workspace after parameter optimization. The larger region shows the workspace optimization for design parameters $r = 1$, $l = 0.825$, and $d = 1.325$. The smaller region shows the workspace for design parameters $r = 1$, $l = 0.975$, $d = 1.15$, and $\gamma = 30°$ given the ball joint constraint. The motion profile for the workspace validation experiment is shown by the dashed line

of the arm length parameter in parallel. The optimal workspace for both the nominal optimization and the ball joint mounting angle optimization are shown in Fig. 2.4. The regions of kinematic lock have been minimized, and there are no disjoint regions. The region for the ball joint constraint is $\sim 60\%$ of the overall workspace. The roll and pitch range achievable is from -32° to 32° and -25° to 35°, respectively. Table 2.2 catalogs the top six parameters and workspace area. The arm length and platform size change inversely proportional to each other as the area slightly decreases. Table 2.3 catalogs the top six parameters given the ball joint angle constraint and workspace area.

Table 2.2: Top 6 maximum workspace parameters

Rank	1	2	3	4	5	6
Area $(°)^2$	4551.9	4547.1	4543.1	4540.9	4536.8	4535.7
l	0.825	0.85	0.875	0.9	0.925	1.05
d	1.325	1.3	1.275	1.25	1.225	1.1

2.6 Path Generation

A simple way to generate a path through the workspace for simulation and experimentation is to use a high fidelity lookup table with ∼1000 increments between the minimum and maximum slider heights. Such a lookup table results in ∼.1° resolution in roll and pitch. For ∼1000 increments between 0 and $5r$, the slider resolution between points is proportional to the nominal scale as $.005r$. Depending on the scale, this may be much larger than the position accuracy of the stepper motors. Interpolation of the lookup table can improve the accuracy of path generation.

2.6.1 Three Axis Interpolation

A three-axis interpolation approach, as shown in Fig. 2.5, is required to determine s_i^*, the commanded slider heights. Given a desired roll-pitch combination, w_d, the nearest roll-pitch point, w_n, is determined by subtracting w_d from all workspace combinations, $w_{(i,j,k)}$, and finding the minimum value. The vector from w_n to w_d, is projected onto each of the slider motion directions using the inner product. The final slider height for each slider i is determined by adding a scaled, proportional amount of the projection to the slider height, s_i^n corresponding to w_n:

$$s_i^* = s_i^n + \frac{2}{3}\sum_{m=1}^{3}\frac{||\langle w_d - w_n, w_m - w_n\rangle||}{||w_m - w_n||}\Delta h_m \tag{2.17}$$

Table 2.3: Top 6 maximum workspace parameters given the ball joint constraint

Rank	1	2	3	4	5	6
Area $(°)^2$	2816.5	2813.9	2812.7	2811.5	2809.2	2805.1
l	0.975	1.0	1.0	0.95	1.0	1.0
d	1.15	1.075	1.125	1.075	1.05	1.1
$\gamma\,(°)$	30	32	30	34	33	31

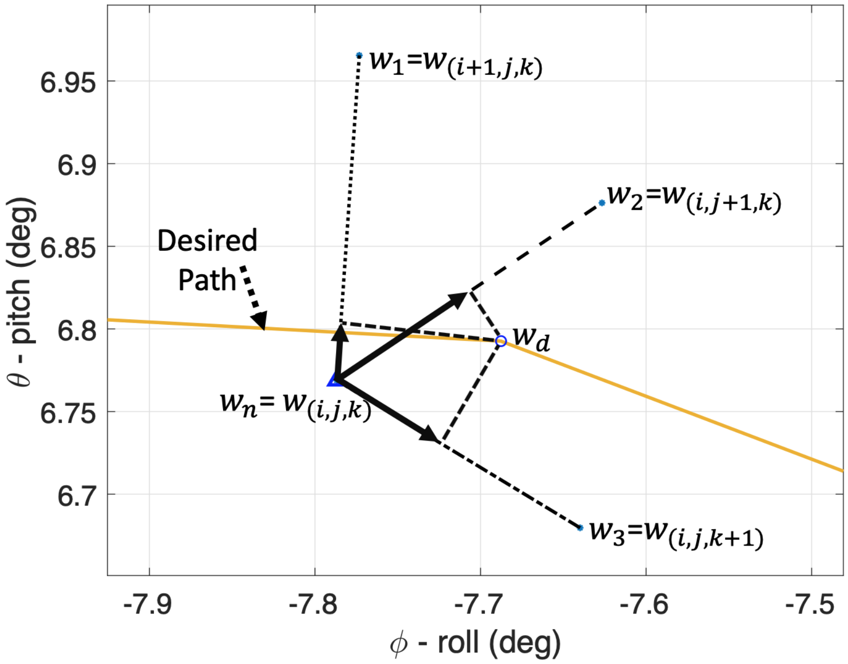

Figure 2.5: Three-axis interpolation approach. The vector from the desired point to the nearest point is projected onto the three directions of motion, then proportionally added to each slider height.

where Δh_m is the slider height change between w_m and w_n. The slider motion profile is then numerically differentiated using a fourth order central difference method to command slider velocity [54].

2.7 Experimental Validation

A prototype was built using the optimal parameters in Table 2.3, scaled up to the minimum size to accommodate an UAV winch payload, resulting in $r = 0.40$ m, $d = 0.46$ m, and $l = 0.39$ m. Fig. 2.6 shows the prototype during testing next to a Matlab simulation showing the same pose. Because the design uses stepper motors and runs in open loop, motion profiles and corresponding slider heights were determined apriori using the three-axis interpolation of the lookup table. Two motion profiles were considered: a profile to validate the workspace and a boat motion profile. Both motion profiles were validated using an

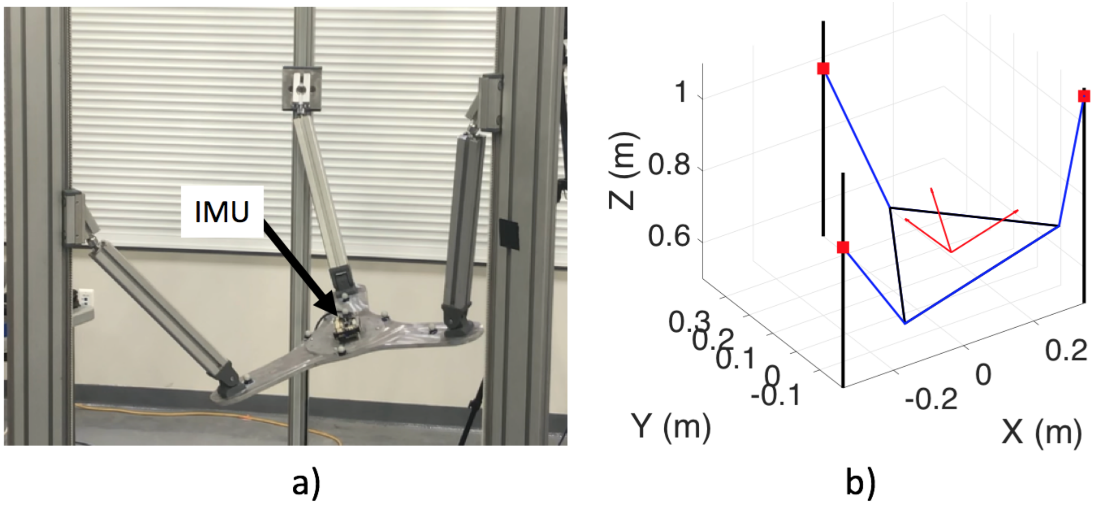

Figure 2.6: Workspace validation. a) Prototype mechanism during workspace motion profile testing. An IMU at the center captures the platform pose. b) Matlab simulator for the same motion profile. Both show near identical pose.

IMU.

2.7.1 Workspace Validation Profile

To test the entire workspace, the ball joint constraint boundary was offset by 25%, 50%, 75%, and 90%. These were connected as the desired motion profile, as seen by the connected level sets path shown in Fig. 2.4. The commanded height of the sliders was adjusted such that the COM had no commanded heave.

Fig. 2.7a shows a typical result from the workspace motion profile. After adjusting for the initialization offset and starting time, the IMU coincides with the commanded profile well. The average error for roll and pitch was 1.2° with a standard deviation of 2.8°. Note that yaw, not shown, is coupled, but remained below 5°.

2.7.2 Boat Motion Profile

An open-source numerical ocean simulator based on the Phillips spectrum was used for generating wave data [56–60]. Fig. 2.8 shows the numerical simulator along with the

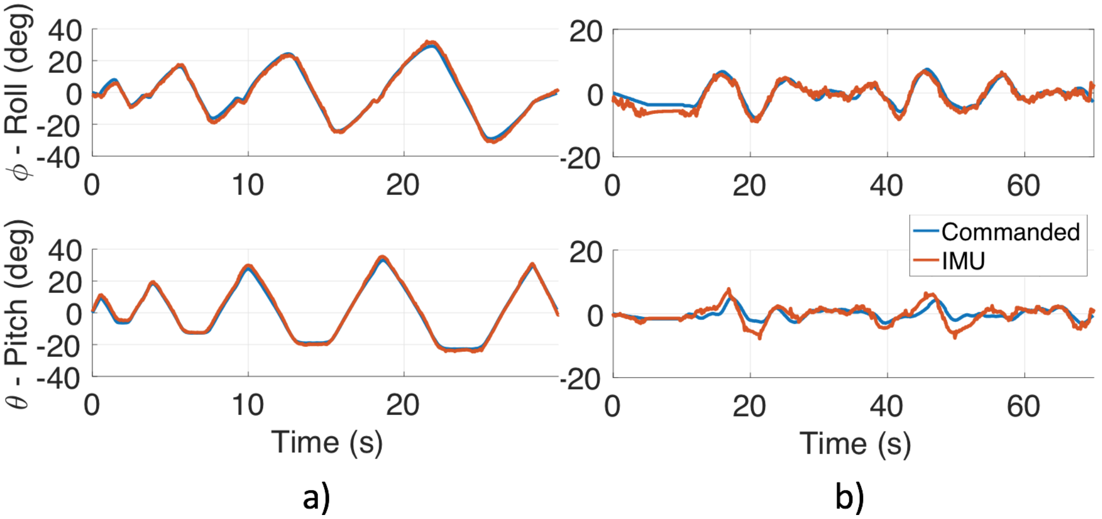

Figure 2.7: Experimental results showing the platform orientation vs. time for a typical trial of the a) Workspace motion profile and b) Wave motion profile. The blue curve is the commanded path, and the red curve the output from the IMU.

specified heave profile. Simulating boat motion in rough waves, or converting known ocean motion to boat motion is a challenging problem [61, 62]. A simplification, used here, is to assume the orientation of the boat is fixed to three separate points on the wave surface, making a plane. From this plane, the specified roll, pitch, and heave can be backed out using a similar calculation to Eq. 2.7, and Eq. 2.8.

Fig. 2.7b shows a typical result from the wave motion profile. The roll and pitch

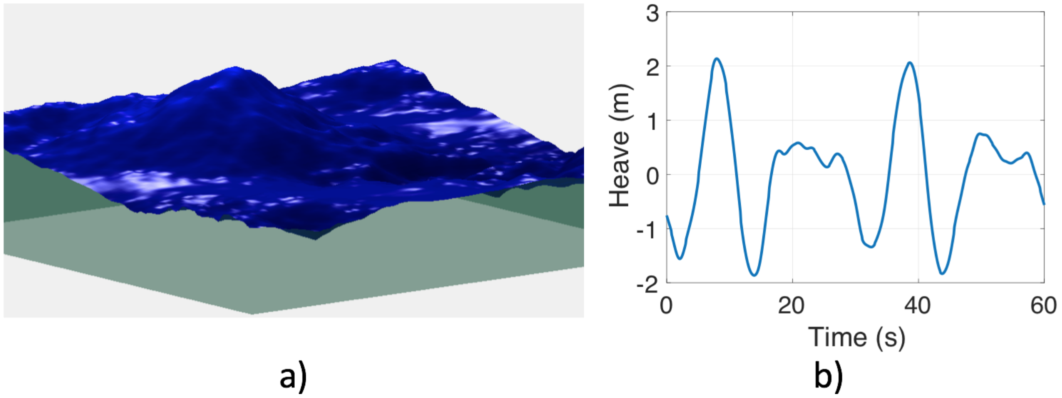

Figure 2.8: Input wave data for the mechanism. a) Numerical simulator for waves up to sea state 4. b) Corresponding boat heave profile.

are seen to follow the commanded paths. The average error for roll and pitch was 1.2° with a standard deviation of 3.1°. The errors in pitch, seen around 20 and 50 seconds can be attributed to spikes in the commanded slider steps, found only after testing. The root cause was linked to the data output from the numerical wave simulator. Using better input data would negate these errors. The vibrations from the stepper motors as slower speeds may have added to the noisier signal.

2.8 Improvements

Since the original publication of this work, a few improvements have been implemented. To improve payload capacity, the original stepper motors were replaced with larger stepper motors, P/N 42Y312S-LW8 from Anaheim Automation. New motor drivers, MLA10641 from Anaheim Automation, running off 110V AC power were used to support the larger motors. For smoother operation, the software was updated to run at 30 Hertz instead of 10 Hertz, and 16:1 microstepping implemented. An IGUS track was mounted to one of the extruded aluminum columns to allow for kink free cable routing to the platform. A hollow pipe was attached to one of the sliders, extending above the frame to be used as a GPS antenna mounting location. Additional boat motion profiles were developed using a Unity engine simulation of a patrol boat using the ultimate water system tool described in Section 5.6 [63].

2.9 Conclusion

In this chapter, a 3-$\underline{\text{P}}$SR parallel mechanism was presented, capable of replicating spectral based ocean wave and boat data for testing a winch system for a tethered UAV. Geometric constraint equations were derived to build a lookup table given the position of the vertical sliders. A parameter optimization resulted in a roll-pitch workspace suitable for replicating ocean waves up to sea state 4. A three-axis interpolation method of the lookup table was presented for more accurate motion profile generation. Experiments were conducted using an IMU to verify the workspace and a wave profile. Experimental results show an error between the actual and desired motion of $\leq 2^\circ$. This ocean wave and boat motion replicator design is low-cost, and easily scale-able for different payload sizes and wave heights. It can be adapted to other use cases by scaling the design parameters and actuator hardware according to the parameter optimization results.

2.10 Acknowledgments

Support for this work was provided by Naval Information Warfare Center Pacific under the Naval Innovative Science and Engineering program and the Department of Defense SMART Scholarship for Service program.

Chapter 2 in full, is a reprint of the material as it appears in IEEE International Conference on Robotics and Automation (ICRA) 2019, K. Talke, D. Drotman, N. Stroumtsos,M. Oliveira, and T. Bewley, “Design and parameter optimization of a 3-$\underline{P}$SR parallel mechanism for replicating wave and boat motion”. The dissertation author was the primary investigator and author of these pages.

Chapter 3

Catenary Tether Shape Analysis for a UAV-USV Team

This chapter analyzes the static catenary hanging cable problem and develops a reference model for tether management driven by relative position and tether length. A recommended relative flying position is presented considering robustness to vertical motion of the USV. An approximate model is presented in the form of a low order polynomial. This provides a computationally inexpensive approach for determining a reference tether length. The proposed model allows for a large range of flying positions while lowering overall power consumption. Experimental testing confirms the validity of the proposed catenary tether model.

The remainder of the chapter is organized as follows. Section 3.1 derives the relevant catenary curve and heave robustness equations. Section 3.2 details the empirical analysis and nondimensionalization over the flying space. Section 3.3 presents and discusses the empirical analysis results. Section 3.4 presents and discusses the experimental results. Section 3.5 details recent improvements. Section 3.6 summarizes the key conclusions.

3.1 Tether Shape Analysis

The goal of the following analysis is to investigate the catenary hanging cable equation in relation to the relative position of the endpoints, and to determine the cable length which can withstand the largest vertical motion of the base endpoint. The analysis assumes that the UAV can lift the cable weight and a winch system operates fast enough to overcome dynamic heave disturbances, wind effects, and tether stiffness, i.e., the tether is assumed to remain in a semi-slack, near minimal tension, quasi-static state. Thus, the static catenary equation, which considers only cable weight and tension is applicable to this case. The desired operating conditions should withstand tether oscillations and wind loading associated with a Douglas sea state 4 [64] and Beaufort wind scale 4-5 [65], i.e., 1.25-2.5 m wave heights over a 5-15 second wave period and wind speeds of 11-21 knots.

3.1.1 Catenary Equation and Parameters Derivation

The free body diagram given in Fig. 3.1 is used to determine the catenary equation and associated parameters. Point A, with angle α, is connected to the USV and the winch mechanism, while point B, with angle β, is connected to the UAV.

A balance of tangential tension and tether weight forces between points B and C, leads to the differential equation:

$$\tan(\beta) = \frac{dy}{dx} = \frac{\lambda g L}{T_0} \tag{3.1}$$

where L is the tether length, λ is the linear density of the tether, g is gravity, and T_0 is the horizontal tension at the vertex. The solution of Eq. 3.1 is given by the general form of the catenary equation [66]:

$$y = y_0 + a\ \cosh(\frac{x - x_0}{a}) = y_0 + \frac{a}{2}\left(e^{\frac{x-x_0}{a}} + e^{-\frac{x-x_0}{a}}\right) \tag{3.2}$$

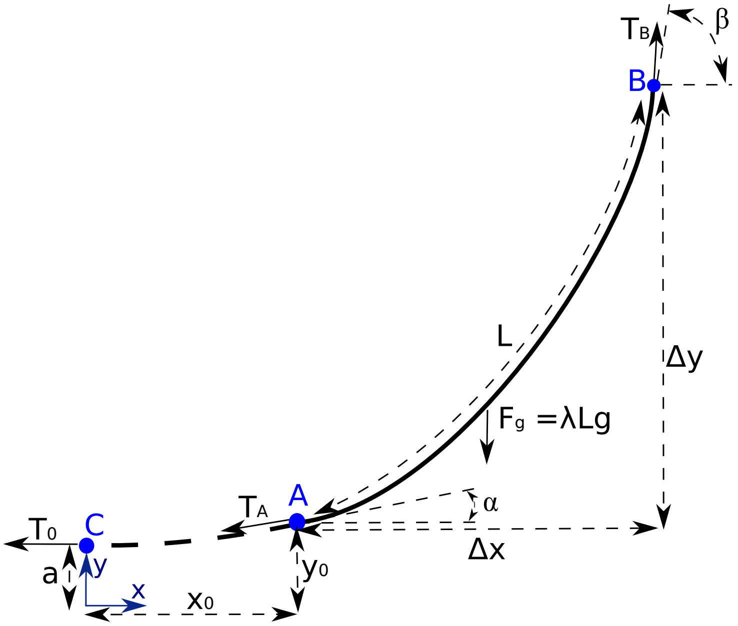

Figure 3.1: Free body diagram of a catenary curve with length, L. The weight of the tether, F_g is offset by the tension at the endpoints, T_0 or T_A, and T_B. Δx and Δy correspond to the relative position, and drive the solution of catenary parameter, a. Point C, the vertex, is used for the determination of the resulting differential equation. x_0 and y_0 represent a shift in the coordinate system.

where y_0 and x_0 are the distances that shift the axes to point A, and a is the catenary parameter defined as:

$$a = \frac{T_0}{\lambda g} \tag{3.3}$$

In relation to the relative position of the endpoints A and B, the catenary parameter, a, can be found numerically from the transcendental equation [67]:

$$\sqrt{L^2 - \Delta y^2} = 2a\ \sinh(\frac{\Delta x}{2a}) \tag{3.4}$$

where $\Delta x, \Delta y$ are the relative positions and L is the known tether length.

The x-axis shift, x_0, can be found once the catenary parameter a has been determined by dividing the quantity $(L + \Delta y)$ and its corresponding catenary equation by $(L - \Delta y)$:

$$\frac{L + \Delta y}{L - \Delta y} = \frac{e^{\frac{x_B - x_0}{a}} - e^{\frac{x_A - x_0}{a}}}{-e^{-\frac{x_B - x_0}{a}} + e^{-\frac{x_A - x_0}{a}}} \tag{3.5}$$

where x_A and x_B are the x-coordinates of points A and B in the coordinate frame. Using the identity:

$$\frac{e^x - e^y}{e^{-y} - e^{-x}} = e^{x+y} \tag{3.6}$$

and solving for x_0 in Eq. 3.5:

$$x_0 = \frac{x_A + x_B}{2} - \frac{a}{2} \ln\left(\frac{L + \Delta y}{L - \Delta y}\right) \tag{3.7}$$

The y-axis shift, y_0, is found by substituting either endpoint into Eq. 3.2:

$$y_0 = y_A - a\ \cosh(\frac{x_A - x_0}{a}) = y_B - a\ \cosh(\frac{x_B - x_0}{a}) \tag{3.8}$$

where y_A and y_B are the y-coordinates of points A and B in this coordinate frame.

The departure angles, α and β, can be found by inserting the derivative of Eq. 3.2 with respect to x into Eq. 3.1.

$$\alpha = \arctan\left(\sinh\left(\frac{-x_0}{a}\right)\right),\ \beta = \arctan\left(\sinh\left(\frac{\Delta x - x_0}{a}\right)\right) \tag{3.9}$$

Performing a balance of forces for points A and B yields the tension at each point. Using the following identities:

$$\begin{gathered}\cos\left(\arctan\left(x\right)\right) = \frac{1}{\sqrt{1 + x^2}},\ \sin\left(\arctan\left(x\right)\right) = \frac{x}{\sqrt{1 + x^2}}, \\ \cosh^2(x) - \sinh^2(x) = 1\end{gathered} \tag{3.10}$$

and knowing that $\cosh(x) > 0$, the tension can be found without having to solve for the angles:

$$T_A = \frac{-\lambda g L \cos\beta}{\sin\alpha\cos\beta - \sin\beta\cos\alpha} = \frac{-\lambda g L \cosh\left(\frac{-x_0}{a}\right)}{\sinh\left(\frac{-x_0}{a}\right) - \sinh\left(\frac{\Delta x - x_0}{a}\right)} \tag{3.11}$$

$$T_B = \frac{-\lambda g L \cos\alpha}{\sin\alpha\cos\beta - \sin\beta\cos\alpha} = \frac{-\lambda g L \cosh\left(\frac{\Delta x - x_0}{a}\right)}{\sinh\left(\frac{-x_0}{a}\right) - \sinh\left(\frac{\Delta x - x_0}{a}\right)} \tag{3.12}$$

Given any relative position and tether length, all necessary parameters for the tether shape and tension are now known.

3.1.2 Heave Robustness

If the assumption that the winch can manage all dynamic disturbances fails, the effects on the UAV can be minimized by operating at a tether length, L_{rob}, best suited to handle heave, the vertical displacement of the USV. The heave robustness tether length allows for equal vertical displacement of the USV to specified limits while the tether length remains unchanged. As shown in Fig. 3.2, in the upward heave case, Δy_1, the limit is chosen to be the slack tether condition, where $\alpha = 0$. In the downward heave scenario, Δy_2, the limit is chosen to be a percentage increase in tension, T_{rob}, from the slack length tension, T_{slack}.

For the upward heave scenario, where the vertex of the curve is at point A, i.e., $x_A = x_0 = 0$, the derivative of Eq. 3.2 with respect to x can substituted into Eq. 3.1, yielding:

$$L = a_1 \ \sinh(\frac{\Delta x}{a_1}) \tag{3.13}$$

The new upward heave catenary parameter, a_1, can be found numerically for this transcendental equation, and Δy_1 can be solved as:

$$\Delta y_1 = \Delta y - a_1 \cosh\left(\frac{\Delta x}{a_1}\right) + a_1 \tag{3.14}$$

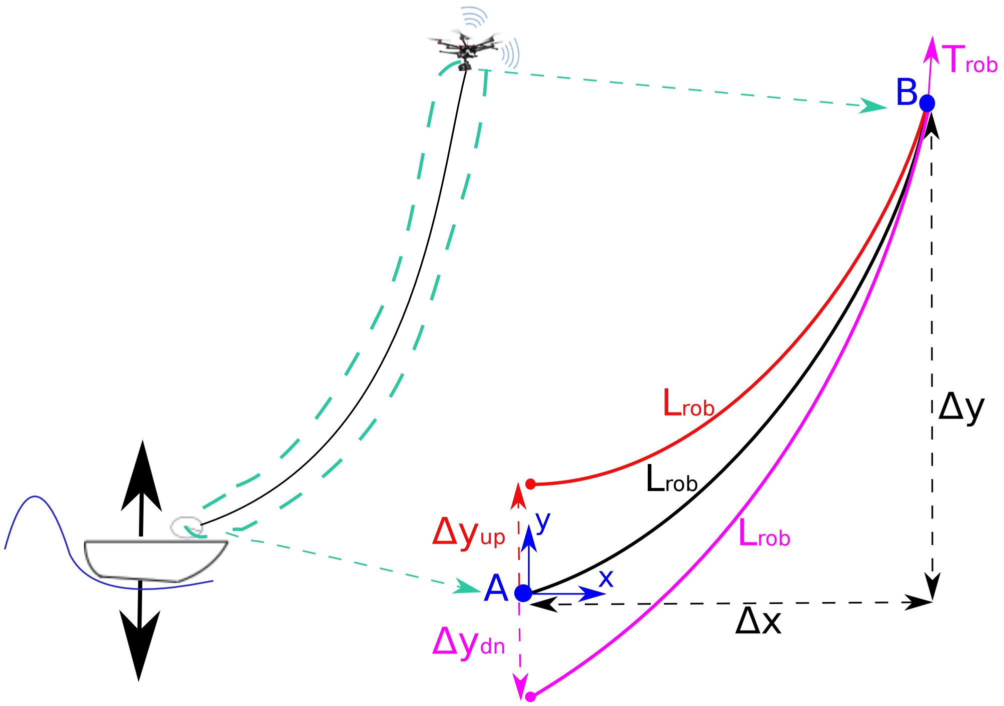

Figure 3.2: Robustness margin determination for heave displacement of the lower endpoint. An operating tether length, L_{rob}, which gives equal heave tolerance both upward, Δy_1, and downward, Δy_2, is desired.

In the downward heave scenario, Δy_2 is introduced into Eq. 3.4, and the new catenary parameter, a_2, cannot be found numerically as both Δy_2 and a_2 are unknown:

$$L_{rob}^2 - (\Delta y_2 + \Delta y)^2 = 2a_2 \ \sinh(\frac{\Delta x}{2a_2}) \tag{3.15}$$

A so-called shooting method approach [54] can be used to find L_{rob}, by assuming $\Delta y_1 = \Delta y_2$. By first solving for Δy_1 using Eq. 3.14 for a given tether length, the catenary parameter, a_2, can be found using Eq. 3.15. With the tension found from Eq. 3.12, L_{rob} can then be found by iterating over the tether length, increasing the length from the slack length, L_{slack}, where $\alpha = 0$, until $T_B \geq T_{rob}$, at which point the tether length will be L_{rob}.

3.2 Analysis of Flying Space

Due to the transcendental nature of Eq. 3.4, a purely analytic solution cannot be found. A "brute force" empirical analysis of the flying space can be performed to find an appropriate relative position for flying and robustness to heave tether length.

3.2.1 Analysis Limits

The flying heights of interest are in the range of $0 < \Delta y \leq 60$ m. The corresponding horizontal offset is $0 < \Delta x \leq 60$ m. Discretization is performed in .5 m increments. For each combination of relative positions, $(\Delta x_i, \Delta y_j)$, 480 tether lengths were considered, limited by a minimum length corresponding to the taut tether length and a maximum length chosen large enough to capture the minimum tension length. A sample discretization is shown in Fig. 3.3. Clearly, operational limits lie between the taut and slack tether length to ensure the tether does not sag into the water. The empirical analysis described involves solving for the minimum tension length, L_{Tmin}, departure angles, α and β, and tether tension, T_B, for each of the 480 tether lengths for all 14,400 combinations of relative position. A tether density of $\lambda = 0.042\ \frac{\text{kg}}{\text{m}}$ was used for analysis and experimentation.

3.2.2 Nondimensionalization

The empirical analysis for each flying height combination can be reduced by finding a scaling factor that results in a non-dimensional relative position parameter. Intuitively, an α and β for the taut, slack, and minimum tension tether shapes should be the same for proportional relative positions, i.e., $(25\text{ m}, 25\text{ m})$ and $(50\text{ m}, 50\text{ m})$. By rearranging Eq. 3.4 and scaling the catenary parameter, a, by the relative height, Δy, the nondimensional

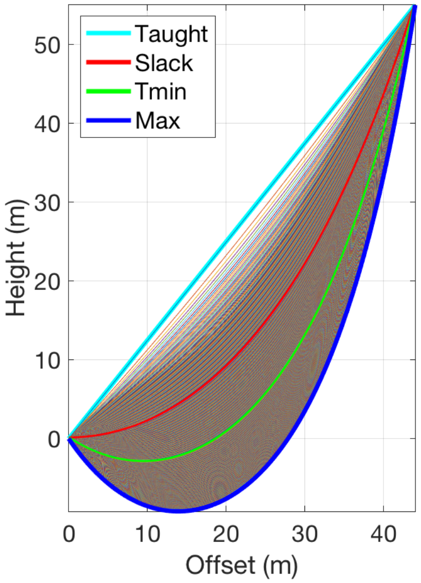

Figure 3.3: Example catenary tether shape discretization for $\Delta y = 55$ m and $\Delta x = 44$ m, with 480 tether lengths discretized evenly between 70.4 m and 92.5 m. The taut tether is shown in cyan; slack tether in red; minimum tension tether in green; max length tether in blue.

relative position parameter is found to be $\Delta x/\Delta y$.

$$\sqrt{\left(\frac{L/\Delta y}{2a}\right)^2 - \left(\frac{1}{2a}\right)^2} = \sinh\left(\frac{\Delta x/\Delta y}{2a}\right) \tag{3.16}$$

The length is now also scaled by the relative height. The relative height scaling propagates through to the tension, as seen in Eq. 3.11 and Eq. 3.12, since tension scales linearly with length. Thus, the empirical analysis for each relative position can be combined by scaling the horizontal offset, tether length, and tension by the relative height at both endpoints.

3.3 Analysis Results

The following results give a convenient model for determining the reference tension, length, and angle parameters for a given relative flying position.

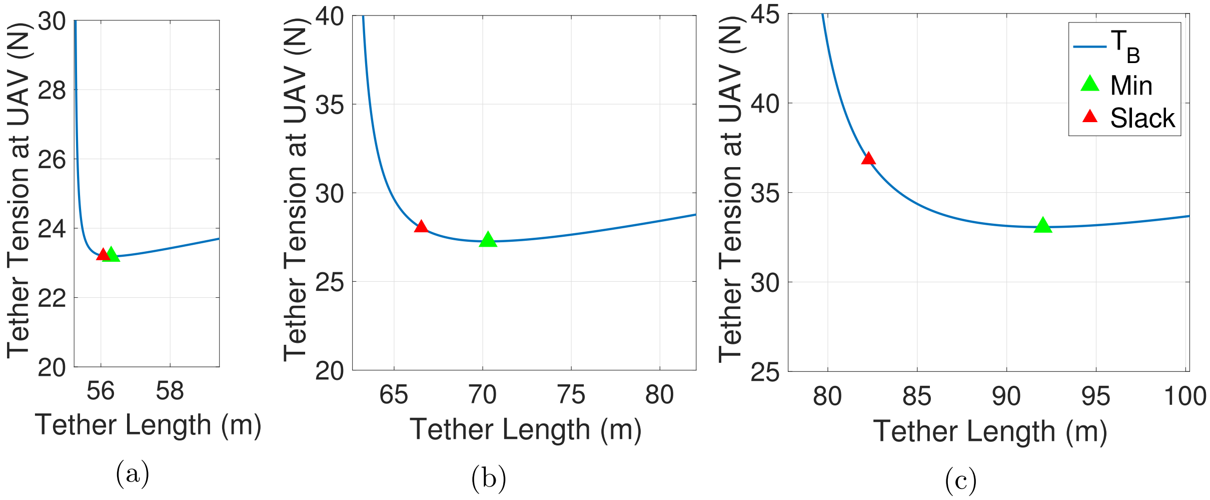

(a)

(b)

(c)

Figure 3.4: Comparison of tether tension vs. length for $\Delta y = 55$ m and (a) $\Delta x = 5$ m, (b) $\Delta x = 30$ m, and (c) $\Delta x = 55$ m. The slack length, shown by the red marker, is shorter and lies to the left of the minimum tension, shown by the green marker. The separation between these two points increases with offset (a)→(c).

3.3.1 Characteristic Result

The tether tension at the UAV for a flying height of $\Delta y = 55$ m and three horizontal offsets is shown in Fig. 3.4. These curves show that a minimum tension length exists, and that operating at that tether length minimizes the UAV thrust and power consumption. To the left of the minimum, tension increases rapidly due to the change in direction of the tension vector at the base. To the right of the minimum, the increase is much slower due to the fact that only tether weight increases while the tension vector direction remains relatively unchanged. In both Fig. 3.3 and Fig. 3.4, the minimum tension length is greater than the slack length and lies outside the operating region. The robustness to heave length lies in the critical region to the left of the slack length since the slack length is the maximum tether length limit due to the risk of fouling.

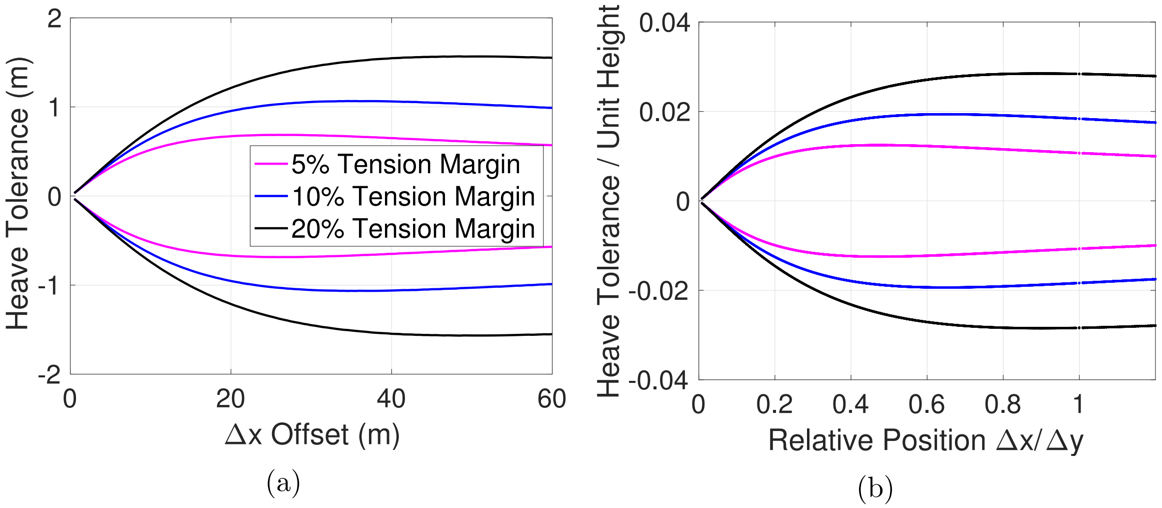

Figure 3.5: Robustness margin empirical results as a function of offset (a) for $\Delta y = 55$ m and (b) combined nondimensionalized data. The two curves for each margin show the heave tolerance in both upward and downward directions, with the origin corresponding to no heave tolerance.

3.3.2 Heave Robustness Margins

The tolerance to vertical displacement of the USV results are shown in Fig. 3.5. The margins increase rapidly with offset until a maximum is reached around 25 m in Fig. 3.5a, or at .46 in Fig. 3.5b for the 5% tension limit margin. The values taper off slowly thereafter. The inflection point corresponds to the point where the shooting method limiting factor switches from the slack length limit to the tension limit. It is also the recommended relative operating position, where the difference between the upward and downward heave tolerance curves is largest.

3.3.3 Tether Tension

Empirical results for the tether tension are shown in Fig. 3.6. For an offset less than 50% of the flying height ($\Delta x/\Delta y \leq .5$), the slack length and heave robustness length tensions remain nominally within 10% of the minimum tension. The nondimensionalized data shown in Fig. 3.6b combines all 14,400 empirical analysis “data” points into individual

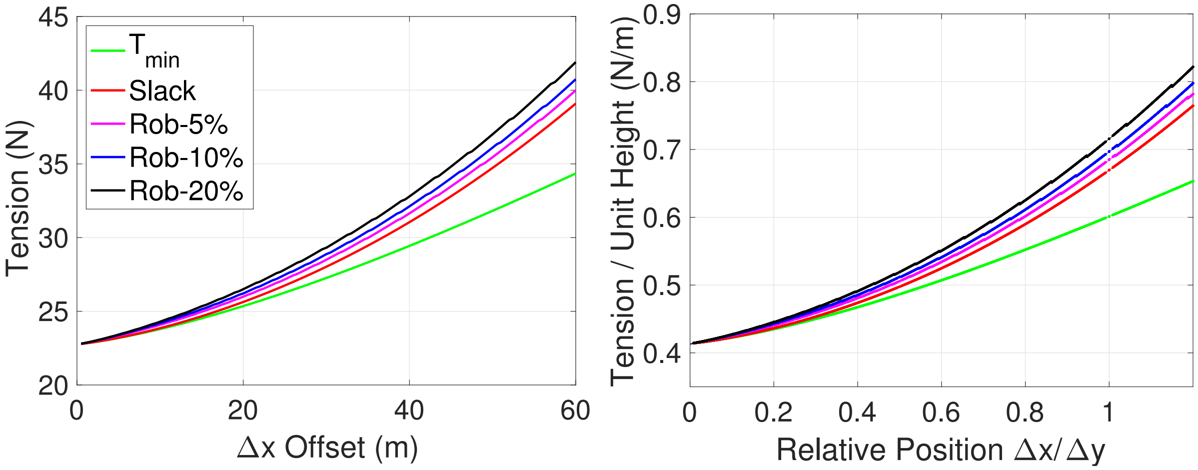

(a) (b)

Figure 3.6: Tension at the UAV empirical results as a function of offset (a) for $\Delta y = 55$ m and (b) combined nondimensionalized data. The heave robustness margin tether tensions have been plotted for a 5%, 10%, and 20% increase in tension from the slack length tension, and are shown slightly offset from the slack length tension curve.

curves that can be approximated as a 3rd order polynomial:

$$T = \lambda \left(c_1 \Delta y + c_2 \Delta x + c_3 \frac{\Delta x^2}{\Delta y} + c_4 \frac{\Delta x^3}{\Delta y^2} \right) \tag{3.17}$$

with coefficients, c_1, c_2, c_3, c_4, and coefficient of determination, R^2, shown in Table 3.1 for normalized $\lambda = 1$. As seen in Eq. 3.12, the tether tension scales linearly with tether density. This is also true for the polynomial fit.

Table 3.1: Nondimensional tension polyfit coefficients

T	c_1	c_2	c_3	c_4	R^2
T_{min}	9.7864	2.0294	3.3904	-0.9513	1
T_{slack}	9.7886	2.0226	3.8953	0.1676	1
T_{rob5}	9.8038	2.5078	3.5501	0.3644	1
T_{rob10}	9.7940	2.8427	3.4364	0.4404	1
T_{rob20}	9.7838	3.1106	3.7257	0.3463	1

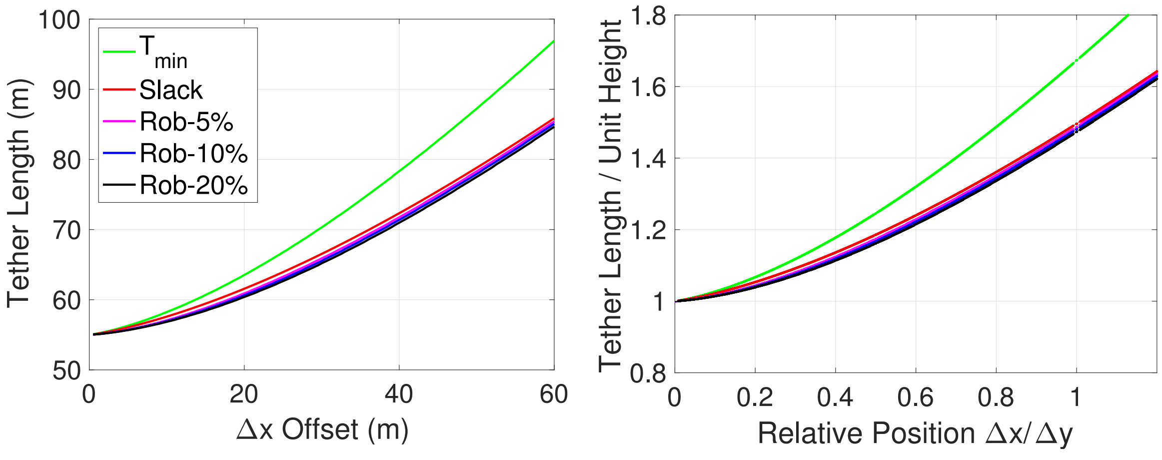

(a) (b)

Figure 3.7: Length empirical results as a function of offset (a) for $\Delta y = 55$ m and (b) combined nondimensionalized data. The tether length increases with offset as physically required, and again the heave robustness lengths offset the slack length data.

3.3.4 Tether Length

The tether length empirical results are shown in Fig. 3.7.

The analysis data can again be fit into a 3rd order polynomial:

$$L = c_1 \Delta y + c_2 \Delta x + c_3 \frac{\Delta x^2}{\Delta y} + c_4 \frac{\Delta x^3}{\Delta y^2} \tag{3.18}$$

with the curve fit coefficients, c_1, c_2, c_3, and c_4, shown in Table 3.2. Given the relative position, a reference length can be computed rather than using a lookup table. A quantitative test to determine the reference tether length using a computer with a 3.1Ghz processor

Table 3.2: Nondimensional tether length polyfit coefficients

L	c_1	c_2	c_3	c_4	R^2
L_{min}	0.9972	0.2406	0.5849	-0.1497	1
L_{slack}	0.9976	0.2094	0.3752	-0.0862	1
L_{rob5}	0.9964	0.1514	0.4674	-0.1280	1
L_{rob10}	0.9974	0.1283	0.4888	-0.1335	1
L_{rob20}	0.9982	0.1127	0.4906	-0.12831	1

and 16GB ram showed an increase in speed of 2300 times for the polynomial evaluation compared to using a lookup table. The least square curve fits have a $R^2 = 1$, giving high confidence in the fit. These polyfit coefficients are independent of linear density.

3.3.5 Departure Angles

The departure angle empirical results are shown in Fig. 3.8. For a horizontal offset less than 50% of the flying height, the heave robustness length angles vary between 40 and 10 degrees and track the minimum tension angle. Thereafter, they are bounded by the slack length angle. The nondimensional data is again modeled as a polynomial:

$$\alpha = c_1 + c_2 \frac{\Delta x}{\Delta y} + c_3 \left(\frac{\Delta x}{\Delta y} \right)^2 + c_4 \left(\frac{\Delta x}{\Delta y} \right)^3 + c_5 \left(\frac{\Delta x}{\Delta y} \right)^4 \tag{3.19}$$

with curve fit coefficients, c_1, c_2, c_3, c_4, and c_5, shown in Table 3.3. In order to keep the R^2 confidence value near 1, a 4th order and only a 2nd order fit were needed for the 5%

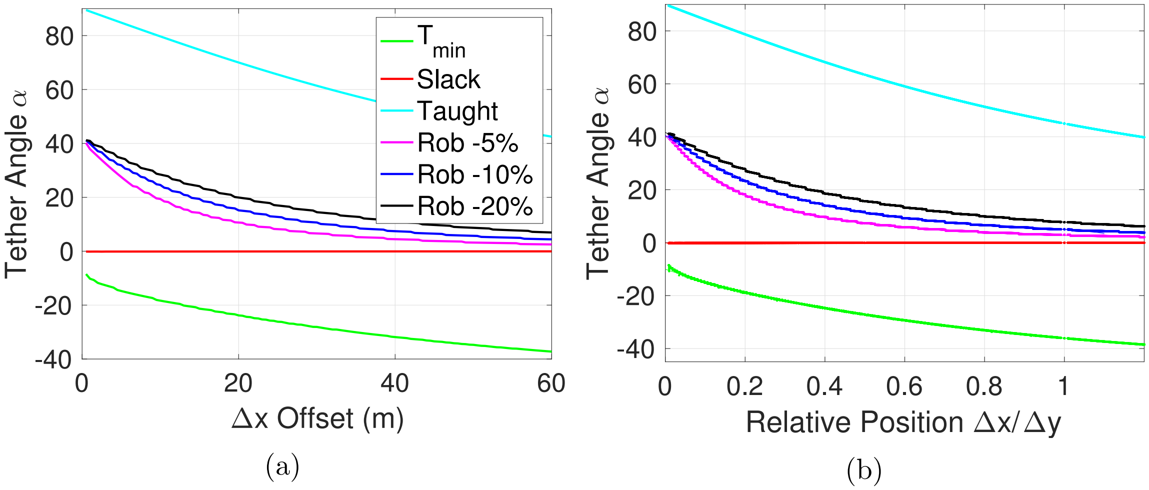

(a) (b)

Figure 3.8: Departure angle at boat empirical results as a function of offset (a) for $\Delta y = 55$ m and (b) combined nondimensionalized data. The minimum tension angle, shown in green, is negative, representing the tether dipping down into the water and a high risk of fouling. The heave robustness angles are shown within the operating region between the taut and slack length angles.

heave robustness and taut angles, respectively. These polyfit coefficients are independent of linear density.

For the angle at the UAV, β, the difference in the minimum tension, heave robustness, and slack length angle is negligible. This is a benefit, since one does not need to reserve critical payload budget for a sensor to measure the angle.

3.3.6 Combined Results

By combining Fig. 3.5a, 3.6a, 3.7a, and 3.8a, for $\Delta y = 55$ m, it can be argued that operating at a horizontal offset set point of 20 m provides $\sim$ .75 m heave tolerance in each direction. For this case, one sacrifices less than a 10% increase in nominal tension, while having enough resolution in tether length and departure angle to give the ability to control to the reference. While these figures exist for every combination of relative position in the analysis, the nondimenionalized curve fit polynomials give a single equation model for any flying position. Given the relative position, the reference heave robustness tether length can be determined, along with the predicted tether tension and departure angles. Indeed, the recommended relative offset for maximizing heave robustness while keeping the nominal tension increase small is $\Delta x/\Delta y \approx .46$.

Table 3.3: Nondimensional angle polyfit coefficients

α	c_1	c_2	c_3	c_4	c_5	R^2
α_{min}	-10.0482	-49.6974	36.8857	-13.2127	-	.99
α_{taut}	90.3299	-62.0733	16.7069	-	-	1
α_{rob5}	40.3217	-162.7497	309.9161	-280.6729	95.8555	.99
α_{rob10}	40.5363	-105.5804	116.5771	-46.5409	-	.99
α_{rob20}	41.6537	-84.6802	79.7592	-28.9605	-	.99

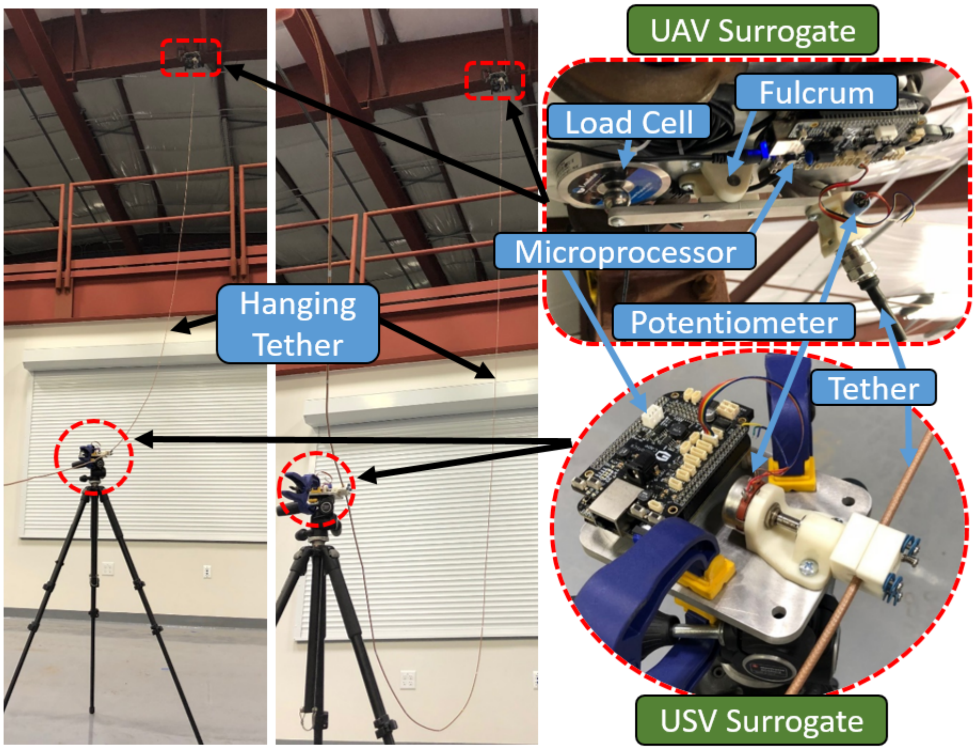

Figure 3.9: Test setup showing two different length configurations on the left, and the UAV surrogate platform and USV surrogate platform on the right. Potentiometers collect departure angles, α and β, and a fulcrum converts the tension load into compression for a load cell to read. A microprocessor was used to read the data in both locations.

3.4 Experimental Validation

The goal of the following experiment is to show that the proposed tether for the given UAV/USV flight scenario conforms to the catenary analysis in Section 3.3.1 and that the approximations detailed in the remainder of Section 3.3 are valid.

3.4.1 Test Setup

The test setup to is shown in Fig. 3.9. The tether is rigidly mounted to a UAV surrogate platform capable of measuring the vertical component of the tether tension, T_{B_v}, and the departure angle, β. The tether is connected to a fulcrum that converts the tension load into compression for the load cell. At both the upper and lower ends of the tether,

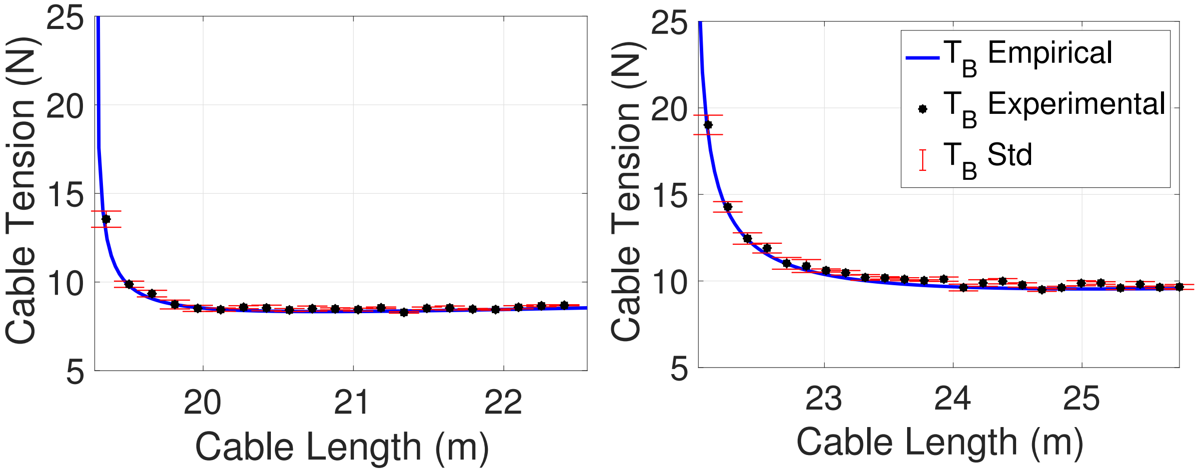

(a) (b)

Figure 3.10: Typical experimental results for tension vs. length, shown for $\Delta y = 18.29$ m and (a) $\Delta x = 6.10$ m, and (b) $\Delta x = 12.19$ m. The mean and standard deviation are shown on top of the empirical analysis results for 20 experiments at each cable length.

a potentiometer measures the departure angle. A microprocessor is used to record the data via a WiFi connection. Using the angle measurement and a force moment balance around the fulcrum, one can calculate the tether tension, T_B. The tether length was marked initially, and recorded for each measurement. Due to the limitations from the building height, testing was performed at three vertical offsets, $\Delta y = 4.87$ m, 12.19 m, and 18.29 m. The horizontal offset for each started test at $\Delta x = 1.52$ m, 3.05 m, and 3.05 m, respectively, and increased in increments of 1.52 m until the vertical offset or the building limit max offset of 13.72 m was reached.

3.4.2 Experimental Results

Static tether tension and departure angle experiments were performed for 18 combinations of vertical and horizontal offsets. Fig. 3.10 shows a typical result for the tension at the UAV surrogate, T_B. The experimental tension results agree with the empirical analysis results for the two relative positions shown. The same agreement was observed for those results not shown. The tension data capture the sharp decline, the minimum, and slow increase as the tether length increases. The small variability, shown by the standard deviation in the measurements is likely due to the tether not completely reaching steady state. Specifically, the standard deviation is greater at the shorter tether lengths. The tether exhibited small dynamic oscillations, particularly when under higher tension. The time for those oscillations to settle out was prohibitively long for data gathering purposes. Given enough time to settle, the standard deviation would likely decrease even more for the shorter lengths, higher tension measurements.

Table 3.4 shows the average error and standard deviation for all tension measurements of the 18 relative position experiments. All experiments had an average error within 7% of the empirical catenary analysis. All but three of the experiments had a standard deviation of less than 3.6%. The three outliers were due to dynamic oscillations caused by the tether not fully reaching steady state. The average error and standard deviation for all measurements was 3.8% ± 3.3%. Comparing the three vertical offsets, the error decreases as Δy increases. Sensor measurement, setup, and cable density errors play a larger role at low Δy due to the smaller overall tensions, i.e., the errors are proportionally larger in this case.

Table 3.4: Tension experimental error ± standard deviation from empirical analysis per relative position

Δx	Δy = 4.87 m	Δy =12.19 m	Δy =18.29 m
1.52 m	6.4 % ± 2.9 %	-	-
3.05 m	6.7 % ± 5.0 %	4.4 % ± 10.9 %	1.8 % ± 1.5 %
4.57 m	2.7 % ± 2.0 %	4.0 % ± 3.4 %	4.5 % ± 5.6 %
6.10 m	-	3.4 % ± 2.7 %	1.6 % ± 1.5 %
7.62 m	-	3.2 % ± 2.3 %	4.9 % ± 2.9 %
9.14 m	-	5.1 % ± 3.6 %	3.3 % ± 2.5 %
10.67 m	-	3.0 % ± 2.1 %	3.5 % ± 2.0 %
12.19 m	-	2.8 % ± 1.9 %	2.5 % ± 1.7 %
13.72 m	-	-	2.7 % ± 2.8 %
Mean	5.2 % ± 3.3%	3.7 % ± 3.8 %	3.1 % ± 2.6%

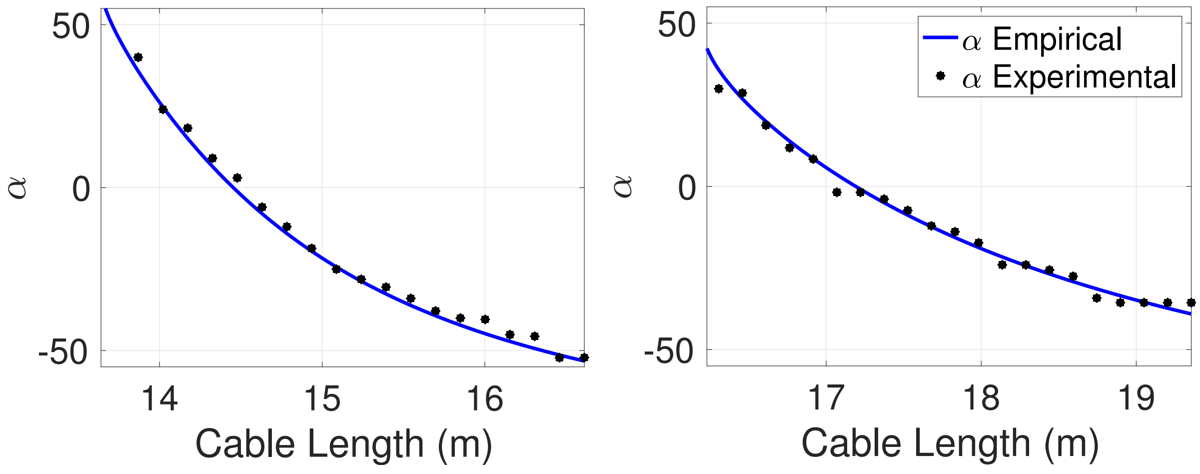

(a) (b)

Figure 3.11: Typical experimental results for α vs. length, shown for $\Delta y = 12.19$ m and (a) $\Delta x = 6.10$ m, and (b) $\Delta x = 10.67$ m. The data shown is the mean of 20 measurements at each length.

Fig. 3.11 shows a typical result for the departure angle, α, at the base. The experimental departure angles agree with the empirical analysis results for the two relative positions shown. This is also observed for those results not shown. The measurements at each length did not vary significantly enough to justify a standard deviation calculation. Much of the error between the empirical analysis and the experimental results can be attributed to the experimental setup. As seen in Fig. 3.9, the tether did not terminate at the base surrogate. The departure angle measurement clamped onto the tether, with the remaining tether maintaining the shape and departure angle only by being held properly by the data gatherer. Fortunately, this measurement, and associated error has minimal or no effect on the tension measurement, T_B, and the tension at the base, T_A, was not measured.

Fig. 3.12 shows typical results for the departure angle, β, at the UAV surrogate. The experimental departure angle results agree with the empirical analysis results for the two relative positions shown, as well as for those not shown. Again, the sensitivity of the potentiometer did not justify a standard deviation calculation.

The experimental results for these 18 relative position operating conditions confirm

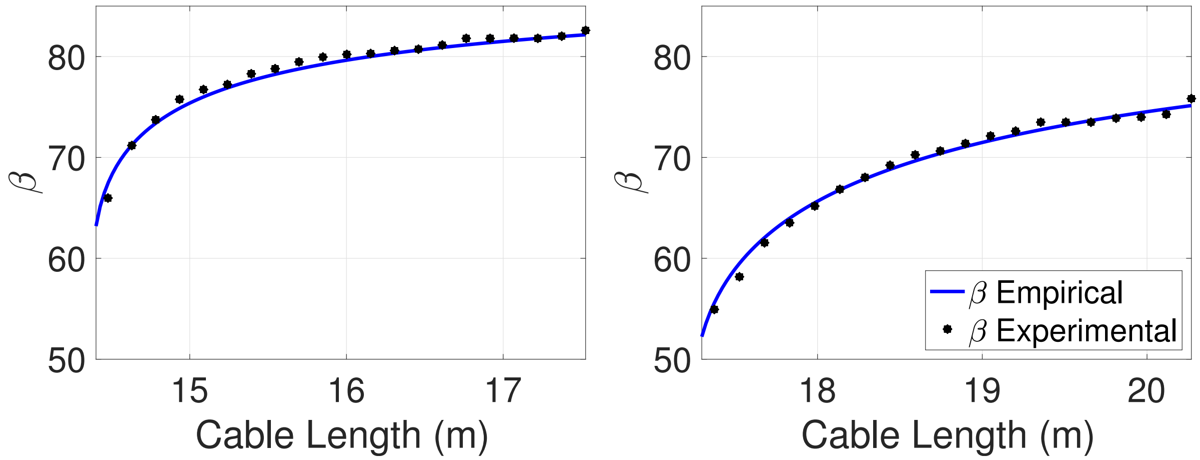

(a) (b)

Figure 3.12: Typical experimental results for β vs. length, shown for $\Delta y = 12.19$ m and (a) $\Delta x = 7.62$ m, and (b) $\Delta x = 12.19$ m. The data shown is the mean of 20 measurements at each length.

the use of the catenary analysis approach for this specific hanging tether, and the analysis in Section 3.3.

3.5 Improvements

During experimental evaluation detailed in Chapter 4, it was realized that the curve fit models developed here, are not valid above a relative position ratio of $\Delta x/\Delta y = 1.2$. Because they are 3rd order, the model fits have an inflection point. For $\Delta x/\Delta y > 1.2$, as described in Section 4.3, a 2nd order model can be extended from the 3rd order model. For clarity when dealing in three dimensions the notation will be changed moving forward to be Δr for the relative radial distance, and Δz for the relative altitude.

3.6 Conclusion

A quasi-static model using the catenary hanging cable equation was developed based on the relative position for a tethered UAV - USV team. An empirical analysis over the flying space determined a minimum tension and heave robustness length for every flying combination. Division of the relative catenary parameters by the flying height transforms the empirical analysis data into individual curves that can be approximated with low order polynomials. The recommended relative offset for maximizing heave robustness is $\Delta x/\Delta y \approx .46$. Experimental tension and departure angle results from 18 relative positions experiments confirmed that the catenary approach is valid. Follow on work already in progress includes the development of a mechanized reel system, the development of a dynamic model, and a controller using this analysis as reference set point.

3.7 Acknowledgments

Support for this work was provided by Naval Information Warfare Center Pacific under the Naval Innovative Science and Engineering program and the Department of Defense SMART Scholarship for Service program.

Chapter 3 in full, is a reprint of the material as it appears in IEEE International Conference on Intelligent Robots and Systems (IROS) 2018, K. Talke, M Oliveira, and T. Bewley, “Tether shape analysis for a UAV - USV team”. The dissertation author was the primary investigator and author of these pages.

Chapter 4

Prototype, Estimator and Controller

In this chapter, a tether management prototype design, relative position estimator, reference model extension, and control system for autonomous tether management are developed. For a tether management system to function outside of a lab environment, it needs to be able to control and measure tether length, provide tether tension or motor torque feedback, measure the tether departure angle, and provide safety precautions to prevent catastrophic forces on the UAV. For a future UAV payload, a coaxial tether with a diameter of 4.5 mm is used, much larger than typical tethers for tethered UAV systems. The tether management problem is more challenging due to the weight and bending stiffness of the tether. The tether management system is split into three subsystems: mechanical, controller, and estimator.

The remainder of the chapter is organized as follows. Section 4.1 details the tether management prototype. Section 4.2 develops a method for tether length control. Section 4.3 extends the reference model to be valid beyond $\Delta r/\Delta z = 1.2$. Section 4.4 details a Kalman filter estimation model for relative altitude. Section 4.5 summarizes the key conclusions.

4.1 Mechanical Design

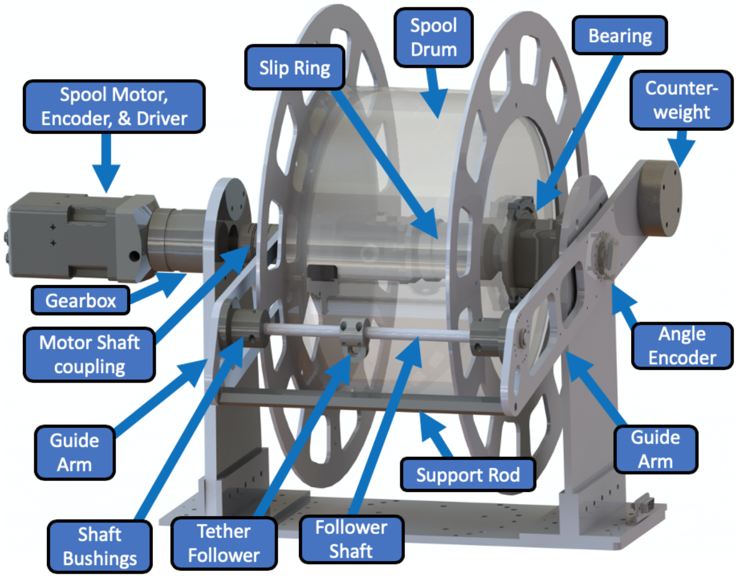

Figure 4.1: Smart reel prototype capable of spooling 100 m of 4.5 mm diameter tether with a 50 mm minimum bend radius. The integrated sensors can measure the tether length, departure angle, and motor torque.

A prototype smart reel system, similar to the non-taut tether management system found in previous work [21], is shown in Fig. 4.1. The prior work used a torsional spring to measure torque, and a non-contact proximity sensor to measure the departure angle of the tether. Our design differs from earlier designs by using the motor current to measure motor torque and using a balanced, contact-based passive tether follower to measure the departure angle of the tether. One of the goals of the experimental approach described in Chapter 5 is to characterize this unique angle measurement approach and its feasibility as a means for feedback. As the tether exits the spool, it feeds through a tether follower attached to guide arms. The follower is free to slide left and right along a shaft as needed for spool winding. The guide arms can rotate freely about the spool. A support rod constrains the two guide arms to rotate together. The guide arms are counter-weighted such that the weight of the arm does not affect the departure angle of the tether. An absolute encoder on the guide arm measures the angular rotation of the guide arm. The balanced freedom of movement of the follower allows for a minimally intrusive measurement of the tether departure angle. A future design improvement will be to convert the follower and follower shaft into a cross-threaded level winding screw to accommodate greater tether lengths and spool neatly. A motor-encoder-gearbox combination connects directly to a slip ring inside the spool drum through a drive shaft and coupling. The slip ring transfers the required power at 400 V and communication signals to allow the spool to spin up to 100 rpm, while also providing the necessary power for sustained UAV flight. A future design improvement will be to incorporate a turntable to allow the entire system to rotate, thereby ensuring the smart reel stays pointed at the UAV.

4.2 Controller Design

For the tether management prototype, a dynamic gain-scheduled discrete-time proportional-derivative (PD) controller running at 50 Hertz is graphically shown in Fig. 4.2. The controller inputs are the estimated relative altitude, $\Delta\tilde{z}_k$, the estimated relative vertical velocity, $\Delta\dot{\tilde{z}}_k$, the measured tether length, L_k, and a slow, 4 Hertz, relative radial

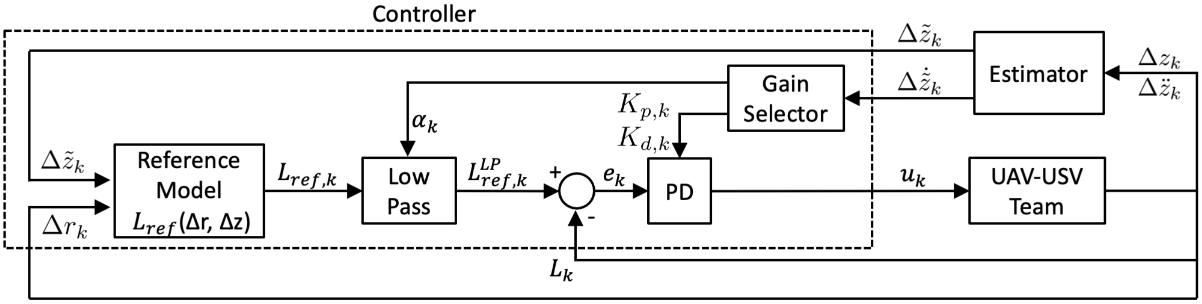

Figure 4.2: Proposed tether management controller. The relative position of the UAV and USV feed into the polynomial model to determine a reference length. Comparison to the measurement estimate from the spool encoder creates an error signal. A PD controller on the spool motor commands the spool to pay out or reel in tether. The low pass filter coefficient and the controller gains are gain scheduled based on the estimated relative velocity.

distance measurement, Δr_k. An error signal, e_k, and its derivative multiplied by the proportional and derivative gains, K_p and K_d, respectively, are used to determine the commanded motor voltage, u_k, the controller input. The gains change depending on the relative velocity between the UAV and USV, with both the gains and velocity thresholds found through experimental testing. The error signal is generated using the difference between the measured tether length, L_k, and a gain-scheduled low-pass filtered reference tether length $L_{ref,k}^{LP}$. The low-pass filter is a typical first order discrete-time filter defined as:

$$L_{ref,k}^{LP} = (1-\alpha)\, L_{ref,k-1}^{LP} + \alpha L_{ref,k} \tag{4.1}$$

where $\alpha \in [0,1]$ is the filter smoothing factor and scheduled depending on how fast the relative altitude changes. The intent of the low-pass filter is to smooth out the reference tether length, $L_{ref,k}$, due to any discontinuities in the relative altitude estimate at slow speeds. At high relative velocities, the relative altitude estimate proved experimentally to be smooth, and α was set to 1 to pass through the reference tether length without filtering it. The gain-scheduler is set up similar to an electronic Schmitt trigger, where the threshold for triggering between states changes depending on specific criteria [68]. Determined experimentally, an α value of 0.2 was used when the relative velocity dropped below 0.3 m/s. If the relative velocity dropped below 0.1 m/s, the threshold would also drop down to 0.1 m/s. This has the effect of smoothly transitioning to a low-pass filtered reference signal when the relative velocity slows down, but abruptly turning off the filter with increasing relative velocity, allowing for the smart reel to respond faster without the low-pass filter-induced lag. The reference tether length, determined by a catenary tether-based heave model previously developed, is dependent on the relative altitude estimate and relative radial distance [69]. Our previous work investigated the heave model based on static catenary hanging cable theory, but did not experimentally validate the model for control of a hanging tether from a dynamically moving UAV or USV.

4.3 Catenary Tether Model

This section will summarize the catenary tether-based heave model developed in our previous work [69], and extend its valid operation range. The static catenary cable equation given by:

$$z = z_0 + a \cosh\left(\frac{r - r_0}{a}\right) = z_0 + \frac{a}{2}\left(e^{\frac{r-r_0}{a}} + e^{-\frac{r-r_0}{a}}\right) \tag{4.2}$$

where a is the catenary parameter, was converted to relative position form:

$$\sqrt{L^2 - \Delta z^2} = 2a \sinh\left(\frac{\Delta r}{2a}\right) \tag{4.3}$$

where Δr and Δz are the radial and vertical distance between the UAV and the USV, and L is the known tether length. Because Eq. 3.4 is a transcendental equation in a, it was empirically analyzed for a range of operating conditions from 0 to 60 m in radial distance and altitude, and varying range of tether lengths. For each relative position, a heave robustness tether shape was determined that allows for equal vertical heave displacement of the USV to specified tension and sag limits while the tether length remains unchanged. The results of the empirical analysis were curve fitted to develop a reference model for tether length, departure angle, and tension, depending only on the relative position between the UAV and USV. A key result from the analysis was a recommended operating relative position ratio, $\Delta r/\Delta z \approx 0.46$. In this work, only the length model will be used, and the simple 3rd-order polynomial is repeated here for reference:

$$L_{ref} = c_1 \Delta z + c_2 \Delta r + c_3 \frac{\Delta r^2}{\Delta z} + c_4 \frac{\Delta r^3}{\Delta z^2} \tag{4.4}$$

with coefficients $c_1 = 0.9964$, $c_2 = 0.1514$, $c_3 = 0.4674$, and $c_4 = -0.1280$. The third order model was originally developed for $\Delta r/\Delta z \leq 1.2$. In that region, the third order

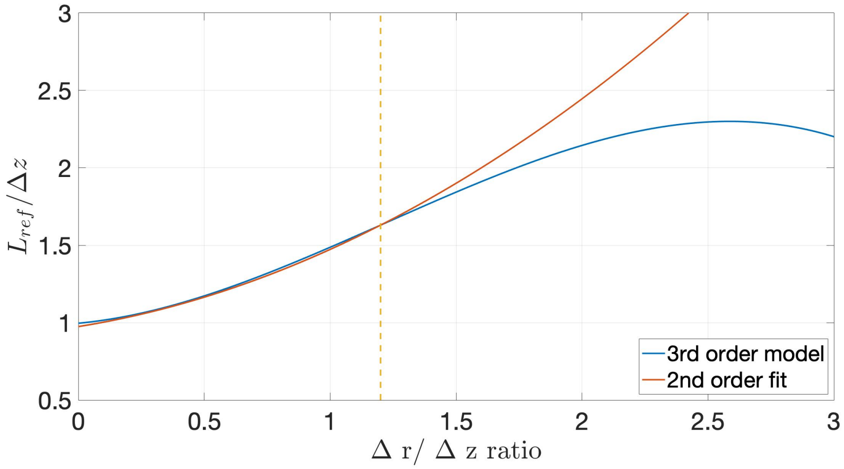

Figure 4.3: Tether reference model showing original 3rd order model, inflection point, and 2nd order fit for relative position ratio $\Delta r/\Delta z > 1.2$

approximation is nominally better than a lower order model. However, outside the region, because this model is third order, it has an inflection point, which occurs at $\Delta r/\Delta z = 1.22$. For $\Delta r/\Delta z > 1.22$, the third order model is no longer physical, and results in a taut tether reference length at $\Delta r/\Delta z = 1.77$. While the goal is to operate at $\Delta r/\Delta z < 1$, the constrained indoor testing environment and other operation scenarios can result in $\Delta r/\Delta z > 1.2$. A second order curve fit model, extrapolated from the third order model, will be used for such operation regions:

$$L_{ref} = d_1\Delta z + d_2\Delta r + d_3\frac{\Delta r^2}{\Delta z} \tag{4.5}$$

with coefficients $d_1 = 0.9748$, $d_2 = 0.2615$, and $d_3 = 0.2370$. The original third order model and the extrapolated second order curve fit model are show in Fig. 4.3. For relative position ratio, $\Delta r/\Delta z \leq 1.1$, the third order model will be used, and for $\Delta r/\Delta z > 1.3$, the second order model will be used. In the region between, $1.2 < \Delta r/\Delta z < 1.3$, a linear combination of the second and third order models is used in order to smooth the transition. A key challenge for this control approach will be the accurate measurement of relative position.

4.4 Sensing and Estimation Filter Design

To address the challenge of determining the relative position, a commercial off the shelf RTK dGPS solution is used. However, RTK dGPS solutions are limited to a maximum 4 Hertz update rate, which is too slow for the developed controller, which runs at 50 Hertz. To augment the estimated relative position during the time in between RTK dGPS measurements, a Kalman filter model was designed to measure and double integrate the acceleration using two IMUs running at 100 Hertz. There are numerous examples of GPS-inertial navigation system (INS) Kalman filters for a variety of applications [70–73], as well as some more specific to using RTK dGPS and UAV navigation [74–77]. To simplify for this scenario, the Kalman filter is restricted to the altitude degree of freedom (DOF) since the primary DOF affecting the tether is the vertical heave motion of the USV, and the UAV is near hover. To account for the bias due to gravity of the accelerometers, they are included in the double integration dynamic model for the Kalman filter as:

$$X = \begin{bmatrix} \Delta z \\ \Delta \dot{z} \\ \Delta \ddot{z} \\ \mu_1 \\ \mu_2 \end{bmatrix}, X_{k+1} = \begin{bmatrix} 1 & \Delta t & 0 & 0 & 0 \\ 0 & 1 & \Delta t & 0 & 0 \\ 0 & 0 & 1 & 0 & 0 \\ 0 & 0 & 0 & 1 & 0 \\ 0 & 0 & 0 & 0 & 1 \end{bmatrix} X_k + \begin{bmatrix} \omega_{z,k} \\ \omega_{\dot{z},k} \\ \omega_{\ddot{z},k} \\ \omega_{\mu_1 k} \\ \omega_{\mu_2,k} \end{bmatrix} \tag{4.6}$$

such that:

$$\begin{aligned}
\Delta z_{k+1} &= \Delta z_k + \Delta t \Delta \dot{z}_k + \omega_{z,k} & \omega_z &= \mathcal{N}(0, \sigma_z) \\
\Delta \dot{z}_{k+1} &= \Delta \dot{z}_k + \Delta t \Delta \ddot{z}_k + \omega_{\dot{z},k} & \omega_{\dot{z}} &= \mathcal{N}(0, \sigma_{\dot{z}}) \\
\Delta \ddot{z}_{k+1} &= \Delta \ddot{z}_k + \omega_{\ddot{z},k} & \omega_{\ddot{z}} &= \mathcal{N}(0, \sigma_{\ddot{z}}) \\
\mu_{1,k+1} &= \mu_k + \omega_{\mu_1,k} & \omega_{\mu_1} &= \mathcal{N}(0, \sigma_{\mu_1}) \\
\mu_{2,k+1} &= \mu_k + \omega_{\mu_2,k} & \omega_{\mu_2} &= \mathcal{N}(0, \sigma_{\mu_2})
\end{aligned} \tag{4.7}$$

where Δz, $\Delta \dot{z}$, $\Delta \ddot{z}$ are the relative position, velocity, and acceleration, respectively, μ_1 and μ_2 are the estimated accelerometer biases, and Δt is the timestep of the filter running at 100 Hertz. All states are assumed to have zero mean and normally distributed system noise. The measurement model is defined as:

$$Y_k = \begin{bmatrix} \Delta z_{dGPS} \\ \Delta \ddot{z}_{Acc_1} \\ \Delta \ddot{z}_{Acc_2} \end{bmatrix}, Y_k = \begin{bmatrix} 1 & 0 & 0 & 0 & 0 \\ 0 & 0 & 1 & 1 & 0 \\ 0 & 0 & 1 & 0 & 1 \end{bmatrix} \begin{bmatrix} \Delta z_k \\ \Delta \dot{z}_k \\ \Delta \ddot{z}_k \\ \mu_{1,k} \\ \mu_{2,k} \end{bmatrix} + \begin{bmatrix} v_{z,k} \\ v_{\ddot{z}_1,k} \\ v_{\ddot{z}_2,k} \end{bmatrix} \tag{4.8}$$

such that:

$$\begin{aligned}
\Delta z_{GPS,k} &= \Delta z_k + v_{z,k} & v_z &= \mathcal{N}(0, \sigma_{dGPS}) \\
\Delta \ddot{z}_{Acc_1,k} &= \Delta \ddot{z}_k + \mu_{1,k} + v_{\ddot{z}_1,k} & v_{\ddot{z}_1} &= \mathcal{N}(0, \sigma_{Acc_1}) \\
\Delta \ddot{z}_{Acc_2.k} &= \Delta \ddot{z}_k + \mu_{2,k} + v_{\ddot{z}_2,k} & v_{\ddot{z}_2} &= \mathcal{N}(0, \sigma_{Acc_2})
\end{aligned} \tag{4.9}$$

where Δz_{dGPS} is the RTK dGPS measurement, and $\Delta \ddot{z}_{Acc_1}$ and $\Delta \ddot{z}_{Acc_2}$ are the vertical accelerations from both IMUs. All measurements are assumed to have zero mean, normally distributed measurement noise. Some care needs to be taken due to the fact that the RTK dGPS measurement is slow, at 4 Hertz. During the time between RTK dGPS measurements, the dGPS covariance, σ_{dGPS}, is artificially set to infinity to zero out the Kalman gain for that state.

4.5 Conclusion

A prototype smart reel was presented, capable of measuring the tether length, departure angle, and tension. The semi-slack hanging tether model, dependent on the relative position between the UAV and USV was extended to operate through a larger relative position range, extending above $\Delta r/\Delta z > 1.2$. With the goal of outdoor operation, a Kalman filter model was developed to fuse a slow, 4 Hertz RTK dGPS based relative position measurement with fast, 100 Hertz inertial measurements, to output a fast, 100 Hertz estimate of the relative position, relative velocity, and inertial sensor bias. A relative velocity-based gain scheduled controller was developed to smooth out any errors and discontinuities seen in the Kalman filter at low relative velocities. A major benefit of this control system is that is is based purely on relative position, regardless of scale.

4.6 Acknowledgments

Support for this work was provided by Naval Information Warfare Center Pacific under the Naval Innovative Science and Engineering program and the Department of Defense SMART Scholarship for Service program.

Chapter 4, in full, has been submitted for publication as it may appear in Field Robotics 2021,K. Talke, F. Birchmore, T. Bewley, “Autonomous Hanging Tether Management and Experimentation for a UAV-USV Team”. The dissertation author was the primary investigator and author of these pages.

Chapter 5

Experimental Validation Procedure

In this chapter, the methodology for evaluating the prototype, reference model, estimation filter, and controller is presented. The experimental approach is split into three stages to first validate the controller and mechanical prototype, tune and validate the estimation filter, and then evaluate the RTK dGPS solution:

1. UAV surrogate testing is performed to validate the controller. To accomplish this, a 100 Hertz infrared camera motion capture (MoCap) system is used for relative position feedback to validate the controller and tune the estimation filter. Then, the estimation filter is evaluated, de-rating the MoCap system feedback down to 4 Hertz to replicate the RTK dGPS measurement.
2. Indoor flight testing is performed to introduce the dynamic variability of the UAV, again using the MoCap system and the estimation filter for relative position feedback.
3. Outdoor flight testing is performed using the RTK dGPS as input into the estimation filter for relative position feedback.

This staged approach will first evaluate the tether reference model, the controller, and the mechanical prototype in a controlled environment, then involve flight dynamics with perfect feedback, then incorporate the estimation filter for increased complexity and difficulty, and finally evaluate the feasibility of the RTK dGPS sensor for feedback. For each of the scenarios described, the smart reel is mounted onto the payload platform of a 3-$\underline{\text{P}}$SR mechanism to replicate wave and boat motion [78]. The sensor subsystem communication design and wave profiles are discussed after the test setup for each scenario.

The remainder of the chapter is organized as follows. Section 5.1 describes the UAV surrogate experimental setup. Section 5.3 details the UAV and indoor flight setup. Section 5.2 describes the process for tuning the Kalman filter model. Section 5.4 describes the dGPS payload, and outdoor test setup. Section 5.5 details the sensor subsystems communication design. Section 5.6 describes the wave profiles developed for the 3-$\underline{\text{P}}$SR wave replication mechanism. Section 5.7 summarizes the key conclusions.

5.1 UAV Surrogate Test Setup

A rigidly mounted load sensor acting as a UAV surrogate was used to evaluate and validate the tether model and controller prior to flying. The UAV surrogate was rigidly mounted just beneath the 7 m high ceiling of the testing facility as shown in Fig. 5.1. The tether was mounted to a rotating connector which measures the arrival angle, β, with a potentiometer. A fulcrum converts the tension load into compression for the load cell to measure the vertical component of the tether tension. Using the angle and vertical load, the geometry of the fulcrum determines the tether tension. A microprocessor was used to read the load and angle data and communicate it to the smart reel for data logging purposes. The wave mechanism was positioned in such a way that the relative position is at the recommended ratio $\Delta r/\Delta z = 0.46$ when the platform is at the bottom of its range [69]. The 3-$\underline{\text{P}}$SR wave replication mechanism runs a prescribed wave profile in open loop in three DOFs: pitch, roll, and heave. The MoCap system was used for ground truth feedback,

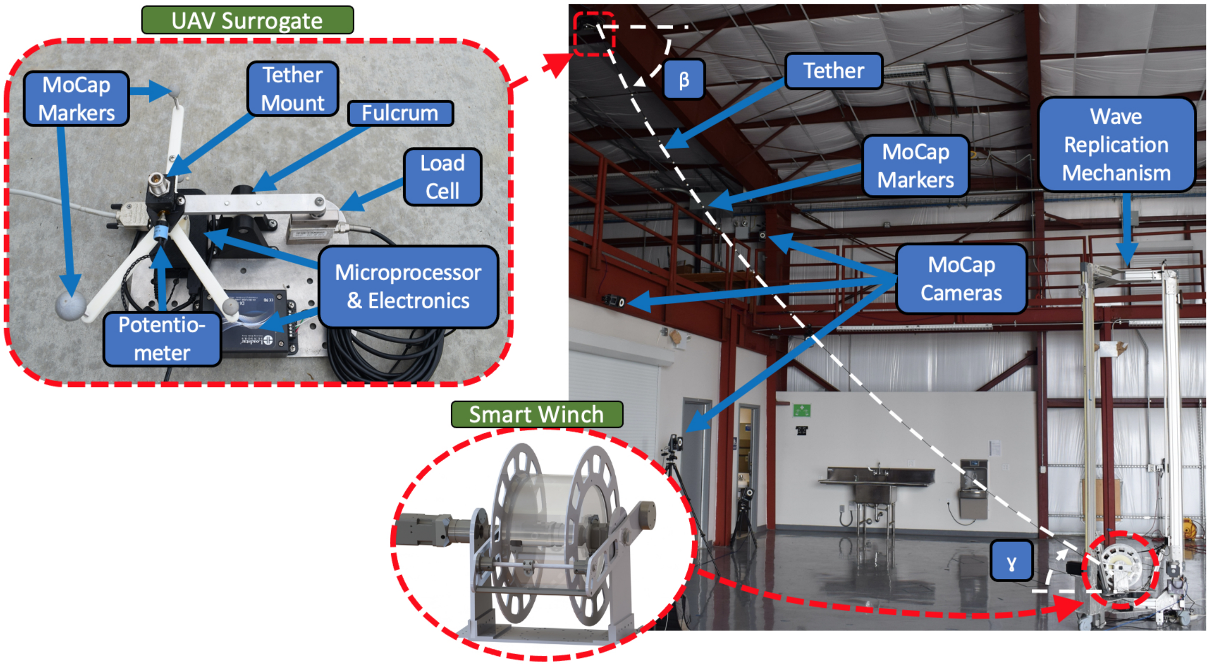

Figure 5.1: UAV surrogate test setup during taut tether testing. The smart reel prototype is mounted on the 3-P̲SR wave replication mechanism. The tether is outlined with a white dashed line to make it more visible. The UAV surrogate components are labeled, as well as the tether departure and arrival angles, γ and β.

and then de-rated to tune and evaluate the estimation filter. Next, a comparatively test evaluated the controller against a typical taut controller. The taut controller maintained a specified torque on the spool, reeling in and paying out as needed to maintain tension on the tether.

5.2 Filter Tuning

The data obtained while validating the controller was then used to tune the estimation filter covariance values. Using the MoCap system as a ground truth measurement, the so-called ad-hoc Twiddle Algorithm was used to refine the Kalman filter covariance values [79, 80]. The algorithm cost metric was modified to use the root mean square error (RMSE) between the measured relative position from the MoCap and the estimated relative

Algorithm 1: Modified Twiddle Algorithm

```
$P = [\sigma_1, \sigma_2, ..., \sigma_m]$
$dP = [\delta\sigma_1, \delta\sigma_2, ..., \delta\sigma_m]$
$n = length(data)$
$\Delta\tilde{z} = kfilter(P, data)$
$Q_{Best} = \sqrt{\frac{1}{n}\sum_{j=0}^{n}\left(\Delta\tilde{z}_j - \Delta z_j\right)^2}$
$l = 1$
while $\frac{1}{m}\sum_{j=0}^{m}(dP_j/P_j)) > .1$ do
    for $i = 1 : m$ do
        $P(i) = P(i) + dP(i)$
        $\Delta\tilde{z} = kfilter(P(i), data)$
        $Q_l = \sqrt{\frac{1}{n}\sum_{j=0}^{n}\left(\Delta\tilde{z}_j - \Delta z_j\right)^2}$
        if $Q_l < Q_{Best}$ then
            $Q_{Best} = Q_l$
            if $dP(i)/P(i) <= 0.5$ then
                $dP(i) = dP(i) * 1.1$
            else
                $dP(i) = P(i) * 0.5$
            end if
        else
            $P(i) = P(i) - 2 * dP(i)$
            $\Delta\tilde{z} = kfilter(P(i), data)$
            $Q_l = \sqrt{\frac{1}{n}\sum_{j=0}^{n}\left(\Delta\tilde{z}_j - \Delta z_j\right)^2}$
            if $Q_l < Q_{Best}$ then
                $Q_{Best} = Q_l$
                if $dP(i)/P(i) <= 0.5$ then
                    $dP(i) = dP(i) * 1.1$
                else
                    $dP(i) = P(i) * 0.5$
                end if
            else
                $P(i) = P(i) + dP(i)$
                $dP(i) = dP(i) * 0.9$
            end if
        end if
    end for
    $l = l + 1$
end while
```

position from the filter, $\Delta\tilde{z}$. To ensure the covariance values do not go negative, the change in parameter was limited to 50% of the current parameter value. Psuedocode for the modified Twiddle Algorithm is shown in Algorithm 1.

5.3 Indoor Flight Test Setup

For indoor flight testing, the UAV surrogate is replaced with a modified DJI S900 hexacopter UAV shown in Fig. 5.2. The UAV is flown in remote control (RC) mode with an open source ArduPilot flight controller. The UAV uses a Pixhawk autopilot, RC and telemetry radios, GPS for outdoor flight, magnetometer, power electronics, and has a tether mounting point on a u-joint to allow for the tether to rotate at the attachment point. Again, the relative position feedback is provided by the infrared camera MoCap system, and then the estimation filter using the de-rated MoCap measurement to imitate the RTK dGPS measurement. The desired relative position is an altitude of 5 m and 2.5 m radial

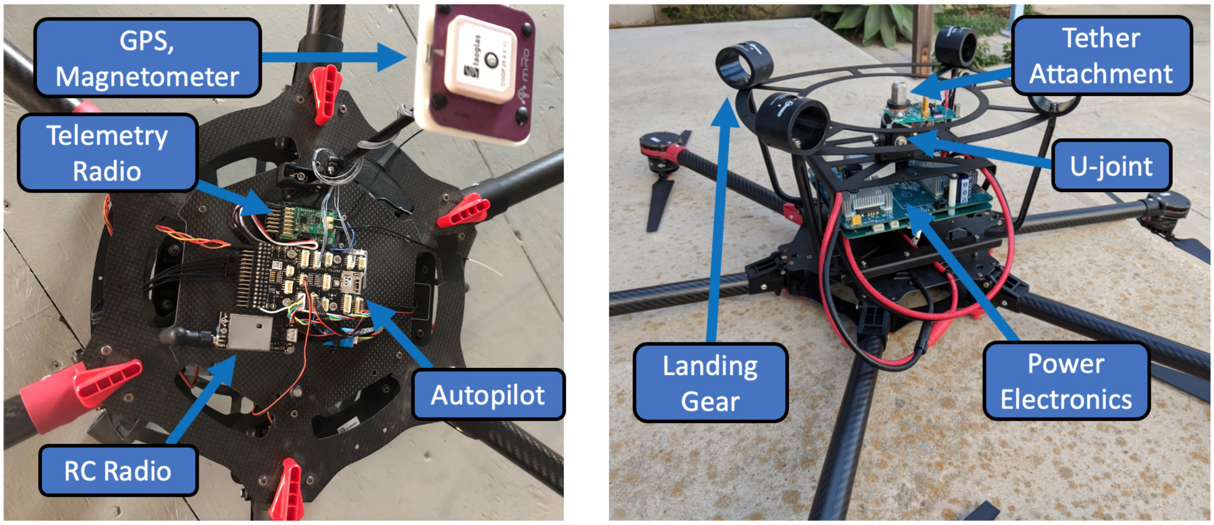

a) b)

Figure 5.2: UAV test setup. a) Topside of the UAV showing flight electronics. b) Underside of the UAV showing the tether attachment point and power electronics.

distance. Indoor flight testing builds on the UAV surrogate experiment by including the UAV, thus introducing more variability in the relative position. Because the UAV flies near the ceiling of the indoor testing facility to attain the largest relative altitude, taut tether testing was not performed. The variability of tether tension during taut controller testing is too great and would likely cause the UAV to crash. Therefore, UAV altitude and position variations will be compared to un-tethered flight. For both the UAV surrogate and indoor flight testing, the limited height of the indoor testing facility resulted in an experiment near the margins of the proposed concept of operation. A scaled down relative position (5 m altitude vs 50 m altitude) has less margin for error. For example, a 0.25 m error in tether length has a greater effect when the overall length is 7 m than when it is 60 m.

5.4 Outdoor Flight Test Setup

For outdoor flight testing, the same 3-$\underline{P}$SR wave replication mechanism and UAV were moved outdoors to allow for higher altitude flight, and a more realistic operational

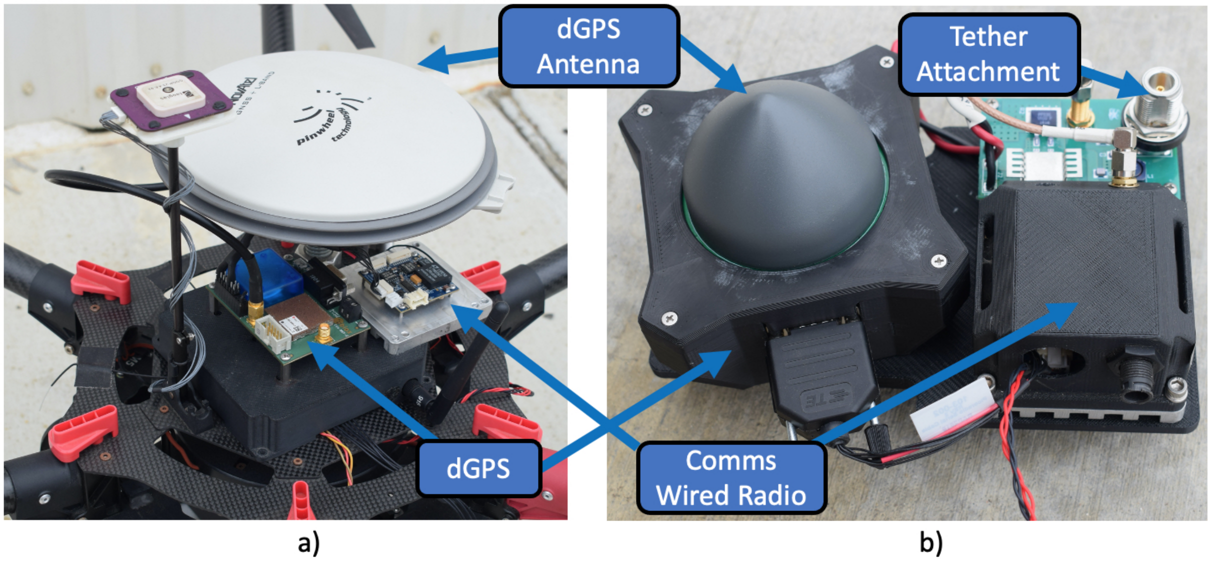

Figure 5.3: RTK dGPS payload in: a) rover mode attached to top of UAV. b) in moving baseline mode attached to the mast on 3-$\underline{P}$SR wave replication mechanism.

scenario. Because the MoCap system does not work well outdoors, nor at the altitude required, the RTK dGPS payload was added to the UAV as shown in Fig. 5.3. An antenna passes the GPS signal into the dGPS chip which then sends data to a radio. Instead of broadcasting the signal via an antenna, it sends the signal down the RF tether to another radio, and then the dGPS chip attached to the top of the mast on the 3-$\underline{P}$SR wave replication mechanism. The desired relative position is an altitude of 30 m and 15 m radial distance. Outdoor flight testing introduces more complexity such as wind, difficulty in measuring the relative position, and a more realistic deployment environment.

5.5 Sensing and Communication Protocol

For autonomous tether management, the developed system needs to sense the dynamics, shape of the tether, and reel in or pay out accordingly. The smart reel design is capable of sensing the tether characteristics including instantaneous tether length, tether departure angle, tether tension, and controlling the tether length, as shown in Fig. 5.4.

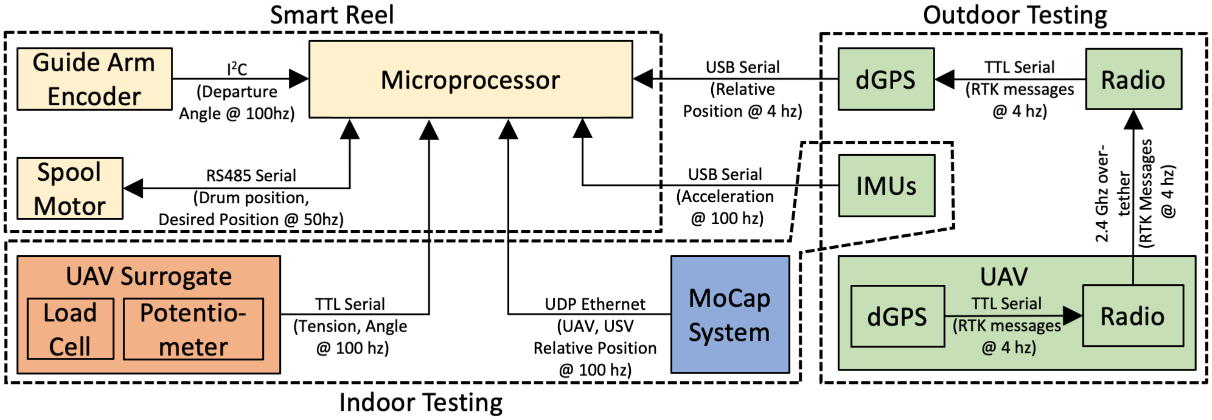

Figure 5.4: Communication protocol diagram between the smart reel controller, UAV surrogate, the MoCap system, and the smart reel microprocessor. The colored blocks represent each subsystem and the lines show what data is being communicated on which protocol at what rate. Note that not all subsystems are active for each of the experimental setups.

During UAV surrogate testing, the tether tension and arrival angle, β, are sent to the smart reel microprocessor for data syncing. For indoor flight testing, the relative position is measured via the MoCap system, and sent to the smart reel microprocessor via a UDP point to point Ethernet network at 100 Hertz. For outdoor flight testing, the airborne dGPS unit sends RTK messages over the tether via a 2.4 GHz radio to the other dGPS unit. The relative position is then transmitted to the microprocessor via USB serial at 4 Hertz. The specific electronic hardware is listed in Table 5.1.

Table 5.1: Prototype Electronics

Electronics	Supplier	Part Number
UAV Surrogate Load Cell	Loadstar Sensor	RAS1-050S-S
UAV Surrogate Microprocessor	beagleboard	BeagleBone Blue
Smart Reel Microprocessor	beagleboard	BeagleBone Blue
Smart Reel Angle Arm Encoder	US Digital	MAE-3
Smart Reel Spool Motor	Moog Animatics	SM23165MT
Estimation Filter IMU-1	InvenSense	MPU-9250
Estimation Filter IMU-2	Lord MicroStrain	3DM-GX5-25
RTK dGPS	u-blox	NEO-M8P-2
dGPS Tether Radio	Airborne Innovations	pDDL2450

5.6 Input Wave Profile

Four distinct wave profiles were developed for testing on the 3-$\underline{\text{P}}$SR wave replication mechanism. The first profile considered only the heave motion of a wave. The heave-only wave profile was derived from the JONSWAP spectrum [81]. A sum of sinusoidal signals with randomized initial phase was used to create the time series heave profile. The resulting four minute wave profile had a 1.6 m peak wave amplitude and a 10 second peak period, approximating sea state 3 on the Douglas Sea Scale [53]. The next three wave profiles include heave, pitch, and roll (HPR), and were taken from a Unity engine simulation of a patrol boat using the ultimate water system tool [63]. Each wave had a heave range up to the maximum heave capability of the 3-$\underline{\text{P}}$SR wave replication mechanism of 2.2 m, pitch range of $\pm18.1, \pm14.5, \pm17.4$ degrees, and roll range of $\pm16.1, \pm21.8, \pm21.1$ degrees, approximating sea state 4. The first two HPR wave profiles were used for tuning the filter, while the last HPR profile was reserved for unbiased testing. The amplitude of the frequency spectrum for each wave profile and a sample wave profile times series is shown in Fig. 5.5.

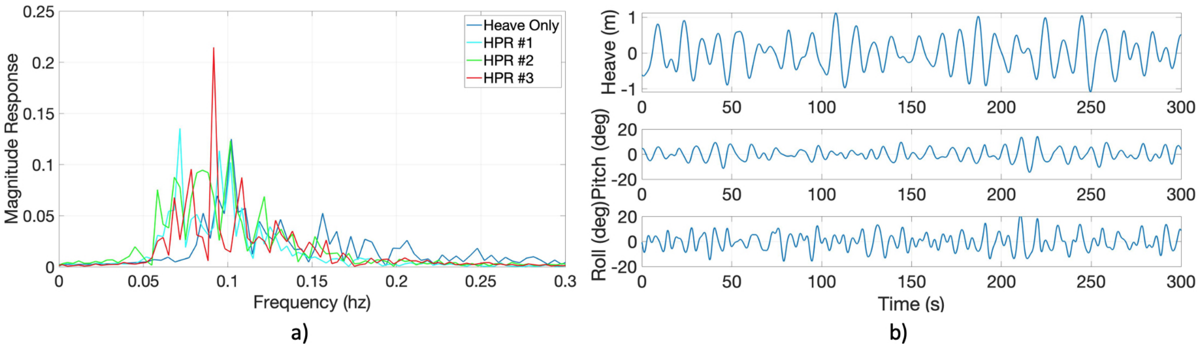

a) b)

Figure 5.5: Experimental wave data for the 3-$\underline{\text{P}}$SR wave replication mechanism. a) The frequency content of the four wave profiles and b) Time series example of the third wave profile.

5.7 Conclusion

A rigorous, phased approach was presented to best evaluate the prototype, controller, and estimation filter. UAV surrogate testing, using a rigidly mounted load cell will validate the proposed controller and reference model against a typical taut tether tension controller. The data gathered will then be used to tune the estimation filter gains, using the MoCap system as a ground truth measurement. Indoor flight testing adds in the varying dynamics of the UAV, evaluating for a varying relative position. Outdoor flight testing will evaluate the proposed dGPS solution in a relevant dynamic environment. Finally, the communication protocol and input wave profiles were described.

5.8 Acknowledgments

Support for this work was provided by Naval Information Warfare Center Pacific under the Naval Innovative Science and Engineering program and the Department of Defense SMART Scholarship for Service program.

Chapter 5, in full, has been submitted for publication as it may appear in Field Robotics 2021,K. Talke, F. Birchmore, T. Bewley, "Autonomous Hanging Tether Management and Experimentation for a UAV-USV Team". The dissertation author was the primary investigator and author of these pages.

Chapter 6

Experimental Results

In this chapter, the experimental testing results are presented. The developed prototype system is validated through indoor motion capture and outdoor RTK dGPS experimentation. Using a UAV surrogate for a perfectly known, controlled environment, the developed estimator and controller are shown to greatly reduce tether tension and forces on the UAV compared to taut tether control. Indoor flight testing shows the successful decoupling of USV heave motion from UAV altitude and position, while also demonstrating a similar UAV altitude and position range compared to un-tethered flight. Finally, outdoor flight testing, using a dGPS and an IMU Kalman filter solution to measure relative position, demonstrates the feasibility of the developed system in an unknown dynamic environment. A hanging tether management system can extend longevity, decrease power consumption, extend mission duration, increase flight altitude, and decrease the required thrust safety margins of the UAV.

The remainder of the chapter is organized as follows. Section 6.1 presents and discusses experimental results for the UAV surrogate testing. Section 6.2 describes tuning the estimation filter and presents the results using the filter for feedback. Section 6.3 presents the results from indoor flight testing. Section 6.4 ptesents the results from outdoor

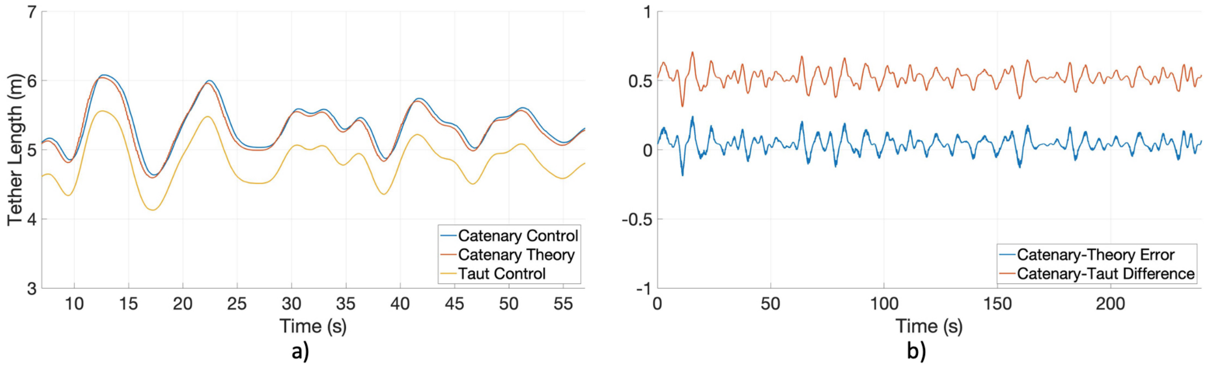

Figure 6.1: Typical tether length experimental results for the UAV surrogate testing. a) Measured tether length for the taut and catenary model-based control. For reference, the commanded wave height and theoretical catenary model length based on the relative position are also shown. b) Error between the measured catenary model-based length controller and the theoretical catenary model-based length. Also shown is the difference between the catenary model-based controller and the taut controller.

flight testing. Section 6.5 summarizes the key conclusions.

6.1 UAV Surrogate

The UAV surrogate results are presented using the MoCap system as feedback to validate the controller and mechanical prototype in four parts: tether length, arrival angle, departure angle, and tether tension. Nine separate wave profile trials (three heave-only, three each for two of the HPR profiles) were performed and one stationary, no-motion wave profile to help tune the estimation filter. For comparative testing, each wave profile was also tested with the tension-based controller.

6.1.1 Tether Length

The tether length results for a typical UAV surrogate experiment are shown in Fig. 6.1a. The catenary model-based controller follows the catenary model-based theory, with a mean error across all runs of 0.022 m and RMSE of 0.028 m as seen in Fig. 6.1b. This shows that the PD controller gains have been tuned well as the actual tether length matches

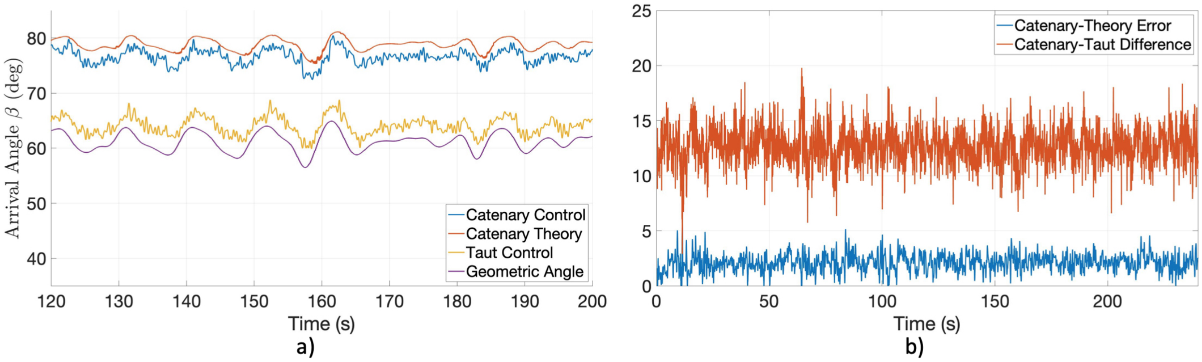

Figure 6.2: Typical arrival angle, β, experimental results for the UAV surrogate testing. a) Arrival angle showing theoretical catenary angle based on the measured tether length and relative position, the measured angle during catenary control, taut control, and the geometric angle based solely on relative position. b) Error between theory and the measured angle showing relatively consistent error. The error between catenary measurement and taut measurement is also consistent with minimal variations.

the model. In comparison, the taut controller tether length follows a similar profile, but has an initial offset. The variations are nearly constant with a mean difference of 0.52 m. The catenary model-based control can be interpreted as a tether length buffer for taut control. If the tether length for taut control was known, the same length trend with a longer initial tether length would result in the catenary model-based tether control. However, the initial length difference changes with respect to the relative position between the UAV and USV, thus the catenary model-based controller is necessary.

6.1.2 Arrival Angle, β

The arrival angle, β, of the tether at the UAV surrogate experiments are shown in Fig. 6.2a. The experimental data was filtered with a low-pass filter with a cutoff frequency of 2 Hertz to remove the high frequency noise inherent in the potentiometer reading. The tether has some elasticity and dynamic effects preventing it from becoming fully taut, resulting in the taut tether angle being slightly greater than the geometric angle. As seen in Fig. 6.2b, the catenary model-based controller followed theory relatively closely, with

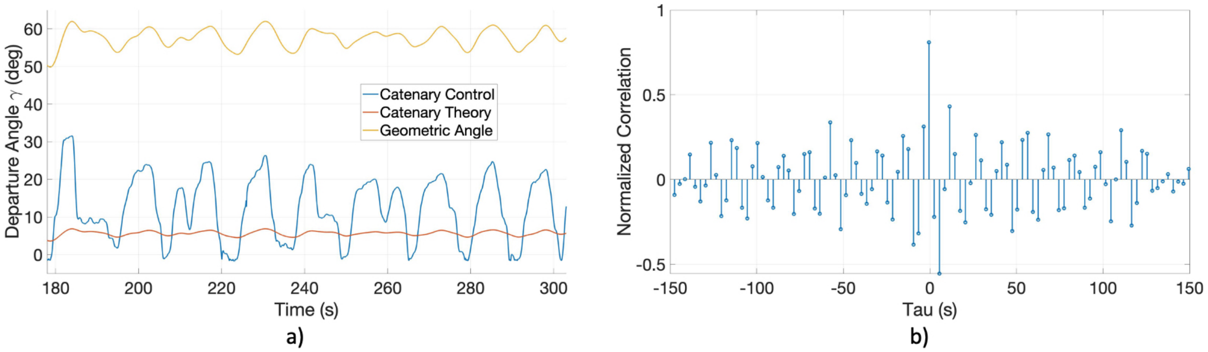

Figure 6.3: Typical departure angle, γ, experimental results for the UAV surrogate testing. a) Departure angle showing the theoretical angle based on the measured tether length and relative position, the measured angle during catenary control, and the geometric angle based solely on relative position. b) Normalized cross correlation between the measured and theoretical departure angles. The two signals are strongly correlated in time as seen by the peak at 0.88 seconds shift.

a mean error of 2.1 degrees, attributable to an initial offset in potentiometer calibration. Interestingly, the taut tether arrival angle shows a similar trend as the catenary model-based controller, as seen by the relatively constant error between the two with a mean error of 12.6 degrees. Similar to the length results, this can be interpreted as the catenary controller providing a constant buffer from the higher tension taut controller. The wave profile has almost the same effect on both test cases, with the main difference being the starting angle.

6.1.3 Departure Angle, γ

The departure angle results of the tether at the winch are shown in Fig. 6.3a. The guide arm measurement technique shows promise, but has a 20 degree dead-band gap in measurement capability as seen by the periodic vertical lines. This error in measurement occurs when the smart reel switches between reeling in and paying out, and the tether contact point on the follower switch from one side to the other. Improvements to the design of the guide arms and follower may improve the angle measurement. However, this angle measurement design inherently colors the measurement by physically contacting the tether. While a stretching out of the departure angle measurement occurs, the trend still

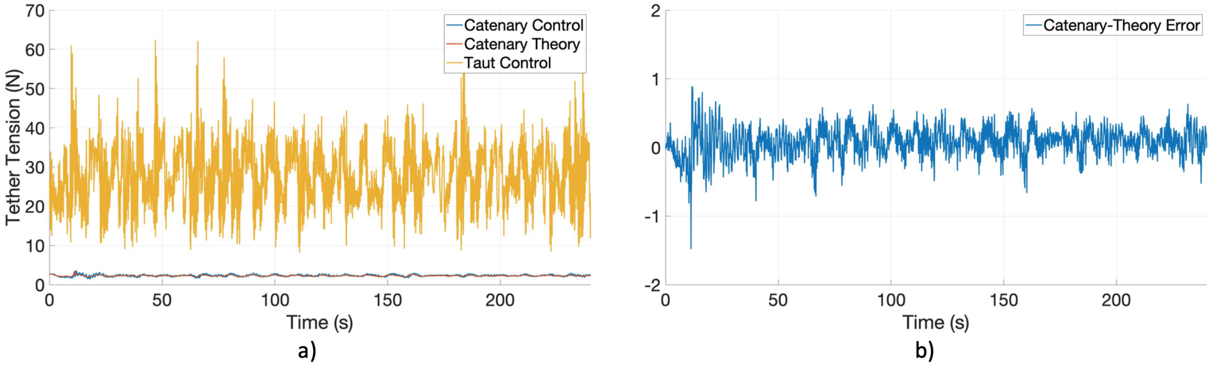

Figure 6.4: Typical experimental UAV surrogate tether tension results. a) Tether tension for both taut and catenary model-based controllers for the same wave profile. The theoretical catenary tether tension based on measured relative position and tether length corresponds well with the experimental catenary controller. b) Error between the catenary model-based controller and the theoretical values

correlates well with the theoretical catenary-based departure angle as seen in the cross correlation in Fig. 6.3b. The normalized correlation peaks at 0.88 seconds lag, and steadily decreases thereafter. Due to the errors in departure angle measurement, a controller with loop closure based on the reference departure angle was not evaluated.

6.1.4 Tether Tension

Fig. 6.4a shows a typical tether tension result for the catenary model-based control and taut tether control. The tether tension using the catenary model-based controller had a mean tension of 2.38 N with a standard deviation of 0.27 N. This corresponds well compared to the theoretical tension based on the measured relative position and tether length. The mean error between the experimental and theory was 0.08 N with a standard deviation of 0.20 N as seen in Fig. 6.4b. This shows that the controller minimized the dynamic effects of tether motion on the UAV in a controlled environment, while having perfect feedback and no external disturbances such as wind. The taut controller had a significantly higher mean tether tension of 27.52 N, with a much larger standard deviation of 7.30 N. Perhaps more significant is the peak-to-peak variation of 2.21 N for catenary

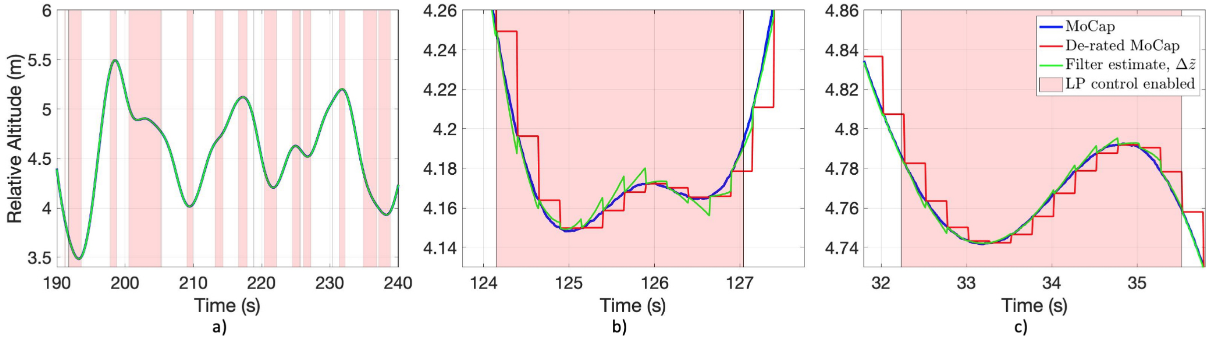

Figure 6.5: Twiddle Algorithm relative altitude tuning results for a) a 50 second time frame of HPR wave profile # 2, b) a 4 second time frame of the heave-only profile, and c) a 4 second time frame of HPR wave profile # 2. The 50 second segment shows the estimation filter tracking the ground truth MoCap measurements. The close up views also show the 4 Hertz de-rated MoCap measurements. The filter fills in the gaps between measurements, but has some errors when the wave profile slows down and changes directions, particularly bad for the heave-only profile.

control and 55.70 N for taut tether control, showing the greater variability of tension for the taut controller. Some of the taut tension variability can be attributed to the friction inherent in the spooling system. The torque setting on the spool motor had to be above the friction-stiction threshold in order to ensure continuous motion and prevent undesired stiction on the drum. A mechanical clutch or other tension sensing method has been shown to limit tension to a more consistent 8 N force, but not to the minimized level of the catenary model-based controller [16].

6.2 Estimation Filter Tuning

The estimation filter tuning results are presented first for the nine wave motion trials and one stationary motion trials using MoCap data as ground truth. The filter is then evaluated through an additional eight wave profile trials using the output of the filter as feedback for control.

Using the Twiddle Algorithm, the covariance gains on the filter were tuned to $\sigma_z = 0.0133$, $\sigma_{\dot{z}} = 8.66e-08$, $\sigma_{\ddot{z}} = 0.453$, $\sigma_{\mu_1} = 1.473$, $\sigma_{\mu_2} = 0.0146$, $\sigma_{\Delta\ddot{z}_{Acc_1}} = 112.94$,

Table 6.1: Estimation Filter Error

	Heave Only	HPR # 1	HPR # 2	Zero Motion
Test Time (s)	883.5	1,027.8	1,032.8	837.4
$\Delta\tilde{z}$ Mean |Error| (m)	0.00256	0.00135	0.00144	0.00111
$\Delta\tilde{z}$ RMSE (m)	0.00418	0.00239	0.00228	0.00298
FOH Mean |Error| (m)	0.00488	0.00280	0.00291	0.0007
FOH RMSE (m)	0.00783	0.00439	0.00443	0.0018

$\sigma_{\Delta\ddot{z}_{Acc_2}} = 91.105$, and when a relative position measurement exists, $\sigma_{\Delta z_{dGPS}} = 0.01$, otherwise $\sigma_{\Delta z_{dGPS}} = \infty$. Fig. 6.5a shows a typical result for one of the HPR wave profiles. The filter properly fills in the gaps between the de-rated MoCap measurements, but has some overshoot errors when the wave profile slows down and changes direction as seen in the shaded regions, shown scaled up in Fig. 6.5b and Fig. 6.5c. The overshoot errors are particularly bad on the heave-only profile. They are attributed to actuator noise and resonance of the three stepper motors on the 3-$\underline{\text{P}}$SR wave replication mechanism actuating in unison. This is also clearly seen in the mean error and RMSE error shown in Table 6.1, as the filter error for the heave-only profile is double that of the other wave profiles. For comparison, the tuned estimation filter outperforms a first-order hold (FOH) estimate using only the de-rated MoCap measurements for all but the stationary motion profile. To account for the errors and overshoot seen when the relative velocity is low, the relative velocity gain-scheduled low-pass filter was implemented on the commanded tether length as previously discussed in Section 4.2. The relative velocity for the same wave profiles is shown in Fig. 6.6. The gain-scheduling for the low-pass filter activates the filter at two different thresholds, as seen in the heave-only profile activating at a threshold of -0.3 m/s at 124.2 seconds, and the HPR wave profile activating at a threshold of 0.1 m/s at 32.5 seconds. The lower magnitude threshold activates if the relative velocity has not gone above the higher magnitude threshold, as seen in the longer HPR profile view between 210

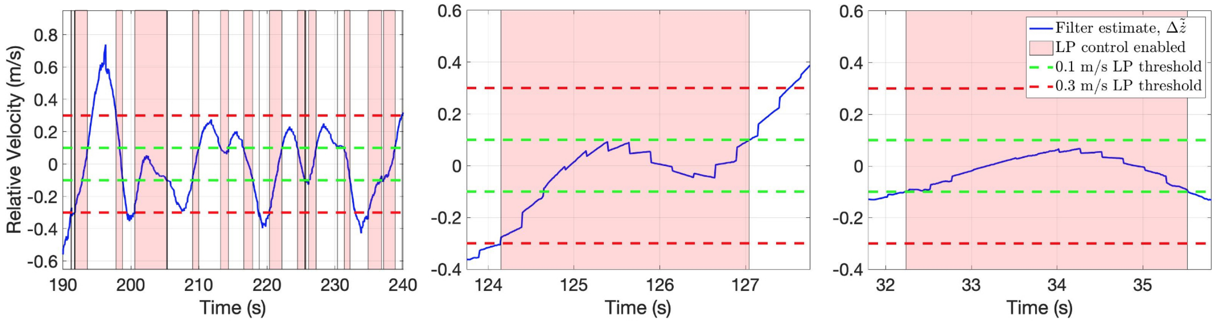

a) b) c)

Figure 6.6: Typical Twiddle Algorithm relative velocity tuning results for the same a) 50 second time frame of HPR wave profile # 2, b) 4 second time frame of the heave-only profile, and c) 4 second time frame of HPR wave profile # 2. The 0.1 and 0.3 m/s gain scheduling thresholds for the low pass filter are shown, and the shaded region where the low pass filter is active.

and 218 seconds. As seen in the shaded region in Fig. 6.5, the gain-scheduler accurately activates the low-pass filter when the relative position errors are largest. The effects of this gain-scheduled low-pass filtering on the tether length will be discussed in the next section.

6.2.1 Estimation Filter-Based Feedback Control

To evaluate the tuned estimation filter performance for feedback control, eight experimental trials were performed, two for each wave profile, including the HPR #3 profile which was not used to tune the filter. Table 6.2 shows the mean error and RMSE error of the tether length compared to the ideal tether length if MoCap has been used for feedback. The gain-scheduled controller worked well across all wave profiles with a mean error of 0.022 m and RMSE of 0.027 m, only slightly different than for the MoCap feedback presented in

Table 6.2: Tether Length Error

	Heave Only	HPR # 1	HPR # 2	HPR # 3	Total
Test Time (s)	514.76	648.04	657.11	645.52	2,465.43
Mean |Error| (m)	0.022	0.019	0.023	0.024	0.022
RMSE (m)	0.027	0.024	0.028	0.029	0.027

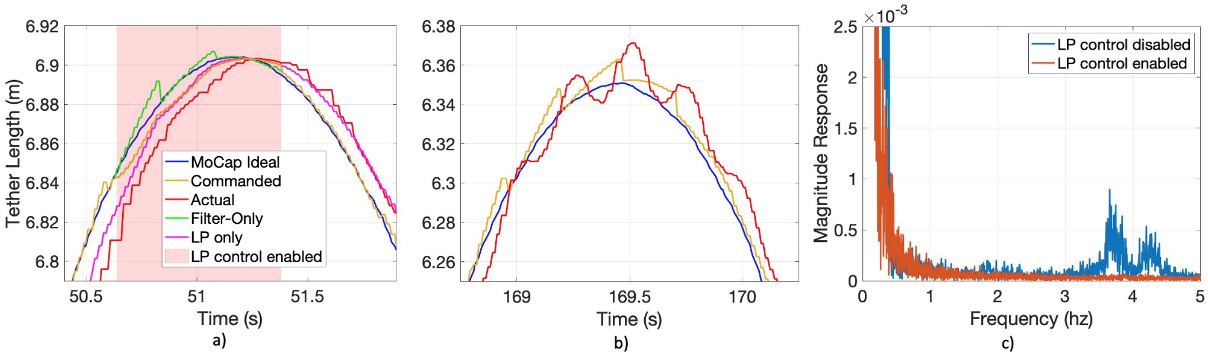

Figure 6.7: Typical tether length results from HPR wave profile # 3 using the estimation filter as feedback showing a) a close up view of the low pass gain scheduler activating, transitioning from using purely estimation filter-based tether reference length to a low pass filter-based tether reference length and back, b) a close up view for a trial run without the low pass gain scheduler, and c) the frequency content of the actual tether length from a) and b).

Section 6.1.1.

Further motivating the need for the gain-scheduled low-pass tether reference length, Fig. 6.7a shows a typical tether length result close up view for one of the HPR #3 trials. When the gain-scheduler changes α from 1 to 0.2, denoted by the shaded region, the commanded tether length transitions from the purely estimation filter-based tether reference length signal to the low-pass filtered tether reference length signal. In doing so, the discontinuities and oscillations present in the estimation filter-based tether reference length signal seen in the shaded region do not propagate through to the commanded tether length. The oscillations in the estimation filter tether reference length generally occurred more when slowing down into a change in direction than when speeding up out of the change in direction. This motivated the dual threshold gain-scheduler, allowing the commanded signal to speed up earlier when exiting the low-pass enabled region as seen by the actual tether length after 51.5 seconds, where it coincides with the low-pass tether reference length signal. In contrast, Fig. 6.7b shows a typical result for another trial where the gain-scheduled low-pass filter was not enabled. The commanded tether reference length signal retains the discontinuities and oscillations from the estimation filter, which

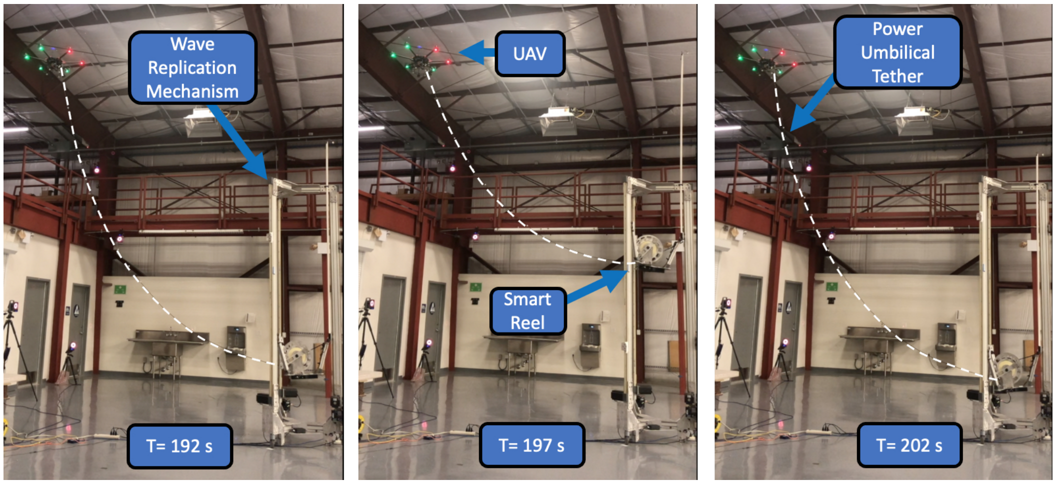

Figure 6.8: Typical experimental indoor flight testing for a single wave period during a HPR #2 wave profile trial at 192, 197 and 202 seconds duration. The tether has been highlighted with a white dashed line to make it more visible. Notice the tether is not taut, and resembles a catenary curve.

ultimately manifests as oscillations in the actual tether length, visibly noticeable on the smart reel. Fig. 6.7c shows the frequency spectrum content of the actual tether length for both trials. The low-pass gain-scheduled controller removes the 4 Hertz frequency content from the tether length output. A downside of implementing the low-pass filter is a small lag as is seen by the main peak of the frequency content occurring at a slightly lower frequency for the low-pass filtered trial. However, the low-pass filter is gain-scheduled to only activate when it is needed, when the relative velocity is low, mitigating the lag effects as much as possible.

6.3 Indoor Flight

Typical experimentation images of one period of a 1.9 m wave of a HPR wave profile trial are shown in Fig. 6.8. The tether is highlighted with the dashed line to make it more visible. The catenary model-based control performed well, with the tether remaining in the shape of a catenary curve throughout the large heave motion. The tether was instrumented

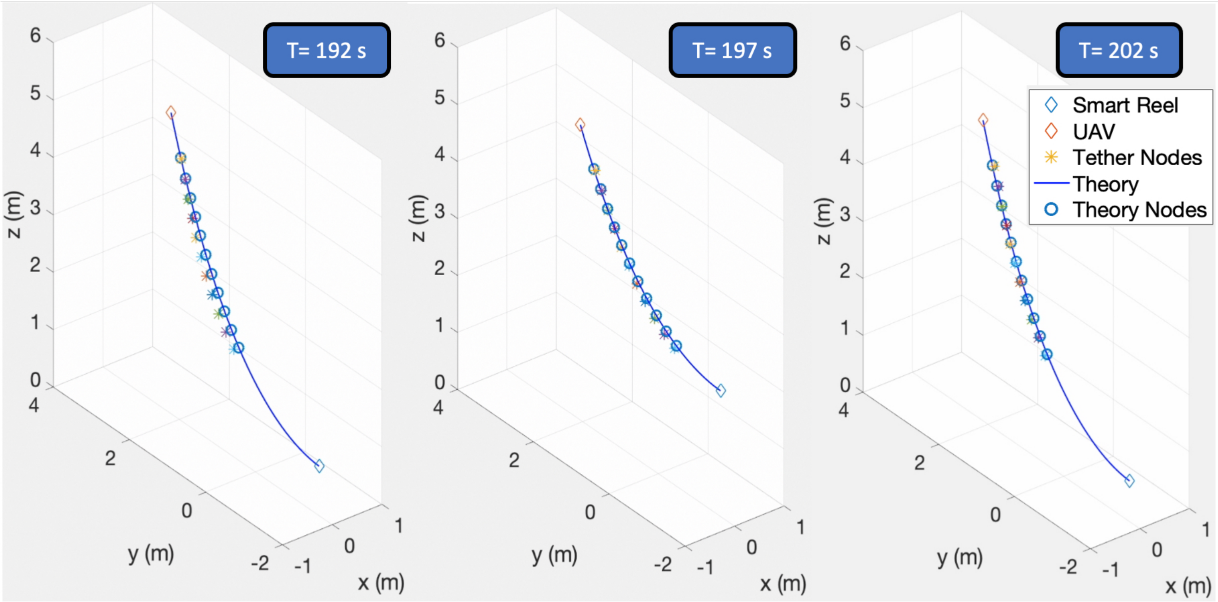

Figure 6.9: Typical experimental indoor flight testing MoCap for a single wave period during a HPR #2 wave profile trial at 192, 197 and 202 seconds duration. Eleven nodes on the tether, as well as the UAV and smart reel locations demonstrate a catenary shaped hanging curve. The theoretical reference catenary curve and the corresponding nodal points are shown for comparison.

with 11 motion capture spheres, or nodes, as seen in Fig. 6.9. The dynamics of the tether motion produced a mean positional error from the catenary theory-based reference shape of 0.076 m over eight separate trials (two per wave profile), with a standard deviation of 0.0378 m. The reaction time of the smart reel is fast enough to mitigate any dynamic effects due to UAV and smart reel motion.

The altitude displacement of the UAV during a typical experiment is shown in Fig. 6.10a. Because there was no position feedback on the UAV flight controller for station keeping, the RC pilot was required to hold altitude and position manually, which proved challenging in the confined testing space. The UAV altitude fluctuated 1.08 m from peak to peak, with a standard deviation of 0.18 m across the eight separate wave motion trials. The UAV position stayed within a circular radius of 0.60 m across all trials. To better gauge the effects of the tether, one un-tethered flight was performed in the same location. For the un-tethered flight, the altitude fluctuated 0.99 m peak to peak, with a standard deviation

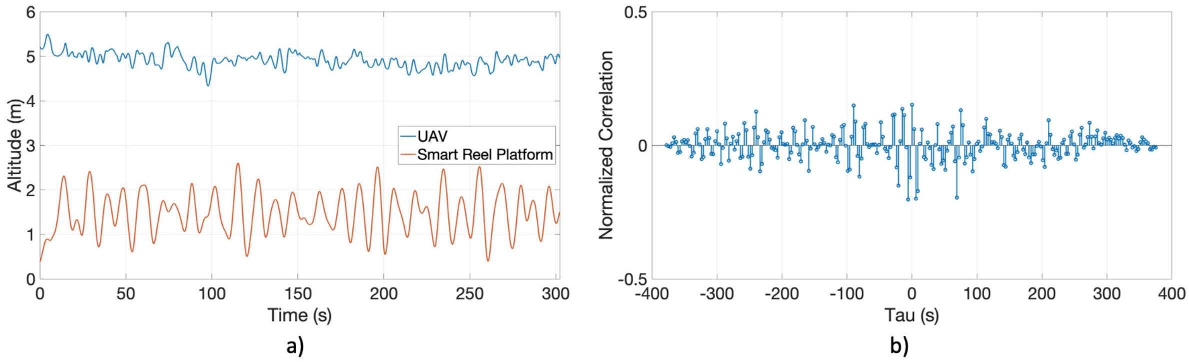

Figure 6.10: Typical altitude results for indoor flight testing for HPR #2. a) UAV altitude and smart reel platform height for a typical experiment. b) Normalized cross correlation between UAV altitude and smart reel platform height. The low correlation demonstrates a successful decoupling of UAV flight from the USV motion.

of 0.18 m, and positional motion within a radius of .48 m, on par with that for tethered flight. This range of motion is within the realm of what a standard UAV flight controller can do using GPS and barometer control outdoors [82, 83]. To further demonstrate the decoupling of the UAV and USV motion, the normalized cross correlation of the measured altitude and wave height is shown in Fig. 6.10b. The amplitude of the cross correlation is relatively flat for all time shifts, under a normalized 0.2. If the tether were pulling on the UAV, a peak near zero lag would be expected. The error statistics for the estimation filter and the tether controller for the indoor flight trials are shown in Table 6.3. Noticeably, the mean error and RMSE for the estimation filter are three to four times greater than those shown in Table 6.1. With the addition of the UAV, both endpoints of the tether are now

Table 6.3: Indoor Flight Estimation Filter and Tether Length Error

	Heave Only	HPR # 1	HPR # 2	HPR # 3
Test Time (s)	512.4	669.1	627.8	605.5
$\Delta\tilde{z}$ Mean |Error| (m)	0.0082	0.0056	0.0054	0.0058
$\Delta\tilde{z}$ RMSE (m)	0.012	0.0083	0.0080	0.0087
L Mean |Error| (m)	0.0118	0.0096	0.0100	0.0099
L RMSE (m)	0.0163	0.0132	0.0135	0.0135

dynamically moving, resulting in a some larger estimation errors. However, these errors are again relegated to the regions of the smart reel changing directions. The key error metric is the tether length error, which has improved compared to the UAV surrogate testing as shown in Table 6.2. The UAV having the ability to move dynamically adds a factor of compliance, while the smart reel decouples large scale motions. The gain-scheduled low-pass filter performs well in preventing errors and discontinuities in the estimation filter from propagating through to the tether length.

In summary, the catenary model-based tether control allows the UAV to hold position and altitude within the bounds of what an RC pilot can achieve. The gain-scheduled low-pass filter successfully mitigates any discontinuities realized in the estimation filter at low speeds. The smart reel successfully decouples the motion of the UAV and USV, while also minimizing induced dynamics on the tether.

6.4 Outdoor Flight

Typical experimentation images of one period of a 1.7 m wave are shown in Fig. 6.11. The tether is highlighted with the dashed line to make it more visible. The catenary model-based control performed well over eight separate trials (two per wave profile), with the tether remaining in the shape of a catenary curve throughout the wave motion. Most notably, compared to the scenario where the tether management controller is turned off, the tether sags below the smart reel and would be fouled in a real deployment scenario.

In switching from the MoCap system to the RTK dGPS system, a few technical challenges needed to be addressed. Fig. 6.12a shows the relative altitude output from the estimation filter and the raw dGPS measurements for a HPR #2 trial run. Notice that the Kalman filter fills in the gaps between the dGPS measurements reasonably well. However, as seen at 98.75 seconds, the RTK dGPS system used was not completely reliable, and

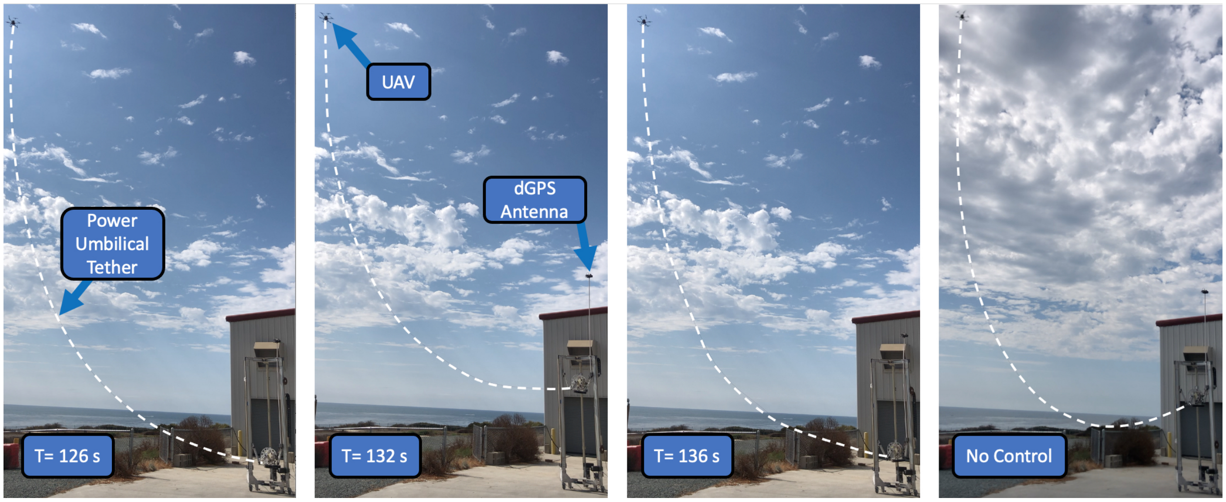

Figure 6.11: Typical outdoor flight testing for HPR #3 at 126, 132, 136 seconds, and no control. The tether has been highlighted with the white dashed line to make it more visible. Notice the tether is not taut, and resembles a catenary curve when the controller is active, whereas the tether has sagged below the platform when no controller is active.

failed to produce a message. This missed message incident occurred at a rate of 1.35%. When the dGPS failed to produce a message, the estimation filter kept dead reckoning using the inertial measurements as desired. However, the following dGPS measurement was often stale and incorrect, as seen at 99.5 seconds. The missed dGPS measurements

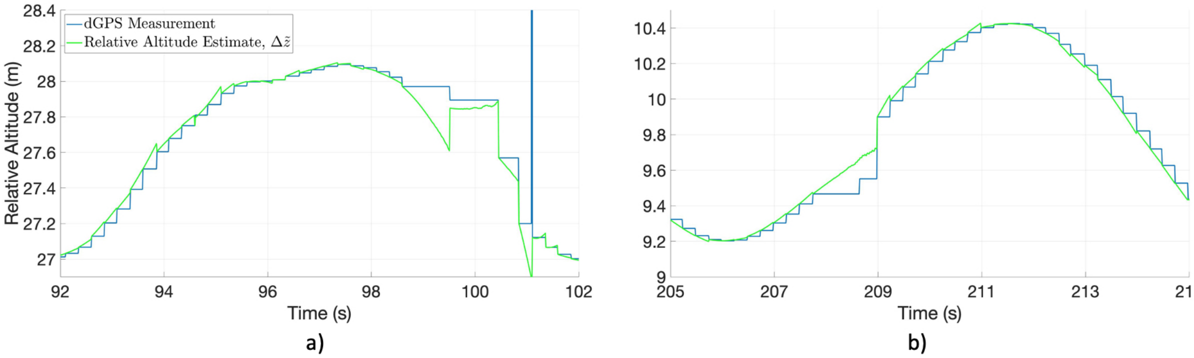

Figure 6.12: Typical relative altitude results for an outdoor flight for a) a HPR #2 trial showing the relative altitude comparing dGPS and estimation filter output for a typical experiment before logic was implemented. Note the errors in the dGPS measurements around 100 seconds. b) a HPR #3 trial showing a similar output after dGPS message logic applied. Note the missed dGPS message at 207.75 seconds and the stale message at 208.65 seconds does not affect the Kalman filter output.

required one second in order for dGPS system to sort itself out before outputting a good message, occasionally producing a completely erroneous measurement, as seen at 113.5 seconds. As seen in Fig. 6.12b for a HPR #3 trial run, logic was implemented to make sure the change in dGPS message timestamps were in line with the change in time from the microprocessor. The missed dGPS message at 207.75 seconds and the stale message at 208.65 seconds does not affect the Kalman filter output. Additional logic was implemented to prevent any change in subsequent dGPS measurements greater than 1 m from being used in the estimation filter. With the addition of logic, the dGPS Kalman filter estimation is a reasonable solution for outdoor operation.

Typical tether length results are shown in Fig. 6.13a for a short 1.5 second section of a HPR #3 trial. Between 113.2 and 113.6 seconds, the low-pass filter activates, and the discontinuities shown in the filter-only output are avoided. When the low-pass filter deactivates at 113.6 seconds and the wave profile speeds up, the lag in the actual tether length decrease as seen by the decreasing gap between the filter only output and the actual tether length. Fig. 6.13b shows a longer, 10 second section of a HPR #2 trial. Notice that the actual tether length stays relatively smooth, with the low-pass filter activating when the relative velocity is low. While the results for the outdoor flight testing are harder to

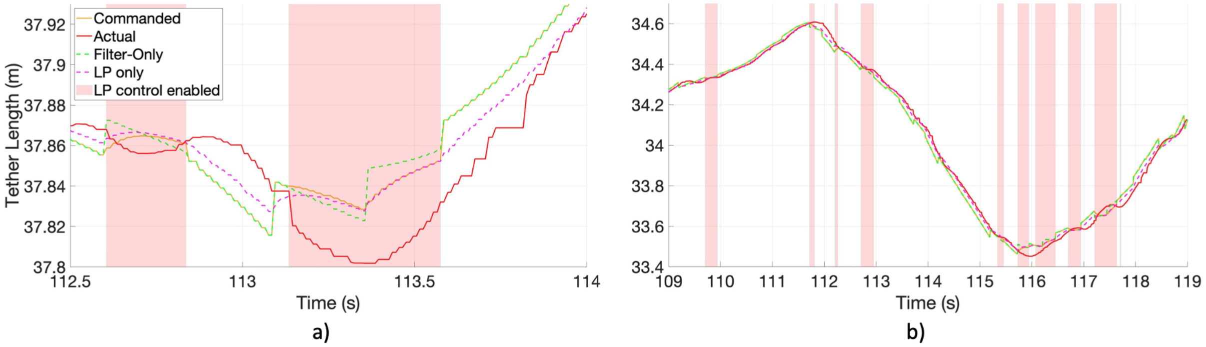

Figure 6.13: Typical tether length results for an outdoor flight for a) a HPR #3 trial showing the commanded and actual tether length. b) a HPR #2 trial showing the commanded and actual tether length for a longer, 10 second section.

analyze since there is no ground truth measurement to base an idealized tether length off, the control scheme shows promise.

6.5 Conclusion

A semi-slack, hanging tether model for tether management of a UAV-USV team was implemented and experimentally validated with a prototype smart reel in a controlled and relevant dynamic environment. The developed prototype smart reel, capable of measuring the tether length, departure angle, and tension, shows promise in using the angle measurement for feedback, but the tether length was ultimately used as a more reliable, accurate measurement. The semi-slack hanging tether model, dependent on the relative position between the UAV and USV was extended to operate through a larger relative position range, extending above $\Delta r/\Delta z > 1.2$. With the goal of outdoor operation, a Kalman filter model was developed to combine a slow, 4 Hertz, RTK dGPS relative position measurement with fast, 100 Hertz inertial measurements, to output a fast, 100 Hertz estimate of the relative position, relative velocity, and inertial sensor bias. The estimation filter was tuned using experimental data from an indoor MoCap system as a ground truth measurement. A relative velocity-based gain-scheduled controller was developed and experimentally validated through three experimental phases: surrogate, indoor flight, and outdoor flight testing.

Experimental testing with a UAV surrogate showed that the controller works well in a controlled environment with no external disturbances. The tether tension agrees closely with the predicted values from catenary theory. More importantly, taut tether control exhibits 12 times more tether tension. The tether length trend for both the taut and catenary model-based control were very similar, but had an initial offset. If the taut tether length was known, an offset buffer would create the same effect. However, that buffer changes depending on the relative position, i.e., the model, controller, and estimation filter are necessary.

Indoor flight testing showed that the catenary controller works well with a UAV at large, dynamically varying relative positions. No correlation between the UAV and USV's altitude was found, demonstrating a successful decoupling of motion. Additionally, the UAV's range of motion was comparable to that of un-tethered flight. The RC pilot was able to perform manual station keeping comparable to that of a GPS controller. Outdoor flight in a representative operational environment showed good results using the RTK dGPS and IMU Kalman filter for relative position feedback, as long as some logic was implemented to ensure the RTK dGPS messages were proper.

For most tethered UAV operational scenarios, one of the ultimate goals is to fly at high altitude. The higher the UAV flies, the more the tether pulls down on the UAV, and the larger thrust authority and margin are required. This tether management system ultimately decreases the safety margins, allowing for higher UAV flight up to and above 50 m, as well as flying from a USV in moderate seas. A major benefit of this control system is that is is based purely on relative position, regardless of scale.

6.6 Acknowledgments

Support for this work was provided by Naval Information Warfare Center Pacific under the Naval Innovative Science and Engineering program and the Department of Defense SMART Scholarship for Service program.

Chapter 6, in full, has been submitted for publication as it may appear in Field Robotics 2021,K. Talke, F. Birchmore, T. Bewley, "Autonomous Hanging Tether Management and Experimentation for a UAV-USV Team". The dissertation author was the primary investigator and author of these pages.

Chapter 7

Three Dimensional Elastic String Pendulum Dynamics

The heave robustness model is based on static hanging cable theory, however does not take the dynamics of the tether into account. Thus, the tether management control and feedback is performed in a quasi-static sense. Compounding that, the accurate measurement of the relative position given existing sensors has proven challenging, and required logic and low-pass filtering to produce a functional result. In order to develop a tether management controller that can specifically counteract tether dynamics such as wind effects, or harmonic amplification, a numerical model, or digital twin environment, capable of simulating the dynamics of the UAV, tether, USV, and wind is required. Before a simulation environment can be developed, the dynamics of the system need to be derived. In this chapter, three dynamic models are derived using Hamilton's principle of least action: a three dimensional elastic string rigid body pendulum, a three dimensional fixed reel elastic string rigid body pendulum, and a three dimensional moving reel elastic string rigid body pendulum with extensions to the UAV-USV team.

7.1 Introduction

Numerous applications of objects connected to cables or strings exist, including cable cranes, tensegrity robotics, towed underwater vehicles, and swings. Under low tension applications, gravitational forces play a significant role in the shape and dynamics of the string, and therefore, the overall movement and dynamics of the attached object. Of particular interest is a low-tension tethered UAV application, where a winch on a small USV controls the length of the tether and the UAV maintains position and altitude for ISR missions. The tether acts as a power and communications umbilical, providing secure data transfer and unlimited flight duration [3–5]. However, a tether limits the mobility of the UAV, and introduces the problem of the tether fouling on the USV or winch if slack, or pulling on the UAV if taut, limiting operation range or at worst destabilizing the UAV flight controls. Appropriate tether management is needed to control the length and dynamics of the tether. Many tether management controllers have been developed, but the majority use a taut tether approach to avoid the tether oscillations [2], improve flight stability [7–11], or enhance landing capability [12–14]. Other systems have considered non-taut tethered flight using a reactive tether management approach [21], or a non-taut catenary model based approach, however no intrinsic tether dynamics were considered [6, 24, 84].

A high fidelity numerical simulation that accurately models tether dynamics is required to develop a non-taut tether controller using modern control techniques. First, the underlying dynamics need to be fully derived and understood. Then, an appropriate numerical approximation of those dynamics needs to be developed and validated. Several dynamic and numerical models have been developed generally focusing on subsurface, underwater tethers. A number of approaches use a lumped mass approach, where the string is discretized into a series of small masses connected with massless spring-dampers [2], or rigid elements [85, 86] between them. Of particular interest in these lumped mass models is how to deal with the changing length of the tether due to a reel or winch [87–89], in which a viable solution was to change the nominal length of the nodes closest to the reel or winch. This has the potential to lead to a large variability in nominal element length for large reel-ins and payouts. Poor scaling of elements can lead to numerical instabilities resulting in a failed simulation. Other lumped mass models used torsional spring-mass dampers between mass nodes [90–92] for instance, to study the cracking of a whip. However, all these approaches assume that they can discretize the string prior to determining the equations of motion.

A more flexible and rigorous approach is to treat the string as a continuous system, first deriving the governing equations of motion according to Hamilton's variational principle of least action. A number of different approaches for discretization may then be considered. A derivation using Hamilton's principle has been presented along with a Lie group variational numerical integrator, though it is incomplete [93]. The Lie group variational integration model focuses on long term energy conservation and stability, at the cost of short term accuracy.

The remainder of the chapter is organized as follows. Section 7.2 presents a complete Hamilton's principle-based derivation of the equations of motion for an elastic string rigid body pendulum. Section 7.3 presents the inertially fixed reel elastic string rigid body pendulum dynamic derivation. Section 7.4 presents the moving reel elastic string rigid body pendulum dynamic derivation. Section 7.5 summarizes the key conclusions.

7.2 Elastic String - Rigid Body Pendulum

This section summarizes and completes the derivation of the three dimensional elastic string pendulum shown in Fig. 7.1 [93]. The tether, with linear density μ, is attached at one end to an inertially fixed pivot with the right handed global coordinate system defined by the orthonormal unit vectors $\hat{\mathbf{e}}_1$, $\hat{\mathbf{e}}_2$, and $\hat{\mathbf{e}}_3$. A point P, along the tether is

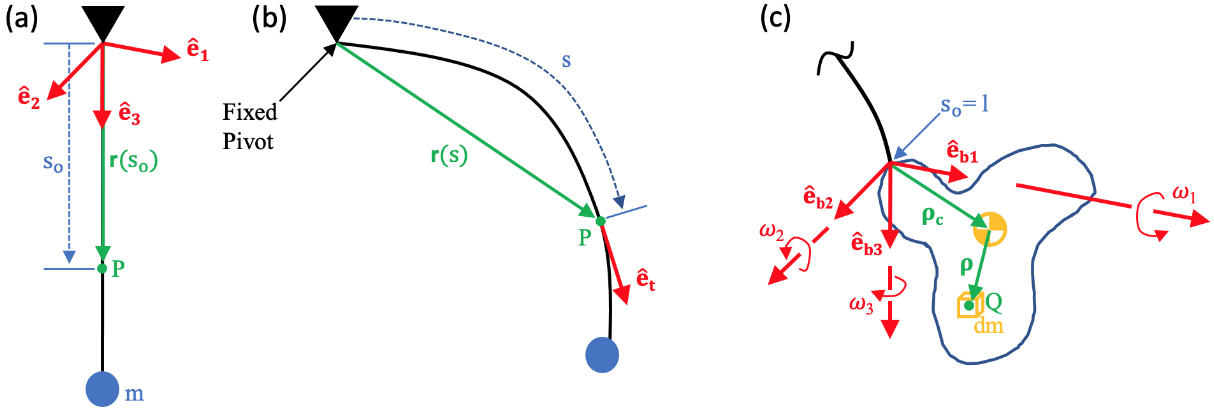

Figure 7.1: Diagrams of (a) simple pendulum, (b) flexible and stretchable string pendulum, and (c) a flexible, stretchable string pendulum with a rigid body mass

defined by the vector $\mathbf{r}_P = \mathbf{r}(s_o)$, where $s_o \in [0, l]$ is the unstretched length of string to that point, and l is the total length of the unstretched string. For the stretched case, the vector $\mathbf{r}(\mathrm{s})$ defines the location of the point, where s is the stretched length of string to point P. The tangent vector to the string at that point is defined as $\hat{\mathbf{e}}_{\mathrm{t}}$. Attached at the other end of the string, with its location defined by $\mathbf{r}_{rb} = \mathbf{r}(l)$ for $s_o = l$, is a rigid body with mass m. Attached at the string mounting point are the body frame, orthonormal unit vectors $\hat{\mathbf{e}}_{\mathrm{b}1}$, $\hat{\mathbf{e}}_{\mathrm{b}2}$, and $\hat{\mathbf{e}}_{\mathrm{b}3}$. The angular velocity vector, $\boldsymbol{\Omega} = \begin{bmatrix} \omega_1 & \omega_2 & \omega_3 \end{bmatrix}^T$ consists of the three rigid body rotations about each of the body frame orthonormal unit vectors. The vector from the string mounting point to the center of mass is $\boldsymbol{\rho}_c$ represented in the body fixed frame. The vector from the center of mass to an infinitesimally small mass, dm, located at point Q, is defined as $\boldsymbol{\rho}$ represented in the body fixed frame.

The Lagrangian needs to be determined. Then, the continuous time equations of motion will be derived using Hamilton's Principle of least action.

7.2.1 Lagrangian

The Lagrangian for this system can be defined as the sum of the potential energy and kinetic energy from the string and rigid body:

$$\mathcal{L} = T_{\text{string}} + T_{\text{rb}} - V_{\text{string}} - V_{\text{rb}} \tag{7.1}$$

Kinetic Energy (T)

The kinetic energy of the string consists of the translational velocity of infinitesimal string mass elements:

$$T_{\text{string}} = \int_0^l \frac{1}{2}\mu \dot{\mathbf{r}}\left(s_o\right) \cdot \dot{\mathbf{r}}\left(s_o\right) ds_o \tag{7.2}$$

where $\dot{\mathbf{r}}\left(s_o\right)$ is the time derivative of $\mathbf{r}\left(s_o\right)$. Similarly, the kinetic energy of the rigid body depends on rectilinear motion and rotational velocity of the rigid body:

$$T_{\text{rb}} = \int_{\text{Body}} \frac{1}{2}\dot{\mathbf{r}}_Q \cdot \dot{\mathbf{r}}_Q dm \tag{7.3}$$

where $\mathbf{r}_Q$ describes the vector from the pivot to the location of a infinitesimal mass element in the rigid body:

$$\mathbf{r}_Q = \mathbf{r}(l) + \left(\boldsymbol{\rho} + \boldsymbol{\rho}_c\right). \tag{7.4}$$

Note that $\boldsymbol{\rho}$ and $\boldsymbol{\rho}_c$ use the body fixed frame basis vectors ($\hat{\mathbf{e}}_{\text{b1}}$, $\hat{\mathbf{e}}_{\text{b2}}$, and $\hat{\mathbf{e}}_{\text{b3}}$). Converting to the global basis vectors yields:

$$\mathbf{r}_Q = \mathbf{r}(l) + \mathbf{R}\left(\boldsymbol{\rho} + \boldsymbol{\rho}_c\right). \tag{7.5}$$

where $\mathbf{R}$ is the rotation matrix to convert from the body fixed frame to the global coordinate frame, as defined in Eq. A.7. By converting into the global frame, the typical tensor analysis which requires meticulous tracking of derivatives, can be simplified into linear algebra using the rotation matrix derivative kinematic relationship given in Eq. A.5. Taking and inserting the derivative of Eq. 7.5 into Eq. 7.3, and rearranging results in:

$$T_{\mathrm{rb}} = \frac{1}{2}\mathrm{m}\dot{\mathsf{r}}\left(l\right) \cdot \dot{\mathsf{r}}\left(l\right) + \mathrm{m}\dot{\mathsf{r}}\left(l\right) \cdot \mathbf{R}\hat{\mathbf{\Omega}}\boldsymbol{\rho}_c + \frac{1}{2}\boldsymbol{\Omega} \cdot \mathbf{\Pi}\boldsymbol{\Omega} \tag{7.6}$$

where $\mathbf{\Pi}$ is the matrix representation of the inertia tensor as defined in Eq. B.2 [93, 94], and the $\hat{\cdot}$ operator denotes a skew symmetric matrix mapping of the cross product of a three dimensional vector as in Eq. A.1. See Appendix B.1 for the complete derivation from Eq. 7.3 to Eq. 7.6. (Note the slight difference in notation, that tensors and vectors will use the sans serif font, and matrices will use the serif font. Clearly seen in the matrix $\hat{\mathbf{\Omega}}$, and vector $\boldsymbol{\Omega}$.)

Potential Energy (V)

In addition to the gravitational potential, the string has internal potential energy (axial strain, torsion, or bending), and needs to be modeled accordingly [95]. For a long string, with the length much greater than the diameter, the string can twist freely and torsion forces are negligible. Below a low tension threshold of approximately 0.5 N, bending can be neglected [96–101]. Here, bending forces could be included via the integral $\int_0^L \frac{1}{2}EI\left(\nu''\right)^2 ds_o$ [102, 103], but would make the analysis considerably more complicated without much benefit. Thus, the potential energy of the string consists solely of the internal elastic energy due to its stretch, and gravity potential for the infinitesimal string mass elements [104]:

$$V_{\text{string}} = \int_0^l \frac{1}{2} EA\epsilon^2 - \mu \mathbf{r}\left(s_o\right) \cdot \mathbf{g} ds_o \tag{7.7}$$

where ϵ is the tangential strain of the string element ds_o, as defined in Eq. B.3, and $\mathbf{g} = g\hat{\mathbf{e}}_3$ is the gravity vector. [93]. Inserting the formal definition of strain for a continuous body results in:

$$V_{\text{string}} = \int_0^l \frac{1}{2} EA\left(\|\mathbf{r}'\left(s_o\right)\|_2 - 1\right)^2 - \mu \mathbf{r}\left(s_o\right) \cdot \mathbf{g} ds_o \tag{7.8}$$

where $()'$ denotes the spatial partial derivative $(\frac{\partial}{\partial s_o})$, and $\|\mathbf{x}\|_2 = \sqrt{\mathbf{x} \cdot \mathbf{x}} = \sqrt{x_1^2 + \cdots x_n^2}$ is the Euclidean distance, or 2-norm. See Appendix B.2 for the complete derivation from Eq. 7.7 to Eq. 7.8.

The potential energy of the rigid body depends only on the gravitational potential of the center of mass:

$$\begin{aligned} V_{\text{rb}} &= -\text{m}\left(\mathbf{r}\left(l\right) + \mathbf{R}\boldsymbol{\rho}_c\right) \cdot \mathbf{g} \\ V_{\text{rb}} &= -\text{m}\mathbf{r}\left(l\right) \cdot \mathbf{g} - \text{m}\mathbf{R}\boldsymbol{\rho}_c \cdot \mathbf{g} \end{aligned} \tag{7.9}$$

Complete Lagrangian

Inserting the kinetic energies from Eq. 7.2, Eq. 7.6, and potential energies from Eq. 7.8, and Eq. 7.9 into Eq. 7.1 gives the total Langrangian energy:

$$\begin{aligned} \mathcal{L} =& \frac{1}{2}\text{m}\dot{\mathbf{r}}\left(l\right) \cdot \dot{\mathbf{r}}\left(l\right) + \text{m}\dot{\mathbf{r}}\left(l\right) \cdot \mathbf{R}\hat{\boldsymbol{\Omega}}\boldsymbol{\rho}_c + \frac{1}{2}\boldsymbol{\Omega} \cdot \boldsymbol{\Pi}\boldsymbol{\Omega} + \int_0^l \frac{1}{2}\mu\dot{\mathbf{r}}\left(s_o\right) \cdot \dot{\mathbf{r}}\left(s_o\right) ds_o + \text{m}\mathbf{r}\left(l\right) \cdot \mathbf{g} \\ &+ \text{m}\mathbf{R}\boldsymbol{\rho}_c \cdot \mathbf{g} + \int_0^l \left\{ -\frac{1}{2}EA\left(\|\mathbf{r}'\left(s_o\right)\|_2 - 1\right)^2 + \mu\mathbf{r}\left(s_o\right) \cdot \mathbf{g} \right\} ds_o \end{aligned} \tag{7.10}$$

7.2.2 Equations of Motion from Hamilton's Principle of Least Action

Using the Lagrangian from Eq. 7.10, the equations of motion can be determined using Hamilton's Principle of least action, defined as [105–107]:

$$\delta \mathcal{S} = \delta \int_{t_1}^{t_2} \mathcal{L}\left(\mathbf{q}, \dot{\mathbf{q}}, t\right) dt = 0 \tag{7.11}$$

where $\mathbf{q}$ and $\dot{\mathbf{q}}$ are the generalized coordinates of the Lagrangian. Taking the variation of the Lagrangian requires integration by parts (IBP) in time, but also IBP in space due to the integral across the string domain and the spatial partial derivative. Because one end of the string is inertially fixed and the length does not change in time, the integral in time and space order can be freely swapped. Taking the variation and repeatedly applying IBP yields (See Appendix C for the complete derivation, following and correcting the derivation given in [93]):

$$\begin{aligned}\int_{t_o}^{t_f} \int_0^l & \left(-\mu \ddot{\mathbf{r}}\left(s_o\right) + \mu \mathbf{g} + EA\left(\frac{\left\|\mathbf{r}'\left(s_o\right)\right\|_2 - 1}{\left\|\mathbf{r}'\left(s_o\right)\right\|_2}\mathbf{r}'\left(s_o\right)\right)'\right) \cdot \delta \mathbf{r}\left(s_o\right) ds_o \\ & + \left(-\mathrm{m}\ddot{\mathbf{r}}\left(l\right) + \mathrm{m}\mathbf{g} - EA\frac{\left\|\mathbf{r}'\left(l\right)\right\|_2 - 1}{\left\|\mathbf{r}'\left(l\right)\right\|_2}\mathbf{r}'\left(l\right) - \mathrm{m}\mathbf{R}\hat{\boldsymbol{\Omega}}^2 \boldsymbol{\rho}_c + \mathrm{m}\mathbf{R}\hat{\boldsymbol{\rho}}_c\dot{\boldsymbol{\Omega}}\right) \cdot \delta \mathbf{r}\left(l\right) \\ & + \left(-\boldsymbol{\Pi}\dot{\boldsymbol{\Omega}} - \hat{\boldsymbol{\Omega}}\boldsymbol{\Pi}\boldsymbol{\Omega} + \mathrm{m}\hat{\boldsymbol{\rho}}_c\mathbf{R}^T\mathbf{g} - \mathrm{m}\hat{\boldsymbol{\rho}}_c\mathbf{R}^T\ddot{\mathbf{r}}\left(l\right)\right) \cdot \boldsymbol{\eta}\, dt = 0\end{aligned} \tag{7.12}$$

From the Hamilton's Principle definition, the variations, $\delta\mathbf{r}\left(s_o\right)$, $\delta\mathbf{r}\left(l\right)$, and $\boldsymbol{\eta}$ are defined such that they equal zero at t_o and t_f, but can be nonzero elsewhere. Thus, for the entire equation to be true, the terms inside the parenthesis needs to be equal to zero, resulting in the equations of motion:

$$\begin{aligned}
\mu\ddot{\mathbf{r}}\left(s_o\right) - \mu\mathbf{g} - EA\frac{\partial}{\partial s}\left(\frac{\left\|\mathbf{r}'\left(s_o\right)\right\|_2 - 1}{\left\|\mathbf{r}'\left(s_o\right)\right\|_2}\mathbf{r}'\left(s_o\right)\right) &= 0 \\
\mathrm{m}\ddot{\mathbf{r}}\left(l\right) - \mathrm{m}\mathbf{g} + EA\frac{\left\|\mathbf{r}'\left(l\right)\right\|_2 - 1}{\left\|\mathbf{r}'\left(l\right)\right\|_2}\mathbf{r}'\left(l\right) + \mathrm{m}\mathbf{R}\hat{\boldsymbol{\Omega}}^2\boldsymbol{\rho}_c - \mathrm{m}\mathbf{R}\hat{\boldsymbol{\rho}}_c\dot{\boldsymbol{\Omega}} &= 0 \qquad (7.13) \\
\boldsymbol{\Pi}\dot{\boldsymbol{\Omega}} + \hat{\boldsymbol{\Omega}}\boldsymbol{\Pi}\boldsymbol{\Omega} - \mathrm{m}\hat{\boldsymbol{\rho}}_c\mathbf{R}^T\mathbf{g} + \mathrm{m}\hat{\boldsymbol{\rho}}_c\mathbf{R}^T\ddot{\mathbf{r}}\left(l\right) &= 0.
\end{aligned}$$

The first equation, a partial differential equation (PDE) is the translation dynamics of the continuous string including gravitational forces, inertia, and internal tension forces. The second, a PDE, and third, an ordinary differential equation (ODE), are the translation and rotational dynamics of the rigid body, respectively, and include coupling forces due to the string attachment. Note that if the body was a point mass, $\boldsymbol{\rho}_c$ would be zero, and the coupling forces would simplify accordingly.

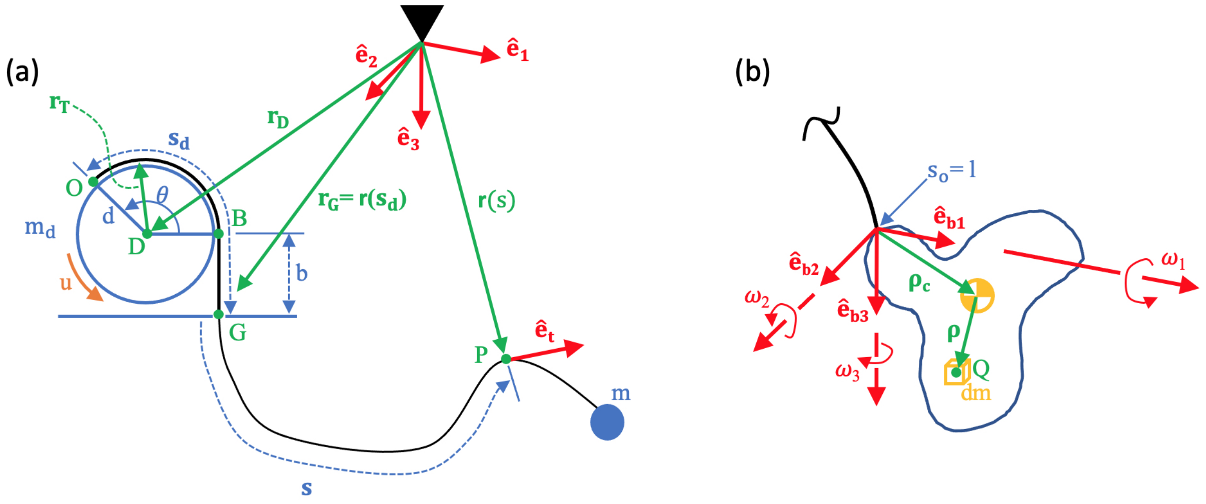

Figure 7.2: Diagrams of (a) flexible and stretchable string pendulum connected to a winch, and (b) a flexible, stretchable string pendulum with a rigid body mass

7.3 Fixed Reel - Elastic String - Rigid Body Pendulum

The natural follow on from the three dimensional elastic pendulum is to replace the fixed pivot with an inertially fixed reel, or winch mechanism. A number of methods attempted to model a winch by keeping the boundary condition fixed while varying the nominal element length [88, 108] or maintaining the nominal element length and adding or subtracting elements as the tether length changes [109]. These approaches lead to inaccuracies and numerical errors or instability in the simulation model. In other work, a cohesive derivation of the reel elastic pendulum dynamics is used to develop a discrete time variational integrator model for tethered satellite applications [110]. However, they assume a Carnot energy loss as the tether exits the reel due to the velocity discontinuity. With the goal of eventually developing an Arbitrary Lagrangian Eulerian (ALE) formulation [111,112], this section summarizes and completes the derivation of the fixed reel elastic string pendulum as shown in Fig. 7.2 [110] .

The string and rigid body have the same characteristics as those described in Section

7.2. Differing in this case, the constrained end of the string is no longer attached to a fixed pivot, but to a reel. The global coordinate system is defined by the orthonormal unit vectors $\hat{\mathbf{e}}_1$, $\hat{\mathbf{e}}_2$, and $\hat{\mathbf{e}}_3$. The location of the center of the reel is at point D is defined by the vector $\mathbf{r}_{\mathrm{D}}$. The drum has a rotational inertia of $J_{\mathrm{d}} = \frac{1}{2}\mathrm{m_d d^2}$, where the radius of the reel is denoted d, and a control moment u. The string is attached to the reel at point O, and the vector from the center of the drum to an infinitesimal string element on the drum is denoted $\mathbf{r}_{\mathrm{T}} = \mathrm{d}\left(\cos\theta\hat{\mathbf{e}}_1 - \sin\theta\hat{\mathbf{e}}_3\right)$. As the reel rotates an angle θ, the string wraps on the reel and is no longer elastic. The string unwraps off the reel at point B, extends a straight distance, b, to a guide-way located at point G, defined by $\mathbf{r}_{\mathrm{G}} = \mathbf{r}(\mathrm{s_d})$, where $\mathrm{s_d}$ is the length of string wrapped on the reel between point O and G. The deployed string is again denoted $\mathrm{s_0}$ for the unstretched length, and s for the stretched length.

7.3.1 Lagrangian

The Lagrangian for this system can be defined as the sum of the potential energy and kinetic energy from the reel, the string and the rigid body:

$$\mathcal{L} = T_{\mathrm{reel}} + T_{\mathrm{string}} + T_{\mathrm{rb}} - V_{\mathrm{reel}} - V_{\mathrm{string}} - V_{\mathrm{rb}} \tag{7.14}$$

Kinetic Energy (T)

The kinetic energy of the reel consists of the translational velocity of string on the reel and the rotational kinetic energy of the drum:

$$T_{\mathrm{reel}} = \int_0^{\mathrm{s_d}} \frac{1}{2}\mu\dot{\mathbf{r}}\left(\mathrm{s_0}\right)\cdot\dot{\mathbf{r}}\left(\mathrm{s_0}\right)d\mathrm{s_0} + \frac{1}{2}J_{\mathrm{d}}\dot{\theta}\left(\mathrm{O}\right)^2$$

The string on the drum is inextensible, and its velocity is constant and equal to the velocity at the guide way, $\dot{\mathbf{r}}\left(\mathrm{s_d}\right) = \dot{\mathrm{s}}_{\mathrm{d}}$. The angular velocity of the drum can be defined as $\dot{\theta}\left(\mathrm{O}\right) = \frac{\dot{\mathrm{s}}_{\mathrm{d}}}{\mathrm{d}}$, and substituting in the moment of inertia results in:

$$T_{\text{reel}} = \frac{1}{2}\left(\mu \mathrm{s}_{\mathrm{d}} + \frac{\mathrm{m}_{\mathrm{d}}}{2}\right)\dot{\mathrm{s}}_{\mathrm{d}}^{2} \tag{7.15}$$

The deployed string kinetic energy consists of the translational velocity of infinitesimal string mass elements, which is the same derivation as in Section 7.2.1 with the exception that the lower limit of the integral is different due to the reel boundary condition:

$$T_{\text{string}} = \int_{\mathrm{s}_{\mathrm{d}}}^{l} \frac{1}{2}\mu \dot{\mathbf{r}}\left(\mathrm{s}_0\right) \cdot \dot{\mathbf{r}}\left(\mathrm{s}_0\right) d\mathrm{s}_0 \tag{7.16}$$

The rigid body kinetic energy, consists of the translational and rotational velocity of the rigid body. This is the same derivation as in Section 7.2.1 resulting in Eq. 7.6, repeated here:

$$T_{\text{rb}} = \frac{1}{2}\mathrm{m}\dot{\mathbf{r}}\left(l\right) \cdot \dot{\mathbf{r}}\left(l\right) + \mathrm{m}\dot{\mathbf{r}}\left(l\right) \cdot \mathbf{R}\hat{\mathbf{\Omega}}\boldsymbol{\rho}_c + \frac{1}{2}\mathbf{\Omega} \cdot \mathbf{\Pi}\mathbf{\Omega} \tag{7.17}$$

Combining the reel, string, and rigid body kinetic energies, from Eq. 7.15, Eq. 7.16 and Eq. 7.17, respectively yields the total kinetic energy:

$$T = \frac{1}{2}\left(\mu \mathrm{s}_{\mathrm{d}} + \frac{\mathrm{m}_{\mathrm{d}}}{2}\right)\dot{\mathrm{s}}_{\mathrm{d}}^{2} + \int_{\mathrm{s}_{\mathrm{d}}}^{l} \frac{1}{2}\mu \dot{\mathbf{r}}\left(\mathrm{s}_0\right) \cdot \dot{\mathbf{r}}\left(\mathrm{s}_0\right) d\mathrm{s}_0 + \frac{1}{2}\mathrm{m}\dot{\mathbf{r}}\left(l\right) \cdot \dot{\mathbf{r}}\left(l\right) + \mathrm{m}\dot{\mathbf{r}}\left(l\right) \cdot \mathbf{R}\hat{\mathbf{\Omega}}\boldsymbol{\rho}_c + \frac{1}{2}\mathbf{\Omega} \cdot \mathbf{\Pi}\mathbf{\Omega} \tag{7.18}$$

Potential Energy (V)

New in this system is the reel potential energy. Because the reel is inertially fixed, the only changing potential energy comes from the change in gravitational potential of the mass of the string on the drum, which is determined by the vector to an infinitesimal string element:

$$V_{\mathrm{reel}} = -\int_0^{\mathrm{s_d}-\mathrm{b}} \mu \left(\mathbf{r}_{\mathrm{D}} + \mathbf{r}_{\mathrm{T}}\right) \cdot \mathbf{g} d\mathrm{s}_0$$

Inserting the definition of $\mathbf{r}_{\mathrm{T}} = \mathrm{d}\left(\cos\theta\hat{\mathbf{e}}_1 - \sin\theta\hat{\mathbf{e}}_3\right)$, and the arc length formula, $\theta = \frac{\mathrm{s}_0}{\mathrm{d}}$, yields:

$$= -\int_0^{\mathrm{s_d}-\mathrm{b}} \mu\mathbf{r}_{\mathrm{D}} \cdot \mathbf{g} d\mathrm{s}_0 + \int_0^{\mathrm{s_d}-\mathrm{b}} \mu \mathrm{gd} \sin\left(\frac{\mathrm{s}_0}{\mathrm{d}}\right) d\mathrm{s}_0$$

Performing the integral results in:

$$V_{\mathrm{reel}} = -\mu\left(\mathrm{s_d} - \mathrm{b}\right)\mathbf{r}_{\mathrm{D}} \cdot \mathbf{g} - \mu \mathrm{gd}^2\left(\cos\left(\frac{\mathrm{s_d} - \mathrm{b}}{\mathrm{d}}\right) - 1\right) \tag{7.19}$$

The deployed string potential energy consists of the internal elasticity and gravity potential for the infinitesimal string mass elements. The derivation is the same as in Section 7.2.1 with the exception that the limits of the integral are different due to the reel boundary condition:

$$V_{\mathrm{string}} = \int_{\mathrm{s_d}}^{l} \frac{1}{2}EA\left(\left\|\mathbf{r}'\left(\mathrm{s}_0\right)\right\|_2 - 1\right)^2 - \mu\mathbf{r}\left(\mathrm{s}_0\right) \cdot \mathbf{g} d\mathrm{s}_0 \tag{7.20}$$

The rigid body again consists of the gravitational potential of the center of mass, identical to the derivation in Section 7.2.1:

$$V_{\mathrm{rb}} = -\mathrm{m}\mathbf{r}\left(l\right)\cdot\mathbf{g} - \mathrm{m}\mathbf{R}\boldsymbol{\rho}_c\cdot\mathbf{g} \tag{7.21}$$

Combining the reel, string and rigid body potential energies, from Eq. 7.19, Eq. 7.20 and Eq. 7.21, respectively yields the total potential energy:

$$\begin{aligned}V &= -\mu\left(\mathrm{s_d}-\mathrm{b}\right)\mathbf{r}_{\mathrm{D}}\cdot\mathbf{g} - \mu\mathrm{g}\mathrm{d}^2\left(\cos\left(\frac{\mathrm{s_d}-\mathrm{b}}{\mathrm{d}}\right)-1\right)\\ &\quad+\int_{\mathrm{s_d}}^{l}\left(\frac{1}{2}EA\left(\left\|\mathbf{r}'\left(\mathrm{s_0}\right)\right\|_2-1\right)^2-\mu\mathbf{r}\left(\mathrm{s_0}\right)\cdot\mathbf{g}\right)d\mathrm{s_0}\\ &\quad-\mathrm{m}\left(\mathbf{r}\left(l\right)+\mathbf{R}\boldsymbol{\rho}_c\right)\cdot\mathbf{g}\end{aligned} \tag{7.22}$$

Complete Lagrangian

Inserting the kinetic energies from Eq. 7.18, and potential energies from Eq. 7.22 into Eq. 7.1 yields the total Langrangian energy:

$$\begin{aligned}L &= \frac{1}{2}\left(\mu\mathrm{s_d}+\frac{\mathrm{m_d}}{2}\right)\dot{\mathrm{s}}_{\mathrm{d}}^2+\int_{\mathrm{s_d}}^{l}\frac{1}{2}\mu\dot{\mathbf{r}}\left(\mathrm{s_0}\right)\cdot\dot{\mathbf{r}}\left(\mathrm{s_0}\right)d\mathrm{s_0}+\frac{1}{2}\mathrm{m}\dot{\mathbf{r}}\left(l\right)\cdot\dot{\mathbf{r}}\left(l\right)+\mathrm{m}\dot{\mathbf{r}}\left(l\right)\cdot\mathbf{R}\hat{\boldsymbol{\Omega}}\boldsymbol{\rho}_c\\ &\quad+\frac{1}{2}\boldsymbol{\Omega}\cdot\boldsymbol{\Pi}\boldsymbol{\Omega}+\mu\left(\mathrm{s_d}-\mathrm{b}\right)\mathbf{r}_{\mathrm{D}}\cdot\mathbf{g}+\mu\mathrm{g}\mathrm{d}^2\left(\cos\left(\frac{\mathrm{s_d}-\mathrm{b}}{\mathrm{d}}\right)-1\right)\\ &\quad-\int_{\mathrm{s_d}}^{l}\left(\frac{1}{2}EA\left(\left\|\mathbf{r}'\left(\mathrm{s_0}\right)\right\|_2-1\right)^2-\mu\mathbf{r}\left(\mathrm{s_0}\right)\cdot\mathbf{g}\right)d\mathrm{s_0}+\mathrm{m}\left(\mathbf{r}\left(l\right)+\mathbf{R}\boldsymbol{\rho}_c\right)\cdot\mathbf{g}\end{aligned} \tag{7.23}$$

7.3.2 Equations of Motion from Extended Hamilton's Principle

A few differences exist from the derivation given in Section 7.2.2, specifically the reel, the effects of the changing boundary condition on the string, and some non-conservative forces from the string velocity discontinuity at the guide-way exit, the guide-way normal force, and the applied winch control moment. The Extended Hamilton's Principle of Least

Action can account for these forces through variations in the virtual work [1, 113, 114]:

$$\delta\mathcal{S} = \delta \int_{t_1}^{t_2} \mathcal{L}\left(\mathbf{q}, \dot{\mathbf{q}}, t\right) + \mathcal{W}_{NC} dt = 0 \tag{7.24}$$

Taking the variation of the Lagrangian requires IBP in time, but also IBP in space due to the integral across the string domain and the spatial partial derivative. Special attention needs to be taken at the boundary conditions. Because the reel end of the string is no longer inertially fixed, the integral in time and space order can no longer be freely swapped. Green's Theorem must be used to integrate over the line integral instead. Taking the variation and repeatedly applying IBP yields (See Appendix C.2 for the complete derivation, following and completing the derivation given in [110]):

$$\begin{aligned}
\int_{t_0}^{t_f} \Bigg\{ \Bigg(& - \left(\mu \mathrm{s_d} + \frac{\mathrm{m_d}}{2}\right) \ddot{\mathrm{s}}_\mathrm{d} + \mu \left(\mathbf{r}_\mathrm{D} - \mathbf{r}_\mathrm{G}\right) \cdot \mathbf{g} - \mu \mathrm{g} \mathrm{d} \sin\left(\frac{\mathrm{s_d} - \mathrm{b}}{\mathrm{d}}\right) \\
& - \mathbf{f}\left(\mathrm{s}_\mathrm{d}^{+}\right) \cdot \mathbf{r}'\left(\mathrm{s}_\mathrm{d}^{+}\right) + \mu \dot{\mathrm{s}}_\mathrm{d}^{2} \left(\|\mathbf{r}'\left(\mathrm{s}_\mathrm{d}^{+}\right)\|_2 - 1\right) + \frac{\mathrm{u}}{\mathrm{d}} \Bigg) \delta \mathrm{s_d} \\
& + \left(\mathrm{m}\mathbf{R}\hat{\boldsymbol{\rho}}_c \dot{\boldsymbol{\Omega}} - \mathrm{m}\ddot{\mathbf{r}}\left(l\right) - \mathrm{m}\mathbf{R}\hat{\boldsymbol{\Omega}}^2 \boldsymbol{\rho}_c + \mathrm{m}\mathbf{g} - \mathbf{f}\left(l\right)\right) \cdot \delta \mathbf{r}\left(l\right) \\
& + \left(-\mathrm{m}\hat{\boldsymbol{\rho}}_c \mathbf{R}^T \ddot{\mathbf{r}}\left(l\right) - \boldsymbol{\Pi}\dot{\boldsymbol{\Omega}} - \hat{\boldsymbol{\Omega}}\boldsymbol{\Pi}\boldsymbol{\Omega} + \mathrm{m}\hat{\boldsymbol{\rho}}_c \mathbf{R}^T \mathbf{g}\right) \cdot \boldsymbol{\eta} \Bigg\} dt \\
& + \int_{\mathrm{s_d}}^{l} \left(\frac{\partial}{\partial \mathrm{s_0}} \mathbf{f}\left(\mathrm{s_0}\right) + \mu \mathbf{g} - \mu \ddot{\mathbf{r}}\left(\mathrm{s_0}\right)\right) \cdot \delta \mathbf{r}\left(\mathrm{s_0}\right) d\mathrm{s_0} \Bigg\} dt = 0
\end{aligned} \tag{7.25}$$

Because the variations $\delta \mathrm{s_d}$, $\delta \mathbf{r}\left(l\right)$, $\boldsymbol{\eta}$, and $\delta \mathbf{r}\left(\mathrm{s_0}\right)$ can be anything nonzero between t_o and t_f, the terms inside the parenthesis needs to be equal to zero, which gives the equations of motion:

$$\begin{aligned}
-\left(\mu \mathrm{s_d} + \frac{\mathrm{m_d}}{2}\right)\ddot{\mathrm{s}}_\mathrm{d} + \mu\left(\mathbf{r}_\mathrm{D} - \mathbf{r}_\mathrm{G}\right)\cdot\mathbf{g} - \mu \mathrm{g}\mathrm{d}\sin\left(\frac{\mathrm{s_d}-\mathrm{b}}{\mathrm{d}}\right)& \\
-\mathbf{f}\left(\mathrm{s}_\mathrm{d}^+\right)\cdot\mathbf{r}'\left(\mathrm{s}_\mathrm{d}^+\right) + \mu\dot{\mathrm{s}}_\mathrm{d}^2\left(\|\mathbf{r}'\left(\mathrm{s}_\mathrm{d}^+\right)\| - 1\right) + \frac{\mathrm{u}}{\mathrm{d}} &= 0 \\
-\mu\ddot{\mathbf{r}}\left(\mathrm{s}_0\right) + \mu\mathbf{g} + EA\frac{\partial}{\partial \mathrm{s}_0}\left(\frac{\|\mathbf{r}'\left(\mathrm{s}_0\right)\|_2 - 1}{\|\mathbf{r}'\left(\mathrm{s}_0\right)\|_2}\mathbf{r}'\left(\mathrm{s}_0\right)\right) &= 0 \quad \mathrm{s}_0\in[\mathrm{s_d}, l]. \\
-\mathrm{m}\ddot{\mathbf{r}}\left(l\right) + \mathrm{m}\mathbf{g} - EA\frac{\|\mathbf{r}'\left(l\right)\|_2 - 1}{\|\mathbf{r}'\left(l\right)\|_2}\mathbf{r}'\left(l\right) - \mathrm{m}\mathbf{R}\hat{\boldsymbol{\Omega}}^2\boldsymbol{\rho}_c + \mathrm{m}\mathbf{R}\hat{\boldsymbol{\rho}}_c\dot{\boldsymbol{\Omega}} &= 0 \\
-\boldsymbol{\Pi}\dot{\boldsymbol{\Omega}} - \hat{\boldsymbol{\Omega}}\boldsymbol{\Pi}\boldsymbol{\Omega} + \mathrm{m}\hat{\boldsymbol{\rho}}_c\mathbf{R}^T\mathbf{g} - \mathrm{m}\hat{\boldsymbol{\rho}}_c\mathbf{R}^T\ddot{\mathbf{r}}\left(l\right) &= 0
\end{aligned} \tag{7.26}$$

The first equation, is for the motion of the winch, in terms of string length on the winch. The second equation, a PDE, is the translation dynamics of the continuous string, and identical to that of the fixed pivot elastic string rigid body pendulum, with the exception of the range of the string where it is valid. The third, a PDE, and fourth, an ODE, are the translation and rotational dynamics of the rigid body, respectively, and identical to that of the fixed pivot elastic string rigid body pendulum.

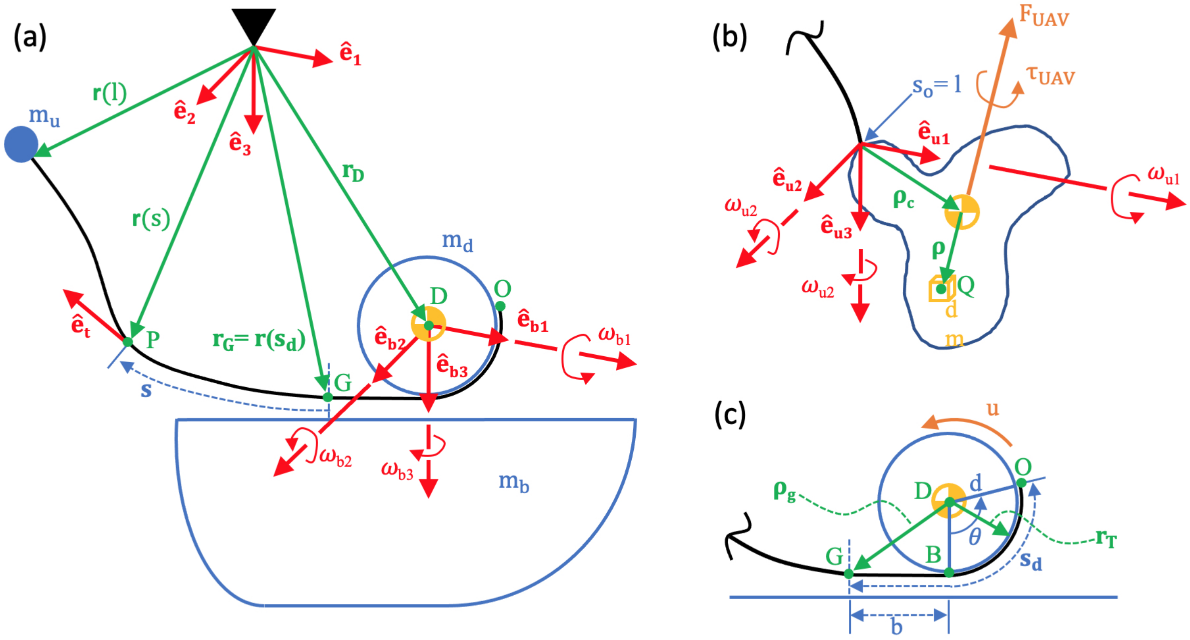

Figure 7.3: Diagrams of (a) overview of moving reel, elastic string, rigid body pendulum, (b) detail view of the rigid body mass, and (c) detail view of the moving reel system

7.4 Moving Reel - Elastic String - Rigid Body Pendulum / UAV

The natural follow on from the inertially fixed reel three dimensional elastic pendulum is to relax the fixed constraint on the reel. Similar numerical models for tethered satellites exist, but they all use celestial gravitational potential ($\frac{GmM}{\mathbf{r}^2}$), and the scale is significantly greater than the tethered UAV-USV scenario such that they ignore many of the dynamic effects of the winch [87, 115–117]. The derivation presented here is modified and extended use a typical Earth-based formulation of gravitational potential, as shown in Fig. 7.3. To simplify the analysis, the winch is assumed to be mounted at the center of mass of the moving object, in this case, a small boat.

The string, rigid body and winch have many of the same characteristics as those described in Section 7.3. Differing in this case, is a boat coordinate system, denoted by the vectors $\hat{\mathbf{e}}_{\mathrm{b1}}$, $\hat{\mathbf{e}}_{\mathrm{b2}}$, and $\hat{\mathbf{e}}_{\mathrm{b3}}$, located at the center of mass of the reel and boat. The mass of the reel is denoted $\mathrm{m_d}$ and the mass of the boat is denoted $\mathrm{m_b}$. The angular velocity vector of the boat, $\mathbf{\Omega}_{\mathrm{b}} = \begin{bmatrix} \omega_{\mathrm{b1}} & \omega_{\mathrm{b2}} & \omega_{\mathrm{b3}} \end{bmatrix}^T$ consists of the three rigid body rotations about each of the body frame orthonormal unit vectors. The coordinate system attached to the rigid body, or in this case, the UAV, is denoted $\hat{\mathbf{e}}_{\mathrm{u1}}$, $\hat{\mathbf{e}}_{\mathrm{u2}}$, and $\hat{\mathbf{e}}_{\mathrm{u3}}$. The mass of the UAV is denoted $\mathrm{m_u}$. The angular velocity vector of the rigid body or UAV, $\mathbf{\Omega}_{\mathrm{u}} = \begin{bmatrix} \omega_{\mathrm{u1}} & \omega_{\mathrm{u2}} & \omega_{\mathrm{u3}} \end{bmatrix}^T$ consists of the three rigid body rotations about each of the body frame orthonormal unit vectors. The overall applied thrust and moment of the UAV are defined as F_{UAV}, and τ_{UAV}, respectively. The location of the center of the reel at point D is again defined by the vector $\mathbf{r}_{\mathrm{D}}$, however is no longer inertially fixed. The drum has a rotational inertia of $J_{\mathrm{d}} = \frac{1}{2}\mathrm{m_d d^2}$, where the radius of the reel is denoted d, and a control moment u. The string is attached to the reel at point O, and the vector from the center of the drum to an infinitessimal string element on the drum is denoted $\mathbf{r}_{\mathrm{T}} = \mathrm{d}\left(\sin\theta\hat{\mathbf{e}}_{\mathrm{b1}} - \cos\theta\hat{\mathbf{e}}_{\mathrm{b3}}\right)$. As the reel rotates an angle θ, the string wraps on the reel and is no longer elastic. The string unwraps off the reel at point B, extends a straight distance, b, to a guide-way located at point G, defined by $\mathbf{r}_{\mathrm{G}} = \mathbf{r}_{\mathrm{D}} + \boldsymbol{\rho}_{\mathrm{g}} = \mathbf{r}(\mathrm{s_d})$, where $\mathrm{s_d}$ is the length of string wrapped on the reel between point O and G, and $\boldsymbol{\rho}_{\mathrm{g}}$ is the vector from the center of the reel to the guide way exit. The deployed string is again denoted $\mathrm{s_0}$ for the unstretched length, and s for the stretched length.

7.4.1 Lagrangian

Kinetic Energy (T)

The Lagrangian for this system can be defined as the sum of the potential energy and kinetic energy from the boat, the reel, the string and the rigid body:

$$\mathcal{L} = T_{\text{boat}} + T_{\text{reel}} + T_{\text{string}} + T_{\text{rb}} - V_{\text{boat}} - V_{\text{reel}} - V_{\text{string}} - V_{\text{rb}} \tag{7.27}$$

The kinetic energy of the boat rigid body consists of the translation and rotation kinetic energy: This is the same derivation as in Section 7.2.1 resulting in Eq. 7.6, repeated here with $\rho_c = 0$:

$$T_{\text{boat}} = \frac{1}{2}\mathrm{m_b}\dot{\mathbf{r}}_{\mathrm{D}} \cdot \dot{\mathbf{r}}_{\mathrm{D}} + \frac{1}{2}\mathbf{\Omega}_{\mathrm{b}} \cdot \mathbf{\Pi}_{\mathrm{b}}\mathbf{\Omega}_{\mathrm{b}} \tag{7.28}$$

The kinetic energy of the reel consists of the motion of the reel and string due to rigid body translation, translation of the string on the reel due to reel rotation, and the rotational kinetic energy of the drum:

$$T_{\text{reel}} = \frac{1}{2}\left(\mathrm{m_r} + \mu \mathrm{s_d}\right)\dot{\mathbf{r}}_{\mathrm{D}} \cdot \dot{\mathbf{r}}_{\mathrm{D}} + \int_0^{\mathrm{s_d}} \frac{1}{2}\mu\dot{\mathbf{r}}\left(\mathrm{s_0}\right) \cdot \dot{\mathbf{r}}\left(\mathrm{s_0}\right) d\mathrm{s_0} + \frac{1}{2}J_{\mathrm{d}}\dot{\theta}\left(O\right)^2$$

The rotation of the reel about the reference point can be neglected as $\mathrm{m_d} << \mathrm{m_b}$, and the effects on the boat motion are negligible. The second and third terms follow the same derivation given in Section 7.3.1 resulting in Eq. 7.15.

$$T_{\text{reel}} = \frac{1}{2}\left(\mathrm{m_r} + \mu \mathrm{s_d}\right)\left(\dot{\mathbf{r}}_{\mathrm{D}} \cdot \dot{\mathbf{r}}_{\mathrm{D}}\right) + \frac{1}{2}\left(\mu \mathrm{s_d} + \frac{\mathrm{m_d}}{2}\right)\dot{\mathrm{s}}_{\mathrm{d}}^2 \tag{7.29}$$

The deployed string kinetic energy consists of the translational velocity of infinitesimal string mass elements, the same derivation as in Section 7.3.1 in Eq. 7.16:

$$T_{\text{string}} = \int_{\mathrm{s_d}}^{l} \frac{1}{2}\mu\dot{\mathbf{r}}\left(\mathrm{s}_0\right)\cdot\dot{\mathbf{r}}\left(\mathrm{s}_0\right) d\mathrm{s}_0 \tag{7.30}$$

The UAV kinetic energy, consists of the translational and rotational velocity of the UAV. This is the same derivation as in Section 7.2.1 resulting in Eq. 7.6, repeated here with updated variables:

$$T_{\text{UAV}} = \frac{1}{2}\mathrm{m_u}\dot{\mathbf{r}}\left(l\right)\cdot\dot{\mathbf{r}}\left(l\right) + \mathrm{m_u}\dot{\mathbf{r}}\left(l\right)\cdot\mathbf{R}_\mathrm{u}\hat{\mathbf{\Omega}}_\mathrm{u}\boldsymbol{\rho}_c + \frac{1}{2}\mathbf{\Omega}_\mathrm{u}\cdot\mathbf{\Pi}_\mathrm{u}\mathbf{\Omega}_\mathrm{u} \tag{7.31}$$

Combining the kinetic energy from the boat, reel, string, and UAV, from Eq. 7.28, Eq. 7.29, Eq. 7.30 and Eq. 7.31, respectively yields the total kinetic energy:

$$\begin{aligned} T &= T_{\text{boat}} + T_{\text{reel}} + T_{\text{string}} + T_{\text{UAV}} \\ &= \frac{1}{2}\left(\mathrm{m_b} + \mathrm{m_d} + \mu\mathrm{s_d}\right)\left(\dot{\mathbf{r}}_\mathrm{D}\cdot\dot{\mathbf{r}}_\mathrm{D}\right) + \frac{1}{2}\left(\mu\mathrm{s_d} + \frac{\mathrm{m_d}}{2}\right)\dot{\mathrm{s}}_\mathrm{d}^2 + \frac{1}{2}\mathbf{\Omega}_\mathrm{b}\cdot\mathbf{\Pi}_\mathrm{b}\mathbf{\Omega}_\mathrm{b} \\ &+ \int_{\mathrm{s_d}}^{l}\frac{1}{2}\mu\dot{\mathbf{r}}\left(\mathrm{s}_0\right)\cdot\dot{\mathbf{r}}\left(\mathrm{s}_0\right)d\mathrm{s}_0 + \frac{1}{2}\mathrm{m_u}\dot{\mathbf{r}}\left(l\right)\cdot\dot{\mathbf{r}}\left(l\right) + \mathrm{m_u}\dot{\mathbf{r}}\left(l\right)\cdot\mathbf{R}_\mathrm{u}\hat{\mathbf{\Omega}}_\mathrm{u}\boldsymbol{\rho}_c + \frac{1}{2}\mathbf{\Omega}_\mathrm{u}\cdot\mathbf{\Pi}_\mathrm{u}\mathbf{\Omega}_\mathrm{u} \end{aligned} \tag{7.32}$$

Potential Energy (V)

New in this setup is the boat potential energy, and the translation potential energy of the reel. The potential energy of the boat consists of the gravitational potential and is the same derivation as in Section 7.2.1:

$$V_{\mathrm{boat}} = -\mathrm{m_b}\mathbf{r}_{\mathrm{D}} \cdot \mathbf{g} \tag{7.33}$$

The potential change of the reel is due to the gravitational potential for the mass of the reel including the mass of string in the guide way, and the mass of string on the reel.

$$V_{\mathrm{reel}} = -\left(\mathrm{m_d} + \mu \mathrm{b}\right)\mathbf{r}_{\mathrm{D}} \cdot \mathbf{g} - \int_0^{\mathrm{s_d}-\mathrm{b}} \mu\left(\mathbf{r}_{\mathrm{D}} + \mathbf{r}_{\mathrm{T}}\right) \cdot \mathbf{g} d\mathrm{s}_0$$

The derivation follows the derivation in Section 7.3.1 and Eq. 7.19, but is slightly different since the reel is rotating, and $\mathbf{r}_{\mathrm{T}}$'s unit vectors are $\hat{\mathbf{e}}_{\mathrm{b1}}$ and $\hat{\mathbf{e}}_{\mathrm{b3}}$:

$$\begin{aligned} V_{\mathrm{reel}} &= -\left(\mathrm{m_d} + \mu \mathrm{b}\right)\mathbf{r}_{\mathrm{D}} \cdot \mathbf{g} - \mu\left(\mathrm{s_d} - \mathrm{b}\right)\mathbf{r}_{\mathrm{D}} \cdot \mathbf{g} - \int_0^{\mathrm{s_d}-\mathrm{b}} \mu \mathbf{r}_{\mathrm{T}} \cdot \mathbf{g} d\mathrm{s}_0 \\ &= -\left(\mathrm{m_d} + \mu \mathrm{s_d}\right)\mathbf{r}_{\mathrm{D}} \cdot \mathbf{g} - \int_0^{\mathrm{s_d}-\mathrm{b}} \mu \mathbf{r}_{\mathrm{T}} \cdot \mathbf{g} d\mathrm{s}_0 \end{aligned}$$

Inserting the definition of $\mathbf{r}_{\mathrm{T}} = \mathrm{d}\left(\sin\theta \hat{\mathbf{e}}_{\mathrm{b1}} - \cos\theta \hat{\mathbf{e}}_{\mathrm{b3}}\right)$, the distance from the center of the reel to an infinitesimal piece of string on the reel, and the arc length formula ($\theta = \frac{\mathrm{s}_0}{\mathrm{d}}$):

$$\begin{aligned}V_{\mathrm{reel}} &= -\left(\mathrm{m_d}+\mu\mathrm{s_d}\right)\mathbf{r}_{\mathrm{D}}\cdot\mathbf{g}-\int_0^{\mathrm{s_d}-\mathrm{b}}\mu\mathrm{d}\left(\sin\theta\hat{\mathbf{e}}_{\mathrm{b1}}-\cos\theta\hat{\mathbf{e}}_{\mathrm{b3}}\right)\cdot\mathbf{g}d\mathrm{s}_0\\ &= -\left(\mathrm{m_d}+\mu\mathrm{s_d}\right)\mathbf{r}_{\mathrm{D}}\cdot\mathbf{g}-\int_0^{\mathrm{s_d}-\mathrm{b}}\mu\mathrm{d}\left(\sin\frac{\mathrm{s}_0}{\mathrm{d}}\hat{\mathbf{e}}_{\mathrm{b1}}-\cos\frac{\mathrm{s}_0}{\mathrm{d}}\hat{\mathbf{e}}_{\mathrm{b3}}\right)\cdot\mathbf{g}d\mathrm{s}_0\\ &= -\left(\mathrm{m_d}+\mu\mathrm{s_d}\right)\mathbf{r}_{\mathrm{D}}\cdot\mathbf{g}-\mu\mathrm{d}^2\left(-\cos\frac{\mathrm{s}_0}{\mathrm{d}}\hat{\mathbf{e}}_{\mathrm{b1}}-\sin\frac{\mathrm{s}_0}{\mathrm{d}}\hat{\mathbf{e}}_{\mathrm{b3}}\right)\Big|_0^{\mathrm{s_d}-\mathrm{b}}\cdot\mathbf{g}\end{aligned}$$

resulting in:

$$V_{\mathrm{reel}}=-\left(\mathrm{m_d}+\mu\mathrm{s_d}\right)\mathbf{r}_{\mathrm{D}}\cdot\mathbf{g}-\mu\mathrm{d}^2\left(\left(1-\cos\frac{\mathrm{s_d}-\mathrm{b}}{\mathrm{d}}\right)\hat{\mathbf{e}}_{\mathrm{b1}}-\sin\frac{\mathrm{s_d}-\mathrm{b}}{\mathrm{d}}\hat{\mathbf{e}}_{\mathrm{b3}}\right)\cdot\mathbf{g} \tag{7.34}$$

The deployed string potential energy consists of the internal elasticity and gravity potential for the infinitesimal string mass elements have the same derivation as in Section 7.3.1 resulting in Eq. 7.20, repeated here:

$$V_{\mathrm{string}}=\int_{\mathrm{s_d}}^{l}\frac{1}{2}EA\left(\left\|\mathbf{r}'\left(\mathrm{s}_0\right)\right\|_2-1\right)^2-\mu\mathbf{r}\left(\mathrm{s}_0\right)\cdot\mathbf{g}d\mathrm{s}_0 \tag{7.35}$$

The UAV consists only of the gravitational potential of a rigid body, which has the same derivation as shown in 7.3.1, but with different variable names:

$$V_{\mathrm{UAV}}=-\mathrm{m_u}\left(\mathbf{r}\left(l\right)+\boldsymbol{\rho}_c\right)\cdot\mathbf{g} \tag{7.36}$$

Combining the boat, reel, string, and UAV potential energies from Eq. 7.33, Eq.

7.34, Eq. 7.35, and Eq. 7.36, respectively yields the total potential energy:

$$\begin{aligned} V &= V_{\text{boat}} + V_{\text{reel}} + V_{\text{string}} + V_{\text{UAV}} \\ &= -\left(\mathrm{m_b} + \mathrm{m_d} + \mu \mathrm{s_d}\right) \mathbf{r}_{\mathrm{D}} \cdot \mathbf{g} - \mu \mathrm{d}^2 \left(\left(1 - \cos \frac{\mathrm{s_d} - \mathrm{b}}{\mathrm{d}} \right) \hat{\mathbf{e}}_{\mathrm{b1}} - \sin \frac{\mathrm{s_d} - \mathrm{b}}{\mathrm{d}} \hat{\mathbf{e}}_{\mathrm{b3}} \right) \cdot \mathbf{g} \\ &+ \int_{\mathrm{s_d}}^{l} \frac{1}{2} EA \left(\|\mathbf{r}'(\mathrm{s_0})\|_2 - 1 \right)^2 - \mu \mathbf{r}(\mathrm{s_0}) \cdot \mathbf{g} d\mathrm{s_0} - \mathrm{m_u} \left(\mathbf{r}(l) + \boldsymbol{\rho}_c \right) \cdot \mathbf{g} \end{aligned} \tag{7.37}$$

Complete Lagrangian

Inserting the kinetic energies from Eq. 7.32, and potential energies from Eq. 7.37 into Eq. 7.1 yields the total Langrangian energy:

$$\begin{aligned} L &= \frac{1}{2} \left(\mathrm{m_b} + \mathrm{m_d} + \mu \mathrm{s_d}\right) \left(\dot{\mathbf{r}}_{\mathrm{D}} \cdot \dot{\mathbf{r}}_{\mathrm{D}} \right) + \frac{1}{2} \left(\mu \mathrm{s_d} + \frac{\mathrm{m_d}}{2} \right) \dot{\mathrm{s}}_{\mathrm{d}}^2 + \frac{1}{2} \boldsymbol{\Omega}_{\mathrm{b}} \cdot \boldsymbol{\Pi}_{\mathrm{b}} \boldsymbol{\Omega}_{\mathrm{b}} \\ &+ \frac{1}{2} \mathrm{m_u} \dot{\mathbf{r}}(l) \cdot \dot{\mathbf{r}}(l) + \mathrm{m_u} \dot{\mathbf{r}}(l) \cdot \mathbf{R}_{\mathrm{u}} \hat{\boldsymbol{\Omega}}_{\mathrm{u}} \boldsymbol{\rho}_c + \frac{1}{2} \boldsymbol{\Omega}_{\mathrm{u}} \cdot \boldsymbol{\Pi}_{\mathrm{u}} \boldsymbol{\Omega}_{\mathrm{u}} \\ &+ \left(\mathrm{m_b} + \mathrm{m_d} + \mu \mathrm{s_d}\right) \mathbf{r}_{\mathrm{D}} \cdot \mathbf{g} + \mu \mathrm{d}^2 \left(\left(1 - \cos \frac{\mathrm{s_d} - \mathrm{b}}{\mathrm{d}} \right) \hat{\mathbf{e}}_{\mathrm{b1}} - \sin \frac{\mathrm{s_d} - \mathrm{b}}{\mathrm{d}} \hat{\mathbf{e}}_{\mathrm{b3}} \right) \cdot \mathbf{g} \\ &+ \int_{\mathrm{s_d}}^{l} \left(\frac{1}{2} \mu \dot{\mathbf{r}}(\mathrm{s_0}) \cdot \dot{\mathbf{r}}(\mathrm{s_0}) - \frac{1}{2} EA \left(\|\mathbf{r}'(\mathrm{s_0})\|_2 - 1 \right)^2 + \mu \mathbf{r}(\mathrm{s_0}) \cdot \mathbf{g} \right) d\mathrm{s_0} + \mathrm{m_u} \left(\mathbf{r}(l) + \boldsymbol{\rho}_c \right) \cdot \mathbf{g} \end{aligned} \tag{7.38}$$

7.4.2 Equations of Motion from Extended Hamilton's Principle

A few differences exist from the derivation given in Section 7.3.2, specifically the addition of a second rigid body, the moving reel effects the simplification due to changing boundary condition on the string at the guide way, and the applied force and moment at the UAV. Again, the Extended Hamilton's Principle of Least Action from Eq. 7.24 will be used. Taking the variation, repeatedly applying IBP, Leibniz' rule, Green's theorem, and applying the boundary conditions at the guide way yields (See Appendix C.3 for the complete derivation, following and completing the derivation given in [117]):

$$
\begin{aligned}
\delta\mathcal{S} = \int_{t_0}^{t_f} \Bigg\{ \Bigg(& -\left(\mathrm{m_b} + \mathrm{m_d} + \mu \mathrm{s_d}\right) \ddot{\mathbf{r}}_{\mathrm{D}} - \mu \dot{\mathrm{s}}_{\mathrm{d}} \dot{\mathbf{r}}_{\mathrm{D}} - \mu \dot{\mathrm{s}}_{\mathrm{d}}^2 \mathbf{r}'\left(\mathrm{s_d^+}\right) + \mu \dot{\mathrm{s}}_{\mathrm{d}} \dot{\mathbf{r}}_{\mathrm{D}} - \mu \dot{\mathrm{s}}_{\mathrm{d}} \mathbf{R}_{\mathrm{b}} \hat{\boldsymbol{\rho}}_g \boldsymbol{\Omega}_{\mathrm{b}} \\
& + \left(\mathrm{m_b} + \mathrm{m_d} + \mu \mathrm{s_d}\right) \mathbf{g} + \mathbf{f}\left(\mathrm{s_d^+}\right) \Bigg) \cdot \delta \mathbf{r}_{\mathrm{D}} \\
+ \Bigg(& - \boldsymbol{\Pi}_{\mathrm{b}} \dot{\boldsymbol{\Omega}}_{\mathrm{b}} - \hat{\boldsymbol{\Omega}}_{\mathrm{b}} \boldsymbol{\Pi}_{\mathrm{b}} \boldsymbol{\Omega}_{\mathrm{b}} - \mu \dot{\mathrm{s}}_{\mathrm{d}}^2 \hat{\boldsymbol{\rho}}_g \mathbf{R}_{\mathrm{b}}^T \mathbf{r}'\left(\mathrm{s_d^+}\right) + \mu \dot{\mathrm{s}}_{\mathrm{d}} \hat{\boldsymbol{\rho}}_g \mathbf{R}_{\mathrm{b}}^T \dot{\mathbf{r}}_{\mathrm{D}} - \mu \dot{\mathrm{s}}_{\mathrm{d}} \hat{\boldsymbol{\rho}}_g^2 \boldsymbol{\Omega}_{\mathrm{b}} \\
& - \mu \mathrm{d}^2 \sin\left(\frac{\mathrm{s_d} - \mathrm{b}}{\mathrm{d}}\right) \hat{\mathbf{e}}_3 \mathbf{R}_{\mathrm{b}}^T \mathbf{g} - \mu \mathrm{d}^2 \left(\cos\left(\frac{\mathrm{s_d} - \mathrm{b}}{\mathrm{d}}\right) - 1\right) \hat{\mathbf{e}}_1 \mathbf{R}_{\mathrm{b}}^T \mathbf{g} \\
& + \hat{\boldsymbol{\rho}}_g \mathbf{R}_{\mathrm{b}}^T \mathbf{f}\left(\mathrm{s_d^+}\right) - \mathrm{u} \hat{\mathbf{e}}_2 \Bigg) \cdot \boldsymbol{\eta}_{\mathrm{b}} \\
+ \Bigg(& \frac{1}{2} \mu \dot{\mathbf{r}}_{\mathrm{D}} \cdot \dot{\mathbf{r}}_{\mathrm{D}} - \left(\mu \mathrm{s_d} + \frac{\mathrm{m_d}}{2}\right) \ddot{\mathrm{s}}_{\mathrm{d}} + \mu \dot{\mathrm{s}}_{\mathrm{d}}^2 \left(\left\|\mathbf{r}'\left(\mathrm{s_d^+}\right)\right\|_2 - 1\right) \\
& - \frac{1}{2} \mu \left(\dot{\mathbf{r}}_{\mathrm{D}} - \mathbf{R}_{\mathrm{b}} \hat{\boldsymbol{\rho}}_g \boldsymbol{\Omega}_{\mathrm{b}}\right) \cdot \left(\dot{\mathbf{r}}_{\mathrm{D}} - \mathbf{R}_{\mathrm{b}} \hat{\boldsymbol{\rho}}_g \boldsymbol{\Omega}_{\mathrm{b}}\right) + \mu \mathbf{r}_{\mathrm{d}} \cdot \mathbf{g} \\
& - \mu \mathrm{d} \cos\left(\frac{\mathrm{s_d} - \mathrm{b}}{\mathrm{d}}\right) \mathbf{R}_{\mathrm{b}} \hat{\mathbf{e}}_3 \cdot \mathbf{g} + \mu \mathrm{d} \sin\left(\frac{\mathrm{s_d} - \mathrm{b}}{\mathrm{d}}\right) \mathbf{R}_{\mathrm{b}} \hat{\mathbf{e}}_1 \cdot \mathbf{g} - \mu \mathbf{r}\left(\mathrm{s_d^+}\right) \cdot \mathbf{g} \\
& - \mathbf{f}\left(\mathrm{s_d^+}\right) \cdot \mathbf{r}'\left(\mathrm{s_d^+}\right) + \frac{\mathrm{u}}{\mathrm{d}} \Bigg) \delta \mathrm{s_d} \\
+ \int_{\mathrm{s_d}}^{l} & \left(-\mu \ddot{\mathbf{r}}\left(\mathrm{s_0}\right) + \mathbf{f}'\left(\mathrm{s_0}\right) + \mu \mathbf{g}\right) \cdot \delta \mathbf{r}\left(\mathrm{s_0}\right) d\mathrm{s_0} \\
+ \Bigg(& \mathrm{m_u} \mathbf{R}_{\mathrm{u}} \hat{\boldsymbol{\rho}}_c \dot{\boldsymbol{\Omega}}_{\mathrm{u}} - \mathrm{m_u} \ddot{\mathbf{r}}\left(l\right) - \mathrm{m_u} \mathbf{R}_{\mathrm{u}} \hat{\boldsymbol{\Omega}}_{\mathrm{u}}^2 \rho_c - \mathbf{f}\left(l\right) + \mathrm{m_u} \mathbf{g} - F_{\mathrm{UAV}} \mathbf{R}_{\mathrm{u}} \hat{\mathbf{e}}_3 \Bigg) \cdot \delta \mathbf{r}\left(l\right) \\
+ \Bigg(& -\mathrm{m_u} \hat{\boldsymbol{\rho}}_c \mathbf{R}_{\mathrm{u}}^T \ddot{\mathbf{r}}\left(l\right) - \boldsymbol{\Pi}_{\mathrm{u}} \dot{\boldsymbol{\Omega}}_{\mathrm{u}} - \hat{\boldsymbol{\Omega}}_{\mathrm{u}} \boldsymbol{\Pi}_{\mathrm{u}} \boldsymbol{\Omega}_{\mathrm{u}} + \mathrm{m_u} \hat{\boldsymbol{\rho}}_c \mathbf{R}_{\mathrm{u}}^T \mathbf{g} + \boldsymbol{\tau}_{\mathrm{UAV}} \Bigg) \cdot \boldsymbol{\eta}_{\mathrm{u}} \Bigg\} dt
\end{aligned}
\tag{7.39}
$$

Because the variations $\delta\mathbf{r}_{\mathrm{D}}$, $\boldsymbol{\eta}_{\mathrm{b}}$, $\delta\mathrm{s}_{\mathrm{d}}$, $\delta\mathbf{r}\left(\mathrm{s}_0\right)$, $\delta\mathbf{r}\left(l\right)$, and $\boldsymbol{\eta}_{\mathrm{u}}$ can be anything nonzero between t_o and t_f, the terms inside the parenthesis needs to be equal to zero, which gives the equations of motion:

- Rigid body (Boat) translation:

$$\begin{aligned}&-\left(\mathrm{m_b}+\mathrm{m_d}+\mu\mathrm{s_d}\right)\ddot{\mathbf{r}}_{\mathrm{D}}-\mu\dot{\mathrm{s}}_{\mathrm{d}}\dot{\mathbf{r}}_{\mathrm{D}}-\mu\dot{\mathrm{s}}_{\mathrm{d}}^2\mathbf{r}'\left(\mathrm{s}_{\mathrm{d}}^+\right)+\mu\dot{\mathrm{s}}_{\mathrm{d}}\dot{\mathbf{r}}_{\mathrm{D}}-\mu\dot{\mathrm{s}}_{\mathrm{d}}\mathbf{R}_{\mathrm{b}}\hat{\boldsymbol{\rho}}_{\mathrm{g}}\boldsymbol{\Omega}_{\mathrm{b}}\\&\quad+\left(\mathrm{m_b}+\mathrm{m_d}+\mu\mathrm{s_d}\right)\mathbf{g}+\mathbf{f}\left(\mathrm{s}_{\mathrm{d}}^+\right)=0\end{aligned}\tag{7.40}$$

- Rigid body (Boat) rotation

$$\begin{aligned}&-\boldsymbol{\Pi}_{\mathrm{b}}\dot{\boldsymbol{\Omega}}_{\mathrm{b}}-\hat{\boldsymbol{\Omega}}_{\mathrm{b}}\boldsymbol{\Pi}_{\mathrm{b}}\boldsymbol{\Omega}_{\mathrm{b}}-\mu\dot{\mathrm{s}}_{\mathrm{d}}^2\hat{\boldsymbol{\rho}}_{\mathrm{g}}\mathbf{R}_{\mathrm{b}}^T\mathbf{r}'\left(\mathrm{s}_{\mathrm{d}}^+\right)+\mu\dot{\mathrm{s}}_{\mathrm{d}}\hat{\boldsymbol{\rho}}_{\mathrm{g}}\mathbf{R}_{\mathrm{b}}^T\dot{\mathbf{r}}_{\mathrm{D}}-\mu\dot{\mathrm{s}}_{\mathrm{d}}\hat{\boldsymbol{\rho}}_{\mathrm{g}}^2\boldsymbol{\Omega}_{\mathrm{b}}\\&\quad-\mu\mathrm{d}^2\sin\left(\frac{\mathrm{s_d}-\mathrm{b}}{\mathrm{d}}\right)\hat{\mathbf{e}}_3\mathbf{R}_{\mathrm{b}}^T\mathbf{g}-\mu\mathrm{d}^2\left(\cos\left(\frac{\mathrm{s_d}-\mathrm{b}}{\mathrm{d}}\right)-1\right)\hat{\mathbf{e}}_1\mathbf{R}_{\mathrm{b}}^T\mathbf{g}\\&\quad+\hat{\boldsymbol{\rho}}_{\mathrm{g}}\mathbf{R}_{\mathrm{b}}^T\mathbf{f}\left(\mathrm{s}_{\mathrm{d}}^+\right)-\mathrm{u}\hat{\mathbf{e}}_2=0\end{aligned}\tag{7.41}$$

- Winch rotation dynamics

$$\begin{aligned}&\frac{1}{2}\mu\dot{\mathbf{r}}_{\mathrm{D}}\cdot\dot{\mathbf{r}}_{\mathrm{D}}-\left(\mu\mathrm{s_d}+\frac{\mathrm{m_d}}{2}\right)\ddot{\mathrm{s}}_{\mathrm{d}}+\mu\dot{\mathrm{s}}_{\mathrm{d}}^2\left(\|\mathbf{r}'\left(\mathrm{s}_{\mathrm{d}}^+\right)\|_2-1\right)\\&\quad-\frac{1}{2}\mu\left(\dot{\mathbf{r}}_{\mathrm{D}}-\mathbf{R}_{\mathrm{b}}\hat{\boldsymbol{\rho}}_{\mathrm{g}}\boldsymbol{\Omega}_{\mathrm{b}}\right)\cdot\left(\dot{\mathbf{r}}_{\mathrm{D}}-\mathbf{R}_{\mathrm{b}}\hat{\boldsymbol{\rho}}_{\mathrm{g}}\boldsymbol{\Omega}_{\mathrm{b}}\right)+\mu\mathbf{r}_{\mathrm{d}}\cdot\mathbf{g}-\mu\mathrm{d}\cos\left(\frac{\mathrm{s_d}-\mathrm{b}}{\mathrm{d}}\right)\mathbf{R}_{\mathrm{b}}\hat{\mathbf{e}}_3\cdot\mathbf{g}\\&\quad+\mu\mathrm{d}\sin\left(\frac{\mathrm{s_d}-\mathrm{b}}{\mathrm{d}}\right)\mathbf{R}_{\mathrm{b}}\hat{\mathbf{e}}_1\cdot\mathbf{g}-\mu r\left(\mathrm{s}_{\mathrm{d}}^+\right)\cdot\mathbf{g}\\&\quad-\mathbf{f}\left(\mathrm{s}_{\mathrm{d}}^+\right)\cdot\mathbf{r}'\left(\mathrm{s}_{\mathrm{d}}^+\right)+\frac{\mathrm{u}}{\mathrm{d}}=0\end{aligned}\tag{7.42}$$

Note above that the $\frac{1}{2}\mu\dot{\mathbf{r}}_{\mathrm{D}}\cdot\dot{\mathbf{r}}_{\mathrm{D}}$ term cancels with the first term of $-\frac{1}{2}\mu\left(\dot{\mathbf{r}}_{\mathrm{D}}-\mathbf{R}_{\mathrm{b}}\hat{\boldsymbol{\rho}}_g\boldsymbol{\Omega}_{\mathrm{b}}\right)\cdot\left(\dot{\mathbf{r}}_{\mathrm{D}}-\mathbf{R}_{\mathrm{b}}\hat{\boldsymbol{\rho}}_g\boldsymbol{\Omega}_{\mathrm{b}}\right)$ after multiplying through.

- String translation dynamics:

$$-\mu\ddot{\mathbf{r}}\left(\mathrm{s}_0\right)+\mathbf{f}'\left(\mathrm{s}_0\right)+\mu\mathbf{g}=0, \qquad \left(\mathrm{s}_0\in\left[\mathrm{s}_\mathrm{d},l\right],\mathbf{r}\left(\mathrm{s}_\mathrm{d}\right)=\mathbf{r}_\mathrm{D}+\mathbf{R}_\mathrm{b}\left(\boldsymbol{\rho}_\mathrm{r}+\boldsymbol{\rho}_\mathrm{g}\right)\right) \tag{7.43}$$

- Rigid Body 2 (UAV) translation dynamics

$$\mathrm{m_u}\mathbf{R}_\mathrm{u}\hat{\boldsymbol{\rho}}_c\dot{\boldsymbol{\Omega}}_\mathrm{u}-\mathrm{m_u}\ddot{\mathbf{r}}\left(l\right)-\mathrm{m_u}\mathbf{R}_\mathrm{u}\hat{\boldsymbol{\Omega}}_\mathrm{u}^2\boldsymbol{\rho}_c-\mathbf{f}\left(l\right)+\mathrm{m_u}\mathbf{g}-F_\mathrm{UAV}\mathbf{R}_\mathrm{u}\hat{\mathbf{e}}_3=0 \tag{7.44}$$

- Rigid Body 2 (UAV) rotation dynamics

$$-\mathrm{m_u}\hat{\boldsymbol{\rho}}_c\mathbf{R}_\mathrm{u}^T\ddot{\mathbf{r}}\left(l\right)-\boldsymbol{\Pi}_\mathrm{u}\dot{\boldsymbol{\Omega}}_\mathrm{u}-\hat{\boldsymbol{\Omega}}_\mathrm{u}\boldsymbol{\Pi}_\mathrm{u}\boldsymbol{\Omega}_\mathrm{u}+\mathrm{m_u}\hat{\boldsymbol{\rho}}_c\mathbf{R}_\mathrm{u}^T\mathbf{g}+\boldsymbol{\tau}_\mathrm{UAV}=0 \tag{7.45}$$

7.5 Conclusion

Three separate dynamic models of elastic string pendulums were developed using Hamilton's principle of least action. The kinetic and potential energy for a rigidly fixed elastic string pendulum with a rigid body on the end were developed. By neglecting torsion and bending effects, the analysis was simplified, and an intuitive partial differential formulation was developed. Leveraging Hamilton's principle of least action, and liberal usage of IBP in both space and time, the variations of the Lagrangian resulted in a simple, continuous body partial differential equations of motion. The natural progression of adding an inertially fixed reel to the pivot end of the string required some additional care in dealing with the boundary conditions, and IBP steps. Because the reel end of the string is no longer fixed, the integral order in time and space can not be freely switched. Leibniz's rule and Green's theorem enabled the successful development of the complete variation, and equations of motion. New to this scenario, was the inclusion of nonconservative virtual work terms, to account for the energy loss at the winch's guide way exit due to a string velocity discontinuity, the guide way normal force, and the applied moment on the reel. Finally, a model was developed for a moving reel mounted on a boat, with an elastic string extending up to a UAV. Again, care needed to be taken with regards to boundary conditions, and the nonconservative virtual work for the applied forces and moments. In the next chapter, leveraging these dynamic models, a numerical simulation model will be developed using Galerkin's method with linear and quadratic shape functions.

7.6 Acknowledgments

Support for this work was provided by Naval Information Warfare Center Pacific under the Naval Innovative Science and Engineering program and the Department of Defense SMART Scholarship for Service program.

Chapter 7, in part, is currently being prepared for submission for publication of the material. K. Talke, J. Friend, T. Bewley. The dissertation author was the primary investigator and author of these pages.

Chapter 8

Three Dimensional Elastic String Pendulum Numerical Model

In order to properly develop a numerical method for time-marching, such as a Runge-Kutta method, the continuous string PDE needs to be discretized into a finite element method [118]. A finite element model developed in other work presented the one dimensional linear shape function, but the derivation is incomplete, and it focuses on developing a discrete time variational integration scheme [93]. In this work, a Runge Kutta method will be used, which requires a first order ODE. The proper, complete Galerkin finite element method, and both the one dimensional linear and quadratic finite element model derivation are presented.

The remainder of the chapter is organized as follows. Section 8.1 presents the theory og the weighted residual integral. Section 8.2 presents the theory of Gauss quadrature. Section 8.3 details the derivation of the linear shape function finite element model. Section 8.4 derives the quadratic shape function finite element model. Section 8.5 summarizes the key conclusions.

8.1 Weighted Residual Integral

The Galerkin finite element method for relies on the weighted residual integral [118]:

$$\int_0^L w(s_o)\, R(s_o)\, ds_o = 0 \tag{8.1}$$

where $R(s_o)$ is the residual of the PDE, and $w(s_o)$ is a weighting function depending on the shape functions used. Inserting the PDE from Eq. 7.13 for $R(s_o)$, yields:

$$\int_0^L w(s_o)\left(\mu\ddot{\mathbf{r}}(s_o) - \mu\mathbf{g} - EA\frac{\partial}{\partial s}\left(\frac{\|\mathbf{r}'(s_o)\|_2 - 1}{\|\mathbf{r}'(s_o)\|_2}\mathbf{r}'(s_o)\right)\right) ds_o = 0$$
$$\int_0^L w(s_o)\left(\mu\ddot{\mathbf{r}}(s_o) - \mu\mathbf{g}\right) ds_o - \int_0^L w(s_o)\left(EA\frac{\partial}{\partial s}\left(\frac{\|\mathbf{r}'(s_o)\|_2 - 1}{\|\mathbf{r}'(s_o)\|_2}\mathbf{r}'(s_o)\right)\right) ds_o = 0.$$

Performing IBP in space on the second term (IBP: $\int_a^b u dv = uv|_a^b - \int_a^b v du$ with $u = w(s_o)$ and $dv = EA\frac{\partial}{\partial s}\left(\frac{\|\mathbf{r}'(s_o)\|_2 - 1}{\|\mathbf{r}'(s_o)\|_2}\mathbf{r}'(s_o)\right) ds_o$) yields:

$$\begin{aligned}\int_0^L w(s_o)\left(\mu\ddot{\mathbf{r}}(s_o) - \mu\mathbf{g}\right) ds_o + \int_0^L EA\left(\frac{\|\mathbf{r}'(s_o)\|_2 - 1}{\|\mathbf{r}'(s_o)\|_2}\mathbf{r}'(s_o)\right)\frac{dw(s_o)}{ds_o} ds_o \\ - w(s_o)\,\mathbf{f}(s_o)\big|_0^L = 0\end{aligned} \tag{8.2}$$

where $\mathbf{f}(s_o)$ is the boundary condition force defined as:

$$\mathbf{f}(s_o) = EA\left(\frac{\|\mathbf{r}'(s_o)\|_2 - 1}{\|\mathbf{r}'(s_o)\|_2}\mathbf{r}'(s_o)\right) \tag{8.3}$$

8.2 Gauss Quadrature

For many finite element methods, the stiffness terms cannot be evaluated analytically. For the three dimensional elastic string pendulum, the one dimensional linear shape functions can be solved analytically, while the quadratic shape functions can not. To evaluate more complicated formulations, Gaussian Quadrature can be used, which approximates the integral as a finite weighted sum [118]:

$$\int_{-1}^{1} f(x)\,dx \approx \sum_{i=1}^{n} w_i f(x_i) \tag{8.4}$$

where the weights, w_i, and evaluation points, x_i, are specified based on the Gaussian Quadrature method. For the one dimensional quadratic shape function method, two point Gauss Quadrature will be used, where $x_1 = \frac{-1}{\sqrt{3}}$, $x_2 = \frac{1}{\sqrt{3}}$, and $w_i = 1$.

8.3 First Order Shape Functions

The string is discretized into N equal sized elements, and $N+1$ nodes defined by the position of the endpoint of the i'th element, $(\mathbf{r}_i, \mathbf{r}_{i+1})$. There are $6(N+1)$ degrees of freedom for the x, y, z position and $\dot{x}, \dot{y}, \dot{z}$ velocity of each node. Each element will have an initial length of $l_0 = \frac{l}{N}$. The one dimensional linear shape function comprises of a natural coordinate $\zeta \in [0,1]$ defining a point between node points within each element. Two shape functions, one with positive and one with negative slope, vary linearly between 1 and 0 between $\zeta \in [0,1]$. (See Appendix D.1 for a complete description of the linear shape function.) The position of a point in the element and its second order derivative in time as a function of ζ are defined as:

$$\begin{aligned}\mathbf{r}(\zeta) &= (1-\zeta)\,\mathbf{r}_i + \zeta\mathbf{r}_{i+1}\\ \ddot{\mathbf{r}}(\zeta) &= (1-\zeta)\,\ddot{\mathbf{r}}_i + \zeta\ddot{\mathbf{r}}_{i+1}.\end{aligned} \tag{8.5}$$

8.3.1 Change of Variables

Performing a change of variables on the weighted residual integral given in Eq. 8.2, from s_o to the natural coordinate of the linear shape function element, $\zeta \in [0,1]$ using Eq.

D.1 yields:

$$\int_0^1 w(\zeta)\left(\mu\ddot{\mathbf{r}}(\zeta) - \mu\mathbf{g}\right) l_0 d\zeta + EA\int_0^1 \left(\frac{\|\mathbf{r}'(\zeta)\|_2 - 1}{\|\mathbf{r}'(\zeta)\|_2}\mathbf{r}'(\zeta)\right)\frac{dw(\zeta)}{d\zeta}\frac{d\zeta}{ds_o} l_0 d\zeta \\ - w(\zeta)\,\mathbf{f}(\zeta)\big|_0^1 = 0. \tag{8.6}$$

For the spatial derivative terms, the proper change of variables from $\mathbf{r}'(s_o)$ to $\mathbf{r}'(\zeta)$ needs to be determined. Taking the derivative via the chain rule, taking the partial derivative of Eq. 8.5 and inserting Eq. D.1 results in:

$$\begin{aligned} \mathbf{r}'(\zeta) &= \frac{\partial}{\partial(s_o)}\left(\mathbf{r}(\zeta)\right) \\ \mathbf{r}'(\zeta) &= \frac{\partial\mathbf{r}(\zeta)}{\partial\zeta}\frac{\partial\zeta}{\partial s_o} \\ \mathbf{r}'(\zeta) &= \left(\mathbf{r}_{i+1} - \mathbf{r}_i\right)\left(\frac{1}{l_0}\right). \end{aligned} \tag{8.7}$$

Plugging Eq. D.1, Eq. 8.5, and Eq. 8.7 into Eq. 8.6, simplifying and reorganizing yields:

$$\mu l_0 \int_0^1 w(\zeta)\left((1-\zeta)\ddot{\mathbf{r}}_i + \zeta\ddot{\mathbf{r}}_{i+1} - \mathbf{g}\right) d\zeta \\ + \frac{EA}{l_0}\frac{\|(\mathbf{r}_{i+1} - \mathbf{r}_i)\|_2 - l_0}{\|(\mathbf{r}_{i+1} - \mathbf{r}_i)\|_2}\left(\mathbf{r}_{i+1} - \mathbf{r}_i\right)\int_0^1 \frac{dw(\zeta)}{d\zeta} d\zeta - \mathbf{f}(\zeta)\, w(\zeta)\big|_0^1 = 0$$

where the elemental force density term, q_i is:

$$q_i = \frac{EA}{l_0}\frac{\|(\mathbf{r}_{i+1} - \mathbf{r}_i)\|_2 - l_0}{\|(\mathbf{r}_{i+1} - \mathbf{r}_i)\|_2}. \tag{8.8}$$

The weighted residual integral results in:

$$\mu l_0 \int_0^1 w(\zeta)\left((1-\zeta)\ddot{\mathbf{r}}_i + \zeta\ddot{\mathbf{r}}_{i+1} - \mathbf{g}\right) d\zeta + q_i\left(\mathbf{r}_{i+1} - \mathbf{r}_i\right)\int_0^1 \frac{dw(\zeta)}{d\zeta} d\zeta - \mathbf{f}(\zeta)\, w(\zeta)\big|_0^1 = 0. \tag{8.9}$$

8.3.2 Shape Function and Global Assembly

The one dimensional linear shape function is one of the few element models that can actually be solved analytically. Using the two shape functions as weights, as defined in Eq. D.2, leads to a system of two equations per element and the elemental stencil (See Appendix D.2 for a complete derivation):

$$\frac{\mu l_0}{6}\begin{bmatrix} 2\mathbf{I}_3 & \mathbf{I}_3 \\ \mathbf{I}_3 & 2\mathbf{I}_3 \end{bmatrix}\begin{bmatrix} \ddot{\mathbf{r}}_i \\ \ddot{\mathbf{r}}_{i+1} \end{bmatrix} = q_i \begin{bmatrix} -\mathbf{I}_3 & \mathbf{I}_3 \\ \mathbf{I}_3 & -\mathbf{I}_3 \end{bmatrix}\begin{bmatrix} \mathbf{r}_i \\ \mathbf{r}_{i+1} \end{bmatrix} + \frac{\mu l_0}{2} g \begin{bmatrix} \mathbf{I}_3 \\ \mathbf{I}_3 \end{bmatrix} \hat{\mathbf{e}}_3 + \begin{bmatrix} -\mathbf{f}_i \\ \mathbf{f}_{i+1} \end{bmatrix} \tag{8.10}$$

where the last term is the elemental boundary conditions. Because the string is discretized into elements in series, the global assembly of elements leads to the following structure:

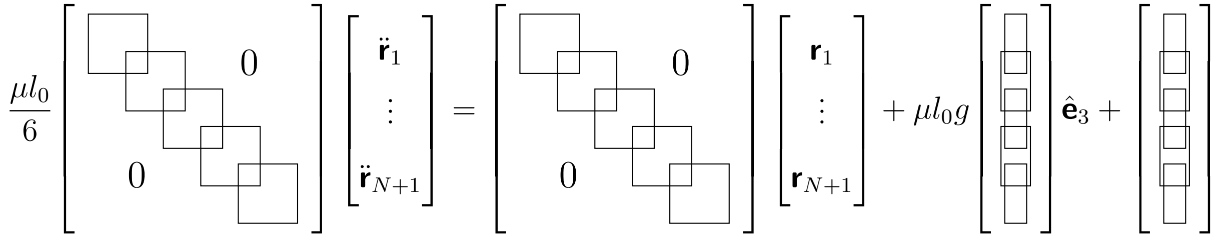

where each element block follows Eq. 8.10. The mass and stiffness sub-matrices are 6 × 6 matrices with three rows and columns in the corners overlapping, and the gravity and boundary condition matrices are tall 6 × 1 with three rows overlapping up, and three rows overlapping down. Wherever blocks overlap, the terms from each element are added together, yielding the following nodal stencil for the i'th internal node:

$$\frac{\mu l_0}{6}\begin{bmatrix} \mathbf{I}_3 & 4\mathbf{I}_3 & \mathbf{I}_3 \end{bmatrix}\begin{bmatrix} \ddot{\mathbf{r}}_{i-1} \\ \ddot{\mathbf{r}}_i \\ \ddot{\mathbf{r}}_{i+1} \end{bmatrix} = \begin{bmatrix} q_{i-1}\mathbf{I}_3 & -\left(q_{i-1}+q_i\right)\mathbf{I}_3 & q_i\mathbf{I}_3 \end{bmatrix}\begin{bmatrix} \mathbf{r}_{i-1} \\ \mathbf{r}_i \\ \mathbf{r}_{i+1} \end{bmatrix} + \mu l_0 \mathbf{g} \tag{8.11}$$

where the boundary conditions for the internal nodes, ($\mathbf{f}_i$), cancel out. Assembling into a system of equations for the string yields the following matrix equation:

$$\mathbf{M}_{\text{str}}\ddot{\mathbf{X}}_{\text{str}} = \mathbf{K}_{\text{str}}\mathbf{X}_{\text{str}} + \mathbf{G}_{\text{str}}\hat{\mathbf{e}}_3 + \mathbf{B}_{\text{str}} \tag{8.12}$$

where the state matrix, $\mathbf{X}_{\text{str}}$, of size $(3N+3)\times 1$, the gravity matrix, $\mathbf{G}_{\text{str}}$, of size $(3N+3)\times 3$, and boundary condition matrix, $\mathbf{B}_{\text{str}}$, of size $(3N+3)\times 1$, are defined as:

$$\mathbf{X}_{\text{str}} = \begin{bmatrix} \mathbf{r}_1 \\ \vdots \\ \mathbf{r}_{N+1} \end{bmatrix}, \ \mathbf{G}_{\text{str}} = \mu l_0 g \begin{bmatrix} \frac{1}{2}\mathbf{I}_3 \\ \mathbf{I}_3 \\ \vdots \\ \mathbf{I}_3 \\ \frac{1}{2}\mathbf{I}_3 \end{bmatrix}, \ \mathbf{B}_{\text{str}} = \begin{bmatrix} -\mathbf{f}_1 \\ 0 \\ \vdots \\ 0 \\ \mathbf{f}_{N+1} \end{bmatrix} \tag{8.13}$$

and the mass matrix, $\mathbf{M}_{\text{str}}$, $(3N+3)\times(3N+3)$ sized, is block tridiagonal:

$$\mathbf{M}_{\text{str}} = \frac{\mu l_0}{6} \begin{bmatrix} 2\mathbf{I}_3 & \mathbf{I}_3 & & & 0 \\ \mathbf{I}_3 & 4\mathbf{I}_3 & \mathbf{I}_3 & & \\ & \ddots & \ddots & \ddots & \\ & & \mathbf{I}_3 & 4\mathbf{I}_3 & \mathbf{I}_3 \\ 0 & & & \mathbf{I}_3 & 2\mathbf{I}_3 \end{bmatrix} \tag{8.14}$$

and the stiffness matrix $\mathbf{K}_{\text{str}}$, also $(3N+3)\times(3N+3)$ sized and block tridiagonal is:

$$\mathbf{K}_{\text{str}} = \begin{bmatrix} -q_1\mathbf{I}_3 & q_1\mathbf{I}_3 & & & 0 \\ q_1\mathbf{I}_3 & -\left(q_1+q_2\right)\mathbf{I}_3 & q_2\mathbf{I}_3 & & \\ & \ddots & \ddots & \ddots & \\ & & q_{N-1}\mathbf{I}_3 & -\left(q_{N-1}+q_N\right)\mathbf{I}_3 & q_N\mathbf{I}_3 \\ 0 & & & q_N\mathbf{I}_3 & -q_N\mathbf{I}_3 \end{bmatrix}. \tag{8.15}$$

8.3.3 c^0 String Boundary Conditions

There are two boundary conditions that need to be addressed: the c^0, or position boundary conditions at each end of the string. For the first string node, the c^0 fixed boundary condition can be enforced by artificially setting the acceleration to zero using model reduction [118]. Model reduction removes the rows and columns associated with the fixed boundary, $\mathbf{r}_1$, yielding:

$$\mathbf{M}'_{\text{str}}\ddot{\mathbf{X}}'_{\text{str}} = \mathbf{K}'_{\text{str}} + \mathbf{X}'_{\text{str}} + \mathbf{G}'_{\text{str}}\hat{\mathbf{e}}_3 + \mathbf{B}'_{\text{str}} \tag{8.16}$$

where

$$\mathbf{X}'_{\text{str}} = \begin{bmatrix} \mathbf{r}_2 \\ \vdots \\ \mathbf{r}_{N+1} \end{bmatrix}, \ \mathbf{G}'_{\text{str}} = \mu l_0 g \begin{bmatrix} \mathbf{I}_3 \\ \vdots \\ \mathbf{I}_3 \\ \frac{1}{2}\mathbf{I}_3 \end{bmatrix}, \ \mathbf{B}'_{\text{str}} = \begin{bmatrix} 0 \\ \vdots \\ 0 \\ \mathbf{f}_{N+1} \end{bmatrix}$$

are three rows shorter now, and $\mathbf{M}'_{\mathrm{str}}$ and $\mathbf{K}'_{\mathrm{str}}$, now $3N \times 3N$ matrices, are:

$$\begin{aligned}
\mathbf{M}'_{\mathrm{str}} &= \frac{\mu l_0}{6}\begin{bmatrix} 4\mathbf{I}_3 & \mathbf{I}_3 & & & 0 \\ \mathbf{I}_3 & 4\mathbf{I}_3 & \mathbf{I}_3 & & \\ & \ddots & \ddots & \ddots & \\ & & \mathbf{I}_3 & 4\mathbf{I}_3 & \mathbf{I}_3 \\ 0 & & & \mathbf{I}_3 & 2\mathbf{I}_3 \end{bmatrix} \\
\mathbf{K}'_{\mathrm{str}} &= \begin{bmatrix} -\left(q_1+q_2\right)\mathbf{I}_3 & q_2\mathbf{I}_3 & & & 0 \\ q_2\mathbf{I}_3 & -\left(q_2+q_3\right)\mathbf{I}_3 & q_3\mathbf{I}_3 & & \\ & \ddots & \ddots & \ddots & \\ & & q_{N-1}\mathbf{I}_3 & -\left(q_{N-1}+q_N\right)\mathbf{I}_3 & q_N\mathbf{I}_3 \\ 0 & & & q_N\mathbf{I}_3 & -q_N\mathbf{I}_3 \end{bmatrix}.
\end{aligned} \tag{8.17}$$

Where the string attaches to the rigid body, the final string node needs to incorporate the forces and coupling from the rigid body. Because the final string node also describes the translation equations of motion for the rigid body, the second equation in Eq. 7.13 can be added to the final row of Eq. 8.16, substituting $\mathbf{r}_{N+1}$ for $\mathbf{r}\left(l\right)$ and defining $\mathbf{f}_{N+1} = \mathbf{f}(l)$ from Eq. 8.3. In order to augment the system with the rotation matrix kinematic relationship given in Eq. A.8 ($\dot{\tilde{\mathbf{r}}}_i = -\hat{\boldsymbol{\Omega}}\tilde{\mathbf{r}}_i$), the second order ODE needs to be converted to a first order ODE by expanding the state. Also augmenting with the third equation of Eq. 7.13 yields:

$$\mathbf{M}\dot{\mathbf{X}} = \mathbf{K}\mathbf{X} + \mathbf{G}\hat{\mathbf{e}}_3 + \mathbf{B} \tag{8.18}$$

where $\mathbf{X}$, now $(6N+12)\times 1$, $\mathbf{G}$, now $(6N+12)\times 3)$ and $\mathbf{B}$, now $(6N+12)\times 1$ are:

$$\mathbf{X} = \left[\begin{array}{c} \mathbf{r}_2 \\ \vdots \\ \mathbf{r}_{N+1} \\ \hline \dot{\mathbf{r}}_2 \\ \vdots \\ \dot{\mathbf{r}}_{N+1} \\ \hline \boldsymbol{\Omega} \\ \tilde{\mathbf{r}}_1 \\ \tilde{\mathbf{r}}_2 \\ \tilde{\mathbf{r}}_3 \end{array}\right], \; \mathbf{G} = \mu l_0 g \left[\begin{array}{c} 0 \\ \vdots \\ 0 \\ \hline \mathbf{I}_3 \\ \vdots \\ \mathbf{I}_3 \\ \left(\frac{1}{2} + \frac{\mathrm{m}}{\mu l_0}\right)\mathbf{I}_3 \\ \hline \frac{\mathrm{m}}{\mu l_0}\hat{\boldsymbol{\rho}}_c \mathbf{R}^T \\ 0 \\ 0 \\ 0 \end{array}\right], \; \mathbf{B} = \left[\begin{array}{c} 0 \\ \vdots \\ 0 \\ \hline 0 \\ \vdots \\ 0 \\ -\mathrm{m}\mathbf{R}\hat{\boldsymbol{\Omega}}^2 \boldsymbol{\rho}_c \\ \hline 0 \\ 0 \\ 0 \\ 0 \end{array}\right], \tag{8.19}$$

$\mathbf{M}$, now $(6N+12)\times(6N+12)$, is:

$$\mathbf{M} = \left[\begin{array}{c|c|cccc} \mathbf{I} & 0 & & 0 & & \\ \hline 0 & \mathbf{M}''_{\text{str}} & & & & \\ & & -\mathrm{m}\mathbf{R}\hat{\boldsymbol{\rho}}_c & & & \\ \hline & \mathrm{m}\hat{\boldsymbol{\rho}}_c\mathbf{R}^T & \boldsymbol{\Pi} & & & \\ 0 & & & \mathbf{I}_3 & & \\ & & & & \mathbf{I}_3 & \\ & & & & & \mathbf{I}_3 \end{array}\right] \tag{8.20}$$

where the identity matrix in the top coner is size $3N$ for the conversion from a second order to first order ODE, and $\mathbf{M}''_{\text{str}}$ is the same as $\mathbf{M}'_{\text{str}}$ from Eq. 8.17 with the exception of the last element in the last row:

$$\mathbf{M}''_{\text{str}} = \frac{\mu l_0}{6} \begin{bmatrix} 4\mathbf{I}_3 & \mathbf{I}_3 & & & 0 \\ \mathbf{I}_3 & 4\mathbf{I}_3 & \mathbf{I}_3 & & \\ & \ddots & \ddots & \ddots & \\ & & \mathbf{I}_3 & 4\mathbf{I}_3 & \mathbf{I}_3 \\ 0 & & & \mathbf{I}_3 & \left(2 + \frac{6\text{m}}{\mu l_0}\right) \mathbf{I}_3 \end{bmatrix}, \tag{8.21}$$

and $\mathbf{K}$, also $(6N + 12) \times (6N + 12)$, has $\mathbf{K}'_{\text{str}}$, from Eq. 8.17 embedded in it:

$$\mathbf{K} = \left[\begin{array}{c:c:cccc} & \mathbf{I}_3 & & & & \\ \hdashline \mathbf{K}'_{\text{str}} & & & & & \\ \hdashline & & -\hat{\boldsymbol{\Omega}}\boldsymbol{\Pi} & & & \\ & & & -\hat{\boldsymbol{\Omega}} & & \\ & & & & -\hat{\boldsymbol{\Omega}} & \\ & & & & & -\hat{\boldsymbol{\Omega}} \end{array}\right] \tag{8.22}$$

where the top $3N$ rows are the conversion from a second order to first order differential equation, the next $3N$ rows are the discretized string nodes, the $(6N + 1)$'th row is the third equation of Eq. 7.13, and the final nine rows are the vector kinematic relationship given in Eq. A.8. Note the nonlinear coupling term in $\mathbf{B}$ for the final string node where it attaches to the rigid body. In addition to the stiffness matrix changing in time, the mass matrix now is also not constant as it includes the rotation matrix for the rigid body.

8.4 Second Order Shape Functions

The string is discretized into N equal sized elements, with $2N + 1$ nodes, defined by the position of the endpoints and midpoint of the j'th element ($\mathbf{r}_{2j-1}$, $\mathbf{r}_{2j}$, $\mathbf{r}_{2j+1}$). There are

$6(2N+1)$ degrees of freedom for the x, y, z position and $\dot{x}, \dot{y}, \dot{z}$ velocity of each node. Each element will have an initial length of $l_0 = \frac{l}{N}$. The one dimensional quadratic shape function comprises of a natural coordinate $\zeta \in [-1, 1]$ defining in each element a point between node points. Three shape functions, two with positive and one with negative slope, vary quadratically between 1 and 0 in the domain $\zeta \in [-1, 1]$, such that only one shape function equals 1 at each endpoint and midpoint, while the other two equal 0. (See Appendix D.3 for a complete description of the quadratic shape function.) The position of a point in an element and its second order derivative in time as a function of ζ are defined as:

$$\begin{aligned} \mathbf{r}(\zeta) &= \left(\frac{\zeta^2 - \zeta}{2}\right) \mathbf{r}_{2j-1} + \left(1 - \zeta^2\right) \mathbf{r}_{2j} + \left(\frac{\zeta^2 + \zeta}{2}\right) \mathbf{r}_{2j+1} \\ \ddot{\mathbf{r}}(\zeta) &= \left(\frac{\zeta^2 - \zeta}{2}\right) \ddot{\mathbf{r}}_{2j-1} + \left(1 - \zeta^2\right) \ddot{\mathbf{r}}_{2j} + \left(\frac{\zeta^2 + \zeta}{2}\right) \ddot{\mathbf{r}}_{2j+1}. \end{aligned} \tag{8.23}$$

8.4.1 Change of Variables

Performing a change of variables on the weighted residual integral given in Eq. 8.2, from s_o to the natural coordinate of the quadratic shape function element, $\zeta \in [-1, 1]$, using Eq. D.4 yields:

$$\begin{aligned} \int_{-1}^{1} w(\zeta) \left(\mu \ddot{\mathbf{r}}(\zeta) - \mu \mathbf{g}\right) \frac{l_0}{2} d\zeta + EA \int_{-1}^{1} \left(\frac{\|\mathbf{r}'(\zeta)\|_2 - 1}{\|\mathbf{r}'(\zeta)\|_2} \mathbf{r}'(\zeta)\right) \frac{dw(\zeta)}{d\zeta} \frac{d\zeta}{ds_o} \frac{l_0}{2} d\zeta \\ - w(\zeta) \mathbf{f}(\zeta) \Big|_{-1}^{1} = 0. \end{aligned} \tag{8.24}$$

For the spatial derivative terms, the proper change of variables from $\mathbf{r}'(s_o)$ to $\mathbf{r}'(\zeta)$ needs to be determined. Taking the partial derivative via the chain rule, inserting Eq. D.4 and the derivative of Eq. 8.23 yields for the j'th element:

$$\begin{aligned}
\mathbf{r}'(\zeta) &= \frac{\partial}{\partial(s_o)}\left(\mathbf{r}(\zeta)\right)\\
\mathbf{r}'(\zeta) &= \frac{\partial \mathbf{r}(\zeta)}{\partial \zeta}\frac{\partial \zeta}{\partial s_o}\\
\mathbf{r}'(\zeta) &= \frac{(2\zeta-1)\,\mathbf{r}_{2j-1}+(-4\zeta)\,\mathbf{r}_{2j}+(2\zeta+1)\,\mathbf{r}_{2j+1}}{l_0}\\
\mathbf{r}'(\zeta) &= \frac{\mathbf{l}(\zeta)}{l_0}
\end{aligned} \tag{8.25}$$

where $\mathbf{l}(\zeta)$ is an elemental length vector defined as:

$$\mathbf{l}(\zeta) = (2\zeta-1)\,\mathbf{r}_{2j-1}+(-4\zeta)\,\mathbf{r}_{2j}+(2\zeta+1)\,\mathbf{r}_{2j+1}. \tag{8.26}$$

Plugging Eq. D.4, Eq. 8.23 and Eq. 8.25 into Eq. 8.24, simplifying and reorganizing the weighted residual integral in terms of ζ yields:

$$\begin{aligned}
&\frac{\mu l_0}{2}\int_{-1}^{1} w(\zeta)\left(\left(\frac{\zeta^2-\zeta}{2}\right)\ddot{\mathbf{r}}_{2j-1}+\left(1-\zeta^2\right)\ddot{\mathbf{r}}_{2j}+\left(\frac{\zeta^2+\zeta}{2}\right)\ddot{\mathbf{r}}_{2j+1}-\mathbf{g}\right)d\zeta\\
&\qquad+\frac{EA}{l_0}\int_{-1}^{1}\left(1-\frac{l_0}{\|\mathbf{l}(\zeta)\|_2}\right)\mathbf{l}(\zeta)\frac{dw(\zeta)}{d\zeta}d\zeta - w(\zeta)\,\mathbf{f}(\zeta)\big|_{-1}^{1} = 0
\end{aligned} \tag{8.27}$$

8.4.2 Shape Functions and Global Assembly

The elastic stiffness terms can not be solved analytically for the one dimensional quadratic element. Using the three shape functions as weights, as defined in Eq. D.5, two point Gauss Quadrature from Eq. 8.4 is applied to the stiffness integral with $x_1 = \frac{-1}{\sqrt{3}}$, $x_2 = \frac{1}{\sqrt{3}}$, and $w_i = 1$. The mass terms are solved analytically, leading to a system of three equations per element with the following elemental stencil (See Appendix D.3 for a complete derivation):

$$\frac{\mu l_0}{30}\begin{bmatrix}4\mathbf{I}_3 & 2\mathbf{I}_3 & -\mathbf{I}_3\\ 2\mathbf{I}_3 & 16\mathbf{I}_3 & 2\mathbf{I}_3\\ -\mathbf{I}_3 & 2\mathbf{I}_3 & 4\mathbf{I}_3\end{bmatrix}\begin{bmatrix}\ddot{\mathbf{r}}_{2j-1}\\ \ddot{\mathbf{r}}_{2j}\\ \ddot{\mathbf{r}}_{2j+1}\end{bmatrix} = \left(\frac{q_j}{6}\begin{bmatrix}-7\mathbf{I}_3 & 8\mathbf{I}_3 & -\mathbf{I}_3\\ 8\mathbf{I}_3 & -16\mathbf{I}_3 & 8\mathbf{I}_3\\ -\mathbf{I}_3 & 8\mathbf{I}_3 & -7\mathbf{I}_3\end{bmatrix} + \frac{2\sqrt{3}\Delta q_j}{3}\begin{bmatrix}\mathbf{I}_3 & -\mathbf{I}_3 & 0\\ -\mathbf{I}_3 & 0 & \mathbf{I}_3\\ 0 & \mathbf{I}_3 & -\mathbf{I}_3\end{bmatrix}\right)\begin{bmatrix}\mathbf{r}_{2j-1}\\ \mathbf{r}_{2j}\\ \mathbf{r}_{2j+1}\end{bmatrix}$$
$$+\frac{\mu l_0}{6}g\begin{bmatrix}\mathbf{I}_3\\ 4\mathbf{I}_3\\ \mathbf{I}_3\end{bmatrix}\hat{\mathbf{e}}_3 + \begin{bmatrix}-\mathbf{f}_{2j-1}\\ 0\\ \mathbf{f}_{2j+1}\end{bmatrix} \tag{8.28}$$

where the last term is the elementary boundary conditions, and the elemental force density, q_j, and force density bias, Δq_j are defined as:

$$q_j = q_j^+ + q_j^-, \quad \Delta q_j = q_j^+ - q_j^- \tag{8.29}$$

where q_j^- and q_j^+ are the two node Gaussian Quadrature biased elemental force density defined in Eq. D.9. When combining the N elements in series, the global assembly of elements yields the following block diagonal overlapping element structure:

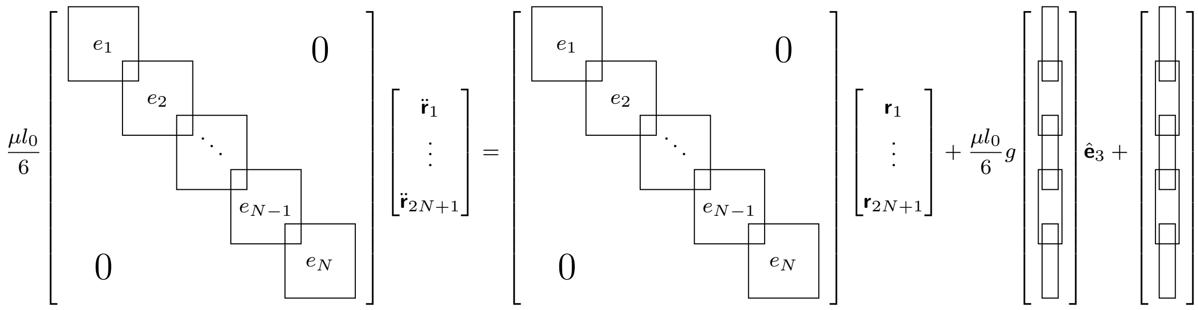

where each element block, e_i, follows Eq. 8.28. The mass and stiffness sub-matrices are 9×9 elemental matrices overlapping in the three rows and columns in the upper and lower corners. The gravity and boundary condition matrices are tall 9×1 with three rows overlapping with the next element. Wherever blocks overlap, the terms from each element are added together, yielding the following nodal stencil for the i'th internal node:

$$
\frac{\mu l_0}{30}
\left[\begin{array}{cc|ccc|cc}
-\mathbf{I}_3 & 2\mathbf{I}_3 & 8\mathbf{I}_3 & 2\mathbf{I}_3 & -\mathbf{I}_3 & & \\
 & & 2\mathbf{I}_3 & 16\mathbf{I}_3 & 2\mathbf{I}_3 & & \\
 & & -\mathbf{I}_3 & 2\mathbf{I}_3 & 8\mathbf{I}_3 & 2\mathbf{I}_3 & -\mathbf{I}_3
\end{array}\right]
\left[\begin{array}{c}
\ddot{\mathbf{r}}_{2j-3} \\
\ddot{\mathbf{r}}_{2j-2} \\ \hline
\ddot{\mathbf{r}}_{2j-1} \\
\ddot{\mathbf{r}}_{2j} \\
\ddot{\mathbf{r}}_{2j+1} \\ \hline
\ddot{\mathbf{r}}_{2j+2} \\
\ddot{\mathbf{r}}_{2j+3}
\end{array}\right]
$$

$$
= \left(\frac{1}{6}
\left[\begin{array}{cc|ccc|cc}
-q_{j-1}\mathbf{I}_3 & 8q_{j-1}\mathbf{I}_3 & \left(-7q_{j-1} - 7q_j\right)\mathbf{I}_3 & 8q_j\mathbf{I}_3 & -q_j\mathbf{I}_3 & & \\
 & & 8q_j\mathbf{I}_3 & -16q_j\mathbf{I}_3 & 8q_j\mathbf{I}_3 & & \\
 & & -q_j\mathbf{I}_3 & 8q_j\mathbf{I}_3 & \left(-7q_j - 7q_{j+1}\right)\mathbf{I}_3 & 8q_{j+1}\mathbf{I}_3 & -q_{j+1}\mathbf{I}_3
\end{array}\right]
\right.
$$

$$
\left. + \frac{2\sqrt{3}}{3}
\left[\begin{array}{cc|ccc|cc}
0 & \Delta q_{j-1}\mathbf{I}_3 & \left(\Delta q_j - \Delta q_{j-1}\right)\mathbf{I}_3 & -\Delta q_j\mathbf{I}_3 & 0 & & \\
 & & -\Delta q_j\mathbf{I}_3 & 0 & \Delta q_j\mathbf{I}_3 & & \\
 & & 0 & \Delta q_j\mathbf{I}_3 & \left(\Delta q_{j+1} - \Delta q_j\right)\mathbf{I}_3 & -\Delta q_{j+1}\mathbf{I}_3 & 0
\end{array}\right]
\right)
\left[\begin{array}{c}
\mathbf{r}_{2j-3} \\
\mathbf{r}_{2j-2} \\ \hline
\mathbf{r}_{2j-1} \\
\mathbf{r}_{2j} \\
\mathbf{r}_{2j+1} \\ \hline
\mathbf{r}_{2j+2} \\
\mathbf{r}_{2j+3}
\end{array}\right]
$$

$$
+ \frac{\mu l_0}{6} g
\begin{bmatrix}
2\mathbf{I}_3 \\
4\mathbf{I}_3 \\
2\mathbf{I}_3
\end{bmatrix}
\hat{\mathbf{e}}_3
$$

Assembling into a global matrix again yields the same matrix equation as in Eq. 8.12, where now the state vector, $\mathbf{X}_{\text{str}}$, of size $(6N+3) \times 1$, the gravity matrix, $\mathbf{G}_{\text{str}}$, of size

$(6N+3)\times 3$, and boundary condition vector, $\mathbf{B}_{\text{str}}$, of size $(6N+3)\times 1$, are defined as:

$$\mathbf{X}_{\text{str}} = \begin{bmatrix} \mathbf{r}_1 \\ \vdots \\ \mathbf{r}_{2N+1} \end{bmatrix}, \; \mathbf{G}_{\text{str}} = \frac{\mu l_0}{6} g \begin{bmatrix} \mathbf{I}_3 \\ 4\mathbf{I}_3 \\ 2\mathbf{I}_3 \\ 4\mathbf{I}_3 \\ \vdots \\ 4\mathbf{I}_3 \\ 2\mathbf{I}_3 \\ 4\mathbf{I}_3 \\ \mathbf{I}_3 \end{bmatrix}, \; \mathbf{B}_{\text{str}} = \begin{bmatrix} -\mathbf{f}_1 \\ 0 \\ \vdots \\ 0 \\ \mathbf{f}_{2N+1} \end{bmatrix} \tag{8.30}$$

and the mass matrix, $\mathbf{M}_{\text{str}}$, a $(6N+3)\times(6N+3)$ matrix, is a symmetric block pentadiagonal matrix defined as:

$$\mathbf{M}_{\text{str}} = \frac{\mu l_0}{30} \begin{bmatrix} 4\mathbf{I}_3 & 2\mathbf{I}_3 & -\mathbf{I}_3 & & & & & & & 0 \\ 2\mathbf{I}_3 & 16\mathbf{I}_3 & 2\mathbf{I}_3 & 0 & & & & & & \\ -\mathbf{I}_3 & 2\mathbf{I}_3 & 8\mathbf{I}_3 & 2\mathbf{I}_3 & -\mathbf{I}_3 & & & & & \\ & 0 & 2\mathbf{I}_3 & 16\mathbf{I}_3 & 2\mathbf{I}_3 & 0 & & & & \\ & & \ddots & \ddots & \ddots & \ddots & \ddots & & & \\ & & & 0 & 2\mathbf{I}_3 & 16\mathbf{I}_3 & 2\mathbf{I}_3 & 0 & & \\ & & & & -\mathbf{I}_3 & 2\mathbf{I}_3 & 8\mathbf{I}_3 & 2\mathbf{I}_3 & -\mathbf{I}_3 \\ & & & & & 0 & 2\mathbf{I}_3 & 16\mathbf{I}_3 & 2\mathbf{I}_3 \\ 0 & & & & & & -\mathbf{I}_3 & 2\mathbf{I}_3 & 4\mathbf{I}_3 \end{bmatrix} \tag{8.31}$$

and the stiffness matrix $\mathbf{K}_{\text{str}}$, also $(6N+3)\times(6N+3)$, is defined as a sum of a pentadiagonal and tridiagonal matrix:

$$
\begin{aligned}
\mathbf{K}_{\text{str}} = \frac{1}{6} & \begin{bmatrix}
-7q_1\mathbf{I}_3 & 8q_1\mathbf{I}_3 & -q_1\mathbf{I}_3 & & & & & & 0 \\
8q_1\mathbf{I}_3 & -16q_1\mathbf{I}_3 & 8q_1\mathbf{I}_3 & 0 & & & & & \\
-q_1\mathbf{I}_3 & 8q_1\mathbf{I}_3 & -\left(7q_1 + 7q_2\right)\mathbf{I}_3 & 8q_2\mathbf{I}_3 & -q_2\mathbf{I}_3 & & & & \\
 & 0 & 8q_2\mathbf{I}_3 & -16q_2\mathbf{I}_3 & 8q_2\mathbf{I}_3 & 0 & & & \\
 & & \ddots & \ddots & \ddots & \ddots & \ddots & & \\
 & & & 0 & 8q_{N-1}\mathbf{I}_3 & 16q_{N-1}\mathbf{I}_3 & 8q_{N-1}\mathbf{I}_3 & 0 & \\
 & & & & -q_{N-1}\mathbf{I}_3 & 8q_{N-1}\mathbf{I}_3 & -\left(7q_{N-1} + 7q_N\right)\mathbf{I}_3 & 8q_N\mathbf{I}_3 & -q_N\mathbf{I}_3 \\
 & & & & & 0 & 8q_N\mathbf{I}_3 & -16q_N\mathbf{I}_3 & 8q_N\mathbf{I}_3 \\
0 & & & & & & -q_N\mathbf{I}_3 & 8q_N\mathbf{I}_3 & -7q_N\mathbf{I}_3
\end{bmatrix} \\
+ \frac{2\sqrt{3}}{3} & \begin{bmatrix}
\Delta q_1\mathbf{I}_3 & -\Delta q_1\mathbf{I}_3 & & & & & 0 \\
-\Delta q_1\mathbf{I}_3 & 0 & \Delta q_1\mathbf{I}_3 & & & & \\
 & \Delta q_1\mathbf{I}_3 & \left(\Delta q_2 - \Delta q_1\right)\mathbf{I}_3 & -\Delta q_2\mathbf{I}_3 & & & \\
 & & \ddots & \ddots & \ddots & & \\
 & & & \Delta q_{N-1}\mathbf{I}_3 & \left(\Delta q_N - \Delta q_{N-1}\right)\mathbf{I}_3 & -\Delta q_N\mathbf{I}_3 & \\
 & & & & -\Delta q_N\mathbf{I}_3 & 0 & \Delta q_N\mathbf{I}_3 \\
0 & & & & & \Delta q_N\mathbf{I}_3 & -\Delta q_N\mathbf{I}_3
\end{bmatrix}
\end{aligned}
\tag{8.32}
$$

8.4.3 c^0 String Boundary Conditions

Similar to the linear shape function, there are two c^0 boundary conditions that need to be addressed: the position boundary condition at each end of the string. Like with the linear shape function, the c^0 fixed boundary condition at the first node can be enforced by artificially setting the acceleration to zero using model reduction. Removing the rows and columns of the global system of equations associated with $\mathbf{r}_1$, yields Eq. 8.16, but now:

$$\mathbf{X}'_{\text{str}} = \begin{bmatrix} \mathbf{r}_2 \\ \vdots \\ \mathbf{r}_{2N+1} \end{bmatrix}, \ \mathbf{G}'_{\text{str}} = \frac{\mu l_0}{6} g \begin{bmatrix} 4\mathbf{I}_3 \\ 2\mathbf{I}_3 \\ 4\mathbf{I}_3 \\ \vdots \\ 4\mathbf{I}_3 \\ 2\mathbf{I}_3 \\ 4\mathbf{I}_3 \\ \mathbf{I}_3 \end{bmatrix}, \ \mathbf{B}'_{\text{str}} = \begin{bmatrix} 0 \\ \vdots \\ 0 \\ \mathbf{f}_{2N+1} \end{bmatrix},$$

$\mathbf{M}'_{\text{str}}$, now a $6N \times 6N$ matrix, is:

$$\mathbf{M}'_{\text{str}} = \frac{\mu l_0}{30} \begin{bmatrix} 16\mathbf{I}_3 & 2\mathbf{I}_3 & 0 & & & & & & 0 \\ 2\mathbf{I}_3 & 8\mathbf{I}_3 & 2\mathbf{I}_3 & -\mathbf{I}_3 & & & & & \\ 0 & 2\mathbf{I}_3 & 16\mathbf{I}_3 & 2\mathbf{I}_3 & 0 & & & & \\ & -\mathbf{I}_3 & 2\mathbf{I}_3 & 8\mathbf{I}_3 & 2\mathbf{I}_3 & -\mathbf{I}_3 & & & \\ & & \ddots & \ddots & \ddots & \ddots & \ddots & & \\ & & & 0 & 2\mathbf{I}_3 & 16\mathbf{I}_3 & 2\mathbf{I}_3 & 0 & \\ & & & & -\mathbf{I}_3 & 2\mathbf{I}_3 & 8\mathbf{I}_3 & 2\mathbf{I}_3 & -\mathbf{I}_3 \\ & & & & & 0 & 2\mathbf{I}_3 & 16\mathbf{I}_3 & 2\mathbf{I}_3 \\ 0 & & & & & & -\mathbf{I}_3 & 2\mathbf{I}_3 & 4\mathbf{I}_3 \end{bmatrix} \tag{8.33}$$

and $\mathbf{K}'_{\mathrm{str}}$, now a $6N \times 6N$ sum of symmetric pentadiagonal and tridiagonal matrices, is:

$$\mathbf{K}'_{\mathrm{str}} = \frac{1}{6}\begin{bmatrix} -16q_1\mathbf{I}_3 & 8q_1\mathbf{I}_3 & 0 & & & & & 0 \\ 8q_1\mathbf{I}_3 & -\left(7q_1 + 7q_2\right)\mathbf{I}_3 & 8q_2\mathbf{I}_3 & -q_2\mathbf{I}_3 & & & & \\ 0 & 8q_2\mathbf{I}_3 & -16q_2\mathbf{I}_3 & 8q_2\mathbf{I}_3 & 0 & & & \\ & \ddots & \ddots & \ddots & \ddots & \ddots & & \\ & & 0 & 8q_{N-1}\mathbf{I}_3 & 16q_{N-1}\mathbf{I}_3 & 8q_{N-1}\mathbf{I}_3 & 0 & \\ & & & -q_{N-1}\mathbf{I}_3 & 8q_{N-1}\mathbf{I}_3 & -\left(7q_{N-1} + 7q_N\right)\mathbf{I}_3 & 8q_N\mathbf{I}_3 & -q_N\mathbf{I}_3 \\ & & & & 0 & 8q_N\mathbf{I}_3 & -16q_N\mathbf{I}_3 & 8q_N\mathbf{I}_3 \\ 0 & & & & & -q_N\mathbf{I}_3 & 8q_N\mathbf{I}_3 & -7q_N\mathbf{I}_3 \end{bmatrix}$$

$$+ \frac{2\sqrt{3}}{3}\begin{bmatrix} 0 & \Delta q_1\mathbf{I}_3 & & & & & 0 \\ \Delta q_1\mathbf{I}_3 & \left(\Delta q_2 - \Delta q_1\right)\mathbf{I}_3 & -\Delta q_2\mathbf{I}_3 & & & & \\ & -\Delta q_2\mathbf{I}_3 & 0 & \Delta q_2\mathbf{I}_3 & & & \\ & & \ddots & \ddots & \ddots & & \\ & & & \Delta q_{N-1}\mathbf{I}_3 & \left(\Delta q_N - \Delta q_{N-1}\right)\mathbf{I}_3 & -\Delta q_N\mathbf{I}_3 & \\ & & & & -\Delta q_N\mathbf{I}_3 & 0 & \Delta q_N\mathbf{I}_3 \\ 0 & & & & & \Delta q_N\mathbf{I}_3 & -\Delta q_N\mathbf{I}_3 \end{bmatrix} \tag{8.34}$$

Similar to with the linear shape function, the final string node, $\mathbf{r}_{2N+1}$, needs to incorporate the forces and coupling from the rigid body by adding the second equation in Eq. 7.13 to the final row of Eq. 8.12. $\mathbf{r}\left(l\right)$ is again substituted for $\mathbf{r}_{2N+1}$ and $\mathbf{f}_{2N+1} = \mathbf{f}(l)$ from Eq. 8.3. Augmenting the system with the third equation of Eq. 7.13 the rotation vector kinematic relationship given in Eq. A.8 ($\dot{\tilde{\mathbf{r}}}_i = -\hat{\mathbf{\Omega}}\tilde{\mathbf{r}}_i$), and expanding the state to convert from a second order to first order ODE yields:

$$\mathbf{M}'\dot{\mathbf{X}}' = \mathbf{K}'\mathbf{X}' + \mathbf{G}'\hat{\mathbf{e}}_3 + \mathbf{B}' \tag{8.35}$$

where $\mathbf{X}'$, now $(12N+12)\times 1$, $\mathbf{G}'$, now $(12N+12)\times 3$, and $\mathbf{B}'$, now $(12N+12)\times 1$, are:

$$\mathbf{X}' = \begin{bmatrix} \boldsymbol{\mathsf{r}}_2 \\ \vdots \\ \boldsymbol{\mathsf{r}}_{2N+1} \\ \hdashline \dot{\boldsymbol{\mathsf{r}}}_2 \\ \vdots \\ \dot{\boldsymbol{\mathsf{r}}}_{2N+1} \\ \hdashline \boldsymbol{\Omega} \\ \tilde{\boldsymbol{\mathsf{r}}}_1 \\ \tilde{\boldsymbol{\mathsf{r}}}_2 \\ \tilde{\boldsymbol{\mathsf{r}}}_3 \end{bmatrix}, \ \mathbf{G}' = \frac{\mu l_0}{6} g \begin{bmatrix} 0 \\ \vdots \\ 0 \\ \hdashline 4\mathbf{I}_3 \\ 2\mathbf{I}_3 \\ \vdots \\ 4\mathbf{I}_3 \\ \left(1 + \frac{6\mathrm{m}}{\mu l_0}\right)\mathbf{I}_3 \\ \hdashline \frac{6\mathrm{m}}{\mu l_0}\hat{\boldsymbol{\rho}}_c \mathbf{R}^T \\ 0 \\ 0 \\ 0 \end{bmatrix}, \ \mathbf{B}' = \begin{bmatrix} 0 \\ \vdots \\ 0 \\ \hdashline 0 \\ \vdots \\ 0 \\ -\mathrm{m}\mathbf{R}\hat{\boldsymbol{\Omega}}^2 \boldsymbol{\rho}_c \\ \hdashline 0 \\ 0 \\ 0 \\ 0 \end{bmatrix}, \tag{8.36}$$

where $\mathbf{M}'$, now $(12N+12)\times(12N+12)$ is the same as Eq. 8.20, but the identity matrix in the top corner is now of size $6N$ for the conversion from a second order to first order ODE, and $\mathbf{M}''_{\mathrm{str}}$ is the same as $\mathbf{M}'_{\mathrm{str}}$ from Eq. 8.33 with the exception of the last element in the last row:

$$\mathbf{M}''_{\mathrm{str}} = \frac{\mu l_0}{30}\begin{bmatrix} 16\mathbf{I}_3 & 2\mathbf{I}_3 & 0 & & & & & & 0 \\ 2\mathbf{I}_3 & 8\mathbf{I}_3 & 2\mathbf{I}_3 & -\mathbf{I}_3 & & & & & \\ 0 & 2\mathbf{I}_3 & 16\mathbf{I}_3 & 2\mathbf{I}_3 & 0 & & & & \\ & -\mathbf{I}_3 & 2\mathbf{I}_3 & 8\mathbf{I}_3 & 2\mathbf{I}_3 & -\mathbf{I}_3 & & & \\ & & \ddots & \ddots & \ddots & \ddots & \ddots & & \\ & & & 0 & 2\mathbf{I}_3 & 16\mathbf{I}_3 & 2\mathbf{I}_3 & 0 & \\ & & & & -\mathbf{I}_3 & 2\mathbf{I}_3 & 8\mathbf{I}_3 & 2\mathbf{I}_3 & -\mathbf{I}_3 \\ & & & & & 0 & 2\mathbf{I}_3 & 16\mathbf{I}_3 & 2\mathbf{I}_3 \\ 0 & & & & & & -\mathbf{I}_3 & 2\mathbf{I}_3 & \left(4 + \frac{30\mathrm{m}}{\mu l_o}\right)\mathbf{I}_3 \end{bmatrix}. \tag{8.37}$$

$\mathbf{K}'$, also $(12N + 12) \times (12N + 12)$, has $\mathbf{K}'_{\mathrm{str}}$, from Eq. 8.34 embedded in it:

$$\mathbf{K}' = \left[\begin{array}{c|c|cccc} & \mathbf{I}_{6N} & & & & \\ \hline \mathbf{K}'_{\mathrm{str}} & & & & & \\ \hline & & -\hat{\mathbf{\Omega}}\mathbf{\Pi} & & & \\ & & & -\hat{\mathbf{\Omega}} & & \\ & & & & -\hat{\mathbf{\Omega}} & \\ & & & & & -\hat{\mathbf{\Omega}} \end{array}\right] \tag{8.38}$$

where the top $6N$ rows are the conversion from second order to first order differential equation, the next $6N$ rows are the discretized string nodes, the $(12N + 1)$'th row is third equation of Eq. 7.13, and the final nine rows are the vector kinematic relationship given in Eq. A.8. Note the nonlinear coupling term in $\mathbf{B}$ for the final string node where it attaches to the rigid body. In addition to the stiffness matrix, the mass matrix needs to be built every time-step iteration, as it includes the rotation matrix which changes in time.

8.4.4 c^1 String Boundary Conditions

Since the string is a continuous body, there exist $N-1$ slope, or c^1 boundary condition between elements. The linear shape functions are incapable of enforcing the c^1 spatial continuity boundary condition, whereas it is possible with quadratic shape functions.

The c^1, or slope boundary condition between elements can only be enforced using Lagrangian multipliers. Lagrangian multipliers enforce a constraint equation, $f_i(\mathbf{q}, t)$ by multiplying the partial derivative of each constraint equation in Pfaffian, or configuration form ($f_i(\mathbf{q}, t) = 0$), by the Lagrange multipliers, λ_i, summed and subtracted from Hamilton's principle of least action in Eq. 7.11 [106, 118]:

$$\delta \mathcal{S} = \delta \int_{t_1}^{t_2} \mathcal{L}\left(\mathbf{q}, \dot{\mathbf{q}}, t\right) dt - \delta \int_{t_1}^{t_2} \sum_{i=1}^{p} \sum_{k=1}^{m} \lambda_i a_{ik} \delta \mathbf{q}_i dt = 0 \tag{8.39}$$

where p is the number of constraint equations, m is the number of generalized coordinates, and $a_{ik} = \frac{\partial f_i}{\partial \mathbf{q}_k}$. Applying to Eq. 8.16 results in the modified equations of motion:

$$\mathbf{M}'_{\text{str}} \ddot{\mathbf{X}}'_{\text{str}} = \mathbf{K}'_{\text{str}} \mathbf{X}'_{\text{str}} + \mathbf{G}'_{\text{str}} \hat{\mathbf{e}}_3 + \mathbf{B}'_{\text{str}} - \sum_{i=1}^{p} \lambda_i \frac{\delta f_i}{\delta \mathbf{q}_k} \tag{8.40}$$

Addressing the string element derivative boundary condition (c^1 boundary), the constraint equation is derived by setting the spatial derivative of one element equal to that of the next element:

$$\mathbf{r}^{k\prime}|_{\zeta=1} = \mathbf{r}^{k+1\prime}|_{\zeta=-1}$$

where k is the element number. The constraint needs to be enforced on both the first and second derivative for model consistency. Using Eq. 8.25, rearranging, and taking the time derivative twice gives the Pfaffian form:

$$\begin{aligned} f_i &= \dot{\mathbf{r}}_{2j-1} - 4\dot{\mathbf{r}}_{2j} + 6\dot{\mathbf{r}}_{2j+1} - 4\dot{\mathbf{r}}_{2j+2} + \dot{\mathbf{r}}_{2j+3} = 0 \\ f_{i+N-1} &= \ddot{\mathbf{r}}_{2j-1} - 4\ddot{\mathbf{r}}_{2j} + 6\ddot{\mathbf{r}}_{2j+1} - 4\ddot{\mathbf{r}}_{2j+2} + \ddot{\mathbf{r}}_{2j+3} = 0 \end{aligned} \tag{8.41}$$

Augmenting Eq. 8.35 with the $6(N-1)$ constraint equations, three for each degree of freedom at the inter-element boundaries, into Eq. 8.40 yields:

$$\mathbf{M}\dot{\mathbf{X}} = \mathbf{K}\mathbf{X} + \mathbf{G}\hat{\mathbf{e}}_3 + \mathbf{B} \tag{8.42}$$

where $\mathbf{X}$, $\mathbf{G}$, $\mathbf{B}$, $\mathbf{K}$ are $\mathbf{X}'$, $\mathbf{G}'$, $\mathbf{B}'$, and $\mathbf{K}'$, respectively from Eq. 8.36 and Eq. 8.38, augmented with $6(N-1)$ rows of zeros:

$$\mathbf{X} = \begin{bmatrix} \mathbf{X}' \\ 0 \end{bmatrix}, \; \mathbf{G} = \begin{bmatrix} \mathbf{G}' \\ 0 \end{bmatrix}, \; \mathbf{B} = \begin{bmatrix} \mathbf{B}' \\ 0 \end{bmatrix}, \; \mathbf{K} = \begin{bmatrix} \mathbf{K}' \\ 0 \end{bmatrix}, \tag{8.43}$$

and $\mathbf{M}$ is now:

$$\mathbf{M} = \left[\begin{array}{c:c} \mathbf{M}' & \mathbf{L}^T \\ \hdashline \mathbf{L} & 0 \end{array}\right] \tag{8.44}$$

where $\mathbf{L}$ is a $6(N-1) \times (12N+12)$ sized matrix defined as:

$$\mathbf{L} = \left[\begin{array}{c:c:c} \mathbf{L}' & 0 & 0 \\ \hdashline 0 & \mathbf{L}' & 0 \end{array}\right] \tag{8.45}$$

where the first $3(N-1)$ rows are for the velocity constraints, the second set of $3(N-1)$ rows for the acceleration constraints, the first and second column block 0's are of size

$3(N-1)\times 6N$, the last column block 0 is $3(N-1)\times 12$ and $\mathbf{L}'$ is $3(N-1)\times 6N$ defined as:

$$\mathbf{L}' = \begin{bmatrix} -4\mathbf{I}_3 & 6\mathbf{I}_3 & -4\mathbf{I}_3 & \mathbf{I}_3 & & & & & & & & \\ & \mathbf{I}_3 & -4\mathbf{I}_3 & 6\mathbf{I}_3 & -4\mathbf{I}_3 & \mathbf{I}_3 & & & & & 0 & \\ & & & \ddots & \ddots & \ddots & \ddots & \ddots & & & & \\ & 0 & & & & \mathbf{I}_3 & -4\mathbf{I}_3 & 6\mathbf{I}_3 & -4\mathbf{I}_3 & \mathbf{I}_3 & & \\ & & & & & & & \mathbf{I}_3 & -4\mathbf{I}_3 & 6\mathbf{I}_3 & -4\mathbf{I}_3 & \mathbf{I}_3 \end{bmatrix} \tag{8.46}$$

8.5 Conclusion

In this chapter, one dimensional linear and quadratic shape functions models were developed for the three dimensional elastic string rigid body pendulum. Using the proper Galerkin finite element method enabling the weighted residual integral yielded a linear shape function model that was analytically solvable. In contrast, the quadratic shape function model is unsolvable, and requires Gaussian quadrature to evaluate the weighted residual integral. For both models, the c^0 boundary conditions were applied at the pivot via model reduction, where the rows and columns associated with those coordinates are removed. At the other end of the string, the rigid body equations of motion were augmented to the formulations. For the quadratic shape function model, the c^1 boundary, or string slope boundary can be enforced. A constraint equation was developed, and enforced using Lagrange multipliers. Both models were augmented into first order differential equations, in order to use Runge-Kutta for time marching.

8.6 Acknowledgments

Support for this work was provided by Naval Information Warfare Center Pacific under the Naval Innovative Science and Engineering program and the Department of

Defense SMART Scholarship for Service program.

Chapter 8, in full is currently being prepared for submission for publication of the material. K. Talke, J. Friend, T. Bewley. The dissertation author was the primary investigator and author of these pages.

Chapter 9

Three Dimensional Pendulum Experimental Validation

This chapter presents the results of simulating the linear and quadratic shape function formulations, as well as the experimental validation work performed.

The remainder of the chapter is organized as follows. Section 9.1 presents the numerical example model problem. Section 9.2 presents the setup and key results from experimental validation. Section 9.3 summarizes the key conclusions.

9.1 Numerical Model Problem

A straightforward model problem to compare and analyze the linear and quadratic shape function formulations is the three dimensional elastic string pendulum described in Fig. 7.1.

9.1.1 Setup

Using the formulations described in Section 8, and the fourth order Runge-Kutta numerical time-marching scheme, a numerical simulation was performed using both the linear and quadratic shape function formulations [54]. The string is 5.875 m long, with a diameter of 4.7 mm, a linear density of $\mu = 0.03\ \frac{\text{kg}}{\text{m}}$, and a Young's modulus of $E = 57.64$ MPa, such that $EA = 1$ kN. One end of the string is attached to the pivot at the X, Y, and Z coordinate $(0, 0, 0)$, and the initial condition of the rigid body attachment is located at $(-0.1456, -5.7318, -1.1417)$ m, to replicate the experimental testing initial conditions described in Section 9.2. The string is discretized into five elements, with the initial locations specified by the hanging catenary cable equation [66, 67, 69]. The rigid body is initially oriented such that the $\hat{\mathbf{e}}_{b3}$ body fixed coordinate vector is co-linear with the global frame coordinate vector $\hat{\mathbf{e}}_2$. The rigid body parameters were chosen to match that of the experimental setup described in Section 9.2. The vector to the center of mass from the attachment point, is $\boldsymbol{\rho} = \begin{bmatrix} 0.0 & 0.0 & 0.03752 \end{bmatrix}^T$ m in body coordinates, and the matrix representation of the inertia tensor is:

$$\mathbf{\Pi} = \begin{bmatrix} 1161.58 & -3.31 & 9.51 \\ -3.31 & 1171.85 & 93.23 \\ 9.51 & 93.23 & 369.85 \end{bmatrix} \frac{\text{kg}}{\text{m}^2},$$

and the mass of the rigid body is specified as 0.432 kg, with no initial rotational velocity. The simulation time-step for the fourth order Runge-Kutta method is set to 0.0001 seconds.

9.1.2 Results

The results of a 4.5 second simulation of the linear shape function formulation of the model problem are shown in Fig. 9.1, showing the shape of the string and rigid body every

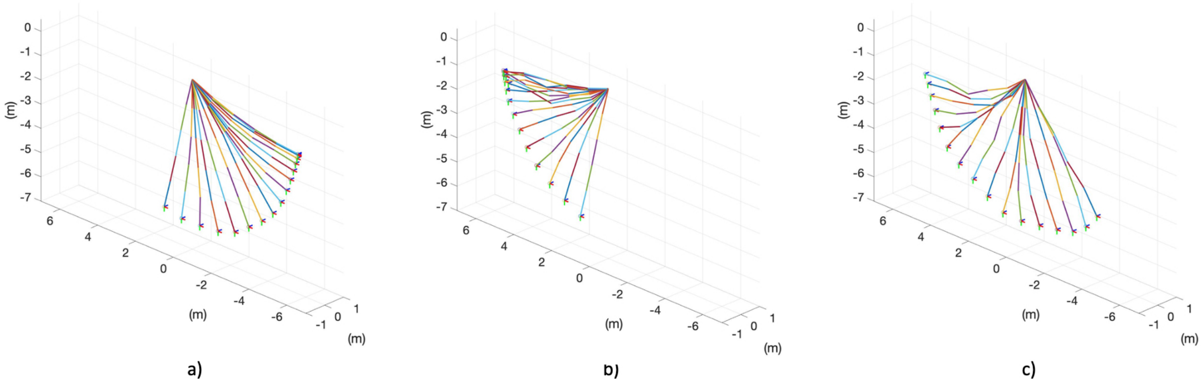

Figure 9.1: Three dimensional pendulum simulation with five linear shape function elements, showing snapshots every 0.1 seconds in the range of a) 0.0 to 1.5 seconds for the initial drop, b) 1.5 to 3.0 seconds for the upswing, and c) 3.0 to 4.5 seconds for the second drop back down.

0.1 seconds. In Fig. 9.1a, the rigid body is released, swings down with a small amount of extension at the bottom of the swing. In Fig. 9.1b, the pendulum continues its apex and then reverses direction. Because the shape functions are linear, the elements are also linear, forming kinks and sharp corners in the string, as evident at the top of the upswing. In Fig. 9.1c, the rigid body swings back down, and starts to swing back up. There are some clear string dynamics captured that are evident by the changing concavity, or slope of the string, noticeable at the bottom of the downswing before the upswing starts.

In comparison, as shown in Fig. 9.2, the exact same simulation was run with the quadratic shape function formulation, again showing the shape of the string and rigid body every 0.1 seconds. The smoothness of the string has now been fixed due to the c^1 boundary condition enforcement. The string dynamics on the second downswing are also more evident now.

Perhaps more indicative of the improvements gained from using the quadratic shape function formulation is the energy transfer between kinteic and potential, as shown in Fig 9.3. The simulation time was extended to 10 seconds, and the trade-off between kinetic and potential energy are clearly evident, as the potential energy decreases/increases as

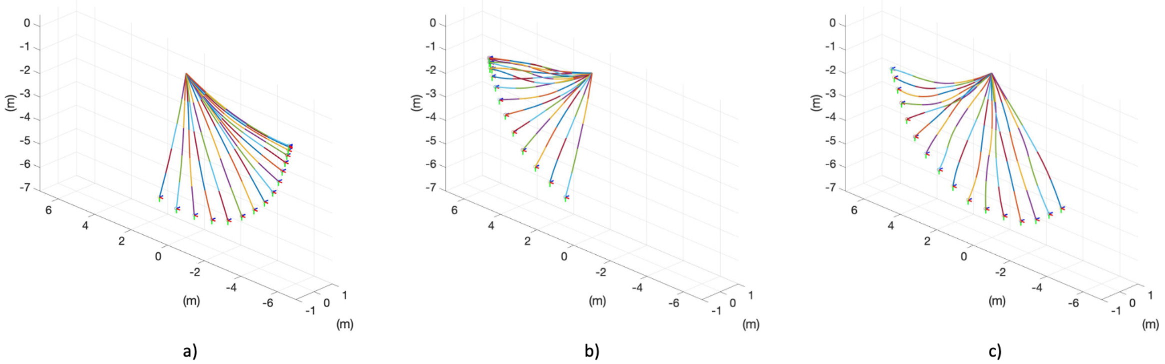

a) b) c)

Figure 9.2: Three dimensional pendulum simulation with five quadratic shape function elements, showing snapshots every 0.1 seconds in the range of a) 0.0 to 1.5 seconds for the initial drop, b) 1.5 to 3.0 seconds for the upswing, and c) 3.0 to 4.5 seconds for the second drop back down.

the kinetic energy increases/decreases. As seen in Fig. 9.3a, the linear shape function introduces numerical instabilities, initially seen in the string elastic potential energy spiking at 5.8 seconds, and then again after 7.5 seconds. In contrast, the quadratic shape function formulation does not spike, with the energy transfer continuing smoothly. The main drawback of the increased accuracy shape function is the increase in simulation time. Running Matlab on a 3.1 Ghz Dual Core Intel I7 processor, the linear shape function formulation simulation lasted only 32.6 seconds for the 10 second pendulum simulation with five elements, whereas the quadratic shape function formulation required 71.2 seconds

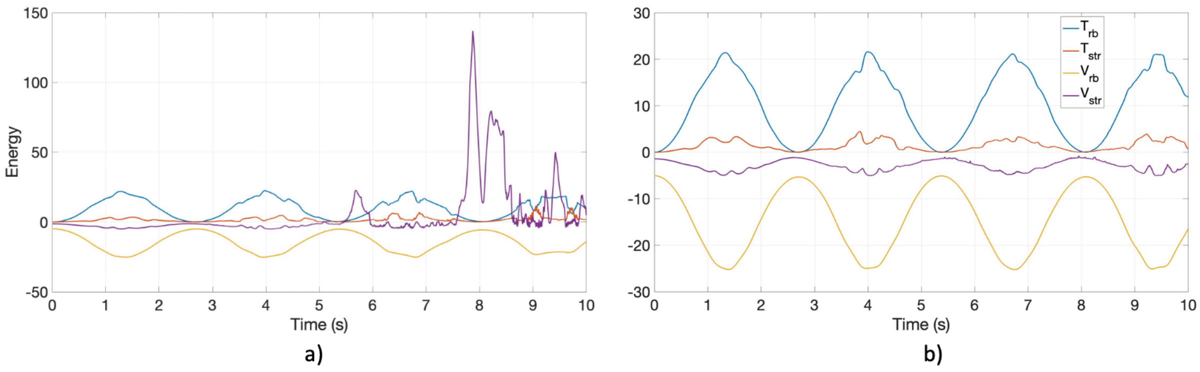

a) b)

Figure 9.3: Energy transfer between kinetic and potential for the rigid body and elastic string for a) linear shape function formulation with five elements and b) quadratic shape function formulation with five elements.

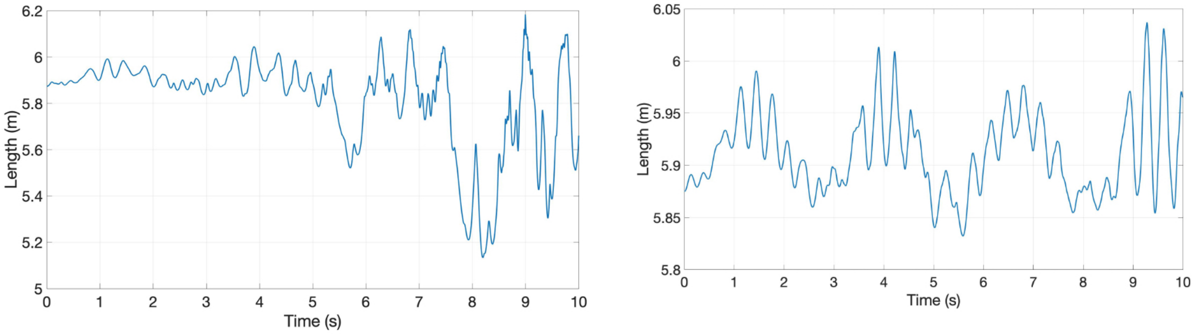

a)

b)

Figure 9.4: Elastic string length simulation results for a) linear shape function formulation with five elements and b) quadratic shape function formulation with five elements.

for the same setup. The string length results for the linear and quadratic simulations are shown in Fig. 9.4. The instability of the linear shape function formulation is clearly see as the stretch and contraction of the string increase with time. This counteracts what a real-world pendulum would do, as it would eventually slow down due to damping, with the string length settling at a steady state length. Interestingly, the simulation string length goes into a compression state, where the overall length is less that the initial 5.875 m, even for the quadratic shape function. In those regions, the force density was artificially set to 0, since no compression is allowed for a string. However, this violates the assumption for not using a bending formulation (tension above a 0.5 N threshold). The addition of bending, or drag to the tether model may alleviate some of these instabilities.

9.2 Experimental Validation

9.2.1 Test Setup

An indoor elastic string rigid body pendulum experiment was developed in order to validate the simulation model, and tune the parameters of the string. The experimental setup is shown in Fig. 9.5. An instrumented pivot is mounted to the ceiling of a 7 m

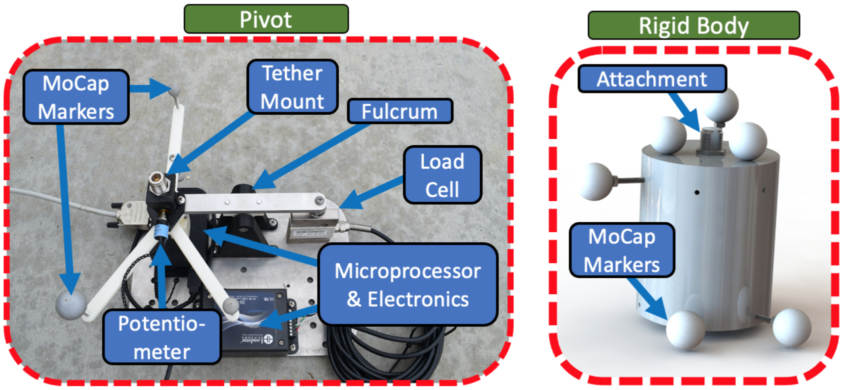

Figure 9.5: Experimental setup showing the pivot and rigid body. The pivot is mounted to the ceiling, and is capable of measuring tether tension and angle. The rigid body is a three dimensional printed object with motion tracking markers attached to it and an internal removable mass.

tall high bay. The pivot has a load cell and potentiometer angle sensor to measure the string reaction force, and the angle of departure. A 5.875 m long coaxial cable, specifically chosen for the tethered UAV-USV application, is mounted to the pivot. At the other end, a modular rigid body is mounted, with an internal, replaceable weight. Attached to the string, the pivot, and the rigid body are motion capture tracking markers. The rigid body is hoisted to an altitude of 6 m, approximately 10 degrees below horizontal, and dropped. The motion capture system accurately measures the position of the rigid body, pivot, and 38 string nodes. A total of nine different experiments were performed, three each with three different rigid body masses (0.443 kg, 0.669 kg, and 1.123 kg).

9.2.2 Results

A typical result for an experimental trial using the 0.443 kg mass rigid body is shown in Fig. 9.6. The experimental results are very similar to those of the simulation, implying that the parameters of the model are reasonable. However, as can be seen by the decreased apex of the upswing in comparison to the simulation, there is significantly more drag on the experimental setup than in the simulation. This can be attributed to

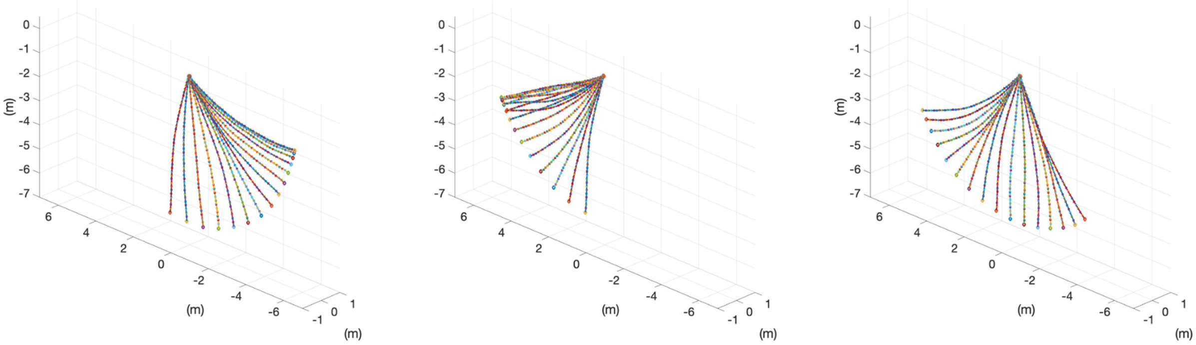

a)

b)

c)

Figure 9.6: Three dimensional pendulum experiment, showing snapshots every 0.1 seconds in the range of a) 0.0 to 1.5 seconds for the initial drop, b) 1.5 to 3.0 seconds for the upswing, and c) 3.0 to 4.5 seconds for the second drop back down.

friction in the pivot, as well as wind drag on the string. A reasonable addition to the simulation model would be to add the non-conservative forces due to drag on the string dependent on the velocity, $F_D = \frac{1}{2}\,\rho\, v^2\, C_D\, A$, where ρ is the density of air, v is the speed of the tether through air, A is the cross-sectional area of the string, and C_D is the drag coefficient [119, 120]. The similarity between the experiment and the simulation point to the simulation model accuracy being decent enough to leverage for further development.

9.3 Conclusion

The linear and quadratic shape function formulations of the three dimensional elastic string pendulum were simulated. The quadratic shape function clearly showed longer stability for the same number of elements, however, required twice as much computation time. A motion capture experiment validated the simulation parameters, but also demonstrated some significant un-modeled damping in the simulation. Adding in a non-conservative damping term can likely improve the simulation model to perfectly match the experiment. The key result here is that the simulation parameters for the UAV-USV team are reasonable.

9.4 Acknowledgments

Support for this work was provided by Naval Information Warfare Center Pacific under the Naval Innovative Science and Engineering program and the Department of Defense SMART Scholarship for Service program.

Chapter 9, in full is currently being prepared for submission for publication of the material. K. Talke, J. Friend, T. Bewley. The dissertation author was the primary investigator and author of these pages.

Chapter 10

Future Work

While the results presented in this dissertation are significant, a few improvements are in progress. Section 10.1 presents a new departure angle measurement prototype. Section 10.2 presents a non-GPS relative position measurement prototype UAV payload. Section 10.3 details future on water experimental validation. Section 10.4 details the extension of the dynamic model and numerical simulation to include an Arbitrary Lagrangian Eulerian formulation. Section 10.5 summarizes the key conclusions.

10.1 Departure Angle Measurement

As detailed in Section 6.1.3, the developed angle measurement approach has a significant deadband which also tends to color the measurement. While the dynamic behavior of the departure angle tends to dissuade its usage for feedback, a better angle measurement method and mechanical design may lead to some unknown benefits. As such, a follow on prototype design using a lasar scanner is shown in Fig. 10.1. Testing and evaluation of this approach will be performed in the near future.

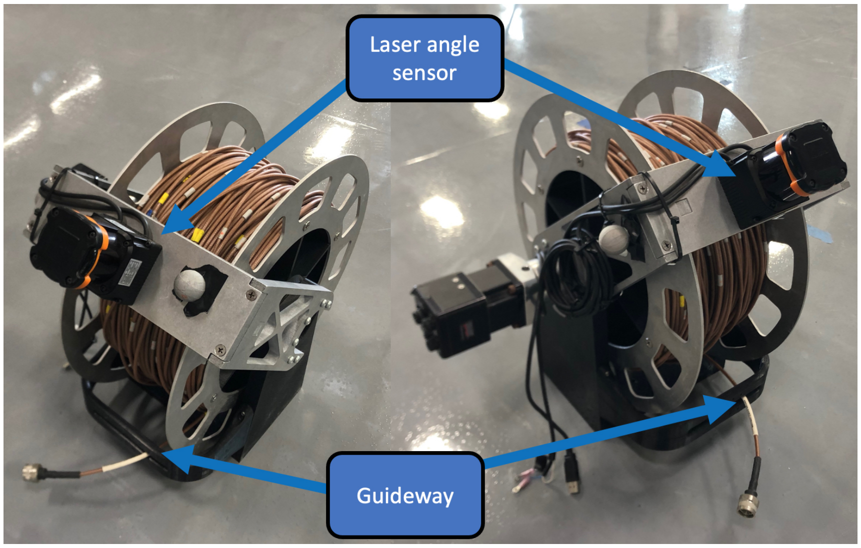

Figure 10.1: Smart reel prototype version 2, leveraging a laser scanner to measure the departure angle

10.2 Non-GPS relative position sensing

A common goal for military operations is to have the ability to function in a limited or restricted GPS environment. A custom optical relative positioning system (ORPS) UAV payload has been developed as shown in Fig. 10.2. A three axis gimbal points a camera and laser range finder at the USV. Using a 2D barcode and a reflective target on the deck of the USV, a range estimate can be found. Using the UAV pose, gimbal pose, and barometric altitude, the range can be converted to relative position, and passed into the control scheme described in Section 4.2.

10.3 On water experimental evaluation

On water experimentation are planned for the existing system, the new laser angle measurement system, and the optical relative position system are planned. The Naval Surface Warfare Center Carderock's MASK facility will be used for indoor motion capture experimentation, where controlled waves can be created up to 1.2 m heave, representative

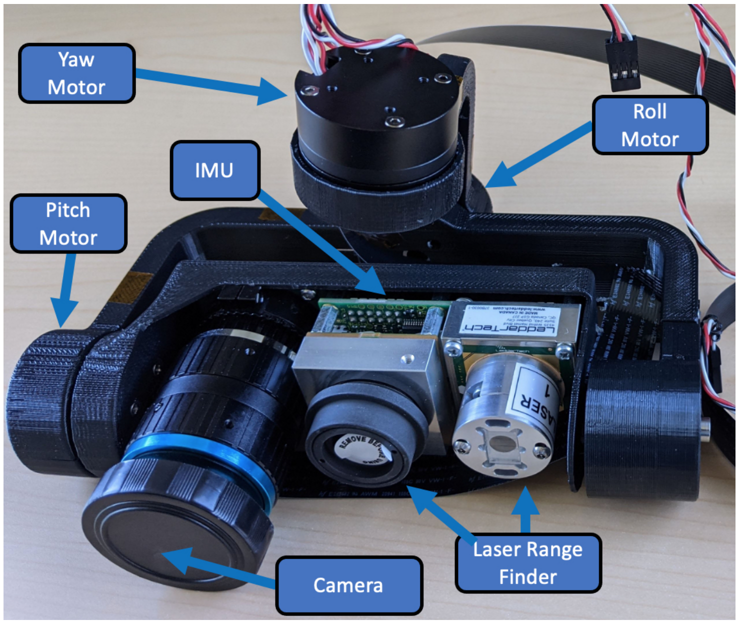

Figure 10.2: Optical relative positioning system gimbal payload. A camera and laser point are controlled to point at the USV, and determine an accurate range estimate

of Sea State 3. The experimental test setup is shown in Fig. 10.3. A small boat will be secured in the center of the wave tank, and the UAV surrogate will be mounted to the catwalk near the 20 m tall ceiling. Following, indoor testing with the UAV will also be

Figure 10.3: NSWC MASK facility test setup. The new protoype winch and ORPS payload will be evaluated in the near future in the controlled wave pool.

performed.

10.4 Simulation model

The greatest remaining challenge is how to accurately model the tether-winch interface boundary condition. Specifically, the changing tether length in relation to elements size, number, and mass due to the reel-in and payout behavior of the winch. Previous attempts have been made to model the interaction by adding a Carnot Energy loss term at the price of decreased accuracy [117]. Two other methods attempted to keep the boundary condition fixed while varying the nominal element length [88,108] or maintained the nominal element length and added or subtracted elements as the tether length changed [109]. These approaches lead to inaccuracies, numerical errors, or instability in the interpolation, and ultimately, the simulation model.

An adaptive fluid-structure interaction modeling method called Arbitrary Lagrangian-Eulerian (ALE) approaches a similar non-linear interface with a mixture of two methods [111,112]. Specifically, leveraging finite element and finite volume methods for a hybrid formulation, such that the grid points can be moved within the fluid. The mesh grid shown in Fig. 10.4 compares a standard Eulerian finite element formulation with an ALE formulation for a prosthetic aortic valve fluid-structure interface [112].

Applying the ALE method to the tether winch boundary would allow for the tether length and mass to change by relocating the nodes effected locally, without interpolating and creating numerical instabilities. Incorporating the ALE method to the winch/tether interface, well-developed accurately modeled UAV dynamics [121] and well-known wind interaction methods [122], the complete tethered UAV – USV team can be accurately modeled. Compared to typical numerical simulation research of challenging environments, the unique opportunity to validate any model developed will be possible due to the

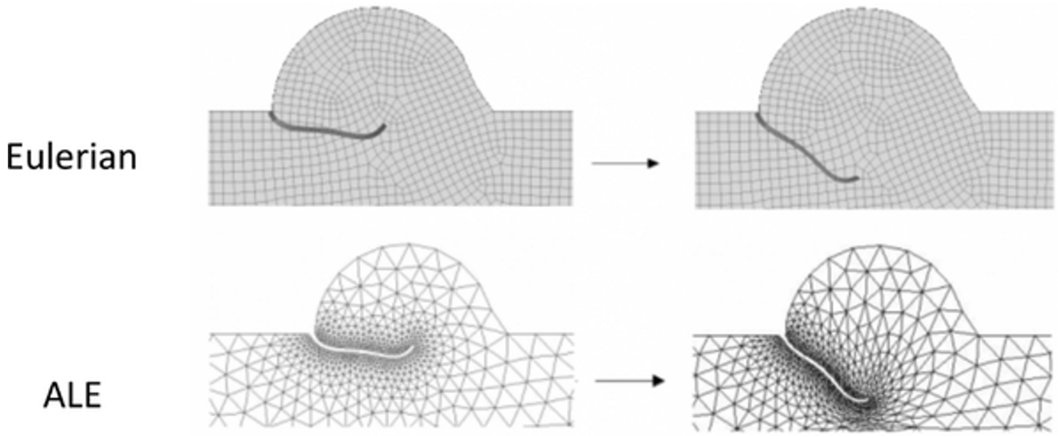

Figure 10.4: Example of a comparison of typical Eulerian meshing methods vs. Arbitrary Lagrangian Eulerian methods for a prosthetic aortic valve [111].

experimental environment already developed. Following the development and validation of the complete UAV-USV team simulation environment, new tether management controllers can be developed leveraging more complex control techniques. An especially interesting approach is to use an H-∞ state space control methodology [123]. The approach sets hard limits by exponentially increasing the control cost to infinity as the state of the system gets near those limits. The obvious limits in this case would be an easily measured tether departure angle that dips too low and could foul with the USV, and an acceptable tension level, also easily measured.

10.5 Conclusion

The work presented in this dissertation is by no means complete, and many continued efforts exist in different directions to continue the progress and work. A new mechanical prototype has been developed for testing a laser departure angle measurement approach. A UAV camera-laser gimbal payload has been developed to provide non-GPS relative position measurements. Continued experimentation at the indoor wave pool facility will take the next steps in validation. Finally, the simulation models will continue to be improved by implementing the winch dynamics, specifically focusing on an ALE approach for simulating the tether length change.

10.6 Acknowledgments

Support for this work was provided by Naval Information Warfare Center Pacific under the Naval Innovative Science and Engineering program and the Department of Defense SMART Scholarship for Service program.

Chapter 11

Conclusion

This dissertation considered the mission of an UAV tethered to a small USV. The tether doubles as a power umbilical and communications link, providing unlimited flight duration and secure data transfer while limiting mobility. Contrary to the majority of existing tethered UAV work which assumes a taut tether for dynamic stability, this dissertation addressed the challenge of tether management for a slack, hanging tether in a dynamic ocean environment up to sea state 4 on the Douglas scale.

For controlled laboratory experimentation, a testing platform capable of replicating wave and boat motion was developed for land-based testing, reducing costs and the design iteration cycle time. The alternative, of relying on weather conditions to test in specific sea states is too costly, time limiting, and dangerous. Chapter 2, presented the design of a novel, low-cost, 3-$\underline{P}$SR parallel mechanism capable of replicating the full scale range of boat motion up to sea state 4: up to 2.2 m heave, 32° roll, and 35° pitch. A design parameter optimization was presented to maximize the roll-pitch workspace. A three-axis interpolation approach was presented to accurately generate a desired path through the roll-pitch workspace. The 3-$\underline{P}$SR parallel mechanism was fabricated and experimentally validated using an IMU. The mechanism was extensively used during experimental testing, and has proven to be a valuable resource.

For semi-slack hanging tether control, a reference model is necessary. Chapter 3 analyzed the static catenary hanging cable problem and developed a model-based approach for tether management driven by relative position and tether length. A recommended relative flying position was presented considering robustness to vertical motion of the USV. An approximate model was presented in the form of a low order polynomial. This provides a computationally inexpensive approach for determining a reference tether length, angle, or tension. The proposed model allows for a large range of flying positions while decreasing tether tension at the UAV, ultimately lowering overall power consumption, increasing flight altitude, payload capacity, and decreasing safety margin requirements.

Chapter 4 developed a tether management prototype design, relative position estimator, and control system for autonomous tether management. The prototype is capable of measuring tether length, departure angle, and tension. With the goal of outdoor operation, a Kalman filter model is developed to fuse a slow, 4 Hertz RTK dGPS relative position measurement with fast, 100 Hertz inertial measurements, to output a fast, 100 Hertz estimate of the relative position, relative velocity, and inertial sensor bias. A relative velocity-based gain scheduled controller was developed to smooth out any errors and discontinuities seen in the Kalman filter output at low relative velocities.

Chapter 5 described the phased testing procedure. The experimental approach was split into three stages: UAV surrogate, indoor flight, and outdoor flight testing in order to first validate the controller and mechanical prototype, tune and validate the estimation filter, and then evaluate the RTK dGPS solution.

Chapter 6 presented the results from experimental testing. The system was experimentally validated through indoor motion capture experimentation and outdoor RTK dGPS experimentation. Indoor experimentation, using a UAV surrogate for a perfectly known, controlled environment, demonstrated the developed estimator and controller greatly reduce tether tension and forces on the UAV compared to taut tether control. Indoor flight testing successfully showed decoupling of USV heave motion from UAV altitude and position, while also demonstrating a similar UAV altitude and position range compared to un-tethered flight. Finally, outdoor flight testing using a dGPS and an IMU-based Kalman filter solution to measure relative position showed the feasibility in an unknown dynamic environment. A hanging tether management system can extend longevity, decrease power consumption, extend mission duration, increase flight altitude, and decrease the required thrust safety margins of the UAV.

Chapter 7 presented a complete derivation of the equations of motion for an elastic string rigid body pendulum, fixed reel elastic string rigid body pendulum, and moving reel elastic string rigid body pendulum. Leveraging Hamilton's principle of least action for the continuous string, extensive use of IBP, Leibniz's rule, Green's theorem, and the line integral, the proper determination of the variation of the associated Lagrangian was presented. Extending the Hamilton's principle to include the variation of non-conservative virtual work enabled the addition of external forces such as the applied moment on the winch. Finally, the equations of motion were determined.

In Chapter 8, the continuous body PDE was discretized via the Galerkin finite element method, developing a formulation for one dimensional linear, and quadratic shape functions. While the linear shape function formulation can be solved analytically, the quadratic shape function formulation required Gaussian quadrature. The c^0 and c^1 boundary conditions were applied via model reduction, and Lagrange multipliers, respectively. The first order ODE matrix equations were developed in order to simulate the system using the Runge-Kutta time marching scheme.

Chapter 9 discussed the simulation results, and compared them to experimental three dimensional pendulum motion capture experiments performed to validate the developed numerical model. The quadratic shape function formulation retains stability, where the linear shape function formulation introduces numerical instabilities. The quadratic shape function simulation formulations show similarities with the real world experiments, but also leaves some room for improvement, specifically requiring the introduction of damping.

Chapter 10 described the extensions of this dissertation. An updated mechanical winch prototype was presented. An optical relative position sensing gimbal payload for the UAV is being developed. On-water experimentation was discussed, and the upcoming simulation approach leveraging ALE was presented. The continuation of this dissertation looks promising.

In summary, the primary contributions of this dissertation include:

1. A novel 3-$\underline{\text{P}}$SR mechanism capable of replicating the pitch, roll, and heave motion of a boat in sea state 4 (see Chapter 2),
2. A catenary hanging cable theory-based model to determine a reference tether length, angle, or tension for maximum heave robustness (see Chapter 3),
3. A relative velocity-based gain scheduled tether management controller (see Chapter 4.2),
4. A Kalman filter model to estimate relative altitude, fusing a slow, relative altitude differential GPS measurement with fast inertial measurements (see Chapter 4.4),
5. The experimental validation of the heave robustness model, filter and controller (see Chapter 6),
6. The derivation of the partial differential equations of motion of a continuous three dimensional elastic string pendulum and UAV-USV team (see Chapter 7), and
7. The development and experimental validation of a quadratic shape function simulation model (see Chapter 8 and Chapter 9).

Appendix A

Math Proofs and Theorems

In this appendix, pertinent mathematical relationships and their proofs will be presented.

A.1 Cross Product, Skew Symmetric Matrix Identities

Define the hatmap ($\hat{\mathbf{x}}$) as a skew symmetric matrix mapping of the cross product for any vector $\mathbf{x} \in \mathbb{R}^3$ as [93, 94]:

$$\begin{aligned} \hat{\mathbf{x}} &= \begin{bmatrix} 0 & -x_3 & x_2 \\ x_3 & 0 & -x_1 \\ -x_2 & x_1 & 0 \end{bmatrix} \\ \mathbf{x} \times \mathbf{y} &= \hat{\mathbf{x}}\mathbf{y} \\ \hat{\mathbf{x}}^T &= -\hat{\mathbf{x}}. \end{aligned} \tag{A.1}$$

Proof:

$$\begin{aligned}
\mathbf{x} \times \mathbf{y} &= \begin{bmatrix} x_2 y_3 - y_2 x_3 \\ x_3 y_1 - y_3 x_1 \\ x_1 y_2 - y_1 x_2 \end{bmatrix} \\
&= \begin{bmatrix} 0 & -x_3 & x_2 \\ x_3 & 0 & -x_1 \\ -x_2 & x_1 & 0 \end{bmatrix} \begin{bmatrix} y_1 \\ y_2 \\ y_3 \end{bmatrix} \\
&= \hat{\mathbf{x}}\mathbf{y}
\end{aligned}$$

The cross product anti-commutative relationship can be expressed as:

$$\begin{gathered}
\mathbf{a} \times \mathbf{b} = -\mathbf{b} \times \mathbf{a} \\
\hat{\mathbf{a}}\mathbf{b} = -\hat{\mathbf{b}}\mathbf{a}.
\end{gathered} \tag{A.2}$$

The mixed product identity can be expressed as:

$$\mathbf{y} \cdot \hat{\mathbf{x}}\mathbf{z} = \hat{\mathbf{z}}\mathbf{y} \cdot \mathbf{x}. \tag{A.3}$$

Proof:

$$
\begin{aligned}
\mathbf{y}\cdot\hat{\mathbf{x}}\mathbf{z} &= \begin{bmatrix} y_1 \\ y_2 \\ y_3 \end{bmatrix} \cdot \begin{bmatrix} 0 & -x_3 & x_2 \\ x_3 & 0 & -x_1 \\ -x_2 & x_1 & 0 \end{bmatrix} \begin{bmatrix} z_1 \\ z_2 \\ z_3 \end{bmatrix} \\
&= \begin{bmatrix} y_1 \\ y_2 \\ y_3 \end{bmatrix} \cdot \begin{bmatrix} x_2z_3 - x_3z_2 \\ x_3z_1 - x_1z_3 \\ x_1z_2 - x_2z_1 \end{bmatrix} \\
&= (x_2y_1z_3 - x_3y_1z_2) + (x_3y_2z_1 - x_1y_2z_3) + (x_1y_3z_2 - x_2y_3z_1) \\
&= \begin{bmatrix} y_3z_2 - y_2z_3 \\ y_1z_3 - y_3z_1 \\ y_2z_1 - y_1z_2 \end{bmatrix} \cdot \begin{bmatrix} x_1 \\ x_2 \\ x_3 \end{bmatrix} \\
&= \begin{bmatrix} 0 & -z_3 & z_2 \\ z_3 & 0 & -z_1 \\ -z_2 & z_1 & 0 \end{bmatrix} \begin{bmatrix} y_1 \\ y_2 \\ y_3 \end{bmatrix} \cdot \begin{bmatrix} x_1 \\ x_2 \\ x_3 \end{bmatrix} \\
\mathbf{y}\cdot\hat{\mathbf{x}}\mathbf{z} &= \hat{\mathbf{z}}\mathbf{y}\cdot\mathbf{x}
\end{aligned}
$$

The hat map of a cross product can be expressed as:

$$\hat{\mathbf{x}}\hat{\mathbf{y}} - \hat{\mathbf{y}}\hat{\mathbf{x}} = (\mathbf{x}\times\mathbf{y})^{\wedge}. \tag{A.4}$$

Proof:

$$
\begin{aligned}
\hat{\mathbf{x}}\hat{\mathbf{y}} - \hat{\mathbf{y}}\hat{\mathbf{x}} &= \begin{bmatrix} 0 & -x_3 & x_2 \\ x_3 & 0 & -x_1 \\ -x_2 & x_1 & 0 \end{bmatrix} \begin{bmatrix} 0 & -y_3 & y_2 \\ y_3 & 0 & -y_1 \\ -y_2 & y_1 & 0 \end{bmatrix} - \begin{bmatrix} 0 & -y_3 & y_2 \\ y_3 & 0 & -y_1 \\ -y_2 & y_1 & 0 \end{bmatrix} \begin{bmatrix} 0 & -x_3 & x_2 \\ x_3 & 0 & -x_1 \\ -x_2 & x_1 & 0 \end{bmatrix} \\
&= \begin{bmatrix} -x_2y_2 - x_3y_3 & x_2y_1 & x_3y_1 \\ x_1y_2 & -x_1y_1 - x_3y_3 & x_3y_2 \\ x_1y_3 & x_2y_3 & -x_1y_1 - x_2y_2 \end{bmatrix} \\
&\qquad - \begin{bmatrix} -x_2y_2 - x_3y_3 & x_1y_2 & x_1y_3 \\ x_2y_1 & -x_1y_1 - x_3y_3 & x_2y_3 \\ x_3y_1 & x_3y_2 & -x_1y_1 - x_2y_2 \end{bmatrix} \\
&= \begin{bmatrix} 0 & x_2y_1 - x_1y_2 & x_3y_1 - x_1y_3 \\ x_1y_2 - x_2y_1 & 0 & x_3y_2 - x_2y_3 \\ x_1y_3 - x_3y_1 & x_2y_3 - x_3y_2 & 0 \end{bmatrix} \\
&= \begin{bmatrix} x_2y_3 - x_3y_2 \\ x_3y_1 - x_1y_3 \\ x_1y_2 - x_2y_1 \end{bmatrix}^{\wedge}
\end{aligned}
$$

$$\hat{\mathbf{x}}\hat{\mathbf{y}} - \hat{\mathbf{y}}\hat{\mathbf{x}} = (\mathbf{x} \times \mathbf{y})^{\wedge}$$

A.2 Rotation Matrix Kinematic Relationship

The derivative of a rotation matrix $\mathbf{R}$ is defined as:

$$\dot{\mathbf{R}} = \mathbf{R}\hat{\boldsymbol{\Omega}}. \tag{A.5}$$

Proof:

The rotation matrix $\mathbf{R}$, is in the special orthogonal group ($\mathbf{R} \in SO(3)$), such that:

$$\mathbf{R}\mathbf{R}^T = \mathbf{R}^T\mathbf{R} = \mathbf{I}.$$

Taking the time derivative and rearranging yields:

$$\begin{aligned} \dot{\mathbf{R}}^T\mathbf{R} + \mathbf{R}^T\dot{\mathbf{R}} &= 0 \\ -\dot{\mathbf{R}}^T\mathbf{R} &= \mathbf{R}^T\dot{\mathbf{R}}, \end{aligned}$$

which implies that $-\dot{\mathbf{R}}^T\mathbf{R}$ is a skew symmetric matrix. In this case, the skew symmetric matrix is of the angular rates [93]:

$$\hat{\mathbf{\Omega}} = \mathbf{R}^T\dot{\mathbf{R}}. \tag{A.6}$$

Solving for $\dot{\mathbf{R}}$ yields:

$$\dot{\mathbf{R}} = \mathbf{R}\hat{\mathbf{\Omega}}.$$

A.3 Rotation Vector Kinematic Relationship

Define $\mathbf{R}$ as three row vectors, or $\mathbf{R}^T$ as three column vectors:

$$\mathbf{R} = \begin{bmatrix} \tilde{\mathbf{r}}_1^T \\ \tilde{\mathbf{r}}_2^T \\ \tilde{\mathbf{r}}_3^T \end{bmatrix}, \qquad \mathbf{R}^T = \begin{bmatrix} \tilde{\mathbf{r}}_1 & \tilde{\mathbf{r}}_2 & \tilde{\mathbf{r}}_3 \end{bmatrix}. \tag{A.7}$$

The matrix kinematic relationship from Eq. A.5 becomes:

$$\dot{\tilde{\mathbf{r}}}_i = \hat{\tilde{\mathbf{r}}}_i \boldsymbol{\Omega} = -\hat{\boldsymbol{\Omega}} \tilde{\mathbf{r}}_i \qquad i = 1, 2, 3 \tag{A.8}$$

Proof:

Starting with Eq. A.5, multiplying out, transposing, and simplifying using the definition of a cross product yields:

$$
\begin{aligned}
\dot{\mathbf{R}} &= \mathbf{R}\hat{\boldsymbol{\Omega}} \\
\begin{bmatrix} \dot{\tilde{\mathbf{r}}}_1^T \\ \dot{\tilde{\mathbf{r}}}_2^T \\ \dot{\tilde{\mathbf{r}}}_3^T \end{bmatrix} &= \begin{bmatrix} \tilde{\mathbf{r}}_1^T \\ \tilde{\mathbf{r}}_2^T \\ \tilde{\mathbf{r}}_3^T \end{bmatrix} \begin{bmatrix} 0 & -\omega_3 & \omega_2 \\ \omega_3 & 0 & -\omega_1 \\ -\omega_2 & \omega_1 & 0 \end{bmatrix} \\
&= \begin{bmatrix} r_{11} & r_{12} & r_{13} \\ r_{21} & r_{22} & r_{23} \\ r_{31} & r_{32} & r_{33} \end{bmatrix} \begin{bmatrix} 0 & -\omega_3 & \omega_2 \\ \omega_3 & 0 & -\omega_1 \\ -\omega_2 & \omega_1 & 0 \end{bmatrix} \\
&= \begin{bmatrix} \omega_3 r_{12} - \omega_2 r_{13} & \omega_1 r_{13} - \omega_3 r_{11} & \omega_2 r_{11} - \omega_1 r_{12} \\ \omega_3 r_{22} - \omega_2 r_{23} & \omega_1 r_{23} - \omega_3 r_{21} & \omega_2 r_{21} - \omega_1 r_{22} \\ \omega_3 r_{32} - \omega_2 r_{33} & \omega_1 r_{33} - \omega_3 r_{31} & \omega_2 r_{31} - \omega_1 r_{32} \end{bmatrix} \\
\begin{bmatrix} \dot{\tilde{\mathbf{r}}}_1^T \\ \dot{\tilde{\mathbf{r}}}_2^T \\ \dot{\tilde{\mathbf{r}}}_3^T \end{bmatrix}^T &= \begin{bmatrix} \omega_3 r_{12} - \omega_2 r_{13} & \omega_1 r_{13} - \omega_3 r_{11} & \omega_2 r_{11} - \omega_1 r_{12} \\ \omega_3 r_{22} - \omega_2 r_{23} & \omega_1 r_{23} - \omega_3 r_{21} & \omega_2 r_{21} - \omega_1 r_{22} \\ \omega_3 r_{32} - \omega_2 r_{33} & \omega_1 r_{33} - \omega_3 r_{31} & \omega_2 r_{31} - \omega_1 r_{32} \end{bmatrix}^T \\
\begin{bmatrix} \dot{\tilde{\mathbf{r}}}_1 & \dot{\tilde{\mathbf{r}}}_2 & \dot{\tilde{\mathbf{r}}}_3 \end{bmatrix} &= \begin{bmatrix} \omega_3 r_{12} - \omega_2 r_{13} & \omega_3 r_{22} - \omega_2 r_{23} & \omega_3 r_{32} - \omega_2 r_{33} \\ \omega_1 r_{13} - \omega_3 r_{11} & \omega_1 r_{23} - \omega_3 r_{21} & \omega_1 r_{33} - \omega_3 r_{31} \\ \omega_2 r_{11} - \omega_1 r_{12} & \omega_2 r_{21} - \omega_1 r_{22} & \omega_2 r_{31} - \omega_1 r_{32} \end{bmatrix} \\
&= \begin{bmatrix} \tilde{\mathbf{r}}_1 \times \boldsymbol{\Omega} & \tilde{\mathbf{r}}_2 \times \boldsymbol{\Omega} & \tilde{\mathbf{r}}_3 \times \boldsymbol{\Omega} \end{bmatrix} \\
&= \begin{bmatrix} \hat{\tilde{\mathbf{r}}}_1 \boldsymbol{\Omega} & \hat{\tilde{\mathbf{r}}}_2 \boldsymbol{\Omega} & \hat{\tilde{\mathbf{r}}}_3 \boldsymbol{\Omega} \end{bmatrix} \\
\Rightarrow \dot{\tilde{\mathbf{r}}}_i &= \hat{\tilde{\mathbf{r}}}_i \boldsymbol{\Omega}, \qquad i = 1, 2, 3.
\end{aligned}
$$

A.4 Variation of Rotation Matrix

The variation of a rotation matrix can be expressed as:

$$\delta\mathbf{R} = \mathbf{R}\hat{\boldsymbol{\eta}} \tag{A.9}$$

where $\hat{\boldsymbol{\eta}} \in SO(3)$, or $\boldsymbol{\eta} \in \mathbb{R}^3$ denotes a variation of skew symmetric matrices that vanishes at t_o, and t_f.

Proof:

The variation of the Rotation matrix is defined as:

$$\delta\mathbf{R} = \left.\frac{d}{d\epsilon}\right|_{\epsilon=0} (\mathbf{R}^{\epsilon})$$

where the variation form of a rotation matrix ($SO(3)$) can be expressed using the matrix exponential [93]:

$$\mathbf{R}^{\epsilon} = \mathbf{R}e^{\epsilon\hat{\boldsymbol{\eta}}} \tag{A.10}$$

where $\epsilon \in \mathbb{R}$. $\hat{\boldsymbol{\eta}}$ is of the form of a skew symmetric matrix, but the vector $\boldsymbol{\eta}$ can be thought of as a typical variation $\delta\mathbf{q}_i$. Taking the variation of the rotation matrix:

$$\begin{aligned}
\delta\mathbf{R} &= \left.\frac{d}{d\epsilon}\right|_{\epsilon=0} (\mathbf{R}^{\epsilon}) \\
&= \left.\frac{d}{d\epsilon}\right|_{\epsilon=0} \left(\mathbf{R}e^{\epsilon\hat{\boldsymbol{\eta}}}\right) \\
&= \left.\mathbf{R}e^{\epsilon\hat{\boldsymbol{\eta}}}\hat{\boldsymbol{\eta}}\right|_{\epsilon=0} \\
&= \mathbf{R}\hat{\boldsymbol{\eta}}
\end{aligned}$$

Splitting the rotation matrix into row vectors as with the derivation of the rotation vector kinematic relationship, Eq. A.8 yields:

$$\delta\tilde{\mathbf{r}}_i = \hat{\tilde{\mathbf{r}}}_i\boldsymbol{\eta}, \qquad i = 1, 2, 3 \tag{A.11}$$

A.5 Variation of R Matrix with Pre- and Post-multiplied Vectors

$$\int_{t_o}^{t_f} \mathbf{x} \cdot \delta\mathbf{R}\mathbf{y}dt = \int_{t_o}^{t_f} \mathbf{x}^T\delta\mathbf{R}\mathbf{y}dt = \int_{t_o}^{t_f} \hat{\mathbf{y}}\mathbf{R}^T\mathbf{x} \cdot \boldsymbol{\eta}dt \tag{A.12}$$

Proof:

The variation of $\mathbf{R}$ is actually the variation of three vectors as in Eq. A.7:

$$\begin{aligned}
\int_{t_o}^{t_f} \mathbf{x} \cdot \delta\mathbf{R}\mathbf{y}dt &= \int_{t_o}^{t_f} \mathbf{x}^T\delta\left(\begin{bmatrix} \tilde{\mathbf{r}}_1^T \\ \tilde{\mathbf{r}}_2^T \\ \tilde{\mathbf{r}}_3^T \end{bmatrix}\right)\mathbf{y}dt \\
&= \int_{t_o}^{t_f} \left(x_1\delta\tilde{\mathbf{r}}_1^T\mathbf{y} + x_2\delta\tilde{\mathbf{r}}_2^T\mathbf{y} + x_3\delta\tilde{\mathbf{r}}_3^T\mathbf{y}\right)dt \\
&= \int_{t_o}^{t_f} \sum_{i=1}^{3} x_i\delta\tilde{\mathbf{r}}_i^T\mathbf{y}dt \\
&= \int_{t_o}^{t_f} \sum_{i=1}^{3} x_i\mathbf{y}^T\delta\tilde{\mathbf{r}}_i dt \\
&= \int_{t_o}^{t_f} \sum_{i=1}^{3} x_i\mathbf{y} \cdot \delta\tilde{\mathbf{r}}_i dt
\end{aligned}$$

where x_i is the scalar quantity i'th term of the $\mathbf{x}$ vector , and dot product notation is used. $\delta\tilde{\mathbf{r}}_i^T\mathbf{y}$ can be transposed because the result is a scalar ($\mathbf{a}^T\mathbf{b} = \mathbf{b}^T\mathbf{a}$). Inserting the vector variation of the rotation matrix definition from Eq. A.11 ($\delta\tilde{\mathbf{r}}_i = \hat{\tilde{\mathbf{r}}}_i\boldsymbol{\eta}$) yields:

$$\begin{aligned}
\int_{t_o}^{t_f} \mathbf{x}\cdot\delta\mathbf{R}\mathbf{y}dt &= \int_{t_o}^{t_f} \sum_{i=1}^{3} x_i\mathbf{y}\cdot\hat{\tilde{\mathbf{r}}}_i\boldsymbol{\eta}dt \\
&= \int_{t_o}^{t_f} -\sum_{i=1}^{3} x_i\mathbf{y}\cdot\hat{\boldsymbol{\eta}}\tilde{\mathbf{r}}_i dt \\
&= \int_{t_o}^{t_f} -\sum_{i=1}^{3} x_i\hat{\tilde{\mathbf{r}}}_i\mathbf{y}\cdot\boldsymbol{\eta}dt \\
&= \int_{t_o}^{t_f} \sum_{i=1}^{3} x_i\hat{\mathbf{y}}\tilde{\mathbf{r}}_i\cdot\boldsymbol{\eta}dt
\end{aligned}$$

Where the hatmap identity from Eq. A.2 ($\hat{\mathbf{a}}\mathbf{b} = -\hat{\mathbf{b}}\mathbf{a}$) was used in the first and third step, and the skew dot product identity from Eq. A.3 ($\mathbf{y}\cdot\hat{\mathbf{x}}\mathbf{z} = \hat{\mathbf{z}}\mathbf{y}\cdot\mathbf{x}$) was used in the second step. Expanding out the sum and simplifying yields:

$$\begin{aligned}
\int_{t_o}^{t_f} \mathbf{x}\cdot\delta\mathbf{R}\mathbf{y}dt &= \int_{t_o}^{t_f} (x_1\hat{\mathbf{y}}\tilde{\mathbf{r}}_1 + x_2\hat{\mathbf{y}}\tilde{\mathbf{r}}_2 + x_3\hat{\mathbf{y}}\tilde{\mathbf{r}}_3)\cdot\boldsymbol{\eta}dt \\
&= \int_{t_o}^{t_f} \begin{bmatrix} \hat{\mathbf{y}}\tilde{\mathbf{r}}_1 & \hat{\mathbf{y}}\tilde{\mathbf{r}}_2 & \hat{\mathbf{y}}\tilde{\mathbf{r}}_3 \end{bmatrix}\mathbf{x}\cdot\boldsymbol{\eta}dt \\
&= \int_{t_o}^{t_f} \hat{\mathbf{y}}\begin{bmatrix} \tilde{\mathbf{r}}_1 & \tilde{\mathbf{r}}_2 & \tilde{\mathbf{r}}_3 \end{bmatrix}\mathbf{x}\cdot\boldsymbol{\eta}dt \\
\int_{t_o}^{t_f} \mathbf{x}^T\delta\mathbf{R}\mathbf{y}dt &= \int_{t_o}^{t_f} \hat{\mathbf{y}}\mathbf{R}^T\mathbf{x}\cdot\boldsymbol{\eta}dt.
\end{aligned}$$

A.6 Variation of Angular Velocity

The variation of the angular velocity vector can be expressed as:

$$\begin{aligned}
\delta\boldsymbol{\Omega} &= \dot{\boldsymbol{\eta}} + \boldsymbol{\Omega}\times\boldsymbol{\eta} \\
\delta\boldsymbol{\Omega} &= \dot{\boldsymbol{\eta}} + \hat{\Omega}\boldsymbol{\eta}.
\end{aligned} \tag{A.13}$$

Proof:

Much like the variation of a rotation matrix, the variation of the skew symmetric mapping of the angular velocity is defined as [93]:

$$\delta \hat{\boldsymbol{\Omega}} = \left.\frac{d}{d\epsilon}\right|_{\epsilon=0} \left(\hat{\boldsymbol{\Omega}}^{\epsilon}\right).$$

$\hat{\boldsymbol{\Omega}}^{\epsilon}$ can be defined using the rotation matrix kinematic relationship from Eq. A.5:

$$\begin{aligned}
\hat{\boldsymbol{\Omega}}^{\epsilon} &= \mathbf{R}^{\epsilon T}\dot{\mathbf{R}}^{\epsilon} \\
&= \left(e^{-\epsilon\hat{\boldsymbol{\eta}}}\mathbf{R}^{T}\right)\left(\dot{\mathbf{R}}e^{\epsilon\hat{\boldsymbol{\eta}}} + \epsilon\mathbf{R}e^{\epsilon\hat{\boldsymbol{\eta}}}\dot{\hat{\boldsymbol{\eta}}}\right) \\
&= e^{-\epsilon\hat{\boldsymbol{\eta}}}\mathbf{R}^{T}\dot{\mathbf{R}}e^{\epsilon\hat{\boldsymbol{\eta}}} + \epsilon e^{-\epsilon\hat{\boldsymbol{\eta}}}\mathbf{R}^{T}\mathbf{R}e^{\epsilon\hat{\boldsymbol{\eta}}}\dot{\hat{\boldsymbol{\eta}}} \\
&= e^{-\epsilon\hat{\boldsymbol{\eta}}}\hat{\boldsymbol{\Omega}}e^{\epsilon\hat{\boldsymbol{\eta}}} + \epsilon e^{-\epsilon\hat{\boldsymbol{\eta}}}e^{\epsilon\hat{\boldsymbol{\eta}}}\dot{\hat{\boldsymbol{\eta}}} \\
&= e^{-\epsilon\hat{\boldsymbol{\eta}}}\hat{\boldsymbol{\Omega}}e^{\epsilon\hat{\boldsymbol{\eta}}} + \epsilon\dot{\hat{\boldsymbol{\eta}}}
\end{aligned}$$

where, in the first step, $\mathbf{R}^{\epsilon T}$ and $\dot{\mathbf{R}}^{\epsilon}$ come from transposing and taking the time derivative using the chain rule of the matrix exponential in Eq. A.10, respectively ($\mathbf{R}^{\epsilon T} = e^{-\epsilon\hat{\boldsymbol{\eta}}}\mathbf{R}^{T}$ and $\dot{\mathbf{R}}^{\epsilon} = \dot{\mathbf{R}}e^{\epsilon\hat{\boldsymbol{\eta}}} + \epsilon\mathbf{R}e^{\epsilon\hat{\boldsymbol{\eta}}}\dot{\hat{\boldsymbol{\eta}}}$). In the third step, $\hat{\boldsymbol{\Omega}}$ is substituted for $\mathbf{R}^{T}\dot{\mathbf{R}}$ using Eq. A.6 ($\hat{\boldsymbol{\Omega}} = \mathbf{R}^{T}\dot{\mathbf{R}}$), and $\mathbf{R} \in SO3$ such that $\mathbf{R}^{T}\mathbf{R} = \mathbf{I}$. In the final step, the matrix exponential simplifies as $e^{-\mathbf{X}}e^{\mathbf{X}} = e^{-\mathbf{X}+\mathbf{X}} = e^{\mathbf{0}} = \mathbf{I}$. Applying the Taylor expansion of the matrix exponential ($e^{-\epsilon\hat{\boldsymbol{\eta}}} = \mathbf{I}_{3x3} - \epsilon\hat{\boldsymbol{\eta}} + \mathcal{O}\left(\epsilon^{2}\right)$) yields:

$$\begin{aligned}
\hat{\boldsymbol{\Omega}}^{\epsilon} &= \left(\mathbf{I}_{3x3} - \epsilon\hat{\boldsymbol{\eta}} + \mathcal{O}\left(\epsilon^{2}\right)\right)\hat{\boldsymbol{\Omega}}\left(\mathbf{I}_{3x3} + \epsilon\hat{\boldsymbol{\eta}} + \mathcal{O}\left(\epsilon^{2}\right)\right) + \epsilon\dot{\hat{\boldsymbol{\eta}}} \\
\hat{\boldsymbol{\Omega}}^{\epsilon} &= \hat{\boldsymbol{\Omega}} + \epsilon\left(\dot{\hat{\boldsymbol{\eta}}} + \hat{\boldsymbol{\Omega}}\hat{\boldsymbol{\eta}} - \hat{\boldsymbol{\eta}}\hat{\boldsymbol{\Omega}}\right) + \mathcal{O}\left(\epsilon^{2}\right)
\end{aligned}$$

Disregarding terms $\mathcal{O}\left(\epsilon^2\right)$ and higher, taking the variation, and using the skew symmetric matrix identity from Eq. A.4 $\left(\hat{\mathbf{x}}\hat{\mathbf{y}} - \hat{\mathbf{y}}\hat{\mathbf{x}} = (\mathbf{x} \times \mathbf{y})^{\wedge}\right)$ results in:

$$\begin{aligned}
\delta\hat{\boldsymbol{\Omega}} &= \left.\frac{d}{d\epsilon}\right|_{\epsilon=0} \left(\hat{\boldsymbol{\Omega}}^{\epsilon}\right) \\
&= \hat{\dot{\boldsymbol{\eta}}} + \hat{\boldsymbol{\Omega}}\hat{\boldsymbol{\eta}} - \hat{\boldsymbol{\eta}}\hat{\boldsymbol{\Omega}} \\
&= \hat{\dot{\boldsymbol{\eta}}} + (\boldsymbol{\Omega} \times \boldsymbol{\eta})^{\wedge}.
\end{aligned}$$

Converting the skew symmetric matrices back into vectors again using the inverse of Eq. A.1 (called a vee map [93]) yields:

$$\begin{aligned}
\delta\boldsymbol{\Omega} &= \dot{\boldsymbol{\eta}} + \boldsymbol{\Omega} \times \boldsymbol{\eta} \\
\delta\boldsymbol{\Omega} &= \dot{\boldsymbol{\eta}} + \hat{\boldsymbol{\Omega}}\boldsymbol{\eta}.
\end{aligned}$$

A.7 Calculus Theorems

The following calculus tools are needed for the derivation of the dynamics with a reel:

- Leibniz rule is used for taking the derivative of an integral when one or more of the limits of the integral are functions of the derivative variable [124–127]:

$$\begin{aligned}\frac{d}{dx}\left(\int_{a(x)}^{b(x)} f\left(x,t\right)dt\right) &= f\left(x,b\left(x\right)\right)\cdot\frac{d}{dx}b\left(x\right) - f\left(x,a\left(x\right)\right)\cdot\frac{d}{dx}a\left(x\right)\\ &+\int_{a(x)}^{b(x)}\frac{\partial}{\partial x}f\left(x,t\right)dt\end{aligned}\tag{A.14}$$

- Green's Theorem states that double integral over a body is equal to the line integral around the border [125–127], as seen in Fig. A.1:

$$\oint_C\left(Ldx+Mdy\right)=\iint_D\left(\frac{\partial M}{\partial x}-\frac{\partial L}{\partial y}\right)dxdy\tag{A.15}$$

- Line Integral is defined as, parameterized over $[a,b]$ [125–127]:

$$\oint_C f\left(r\right)ds=\int_a^b f\left(r\left(t\right)\right)\left|\dot{r}\left(t\right)\right|dt\tag{A.16}$$

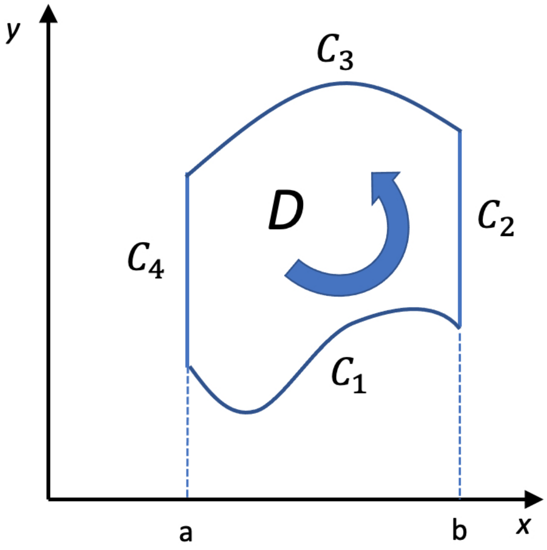

Figure A.1: Green's theorem

Appendix B

Lagrangian Derivation

In this appendix, the complete derivation of the Lagrangian is presented for the three dimensional elastic string rigid body pendulum.

B.1 Rigid Body Kinetic Energy

Taking the derivative of Eq. 7.5 yields:

$$\begin{aligned}\dot{\mathbf{r}}_Q &= \dot{\mathbf{r}}\left(l\right) + \dot{\mathbf{R}}\left(\boldsymbol{\rho} + \boldsymbol{\rho}_c\right)\\ &= \dot{\mathbf{r}}\left(l\right) + \mathbf{R}\hat{\boldsymbol{\Omega}}\left(\boldsymbol{\rho} + \boldsymbol{\rho}_c\right)\end{aligned} \tag{B.1}$$

where the $\hat{\cdot}$ operator denotes a skew symmetric matrix mapping of the cross product of a three dimensional vector defined in Eq. A.1, and the derivative of a rotation matrix ($\dot{\mathbf{R}} = \mathbf{R}\hat{\boldsymbol{\Omega}}$) is defined in Eq. A.5. Note that the vectors $\boldsymbol{\rho}$ and $\boldsymbol{\rho}_c$ are constant in the body fixed frame, and therefore their derivative is zero, $\dot{\boldsymbol{\rho}} = 0$ and $\dot{\boldsymbol{\rho}}_c = 0$. Inserting Eq. B.1 back into Eq. 7.3, using the definition of a dot product, transposing and expanding gives:

$$
\begin{aligned}
T_{\text{rb}} &= \int_{\text{Body}} \frac{1}{2}\Big(\dot{\mathbf{r}}\left(l\right) + \mathbf{R}\hat{\boldsymbol{\Omega}}\left(\boldsymbol{\rho}+\boldsymbol{\rho}_c\right)\Big) \cdot \Big(\dot{\mathbf{r}}\left(l\right) + \mathbf{R}\hat{\boldsymbol{\Omega}}\left(\boldsymbol{\rho}+\boldsymbol{\rho}_c\right)\Big)\, dm \\
&= \int_{\text{Body}} \frac{1}{2}\Big(\dot{\mathbf{r}}\left(l\right) + \mathbf{R}\hat{\boldsymbol{\Omega}}\left(\boldsymbol{\rho}+\boldsymbol{\rho}_c\right)\Big)^T \Big(\dot{\mathbf{r}}\left(l\right) + \mathbf{R}\hat{\boldsymbol{\Omega}}\left(\boldsymbol{\rho}+\boldsymbol{\rho}_c\right)\Big)\, dm \\
&= \int_{\text{Body}} \frac{1}{2}\Big(\dot{\mathbf{r}}\left(l\right)^T + \left(\boldsymbol{\rho}+\boldsymbol{\rho}_c\right)^T \hat{\boldsymbol{\Omega}}^T\mathbf{R}^T\Big) \Big(\dot{\mathbf{r}}\left(l\right) + \mathbf{R}\hat{\boldsymbol{\Omega}}\left(\boldsymbol{\rho}+\boldsymbol{\rho}_c\right)\Big)\, dm \\
&= \int_{\text{Body}} \frac{1}{2}\dot{\mathbf{r}}\left(l\right)^T\dot{\mathbf{r}}\left(l\right) + \frac{1}{2}\left(\boldsymbol{\rho}+\boldsymbol{\rho}_c\right)^T \hat{\boldsymbol{\Omega}}^T\mathbf{R}^T\dot{\mathbf{r}}\left(l\right) + \frac{1}{2}\dot{\mathbf{r}}\left(l\right)^T\mathbf{R}\hat{\boldsymbol{\Omega}}\left(\boldsymbol{\rho}+\boldsymbol{\rho}_c\right) \\
&\qquad + \frac{1}{2}\left(\boldsymbol{\rho}+\boldsymbol{\rho}_c\right)^T \hat{\boldsymbol{\Omega}}^T\mathbf{R}^T\mathbf{R}\hat{\boldsymbol{\Omega}}\left(\boldsymbol{\rho}+\boldsymbol{\rho}_c\right) dm.
\end{aligned}
$$

Because the end result is a scalar, the second term can be transposed and combined with the third term, and the fourth term simplifies since $\mathbf{R} \in SO(3)$ and $\mathbf{R}^T\mathbf{R} = \mathbf{I}$, yielding:

$$
\begin{aligned}
T_{\text{rb}} &= \frac{1}{2}\mathrm{m}\dot{\mathbf{r}}\left(l\right)^T\dot{\mathbf{r}}\left(l\right) + \int_{\text{Body}} \dot{\mathbf{r}}\left(l\right)^T\mathbf{R}\hat{\boldsymbol{\Omega}}\left(\boldsymbol{\rho}+\boldsymbol{\rho}_c\right) dm + \int_{\text{Body}} \frac{1}{2}\left(\boldsymbol{\rho}+\boldsymbol{\rho}_c\right)^T \hat{\boldsymbol{\Omega}}^T\hat{\boldsymbol{\Omega}}\left(\boldsymbol{\rho}+\boldsymbol{\rho}_c\right) dm \\
&= \frac{1}{2}\mathrm{m}\dot{\mathbf{r}}\left(l\right)^T\dot{\mathbf{r}}\left(l\right) + \int_{\text{Body}} \dot{\mathbf{r}}\left(l\right)^T\mathbf{R}\hat{\boldsymbol{\Omega}}\left(\boldsymbol{\rho}+\boldsymbol{\rho}_c\right) dm + \int_{\text{Body}} \frac{1}{2}\Big(\hat{\boldsymbol{\Omega}}\left(\boldsymbol{\rho}+\boldsymbol{\rho}_c\right)\Big)^T \hat{\boldsymbol{\Omega}}\left(\boldsymbol{\rho}+\boldsymbol{\rho}_c\right) dm \\
&= \frac{1}{2}\mathrm{m}\dot{\mathbf{r}}\left(l\right)^T\dot{\mathbf{r}}\left(l\right) + \mathrm{m}\dot{\mathbf{r}}\left(l\right)^T\mathbf{R}\hat{\boldsymbol{\Omega}}\boldsymbol{\rho}_c + \int_{\text{Body}} -\frac{1}{2}\left(\left(\boldsymbol{\rho}+\boldsymbol{\rho}_c\right)^\wedge\boldsymbol{\Omega}\right)^T\left(\boldsymbol{\rho}+\boldsymbol{\rho}_c\right)^\wedge\boldsymbol{\Omega} dm \\
&= \frac{1}{2}\mathrm{m}\dot{\mathbf{r}}\left(l\right)^T\dot{\mathbf{r}}\left(l\right) + \mathrm{m}\dot{\mathbf{r}}\left(l\right)^T\mathbf{R}\hat{\boldsymbol{\Omega}}\boldsymbol{\rho}_c + \int_{\text{Body}} -\frac{1}{2}\boldsymbol{\Omega}^T\left(\boldsymbol{\rho}+\boldsymbol{\rho}_c\right)^\wedge\left(\boldsymbol{\rho}+\boldsymbol{\rho}_c\right)^\wedge\boldsymbol{\Omega} dm \\
&= \frac{1}{2}\mathrm{m}\dot{\mathbf{r}}\left(l\right)\cdot\dot{\mathbf{r}}\left(l\right) + \mathrm{m}\dot{\mathbf{r}}\left(l\right)\cdot\mathbf{R}\hat{\boldsymbol{\Omega}}\boldsymbol{\rho}_c + \frac{1}{2}\boldsymbol{\Omega}\cdot\boldsymbol{\Pi}\boldsymbol{\Omega}
\end{aligned}
$$

where $\int_{\text{Body}} \boldsymbol{\rho}\, dm = 0$ and $\int_{\text{Body}} dm = \mathrm{m}$ for the second term. The skew symmetric identities from Eq. A.2 ($\hat{\mathbf{a}}\mathbf{b} = -\hat{\mathbf{b}}\mathbf{a}$) and Eq. A.1 ($\hat{\mathbf{x}}^T = -\hat{\mathbf{x}}$) were used for the third term. The matrix representation of the inertia tensor is defined as [93, 106]:

$$
\boldsymbol{\Pi} = -\int_{\text{Body}} \left(\boldsymbol{\rho}+\boldsymbol{\rho}_c\right)^\wedge\left(\boldsymbol{\rho}+\boldsymbol{\rho}_c\right)^\wedge dm, \tag{B.2}
$$

noting that expressing the matrix representation of the inertia tensor in the body coordinates produces:

$$\mathbf{\Pi} = \begin{bmatrix} J_{11} & J_{12} & J_{13} \\ J_{21} & J_{22} & J_{23} \\ J_{31} & J_{32} & J_{33} \end{bmatrix}.$$

where J_{ii} are the principle moments of inertia, and J_{ij} are the products of inertia.

B.2 String Potential Energy

The tangential strain, ϵ, or relative length change produced by stress ($\frac{\Delta l}{l}$), is formally defined for a continuous body as [93, 128, 129]:

$$\begin{aligned} \epsilon &= \lim_{\Delta s_o \to 0} \frac{\Delta s\left(s_o\right) - \Delta s_o}{\Delta s_o} \\ \epsilon &= \lim_{\Delta s_o \to 0} \frac{\Delta s\left(s_o\right)}{\Delta s_o} - 1 \\ \epsilon &= s'\left(s_o\right) - 1 \end{aligned} \tag{B.3}$$

where $()'$ denotes the spatial partial derivative ($\frac{\partial}{\partial s_o}$). The tangential unit vector $\hat{\mathbf{e}}_t$ is required to determine the spatial partial derivative:

$$\begin{aligned} \hat{\mathbf{e}}_t &= \frac{\partial \mathbf{r}\left(s_o\right)}{\partial s\left(s_o\right)} \\ \hat{\mathbf{e}}_t &= \frac{\partial \mathbf{r}\left(s_o\right)}{\partial s_o} \frac{\partial s_o}{\partial s\left(s_o\right)} \\ \hat{\mathbf{e}}_t &= \frac{\mathbf{r}'\left(s_o\right)}{s'\left(s_o\right)} \end{aligned}$$

Because $\hat{\mathbf{e}}_t$ has unit length:

$$s'(s_o) = \|\mathbf{r}'(s_o)\|_2. \tag{B.4}$$

Inserting Eq. B.3 and Eq. B.4 into Eq. 7.7 yields the potential energy of the string:

$$\begin{aligned}
V_{\text{string}} &= \int_0^l \frac{1}{2} EA\epsilon^2 - \mu\mathbf{r}(s_o) \cdot \mathbf{g} ds_o \\
V_{\text{string}} &= \int_0^l \frac{1}{2} EA\left(s'(s_o) - 1\right)^2 - \mu\mathbf{r}(s_o) \cdot \mathbf{g} ds_o \\
V_{\text{string}} &= \int_0^l \frac{1}{2} EA\left(\|\mathbf{r}'(s_o)\|_2 - 1\right)^2 - \mu\mathbf{r}(s_o) \cdot \mathbf{g} ds_o.
\end{aligned}$$

Appendix C

Hamilton's Principle Variation Derivations

In this appendix, the complete derivation of the equations of motion are presented for the thee dimensional elastic string rigid body pendulum, the fixed reel elastic string rigid body pendulum, and the moving reel elastic string rigid body pendulum.

C.1 Elastic String - Rigid Body Pendulum

Inserting the Lagrangian from Eq. 7.10 into Hamilton's principle of least action from Eq. 7.11 yields:

$$\begin{aligned}\delta\mathcal{S} =&\delta\int_{t_0}^{t_f}\left(\frac{1}{2}\mathrm{m}\dot{\mathbf{r}}\left(l\right)\cdot\dot{\mathbf{r}}\left(l\right)+\mathrm{m}\dot{\mathbf{r}}\left(l\right)\cdot\mathbf{R}\hat{\mathbf{\Omega}}\boldsymbol{\rho}_c+\frac{1}{2}\mathbf{\Omega}\cdot\mathbf{\Pi}\mathbf{\Omega}+\int_0^l\frac{1}{2}\mu\dot{\mathbf{r}}\left(s_o\right)\cdot\dot{\mathbf{r}}\left(s_o\right)ds_o\right.\\&\left.+\mathrm{m}\mathbf{r}\left(l\right)\cdot\mathbf{g}+\mathrm{m}\mathbf{R}\boldsymbol{\rho}_c\cdot\mathbf{g}+\int_0^l\left\{-\frac{1}{2}EA\left(\left\|\mathbf{r}'\left(s_o\right)\right\|_2-1\right)^2+\mu\mathbf{r}\left(s_o\right)\cdot\mathbf{g}\right\}ds_o\right)dt=0.\end{aligned}\tag{C.1}$$

Each term will be evaluated individually:

1. $\delta \int_{t_0}^{t_f} \frac{1}{2}\mathrm{m}\dot{\mathbf{r}}(l) \cdot \dot{\mathbf{r}}(l)\, dt$

   Taking the variation yields:

$$
\begin{aligned}
\delta \int_{t_0}^{t_f} \frac{1}{2}\mathrm{m}\dot{\mathbf{r}}(l) \cdot \dot{\mathbf{r}}(l)\, dt &= \int_{t_0}^{t_f} \frac{1}{2}\mathrm{m}\delta\left(\dot{\mathbf{r}}(l) \cdot \dot{\mathbf{r}}(l)\right) dt \\
&= \int_{t_0}^{t_f} \frac{1}{2}\mathrm{m}\left(\delta\dot{\mathbf{r}}(l) \cdot \dot{\mathbf{r}}(l) + \dot{\mathbf{r}}(l) \cdot \delta\dot{\mathbf{r}}(l)\right) dt \\
&= \int_{t_0}^{t_f} \frac{1}{2}\mathrm{m}\left(2\dot{\mathbf{r}}(l) \cdot \delta\dot{\mathbf{r}}(l)\right) dt \\
&= \int_{t_0}^{t_f} \mathrm{m}\dot{\mathbf{r}}(l) \cdot \delta\dot{\mathbf{r}}(l)\, dt.
\end{aligned}
$$

   Because $\delta\dot{\mathbf{r}}(l)$ is undefined, IBP in time is required, (IBP: $\int_a^b u dv = uv|_a^b - \int_a^b v du$ with $u = \mathrm{m}\dot{\mathbf{r}}(l)$ and $dv = \delta\dot{\mathbf{r}}(l)$):

$$
\delta \int_{t_0}^{t_f} \frac{1}{2}\mathrm{m}\dot{\mathbf{r}}(l) \cdot \dot{\mathbf{r}}(l)\, dt = \mathrm{m}\dot{\mathbf{r}}(l) \cdot \cancelto{0}{\delta\mathbf{r}(l)|_{t_0}^{t_f}} - \int_{t_0}^{t_f} \mathrm{m}\ddot{\mathbf{r}}(l) \cdot \delta\mathbf{r}(l)\, dt
$$

   The term above cancels to zero because $\delta\mathbf{r}(l)$ is defined as a variation that vanishes at t_0 and t_f, resulting in:

$$
\delta \int_{t_0}^{t_f} \frac{1}{2}\mathrm{m}\dot{\mathbf{r}}(l) \cdot \dot{\mathbf{r}}(l)\, dt = -\int_{t_0}^{t_f} \mathrm{m}\ddot{\mathbf{r}}(l) \cdot \delta\mathbf{r}(l)\, dt \qquad \text{(C.2)}
$$

2. $\delta \int_{t_0}^{t_f} \mathrm{m}\dot{\mathbf{r}}(l) \cdot \mathbf{R}\hat{\boldsymbol{\Omega}}\boldsymbol{\rho}_c dt$

Taking the variation yields:

$$\begin{aligned}\delta \int_{t_0}^{t_f} \mathrm{m}\dot{\mathbf{r}}\left(l\right)\cdot \mathbf{R}\hat{\mathbf{\Omega}}\boldsymbol{\rho}_c dt &= \int_{t_0}^{t_f} \mathrm{m}\mathbf{R}\hat{\mathbf{\Omega}}\boldsymbol{\rho}_c \cdot \delta\dot{\mathbf{r}}\left(l\right) + \mathrm{m}\dot{\mathbf{r}}\left(l\right)\cdot\delta\left(\mathbf{R}\hat{\mathbf{\Omega}}\boldsymbol{\rho}_c\right) dt \\ &= \int_{t_0}^{t_f} \mathrm{m}\mathbf{R}\hat{\mathbf{\Omega}}\boldsymbol{\rho}_c \cdot \delta\dot{\mathbf{r}}\left(l\right) + \mathrm{m}\dot{\mathbf{r}}\left(l\right)\cdot\delta\mathbf{R}\hat{\mathbf{\Omega}}\boldsymbol{\rho}_c + \mathrm{m}\dot{\mathbf{r}}\left(l\right)^T\mathbf{R}\delta\left(\hat{\mathbf{\Omega}}\boldsymbol{\rho}_c\right) dt \\ &= \int_{t_0}^{t_f} \mathrm{m}\mathbf{R}\hat{\mathbf{\Omega}}\boldsymbol{\rho}_c \cdot \delta\dot{\mathbf{r}}\left(l\right) + \mathrm{m}\dot{\mathbf{r}}\left(l\right)\cdot\delta\mathbf{R}\hat{\mathbf{\Omega}}\boldsymbol{\rho}_c - \mathrm{m}\dot{\mathbf{r}}\left(l\right)^T\mathbf{R}\hat{\boldsymbol{\rho}}_c\cdot\delta\mathbf{\Omega} dt,\end{aligned}$$

where the chain rule was used in the first and second step since $\dot{\mathbf{r}}\left(l\right)$, $\mathbf{R}$ and $\mathbf{\Omega}$ are time dependent. In the second step, $\dot{\mathbf{r}}\left(l\right)$ was transposed to convert from dot product notation. In the final step, the hatmap identity given in Eq. A.2 ($\hat{\mathbf{x}}\mathbf{y} = -\hat{\mathbf{y}}\mathbf{x}$) was used before taking the variation of $\mathbf{\Omega}$. Because $\delta\dot{\mathbf{r}}\left(l\right)$ is again undefined in the first term of the variation, IBP in time ($\int_a^b udv = uv|_a^b - \int_a^b vdu$) is again required, with $u = \mathrm{m}\mathbf{R}\hat{\mathbf{\Omega}}\boldsymbol{\rho}_c$, $dv = \delta\dot{\mathbf{r}}\left(l\right)$:

$$\begin{aligned}\int_{t_0}^{t_f} \mathrm{m}\mathbf{R}\hat{\mathbf{\Omega}}\boldsymbol{\rho}_c \cdot \delta\dot{\mathbf{r}}\left(l\right) dt &= \mathrm{m}\mathbf{R}\hat{\mathbf{\Omega}}\boldsymbol{\rho}_c \cdot \cancelto{0}{\delta\mathbf{r}\left(l\right)|_{t_0}^{t_f}} - \int_{t_0}^{t_f} \frac{d}{dt}\left(\mathrm{m}\mathbf{R}\hat{\mathbf{\Omega}}\boldsymbol{\rho}_c\right)\cdot\delta\mathbf{r}\left(l\right) dt \\ &= -\int_{t_0}^{t_f} \mathrm{m}\dot{\mathbf{R}}\hat{\mathbf{\Omega}}\boldsymbol{\rho}_c\cdot\delta\mathbf{r}\left(l\right) dt - \int_{t_0}^{t_f} \mathrm{m}\mathbf{R}\frac{d}{dt}\left(\hat{\mathbf{\Omega}}\boldsymbol{\rho}_c\right)\cdot\delta\mathbf{r}\left(l\right) dt \\ &= -\int_{t_0}^{t_f} \mathrm{m}\mathbf{R}\hat{\mathbf{\Omega}}\hat{\mathbf{\Omega}}\boldsymbol{\rho}_c\cdot\delta\mathbf{r}\left(l\right) dt + \int_{t_0}^{t_f} \mathrm{m}\mathbf{R}\frac{d}{dt}\left(\hat{\boldsymbol{\rho}}_c\Omega\right)\cdot\delta\mathbf{r}\left(l\right) dt \\ &= -\int_{t_0}^{t_f} \mathrm{m}\mathbf{R}\hat{\mathbf{\Omega}}^2\boldsymbol{\rho}_c\cdot\delta\mathbf{r}\left(l\right) dt + \int_{t_0}^{t_f} \mathrm{m}\mathbf{R}\hat{\boldsymbol{\rho}}_c\dot{\mathbf{\Omega}}\cdot\delta\mathbf{r}\left(l\right) dt\end{aligned}$$

where $\delta\mathbf{r}\left(l\right)$ is defined to vanish at $t = t_0$ and $t = t_f$, the chain rule is used for the time derivative, the hatmap identity defined in Eq. A.2 ($\hat{\mathbf{x}}\mathbf{y} = -\hat{\mathbf{y}}\mathbf{x}$) is used to take the derivative of $\mathbf{\Omega}$, and the kinematic relationship defined in Eq. A.5 ($\dot{\mathbf{R}} = \mathbf{R}\hat{\mathbf{\Omega}}$) is inserted for the derivative of the rotation matrix.

For the second term of the variation, following the same derivation as in Eq. A.12

$(\int_{t_0}^{t_f} \mathbf{x} \cdot \delta \mathbf{R} \mathbf{y} dt = \int_{t_0}^{t_f} \hat{\mathbf{y}} \mathbf{R}^T \mathbf{x} \cdot \boldsymbol{\eta} dt)$ yields:

$$\int_{t_0}^{t_f} \mathrm{m}\dot{\mathbf{r}}\left(l\right) \cdot \delta\mathbf{R}\hat{\boldsymbol{\Omega}}\boldsymbol{\rho}_c dt = \int_{t_0}^{t_f} \mathrm{m}\left(\hat{\boldsymbol{\Omega}}\boldsymbol{\rho}_c\right)^{\wedge} \mathbf{R}^T\dot{\mathbf{r}}\left(l\right)\cdot\boldsymbol{\eta} dt$$

where $\boldsymbol{\eta}$ is a variation of skew symmetric matrices.

For the third term of the variation, rearranging yields:

$$\begin{aligned} -\int_{t_0}^{t_f} \mathrm{m}\dot{\mathbf{r}}\left(l\right)^T \mathbf{R}\hat{\boldsymbol{\rho}}_c \cdot \delta\boldsymbol{\Omega} dt &= -\int_{t_0}^{t_f} \mathrm{m}\hat{\boldsymbol{\rho}}_c^T \mathbf{R}^T \dot{\mathbf{r}}\left(l\right) \cdot \delta\boldsymbol{\Omega} dt \\ &= \int_{t_0}^{t_f} \mathrm{m}\hat{\boldsymbol{\rho}}_c \mathbf{R}^T \dot{\mathbf{r}}\left(l\right) \cdot \delta\boldsymbol{\Omega} dt \end{aligned}$$

where the $\dot{\mathbf{r}}\left(l\right)^T \mathbf{R}\hat{\boldsymbol{\rho}}_c$ term is transposed due to the fact that the result of the dot product is a scalar, and using the skew symmetric matrix identity defined in Eq. A.1 $(\hat{\mathbf{x}}^T = -\hat{\mathbf{x}})$. Inserting the definition of the variation of the angular velocity from Eq. A.13 $(\delta\boldsymbol{\Omega} = \dot{\boldsymbol{\eta}} + \hat{\boldsymbol{\Omega}}\boldsymbol{\eta})$ and multiplying terms out yields:

$$\begin{aligned} -\int_{t_0}^{t_f} \mathrm{m}\dot{\mathbf{r}}\left(l\right)^T \mathbf{R}\hat{\boldsymbol{\rho}}_c \cdot \delta\boldsymbol{\Omega} dt &= \int_{t_0}^{t_f} \mathrm{m}\hat{\boldsymbol{\rho}}_c \mathbf{R}^T \dot{\mathbf{r}}\left(l\right) \cdot \left(\dot{\boldsymbol{\eta}} + \hat{\boldsymbol{\Omega}}\boldsymbol{\eta}\right) dt \\ &= \int_{t_0}^{t_f} \mathrm{m}\hat{\boldsymbol{\rho}}_c \mathbf{R}^T \dot{\mathbf{r}}\left(l\right) \cdot \dot{\boldsymbol{\eta}} dt + \int_{t_0}^{t_f} \mathrm{m}\hat{\boldsymbol{\rho}}_c \mathbf{R}^T \dot{\mathbf{r}}\left(l\right) \cdot \hat{\boldsymbol{\Omega}}\boldsymbol{\eta} dt. \end{aligned}$$

Because $\dot{\boldsymbol{\eta}}$ is undefined, IBP in time is required $(\int_a^b u dv = uv|_a^b - \int_a^b v du$, with $u = \mathrm{m}\hat{\boldsymbol{\rho}}_c \mathbf{R}^T \dot{\mathbf{r}}\left(l\right)$, and $dv = \dot{\boldsymbol{\eta}})$. Inserting the kinematic relationship given in Eq. A.5

$(\dot{\mathbf{R}}^T = -\hat{\boldsymbol{\Omega}}\mathbf{R}^T)$:

$$\begin{aligned}\int_{t_0}^{t_f} \mathrm{m}\hat{\boldsymbol{\rho}}_c\mathbf{R}^T\dot{\mathbf{r}}\left(l\right)\cdot\dot{\boldsymbol{\eta}}dt &= \mathrm{m}\hat{\boldsymbol{\rho}}_c\mathbf{R}^T\dot{\mathbf{r}}\left(l\right)\cdot\cancelto{0}{\boldsymbol{\eta}\big|_{t_0}^{t_f}} \\ &\qquad - \int_{t_0}^{t_f} \mathrm{m}\hat{\boldsymbol{\rho}}_c\mathbf{R}^T\ddot{\mathbf{r}}\left(l\right)\cdot\boldsymbol{\eta}dt - \int_{t_0}^{t_f} \mathrm{m}\hat{\boldsymbol{\rho}}_c\dot{\mathbf{R}}^T\dot{\mathbf{r}}\left(l\right)\cdot\boldsymbol{\eta}dt \\ &\qquad = -\int_{t_0}^{t_f} \mathrm{m}\hat{\boldsymbol{\rho}}_c\mathbf{R}^T\ddot{\mathbf{r}}\left(l\right)\cdot\boldsymbol{\eta}dt + \int_{t_0}^{t_f} \mathrm{m}\hat{\boldsymbol{\rho}}_c\hat{\boldsymbol{\Omega}}\mathbf{R}^T\dot{\mathbf{r}}\left(l\right)\cdot\boldsymbol{\eta}dt\end{aligned}$$

Using the skew symmetric matrix identity defined in Eq. A.1 ($\hat{\mathbf{x}}^T = -\hat{\mathbf{x}}$), and the skew dot product identity from Eq. A.3 ($\mathbf{y}\cdot\hat{\mathbf{x}}\mathbf{z} = \hat{\mathbf{z}}\mathbf{y}\cdot\mathbf{x}$) yields:

$$\begin{aligned}\int_{t_0}^{t_f} \mathrm{m}\hat{\boldsymbol{\rho}}_c\mathbf{R}^T\dot{\mathbf{r}}\left(l\right)\cdot\hat{\boldsymbol{\Omega}}\boldsymbol{\eta}dt &= -\int_{t_0}^{t_f} \mathrm{m}\hat{\boldsymbol{\rho}}_c\mathbf{R}^T\dot{\mathbf{r}}\left(l\right)\cdot\hat{\boldsymbol{\eta}}\boldsymbol{\Omega}dt \\ &= -\int_{t_0}^{t_f} \mathrm{m}\hat{\boldsymbol{\Omega}}\hat{\boldsymbol{\rho}}_c\mathbf{R}^T\dot{\mathbf{r}}\left(l\right)\cdot\boldsymbol{\eta}dt.\end{aligned}$$

Combining yields the third term of the variation:

$$\begin{aligned}&-\int_{t_0}^{t_f} \mathrm{m}\dot{\mathbf{r}}\left(l\right)^T\mathbf{R}\hat{\boldsymbol{\rho}}_c\cdot\delta\boldsymbol{\Omega}dt = \\ &\qquad\int_{t_0}^{t_f}\Big(-\mathrm{m}\hat{\boldsymbol{\rho}}_c\mathbf{R}^T\ddot{\mathbf{r}}\left(l\right) + \mathrm{m}\hat{\boldsymbol{\rho}}_c\hat{\boldsymbol{\Omega}}\mathbf{R}^T\dot{\mathbf{r}}\left(l\right) - \mathrm{m}\hat{\boldsymbol{\Omega}}\hat{\boldsymbol{\rho}}_c\mathbf{R}^T\dot{\mathbf{r}}\left(l\right)\Big)\cdot\boldsymbol{\eta}dt.\end{aligned}$$

Combining all three variation terms yields:

$$\begin{aligned}\delta\int_{t_0}^{t_f} \mathrm{m}\dot{\mathbf{r}}\left(l\right)\cdot\mathbf{R}\hat{\boldsymbol{\Omega}}\boldsymbol{\rho}_c dt = \int_{t_0}^{t_f}&\Big\{\Big(-\mathrm{m}\mathbf{R}\hat{\boldsymbol{\Omega}}^2\boldsymbol{\rho}_c + \mathrm{m}\mathbf{R}\hat{\boldsymbol{\rho}}_c\dot{\boldsymbol{\Omega}}\Big)\cdot\delta\mathbf{r}\left(l\right) \\ &+\Big(\mathrm{m}\left(\hat{\boldsymbol{\Omega}}\boldsymbol{\rho}_c\right)^{\wedge}\mathbf{R}^T\dot{\mathbf{r}}\left(l\right) - \mathrm{m}\hat{\boldsymbol{\rho}}_c\mathbf{R}^T\ddot{\mathbf{r}}\left(l\right) \\ &\qquad+\mathrm{m}\hat{\boldsymbol{\rho}}_c\hat{\boldsymbol{\Omega}}\mathbf{R}^T\dot{\mathbf{r}}\left(l\right) - \mathrm{m}\hat{\boldsymbol{\Omega}}\hat{\boldsymbol{\rho}}_c\mathbf{R}^T\dot{\mathbf{r}}\left(l\right)\Big)\cdot\boldsymbol{\eta}\Big\}dt.\end{aligned}$$

Rearranging and simplifying terms yields:

$$\begin{aligned}
&\delta \int_{t_0}^{t_f} \mathrm{m}\dot{\mathbf{r}}(l)\cdot \mathbf{R}\hat{\boldsymbol{\Omega}}\boldsymbol{\rho}_c dt = \\
&\quad = \int_{t_0}^{t_f} \Big\{ \Big(-\mathrm{m}\mathbf{R}\hat{\boldsymbol{\Omega}}^2\boldsymbol{\rho}_c + \mathrm{m}\mathbf{R}\hat{\boldsymbol{\rho}}_c\dot{\boldsymbol{\Omega}} \Big)\cdot \delta\mathbf{r}(l) \\
&\qquad\quad + \Big(-\mathrm{m}\hat{\boldsymbol{\rho}}_c\mathbf{R}^T\ddot{\mathbf{r}}(l) + \mathrm{m}\Big[\Big(\hat{\boldsymbol{\Omega}}\boldsymbol{\rho}_c\Big)^{\wedge} + \hat{\boldsymbol{\rho}}_c\hat{\boldsymbol{\Omega}} - \hat{\boldsymbol{\Omega}}\hat{\boldsymbol{\rho}}_c \Big]\mathbf{R}^T\dot{\mathbf{r}}(l) \Big)\cdot\boldsymbol{\eta} \Big\} dt \\
&\quad = \int_{t_0}^{t_f} \Big\{ \Big(-\mathrm{m}\mathbf{R}\hat{\boldsymbol{\Omega}}^2\boldsymbol{\rho}_c + \mathrm{m}\mathbf{R}\hat{\boldsymbol{\rho}}_c\dot{\boldsymbol{\Omega}} \Big)\cdot \delta\mathbf{r}(l) \\
&\qquad\quad + \left(-\mathrm{m}\hat{\boldsymbol{\rho}}_c\mathbf{R}^T\ddot{\mathbf{r}}(l) + \mathrm{m}\cancelto{0}{\Big[\hat{\boldsymbol{\Omega}}\hat{\boldsymbol{\rho}}_c - \hat{\boldsymbol{\rho}}_c\hat{\boldsymbol{\Omega}} + \hat{\boldsymbol{\rho}}_c\hat{\boldsymbol{\Omega}} - \hat{\boldsymbol{\Omega}}\hat{\boldsymbol{\rho}}_c \Big]}\mathbf{R}^T\dot{\mathbf{r}}(l) \right)\cdot\boldsymbol{\eta} \Bigg\} dt
\end{aligned}$$

where the skew symmetric identity from Eq. A.4 ($\hat{\mathbf{x}}\hat{\mathbf{y}} - \hat{\mathbf{y}}\hat{\mathbf{x}} = (\mathbf{x}\times\mathbf{y})^{\wedge}$) canceled out the terms inside the square brackets, resulting in:

$$\delta \int_{t_0}^{t_f} \mathrm{m}\dot{\mathbf{r}}(l)\cdot \mathbf{R}\hat{\boldsymbol{\Omega}}\boldsymbol{\rho}_c dt = \int_{t_0}^{t_f} \Big\{ \Big(-\mathrm{m}\mathbf{R}\hat{\boldsymbol{\Omega}}^2\boldsymbol{\rho}_c + \mathbf{R}\hat{\boldsymbol{\rho}}_c\dot{\boldsymbol{\Omega}} \Big)\cdot\delta\mathbf{r}(l) - \mathrm{m}\hat{\boldsymbol{\rho}}_c\mathbf{R}^T\ddot{\mathbf{r}}(l)\cdot\boldsymbol{\eta} \Big\} dt. \tag{C.3}$$

3. $\delta \int_{t_0}^{t_f} \frac{1}{2}\boldsymbol{\Omega}\cdot\boldsymbol{\Pi}\boldsymbol{\Omega}dt$

   Taking the variation yields:

$$
\begin{aligned}
\delta\int_{t_o}^{t_f}\frac{1}{2}\boldsymbol{\Omega}\cdot\boldsymbol{\Pi}\boldsymbol{\Omega}dt &= \int_{t_o}^{t_f}\frac{1}{2}\left(\boldsymbol{\Omega}\cdot\boldsymbol{\Pi}\delta\boldsymbol{\Omega}+\delta\boldsymbol{\Omega}\cdot\boldsymbol{\Pi}\boldsymbol{\Omega}\right)dt\\
&= \int_{t_o}^{t_f}\boldsymbol{\Pi}\boldsymbol{\Omega}\cdot\delta\boldsymbol{\Omega}dt\\
&= \int_{t_o}^{t_f}\boldsymbol{\Pi}\cdot\boldsymbol{\Omega}\cdot\left(\dot{\boldsymbol{\eta}}+\hat{\boldsymbol{\Omega}}\boldsymbol{\eta}\right)dt\\
&= \int_{t_o}^{t_f}\boldsymbol{\Pi}\boldsymbol{\Omega}\cdot\dot{\boldsymbol{\eta}}dt-\int_{t_o}^{t_f}\boldsymbol{\Pi}\boldsymbol{\Omega}\cdot\hat{\boldsymbol{\eta}}\boldsymbol{\Omega}dt\\
&= \boldsymbol{\Pi}\boldsymbol{\Omega}\cancelto{0}{\boldsymbol{\eta}|_{t_o}^{t_f}}-\int_{t_o}^{t_f}\boldsymbol{\Pi}\dot{\boldsymbol{\Omega}}\cdot\boldsymbol{\eta}dt-\int_{t_o}^{t_f}\hat{\boldsymbol{\Omega}}\boldsymbol{\Pi}\boldsymbol{\Omega}\cdot\boldsymbol{\eta}dt
\end{aligned}
$$

where the variation of the angular velocity from Eq. A.13 ($\delta\boldsymbol{\Omega}=\dot{\boldsymbol{\eta}}+\hat{\boldsymbol{\Omega}}\boldsymbol{\eta}$) was inserted, and the cross product relationship from Eq. A.2 $\left(\hat{\mathbf{a}}\mathbf{b}=-\hat{\mathbf{b}}\mathbf{a}\right)$ was used to switch the hat map and expand. Again, because $\dot{\boldsymbol{\eta}}$ is undefined, IBP in time (IBP: $\int_a^b udv = uv|_a^b-\int_a^b vdu$, with $u=\boldsymbol{\Pi}\cdot\boldsymbol{\Omega}$ and $dv=\dot{\boldsymbol{\eta}}$) is required. The skew dot product identity from Eq. A.3 ($\mathbf{y}\cdot\hat{\mathbf{x}}\mathbf{z}=\hat{\mathbf{z}}\mathbf{y}\cdot\mathbf{x}$) was used for the final two steps. Because $\boldsymbol{\eta}$ is defined as a variation that vanishes at t_o and t_f, the final variation of the third term results in:

$$
\delta\int_{t_0}^{t_f}\frac{1}{2}\boldsymbol{\Omega}\cdot\boldsymbol{\Pi}\boldsymbol{\Omega}dt=\int_{t_o}^{t_f}\left(-\boldsymbol{\Pi}\dot{\boldsymbol{\Omega}}-\hat{\boldsymbol{\Omega}}\boldsymbol{\Pi}\boldsymbol{\Omega}\right)\cdot\boldsymbol{\eta}dt. \tag{C.4}
$$

4. $\delta\int_{t_0}^{t_f}\int_0^l\frac{1}{2}\mu\dot{\mathbf{r}}\left(s_o\right)\cdot\dot{\mathbf{r}}\left(s_o\right)ds_odt$

Taking the variation yields:

$$\begin{aligned}
\delta \int_{t_0}^{t_f} \int_0^l \frac{1}{2}\mu \dot{\mathbf{r}}\left(s_o\right) \cdot \dot{\mathbf{r}}\left(s_o\right) ds_o dt &= \int_{t_0}^{t_f} \int_0^l \frac{1}{2}\mu \left(\delta \dot{\mathbf{r}}\left(s_o\right) \cdot \dot{\mathbf{r}}\left(s_o\right) + \dot{\mathbf{r}}\left(s_o\right) \cdot \delta \dot{\mathbf{r}}\left(s_o\right)\right) ds_o dt \\
&= \int_{t_0}^{t_f} \int_0^l \frac{1}{2}\mu \left(2\dot{\mathbf{r}}\left(s_o\right) \cdot \delta \dot{\mathbf{r}}\left(s_o\right)\right) ds_o dt \\
&= \int_{t_0}^{t_f} \int_0^l \mu \dot{\mathbf{r}}\left(s_o\right) \cdot \delta \dot{\mathbf{r}}\left(s_o\right) ds_o dt \\
&= \int_0^l \int_{t_0}^{t_f} \mu \dot{\mathbf{r}}\left(s_o\right) \cdot \delta \dot{\mathbf{r}}\left(s_o\right) dt ds_o \\
&= \int_0^l \left(\mu \dot{\mathbf{r}}\left(s_o\right) \cdot \cancelto{0}{\delta \mathbf{r}\left(s_o\right)\big|_{t_0}^{t_f}} - \int_{t_0}^{t_f} \mu \ddot{\mathbf{r}}\left(s_o\right) \cdot \delta \mathbf{r}\left(s_o\right) dt\right) ds_o
\end{aligned}$$

where the integral order can be swapped because the string is a fixed length and the boundary conditions do not change in time. Since $\delta \dot{\mathbf{r}}\left(s_o\right)$ is undefined, IBP in time (IBP: $\int_a^b u dv = uv|_a^b - \int_a^b v du$ with $u = \mu \dot{\mathbf{r}}\left(s_o\right)$ and $dv = \delta \dot{\mathbf{r}}\left(s_o\right)$) is required. The first term cancels to zero because $\delta \mathbf{r}\left(s_o\right)$ is defined as a variation that vanishes at t_0 and t_f. After swapping the integral order back again yields the final variation of the fourth term:

$$\int_{t_0}^{t_f} \delta \int_0^l \frac{1}{2}\mu \dot{\mathbf{r}}\left(s_o\right) \cdot \dot{\mathbf{r}}\left(s_o\right) ds_o dt = -\int_{t_0}^{t_f} \int_0^l \mu \ddot{\mathbf{r}}\left(s_o\right) \cdot \delta \mathbf{r}\left(s_o\right) ds_o dt. \tag{C.5}$$

5. $\delta \int_{t_0}^{t_f} \mathrm{m}\mathbf{r}\left(l\right) \cdot \mathbf{g} dt$

Taking the variation yields:

$$\delta \int_{t_0}^{t_f} \mathrm{m}\mathbf{r}\left(l\right) \cdot \mathbf{g} dt = \int_{t_0}^{t_f} \mathrm{m}\mathbf{g} \cdot \delta \mathbf{r}\left(l\right) dt \tag{C.6}$$

where the order was switched due to the dot product.

6. $\delta \int_{t_0}^{t_f} \mathrm{m}\mathbf{R}\boldsymbol{\rho}_c \cdot \mathbf{g} dt$

Taking the variation yields:

$$\delta \int_{t_0}^{t_f} \mathrm{m}\mathbf{R}\boldsymbol{\rho}_c \cdot \mathbf{g} dt = \int_{t_0}^{t_f} \mathrm{m}\mathbf{g} \cdot \delta \mathbf{R}\boldsymbol{\rho}_c dt.$$

Following the same derivation as in Eq. A.12 ($\int_{t_0}^{t_f} \mathbf{x} \cdot \delta \mathbf{R}\mathbf{y} dt = \int_{t_0}^{t_f} \hat{\mathbf{y}}\mathbf{R}^T \mathbf{x} \cdot \boldsymbol{\eta} dt$) yields:

$$\delta \int_{t_0}^{t_f} \mathrm{m}\mathbf{R}\boldsymbol{\rho}_c \cdot \mathbf{g} dt = \int_{t_0}^{t_f} \mathrm{m}\hat{\boldsymbol{\rho}}_c \mathbf{R}^T \mathbf{g} \cdot \boldsymbol{\eta} dt \tag{C.7}$$

7. $\delta \int_{t_0}^{t_f} \int_0^l -\frac{1}{2} EA \left(\|\mathbf{r}'(s_o)\|_2 - 1\right)^2 ds_o dt$

Taking the variation yields:

$$\begin{aligned}
\delta \int_{t_0}^{t_f} \int_0^l -\frac{1}{2} EA \left(\|\mathbf{r}'(s_o)\|_2 - 1\right)^2 ds_o dt \\
&= \int_{t_o}^{t_f} \int_0^l -\frac{1}{2} EA \delta \left(\left(\|\mathbf{r}'(s_o)\|_2 - 1\right)^2\right) ds_o dt \\
&= \int_{t_o}^{t_f} \int_0^l -EA \left(\|\mathbf{r}'(s_o)\|_2 - 1\right) \delta \left(\|\mathbf{r}'(s_o)\|_2 - 1\right) ds_o dt.
\end{aligned}$$

Continuing just the variation term yields:

$$\begin{aligned}
\delta \left(\|\mathbf{r}'(s_o)\|_2 - 1\right) &= \delta \left(\sqrt{\mathbf{r}'(s_o) \cdot \mathbf{r}'(s_o)} - 1\right) \\
&= \frac{\delta \left(\mathbf{r}'(s_o) \cdot \mathbf{r}'(s_o)\right)}{2\sqrt{\mathbf{r}'(s_o) \cdot \mathbf{r}'(s_o)}} \\
&= \frac{\mathbf{r}'(s_o) \delta \mathbf{r}'(s_o) + \delta \mathbf{r}'(s_o) \mathbf{r}'(s_o)}{2\|\mathbf{r}'(s_o)\|_2} \\
&= \frac{2\mathbf{r}'(s_o) \delta \mathbf{r}'(s_o)}{2\|\mathbf{r}'(s_o)\|_2} \\
\delta \left(\|\mathbf{r}'(s_o)\|_2 - 1\right) &= \frac{\mathbf{r}'(s_o)}{\|\mathbf{r}'(s_o)\|_2} \cdot \delta \mathbf{r}'(s_o).
\end{aligned}$$

Substituting back in and rearranging yields:

$$\begin{aligned}
\delta \int_{t_0}^{t_f} \int_0^l -\frac{1}{2} EA \left(\|\mathbf{r}'(s_o)\|_2 - 1\right)^2 ds_o dt \\
&= \int_{t_o}^{t_f} \int_0^l -EA \left(\|\mathbf{r}'(s_o)\|_2 - 1\right) \frac{\mathbf{r}'(s_o)}{\|\mathbf{r}'(s_o)\|_2} \cdot \delta \mathbf{r}'(s_o)\, ds_o dt \\
&= \int_{t_o}^{t_f} \int_0^l -EA \frac{\|\mathbf{r}'(s_o)\|_2 - 1}{\|\mathbf{r}'(s_o)\|_2} \mathbf{r}'(s_o) \cdot \delta \mathbf{r}'(s_o)\, ds_o dt.
\end{aligned}$$

Because $\delta\mathbf{r}'(s_o)$ is undefined, IBP in space (IBP: $\int_a^b u dv = uv|_a^b - \int_a^b v du$ with $u = -EA \frac{\|\mathbf{r}'(s_o)\|_2 - 1}{\|\mathbf{r}'(s_o)\|_2} \mathbf{r}'(s_o)$ and $dv = \delta\mathbf{r}'(s_o)$) is required.

$$\begin{aligned}
\delta \int_{t_0}^{t_f} \int_0^l -\frac{1}{2} EA \left(\|\mathbf{r}'(s_o)\|_2 - 1\right)^2 ds_o dt \\
&= \int_{t_o}^{t_f} \left\{ -EA \frac{\|\mathbf{r}'(s_o)\|_2 - 1}{\|\mathbf{r}'(s_o)\|_2} \mathbf{r}'(s_o) \cdot \delta \mathbf{r}(s_o) \Big|_0^l \right. \\
&\qquad \left. + \int_0^l EA \left(\frac{\|\mathbf{r}'(s_o)\|_2 - 1}{\|\mathbf{r}'(s_o)\|_2} \mathbf{r}'(s_o) \right)' \cdot \delta r(s_o)\, ds_o \right\} dt
\end{aligned}$$

Only half of the first term above cancels to 0 as only $\delta\mathbf{r}(0) = 0$ due to the boundary condition at the fixed end, while $\delta\mathbf{r}(l) \neq 0$, resulting in:

$$\begin{aligned}
\delta \int_{t_0}^{t_f} \int_0^l -\frac{1}{2} EA \left(\|\mathbf{r}'(s_o)\|_2 - 1\right)^2 ds_o dt \\
&= \int_{t_o}^{t_f} \left\{ -EA \frac{\|\mathbf{r}'(l)\|_2 - 1}{\|\mathbf{r}'(l)\|_2} \mathbf{r}'(l) \cdot \delta \mathbf{r}(l) \right. \\
&\qquad \left. + \int_0^l EA \left(\frac{\|\mathbf{r}'(s_o)\|_2 - 1}{\|\mathbf{r}'(s_o)\|_2} \mathbf{r}'(s_o) \right)' \cdot \delta \mathbf{r}(s_o)\, ds_o \right\} dt.
\end{aligned} \tag{C.8}$$

8. $\delta \int_{t_0}^{t_f} \int_0^l \mu \mathbf{r}(s_o) \cdot \mathbf{g} ds_o dt$

Taking the variation yields:

$$\delta \int_{t_0}^{t_f} \int_0^l \mu \mathbf{r}\left(s_o\right) \cdot \mathbf{g} ds_o dt = \int_{t_0}^{t_f} \int_0^l \mu \mathbf{g} \cdot \delta \mathbf{r}\left(s_o\right) ds_o dt. \tag{C.9}$$

Inserting Eq. C.2 through Eq. C.9 into Eq. C.1 yields the completed variation for the three dimensional elastic string pendulum:

$$\begin{aligned}
\delta \mathcal{S} = \delta \int_{t_0}^{t_f} & \left(\frac{1}{2}\mathrm{m}\dot{\mathbf{r}}\left(l\right) \cdot \dot{\mathbf{r}}\left(l\right) + \mathrm{m}\dot{\mathbf{r}}\left(l\right) \cdot \mathbf{R}\hat{\mathbf{\Omega}}\boldsymbol{\rho}_c + \frac{1}{2}\mathbf{\Omega} \cdot \mathbf{\Pi}\mathbf{\Omega} + \int_0^l \frac{1}{2}\mu \dot{\mathbf{r}}\left(s_o\right) \cdot \dot{\mathbf{r}}\left(s_o\right) ds_o \right. \\
& \left. + \mathrm{m}\mathbf{r}\left(l\right) \cdot \mathbf{g} + \mathrm{m}\mathbf{R}\boldsymbol{\rho}_c \cdot \mathbf{g} + \int_0^l \left\{ -\frac{1}{2} EA \left(\left\|\mathbf{r}'\left(s_o\right)\right\|_2 - 1\right)^2 + \mu \mathbf{r}\left(s_o\right) \cdot \mathbf{g} \right\} ds_o \right) \\
= \int_{t_o}^{t_f} & \int_0^l \left(-\mu \ddot{\mathbf{r}}\left(s_o\right) + \mu \mathbf{g} + EA \left(\frac{\left\|\mathbf{r}'\left(s_o\right)\right\|_2 - 1}{\left\|\mathbf{r}'\left(s_o\right)\right\|_2} \mathbf{r}'\left(s_o\right)\right)'\right) \cdot \delta \mathbf{r}\left(s_o\right) ds_o \\
& + \left(-\mathrm{m}\ddot{\mathbf{r}}\left(l\right) + \mathrm{m}\mathbf{g} - EA \frac{\left\|\mathbf{r}'\left(l\right)\right\|_2 - 1}{\left\|\mathbf{r}'\left(l\right)\right\|_2} \mathbf{r}'\left(l\right) - \mathrm{m}\mathbf{R}\hat{\mathbf{\Omega}}^2 \boldsymbol{\rho}_c + \mathrm{m}\mathbf{R}\hat{\boldsymbol{\rho}}_c \dot{\mathbf{\Omega}}\right) \cdot \delta \mathbf{r}\left(l\right) \\
& + \left(-\mathbf{\Pi} \cdot \dot{\mathbf{\Omega}} - \hat{\mathbf{\Omega}}\mathbf{\Pi}\mathbf{\Omega} + \mathrm{m}\hat{\boldsymbol{\rho}}_c \mathbf{R}^T \mathbf{g} - \mathrm{m}\hat{\boldsymbol{\rho}}_c \mathbf{R}^T \ddot{\mathbf{r}}\left(l\right)\right) \cdot \boldsymbol{\eta} \, dt = 0.
\end{aligned} \tag{C.10}$$

C.2 Fixed Reel - Elastic String - Rigid Body Pendulum

Inserting the Lagrangian from Eq. 7.23 into the Extended Hamilton's principle of least action from Eq. 7.24 yields:

$$\begin{aligned}\delta\mathcal{S} = \delta\int_{t_0}^{t_f}\Bigg(&\frac{1}{2}\left(\mu\mathrm{s_d}+\frac{\mathrm{m_d}}{2}\right)\dot{\mathrm{s}}_\mathrm{d}^2 + \int_{\mathrm{s_d}}^{l}\frac{1}{2}\mu\dot{\mathbf{r}}\left(\mathrm{s_o}\right)\cdot\dot{\mathbf{r}}\left(\mathrm{s_o}\right)d\mathrm{s_o} + \frac{1}{2}\mathrm{m}\dot{\mathbf{r}}\left(l\right)\cdot\dot{\mathbf{r}}\left(l\right) + \mathrm{m}\dot{\mathbf{r}}\left(l\right)\cdot\mathbf{R}\hat{\boldsymbol{\Omega}}\boldsymbol{\rho}_c\\ &+\frac{1}{2}\boldsymbol{\Omega}\cdot\boldsymbol{\Pi}\boldsymbol{\Omega} + \mu\left(\mathrm{s_d}-\mathrm{b}\right)\mathbf{r}_D\cdot\mathbf{g} + \mu\mathrm{g}\mathrm{d}^2\left(\cos\left(\frac{\mathrm{s_d}-\mathrm{b}}{\mathrm{d}}\right)-1\right) + \mathrm{m}\mathbf{r}\left(l\right)\cdot\mathbf{g}\\ &+\mathrm{m}\mathbf{R}\boldsymbol{\rho}_c\cdot\mathbf{g} + \int_{\mathrm{s_d}}^{l}\left\{-\frac{1}{2}EA\left(\|\mathbf{r}'\left(\mathrm{s_o}\right)\|_2-1\right)^2+\mu\mathbf{r}\left(\mathrm{s_o}\right)\cdot\mathbf{g}\right\}d\mathrm{s_o}+\mathcal{W}_{\mathrm{NC}}\Bigg)dt = 0.\end{aligned} \tag{C.11}$$

Each term will be evaluated individually:

1. $\delta\int_{t_0}^{t_f}\frac{1}{2}\left(\mu\mathrm{s_d}+\frac{\mathrm{m_d}}{2}\right)\dot{\mathrm{s}}_\mathrm{d}^2 dt$

   Taking the variation yields:

$$\delta\int_{t_0}^{t_f}\frac{1}{2}\left(\mu\mathrm{s_d}+\frac{\mathrm{m_d}}{2}\right)\dot{\mathrm{s}}_\mathrm{d}^2 dt = \int_{t_0}^{t_f}\left(\left(\mu\mathrm{s_d}+\frac{\mathrm{m_d}}{2}\right)\dot{\mathrm{s}}_\mathrm{d}\delta\dot{\mathrm{s}}_\mathrm{d}+\frac{1}{2}\mu\dot{\mathrm{s}}_\mathrm{d}^2\delta\mathrm{s_d}\right)dt$$

   Because $\delta\dot{\mathrm{s}}_\mathrm{d}$ is undefined for the first term, IBP in time is required, (IBP: $\int_a^b udv = uv|_a^b - \int_a^b vdu$ with $u = \left(\mu\mathrm{s_d}+\frac{\mathrm{m_d}}{2}\right)\dot{\mathrm{s}}_\mathrm{d}$ and $dv = \delta\dot{\mathrm{s}}_\mathrm{d}$) yields:

$$\begin{aligned}&\int_{t_0}^{t_f}\left(\mu\mathrm{s_d}+\frac{\mathrm{m_d}}{2}\right)\dot{\mathrm{s}}_\mathrm{d}\delta\dot{\mathrm{s}}_\mathrm{d}dt\\ &\qquad= \left(\mu\mathrm{s_d}+\frac{\mathrm{m_d}}{2}\right)\dot{\mathrm{s}}_\mathrm{d}\cancelto{0}{\delta\mathrm{s_d}|_{t_0}^{t_f}} - \int_{t_0}^{t_f}\left(\mu\mathrm{s_d}\ddot{\mathrm{s}}_\mathrm{d}\delta\mathrm{s_d}+\frac{\mathrm{m_d}}{2}\ddot{\mathrm{s}}_\mathrm{d}\delta\mathrm{s_d}+\mu\dot{\mathrm{s}}_\mathrm{d}^2\delta\mathrm{s_d}\right)dt\\ &\qquad= -\int_{t_0}^{t_f}\left(\left(\mu\mathrm{s_d}+\frac{\mathrm{m_d}}{2}\right)\ddot{\mathrm{s}}_\mathrm{d}+\mu\dot{\mathrm{s}}_\mathrm{d}^2\right)\delta\mathrm{s_d}dt\end{aligned}$$

yields the variation of the first term of Eq. C.11:

$$\begin{aligned}\delta\int_{t_0}^{t_f}\frac{1}{2}\left(\mu \mathrm{s_d}+\frac{\mathrm{m_d}}{2}\right)\dot{\mathrm{s}}_{\mathrm{d}}^2 dt &= \int_{t_0}^{t_f}\left(-\left(\mu \mathrm{s_d}+\frac{\mathrm{m_d}}{2}\right)\ddot{\mathrm{s}}_d-\mu\dot{\mathrm{s}}_{\mathrm{d}}^2+\frac{1}{2}\mu\dot{\mathrm{s}}_{\mathrm{d}}^2\right)\delta \mathrm{s_d} dt \\ &= \int_{t_0}^{t_f}\left(-\left(\mu \mathrm{s_d}+\frac{\mathrm{m_d}}{2}\right)\ddot{\mathrm{s}}_{\mathrm{d}}-\frac{1}{2}\mu\dot{\mathrm{s}}_{\mathrm{d}}^2\right)\delta \mathrm{s_d} dt\end{aligned} \tag{C.12}$$

2. $\delta\int_{t_0}^{t_f}\int_{\mathrm{s_d}}^{l}\frac{1}{2}\mu\dot{\mathbf{r}}(\mathrm{s_0})\cdot\dot{\mathbf{r}}(\mathrm{s_0})\,d\mathrm{s_0}dt$

The second term of Eq. C.11 looks very similar to the derivation from Section C.1, but the lower limit on the integral ($\mathrm{s_d}$) is a function of time which makes it impossible to switch the order of the integral. In this case, first use Leibniz rule given in Eq. A.14 to take the variation [124–126]:

$$\begin{aligned}&\delta\int_{t_0}^{t_f}\int_{\mathrm{s_d}}^{l}\frac{1}{2}\mu\dot{\mathbf{r}}(\mathrm{s_0})\cdot\dot{\mathbf{r}}(\mathrm{s_0})\,d\mathrm{s_0}dt \\ &\qquad = \int_{t_0}^{t_f}-\frac{1}{2}\mu\dot{\mathbf{r}}\left(\mathrm{s_d^+}\right)\cdot\dot{\mathbf{r}}\left(\mathrm{s_d^+}\right)\delta\mathrm{s_d}dt+\int_{t_0}^{t_f}\int_{\mathrm{s_d}}^{l}\mu\dot{\mathbf{r}}(\mathrm{s_0})\cdot\delta\dot{\mathbf{r}}(\mathrm{s_0})\,d\mathrm{s_0}dt\end{aligned}$$

where $\mathrm{s_d^+}$ is the material point just outside the guide way exit. For the second term, $\mathrm{s_d}$ in the limit of the integral prevents swapping the integral order for IBP. In order to use Green's theorem given in Eq. A.15, $\dot{\mathbf{r}}(\mathrm{s_0})\cdot\delta\dot{\mathbf{r}}(\mathrm{s_0})$ needs to be determined [110,125–127]. Using the chain rule and rearranging yields:

$$\begin{aligned}\frac{\mathrm{d}}{dt}\left(\dot{\mathbf{r}}(\mathrm{s_0})\cdot\delta\mathbf{r}(\mathrm{s_0})\right) &= \dot{\mathbf{r}}(\mathrm{s_0})\cdot\delta\dot{\mathbf{r}}(\mathrm{s_0})+\ddot{\mathbf{r}}(\mathrm{s_0})\cdot\delta\mathbf{r}(\mathrm{s_0}) \\ \dot{\mathbf{r}}(\mathrm{s_0})\cdot\delta\dot{\mathbf{r}}(\mathrm{s_0}) &= \frac{\mathrm{d}}{dt}\left(\dot{\mathbf{r}}(\mathrm{s_0})\cdot\delta\mathbf{r}(\mathrm{s_0})\right)-\ddot{\mathbf{r}}(\mathrm{s_0})\cdot\delta\mathbf{r}(\mathrm{s_0}).\end{aligned}$$

Substituting into the equation above gives:

$$\begin{aligned}\delta \int_{t_0}^{t_f} \int_{\mathrm{s_d}}^{l} \frac{1}{2}\mu \dot{\mathbf{r}}\left(\mathrm{s}_0\right) \cdot \dot{\mathbf{r}}\left(\mathrm{s}_0\right) d\mathrm{s}_0 dt \\ &= \int_{t_0}^{t_f} -\frac{1}{2}\mu \dot{\mathbf{r}}\left(\mathrm{s_d^+}\right) \cdot \dot{\mathbf{r}}\left(\mathrm{s_d^+}\right) \delta \mathrm{s_d} dt \\ &+ \int_{t_0}^{t_f} \int_{\mathrm{s_d}}^{l} \mu \frac{\partial}{\partial t}\left(\dot{\mathbf{r}}\left(\mathrm{s}_0\right) \cdot \delta \mathbf{r}\left(\mathrm{s}_0\right)\right) d\mathrm{s}_0 dt - \int_{t_0}^{t_f} \int_{\mathrm{s_d}}^{l} \mu \ddot{\mathbf{r}}\left(\mathrm{s}_0\right) \cdot \delta \mathbf{r}\left(\mathrm{s}_0\right) d\mathrm{s}_0 dt\end{aligned}$$

A boundary condition can be applied at the guide way entrance. The guide way, given by $\mathbf{r}_G = \mathbf{r}\left(\mathrm{s_d}\right)$, is inertially fixed, implying $\dot{\mathbf{r}}_G = 0$. Using the chain rule and rearranging yields:

$$\begin{aligned}\dot{\mathbf{r}}_G = \dot{\mathbf{r}}\left(s_{\mathrm{d}}^{+}\right) + \mathbf{r}'\left(\mathrm{s_d^+}\right) \dot{\mathrm{s}}_{\mathrm{d}} = 0 \\ \dot{\mathbf{r}}\left(\mathrm{s_d^+}\right) = -\mathbf{r}'\left(\mathrm{s_d^+}\right) \dot{\mathrm{s}}_{\mathrm{d}}\end{aligned} \tag{C.13}$$

Substituting into the equation above gives:

$$\begin{aligned}\delta \int_{t_0}^{t_f} \int_{\mathrm{s_d}}^{l} \frac{1}{2}\mu \dot{\mathbf{r}}\left(\mathrm{s}_0\right) \cdot \dot{\mathbf{r}}\left(\mathrm{s}_0\right) d\mathrm{s}_0 dt \\ &= \int_{t_0}^{t_f} -\frac{1}{2}\mu \dot{\mathrm{s}}_{\mathrm{d}}^2 \mathbf{r}'\left(\mathrm{s_d^+}\right) \cdot \mathbf{r}'\left(\mathrm{s_d^+}\right) \delta \mathrm{s_d} dt \\ &+ \int_{t_0}^{t_f} \int_{\mathrm{s_d}}^{l} \mu \frac{\partial}{\partial t}\left(\dot{\mathbf{r}}\left(\mathrm{s}_0\right) \cdot \delta \mathbf{r}\left(\mathrm{s}_0\right)\right) d\mathrm{s}_0 dt - \int_{t_0}^{t_f} \int_{\mathrm{s_d}}^{l} \mu \ddot{\mathbf{r}}\left(\mathrm{s}_0\right) \cdot \delta \mathbf{r}\left(\mathrm{s}_0\right) d\mathrm{s}_0 dt\end{aligned}$$

Use Green's theorem given in Eq. A.15 $\left(\oint_C \left(L dx + M dy\right) = \iint_D \left(\frac{\partial M}{\partial x} - \frac{\partial L}{\partial y}\right) dx dy\right)$ on the second term (with $x = \mathrm{s}_0$, $y = t$, $M = 0$, and $L = \mu \dot{\mathbf{r}}\left(\mathrm{s}_0\right) \cdot \delta \mathbf{r}\left(\mathrm{s}_0\right)$) and the definition of a line integral given in Eq. A.16 ($\oint_C f\left(\mathbf{r}\right) ds = \int_a^b f\left(\mathbf{r}\left(t\right)\right) |\dot{\mathbf{r}}\left(t\right)| dt$) for the four edges parameterized by $[t_0, t_f] \times [\mathrm{s_d}, l]$:

(a) $t = t_0$, $\mathrm{s}_0 \in [\mathrm{s}_\mathrm{d}(t_o), l]$:

$$\oint_C \mu \dot{\mathbf{r}}(\mathrm{s}_0) \cdot \delta \mathbf{r}(\mathrm{s}_0)\, d\mathrm{s}_0 = 0$$

because $\delta \mathbf{r}(\mathrm{s}_0) = 0$ for $t = t_o$.

(b) $t = t_f$, $\mathrm{s}_0 \in [\mathrm{s}_\mathrm{d}(t_o), l]$:

$$\oint_C \mu \dot{\mathbf{r}}(\mathrm{s}_0) \cdot \delta \mathbf{r}(\mathrm{s}_0)\, d\mathrm{s}_0 = 0$$

because $\delta \mathbf{r}(\mathrm{s}_0) = 0$ for $t = t_f$.

(c) $t \in [t_o, t_f]$, $\mathrm{s}_0 = \mathrm{s}_\mathrm{d}(t)$:

$$\oint_C \mu \dot{\mathbf{r}}(\mathrm{s}_0) \cdot \delta \mathbf{r}(\mathrm{s}_0)\, d\mathrm{s}_0 = \int_{t_0}^{t_f} \mu \dot{\mathbf{r}}\left(\mathrm{s}_\mathrm{d}^+\right) \cdot \delta \mathbf{r}\left(\mathrm{s}_\mathrm{d}^+\right) \dot{\mathrm{s}}_\mathrm{d} dt$$

where s_d^+ is the material point just outside the guide way exit. The guide way entrance boundary condition can be applied again. The guide way, given by $\mathbf{r}_G = \mathbf{r}(\mathrm{s}_\mathrm{d})$, is inertially fixed, implying $\dot{\mathbf{r}}_G = 0$. Using the chain rule and rearranging yields:

$$\begin{aligned} \delta \mathbf{r}_G = \delta \mathbf{r}\left(\mathrm{s}_\mathrm{d}^+\right) + \mathbf{r}'\left(\mathrm{s}_\mathrm{d}^+\right) \delta \mathrm{s}_\mathrm{d} = 0 \\ \delta \mathbf{r}\left(\mathrm{s}_\mathrm{d}^+\right) = -\mathbf{r}'\left(\mathrm{s}_\mathrm{d}^+\right) \delta \mathrm{s}_\mathrm{d} \end{aligned} \tag{C.14}$$

Substituting Eq. C.13 and Eq. C.14 into the equation above yields:

$$\oint_C \mu \dot{\mathbf{r}}(\mathrm{s}_0) \cdot \delta \mathbf{r}(\mathrm{s}_0)\, d\mathrm{s}_0 = \int_{t_0}^{t_f} \mu \dot{\mathrm{s}}_\mathrm{d}^2 \mathbf{r}'\left(\mathrm{s}_\mathrm{d}^+\right) \cdot \mathbf{r}'\left(\mathrm{s}_\mathrm{d}^+\right) \delta \mathrm{s}_\mathrm{d} dt$$

(d) $t \in [t_o, t_f]$, $\mathrm{s}_0 = l$:

$$\oint_C \mu \dot{\mathbf{r}}\left(\mathrm{s}_0\right) \cdot \delta \mathbf{r}\left(\mathrm{s}_0\right) d\mathrm{s}_0 = \cancelto{0}{\int_{t_0}^{t_f} \mu \dot{\mathbf{r}}\left(l\right) \cdot \delta \mathbf{r}\left(l\right) \dot{l} dt}$$

because $\mathrm{s}_0 = l$ is constant, and $\dot{l} = 0$. This corresponds to a fixed connection at the rigid body (no reel on the rigid body).

which gives us the variation of the second term of Eq. C.11:

$$\begin{aligned}
&\delta \int_{t_0}^{t_f} \int_{\mathrm{s_d}}^{l} \frac{1}{2} \mu \dot{\mathbf{r}}\left(\mathrm{s}_0\right) \cdot \dot{\mathbf{r}}\left(\mathrm{s}_0\right) d\mathrm{s}_0 dt \\
&\qquad = \int_{t_0}^{t_f} \left\{ - \int_{\mathrm{s_d}}^{l} \mu \ddot{\mathbf{r}}\left(\mathrm{s}_0\right) \cdot \delta \mathbf{r}\left(\mathrm{s}_0\right) d\mathrm{s}_0 \right. \\
&\qquad\qquad \left. - \frac{1}{2} \mu \dot{\mathrm{s}}_{\mathrm{d}}^2 \mathbf{r}'\left(\mathrm{s}_{\mathrm{d}}^{+}\right) \cdot \mathbf{r}'\left(\mathrm{s}_{\mathrm{d}}^{+}\right) \delta \mathrm{s_d} + \mu \dot{\mathrm{s}}_{\mathrm{d}}^2 \mathbf{r}'\left(\mathrm{s}_{\mathrm{d}}^{+}\right) \cdot \mathbf{r}'\left(\mathrm{s}_{\mathrm{d}}^{+}\right) \delta \mathrm{s_d} \right\} dt
\end{aligned}$$

which simplifies to:

$$\begin{aligned}
&\delta \int_{t_0}^{t_f} \int_{\mathrm{s_d}}^{l} \frac{1}{2} \mu \dot{\mathbf{r}}\left(\mathrm{s}_0\right) \cdot \dot{\mathbf{r}}\left(\mathrm{s}_0\right) d\mathrm{s}_0 dt \\
&\qquad = \int_{t_0}^{t_f} \left\{ - \int_{\mathrm{s_d}}^{l} \mu \ddot{\mathbf{r}}\left(\mathrm{s}_0\right) \cdot \delta \mathbf{r}\left(\mathrm{s}_0\right) d\mathrm{s}_0 + \frac{1}{2} \mu \dot{\mathrm{s}}_{\mathrm{d}}^2 \mathbf{r}'\left(\mathrm{s}_{\mathrm{d}}^{+}\right) \cdot \mathbf{r}'\left(\mathrm{s}_{\mathrm{d}}^{+}\right) \delta \mathrm{s_d} \right\} dt
\end{aligned} \tag{C.15}$$

3. $\delta \int_{t_0}^{t_f} \frac{1}{2} \mathrm{m} \dot{\mathbf{r}}\left(l\right) \cdot \dot{\mathbf{r}}\left(l\right) dt$

The third term follows the same derivation as the first term in Section C.1

$$\delta \int_{t_0}^{t_f} \frac{1}{2} \mathrm{m} \dot{\mathbf{r}}\left(l\right) \cdot \dot{\mathbf{r}}\left(l\right) dt = - \int_{t_0}^{t_f} \mathrm{m} \ddot{\mathbf{r}}\left(l\right) \cdot \delta \mathbf{r}\left(l\right) dt \tag{C.16}$$

4. $\delta \int_{t_0}^{t_f} \mathrm{m} \dot{\mathbf{r}}\left(l\right) \cdot \mathbf{R} \hat{\boldsymbol{\Omega}} \boldsymbol{\rho}_c dt$

The fourth terms follow the same derivation as the second term in Section C.1:

$$\delta \int_{t_0}^{t_f} \mathrm{m}\dot{\mathbf{r}}(l) \cdot \mathbf{R}\hat{\boldsymbol{\Omega}}\boldsymbol{\rho}_c dt = \int_{t_0}^{t_f} \left\{ \left(-\mathrm{m}\mathbf{R}\hat{\boldsymbol{\Omega}}^2 \boldsymbol{\rho}_c + \mathrm{m}\mathbf{R}\hat{\boldsymbol{\rho}}_c \dot{\boldsymbol{\Omega}} \right) \cdot \delta\mathbf{r}(l) - \mathrm{m}\hat{\boldsymbol{\rho}}_c \mathbf{R}^T \ddot{\mathbf{r}}(l) \cdot \boldsymbol{\eta} \right\} dt. \tag{C.17}$$

5. $\delta \int_{t_0}^{t_f} \frac{1}{2}\boldsymbol{\Omega} \cdot \boldsymbol{\Pi}\boldsymbol{\Omega} dt$

The fifth term follows the same derivation as the third term in Section C.1:

$$\delta \int_{t_0}^{t_f} \frac{1}{2}\boldsymbol{\Omega} \cdot \boldsymbol{\Pi}\boldsymbol{\Omega} dt = \int_{t_o}^{t_f} \left(-\boldsymbol{\Pi}\dot{\boldsymbol{\Omega}} - \hat{\boldsymbol{\Omega}}\boldsymbol{\Pi}\boldsymbol{\Omega} \right) \cdot \boldsymbol{\eta} dt. \tag{C.18}$$

6. $\delta \int_{t_0}^{t_f} \mu \left(\mathrm{s_d} - \mathrm{b} \right) \mathbf{r}_G \cdot \mathbf{g} dt$

The only varying parameter is $\mathrm{s_d}$. Taking the variation yields:

$$\delta \int_{t_0}^{t_f} \mu \left(\mathrm{s_d} - \mathrm{b} \right) \mathbf{r}_G \cdot \mathbf{g} = \int_{t_0}^{t_f} \mu \left(\mathbf{r}_G \cdot \mathbf{g} \right) \delta \mathrm{s_d} dt. \tag{C.19}$$

7. $\delta \int_{t_0}^{t_f} \mu \mathrm{g}\mathrm{d}^2 \left(\cos\left(\frac{\mathrm{s_d} - \mathrm{b}}{\mathrm{d}} \right) - 1 \right) dt$

The only varying parameter is $\mathrm{s_d}$. Taking the variation yields:

$$\begin{aligned} \delta \int_{t_0}^{t_f} \mu \mathrm{g}\mathrm{d}^2 \left(\cos\left(\frac{\mathrm{s_d} - \mathrm{b}}{\mathrm{d}} \right) - 1 \right) dt &= \int_{t_0}^{t_f} -\mu \mathrm{g}\mathrm{d}^2 \sin\left(\frac{\mathrm{s_d} - \mathrm{b}}{\mathrm{d}} \right) \frac{1}{\mathrm{d}} \delta \mathrm{s_d} dt \\ &= -\int_{t_0}^{t_f} \mu \mathrm{g}\mathrm{d} \sin\left(\frac{\mathrm{s_d} - \mathrm{b}}{\mathrm{d}} \right) \delta \mathrm{s_d} dt. \end{aligned} \tag{C.20}$$

8. $\delta \int_{t_0}^{t_f} \mathrm{m}\mathbf{r}(l) \cdot \mathbf{g} dt$

The eighth term follows the same derivation as the fifth term in Section C.1:

$$\delta \int_{t_0}^{t_f} \mathrm{m}\mathbf{r}\left(l\right) \cdot \mathbf{g} dt = \int_{t_0}^{t_f} \mathrm{m}\mathbf{g} \cdot \delta \mathbf{r}\left(l\right) dt \tag{C.21}$$

9. $\delta \int_{t_0}^{t_f} \mathrm{m}\mathbf{R}\boldsymbol{\rho}_c \cdot \mathbf{g} dt$

   The ninth term follows the same derivation as the sixth term in Section C.1, repeating Eq. C.7:

$$\delta \int_{t_0}^{t_f} \mathrm{m}\mathbf{R}\boldsymbol{\rho}_c \cdot \mathbf{g} dt = \int_{t_0}^{t_f} \mathrm{m}\hat{\boldsymbol{\rho}}_c \mathbf{R}^T \mathbf{g} \cdot \boldsymbol{\eta} dt \tag{C.22}$$

10. $\int_{\mathrm{s_d}}^{l} -\frac{1}{2} EA \left(\left\|\mathbf{r}'\left(\mathrm{s_o}\right)\right\|_2 - 1\right)^2 d\mathrm{s_o}$

    The terms inside the spatial integral of Eq. C.11 need to follow the Leibniz rule in Eq. A.14 ($\frac{\mathrm{d}}{dx}\left(\int_{a(x)}^{b(x)} f\left(x,t\right) dt\right) = f\left(x, b\left(x\right)\right) \cdot \frac{\mathrm{d}}{dx} b\left(x\right) - f\left(x, a\left(x\right)\right) \cdot \frac{\mathrm{d}}{dx} a\left(x\right) + \int_{a(x)}^{b(x)} \frac{\partial}{\partial x} f\left(x,t\right) dt$, with $a\left(x\right) = \mathrm{s_d}, b\left(x\right) = l$, and $f\left(x,t\right) = -\frac{1}{2} EA \left(\left\|\mathbf{r}'\left(\mathrm{s_o}\right)\right\|_2 - 1\right)^2$):

$$\begin{aligned} &\delta \int_{t_o}^{t_f} \left\{ \int_{\mathrm{s_d}}^{l} -\frac{1}{2} EA \left(\left(\left\|\mathbf{r}'\left(\mathrm{s_0}\right)\right\|_2 - 1\right)^2 \right) d\mathrm{s_0} \right\} dt \\ &\quad = \int_{t_o}^{t_f} \left\{ \left(\frac{1}{2} EA \left(\left\|\mathbf{r}'\left(\mathrm{s_d^+}\right)\right\|_2 - 1\right)^2 \right) \delta \mathrm{s_d} - \int_{\mathrm{s_d}}^{l} \delta \left(\frac{1}{2} EA \left(\left(\left\|\mathbf{r}'\left(\mathrm{s_0}\right)\right\|_2 - 1\right)^2 \right) d\mathrm{s_0} \right) \right\} dt \end{aligned}$$

    The second term then follows a similar derivation to that of the seventh term in Section C.1, but with $\delta \mathbf{r}\left(\mathrm{s_d^+}\right) \neq 0$. Starting with the result of IBP:

$$\begin{aligned}
&\int_{t_o}^{t_f}\int_{\mathrm{s_d}}^{l}\delta\left(-\frac{1}{2}EA\left(\left(\|\mathbf{r}'(\mathrm{s}_0)\|_2-1\right)^2\right)\right)d\mathrm{s}_0dt\\
&=\int_{t_o}^{t_f}\left\{-EA\frac{\|\mathbf{r}'(\mathrm{s}_0)\|_2-1}{\|\mathbf{r}'(\mathrm{s}_0)\|_2}\mathbf{r}'(\mathrm{s}_0)\cdot\delta\mathbf{r}(\mathrm{s}_0)\Big|_{\mathrm{s_d}}^{l}\right.\\
&\qquad\qquad\left.+\int_{\mathrm{s_d}}^{l}EA\left(\frac{\|\mathbf{r}'(\mathrm{s}_0)\|_2-1}{\|\mathbf{r}'(\mathrm{s}_0)\|_2}\mathbf{r}'(\mathrm{s}_0)\right)'\cdot\delta\mathbf{r}(\mathrm{s}_0)\,d\mathrm{s}_0\right\}dt\\
&=\int_{t_o}^{t_f}\left\{-EA\frac{\|\mathbf{r}'(l)\|_2-1}{\|\mathbf{r}'(l)\|_2}\mathbf{r}'(l)\cdot\delta\mathbf{r}(l)+EA\frac{\|\mathbf{r}'\left(\mathrm{s_d^+}\right)\|_2-1}{\|\mathbf{r}'\left(\mathrm{s_d^+}\right)\|_2}\mathbf{r}'\left(\mathrm{s_d^+}\right)\cdot\delta\mathbf{r}\left(\mathrm{s_d^+}\right)\right.\\
&\qquad\left.+\int_{\mathrm{s_d}}^{l}EA\left(\frac{\|\mathbf{r}'(\mathrm{s}_0)\|_2-1}{\|\mathbf{r}'(\mathrm{s}_0)\|_2}\mathbf{r}'(\mathrm{s}_0)\right)'\cdot\delta\mathbf{r}(\mathrm{s}_0)\,d\mathrm{s}_0\right\}dt
\end{aligned}$$

Plugging this into the results of the Leibniz rule step yields:

$$\begin{aligned}
&\delta\int_{t_o}^{t_f}\int_{\mathrm{s_d}}^{l}-\frac{1}{2}EA\left(\|\mathbf{r}'(\mathrm{s}_0)\|_2-1\right)^2d\mathrm{s}_0dt=\\
&\qquad\int_{t_o}^{t_f}\left\{\left(\frac{1}{2}EA\left(\left(\|\mathbf{r}'\left(\mathrm{s_d^+}\right)\|_2-1\right)^2\right)\right)\delta\mathrm{s_d}-\mathbf{f}(l)\cdot\delta\mathbf{r}(l)\right.\\
&\qquad\qquad\left.+\mathbf{f}\left(\mathrm{s_d^+}\right)\cdot\delta\mathbf{r}\left(\mathrm{s_d^+}\right)+\int_{\mathrm{s_d}}^{l}\left(\mathbf{f}'(\mathrm{s}_0)\right)\cdot\delta\mathbf{r}(\mathrm{s}_0)\,d\mathrm{s}_0\right\}dt
\end{aligned}$$

where

$$\mathbf{f}(x)=EA\left(\frac{\|\mathbf{r}'(x)\|_2-1}{\|\mathbf{r}'(x)\|_2}\mathbf{r}'(x)\right)\qquad\text{(C.23)}$$

is the elastic string tension at point x. Apply the inertially fixed guide way exit condition given in Eq. C.14 $\left(\delta\mathbf{r}\left(\mathrm{s_d^+}\right)=-\mathbf{r}'\left(\mathrm{s_d^+}\right)\delta\mathrm{s_d}\right)$ to $\int_{t_0}^{t_f}\mathbf{f}\left(\mathrm{s_d^+}\right)\cdot\delta\mathbf{r}\left(\mathrm{s_d^+}\right)dt$ yields the tenth term of Eq. C.11:

$$\begin{aligned}\delta\int_{t_o}^{t_f}\int_{\mathrm{s_d}}^{l}-\frac{1}{2}EA\left(\|\mathbf{r}'(\mathrm{s}_0)\|_2-1\right)^2 d\mathrm{s}_0 dt = \\ \int_{t_o}^{t_f}\left\{\left(\frac{1}{2}EA\left(\left(\|\mathbf{r}'\left(\mathrm{s}_\mathrm{d}^{+}\right)\|_2-1\right)^2\right)-\mathbf{f}\left(\mathrm{s}_\mathrm{d}^{+}\right)\cdot\mathbf{r}'\left(\mathrm{s}_\mathrm{d}^{+}\right)\right)\delta\mathrm{s}_\mathrm{d}\right. \\ \left.-\mathbf{f}(l)\cdot\delta\mathbf{r}(l)+\int_{\mathrm{s_d}}^{l}\left(\mathbf{f}'(\mathrm{s}_0)\right)\cdot\delta\mathbf{r}(\mathrm{s}_0)\,d\mathrm{s}_0\right\}dt\end{aligned} \tag{C.24}$$

11. $\int_{\mathrm{s_d}}^{l}\mu\mathbf{r}(\mathrm{s_o})\cdot\mathbf{g}d\mathrm{s_o}$

    The terms inside the spatial integral of Eq. C.11 need to follow the Leibniz rule in Eq. A.14 ($\frac{\mathrm{d}}{dx}\left(\int_{a(x)}^{b(x)}f(x,t)\,dt\right)=f(x,b(x))\cdot\frac{\mathrm{d}}{dx}b(x)-f(x,a(x))\cdot\frac{\mathrm{d}}{dx}a(x)+\int_{a(x)}^{b(x)}\frac{\partial}{\partial x}f(x,t)\,dt$, with $a(x)=\mathrm{s_d}, b(x)=l$, and $f(x,t)=\mu\mathbf{r}(\mathrm{s_o})\cdot\mathbf{g}$) :

$$\begin{aligned}\delta\int_{t_o}^{t_f}\int_{\mathrm{s_d}}^{l}\mu\mathbf{r}(\mathrm{s}_0)\cdot\mathbf{g}d\mathrm{s}_0dt &= -\int_{t_o}^{t_f}\mu\mathbf{r}\left(\mathrm{s}_\mathrm{d}^{+}\right)\cdot\mathbf{g}\delta\mathrm{s}_\mathrm{d}+\int_{\mathrm{s_d}}^{l}\delta\left(\mu\mathbf{r}(\mathrm{s}_0)\cdot\mathbf{g}\right)d\mathrm{s}_0dt \\ &= -\int_{t_o}^{t_f}\mu\mathbf{r}\left(\mathrm{s}_\mathrm{d}^{+}\right)\cdot\mathbf{g}\delta\mathrm{s}_\mathrm{d}+\int_{\mathrm{s_d}}^{l}\mu\mathbf{g}\cdot\delta\mathbf{r}(\mathrm{s}_0)\,d\mathrm{s}_0dt\end{aligned} \tag{C.25}$$

    where the first term of the Leibniz rule goes to zero because $\frac{d}{d\mathrm{s}_0}(l)=0$, and $\mathrm{s}_\mathrm{d}^{+}$ denotes the string point just outside the reel guide way.

12. $\delta\int_{t_0}^{t_f}\mathcal{W}_{\mathrm{NC}}dt$

    There are three nonconservative forces that need to be accounted for: the string velocity discontinuity at the guide way, the guide way normal or restraint force, and the control moment on the reel.

    (a) String Velocity Discontinuity: Because the string is inextensible when it is spooled up on the reel, and extensible when it is deployed, there exists a velocity discontinuity at the guide way exit. The magnitude of the guide way string velocity at the guide way exit, given in Eq. C.13, just inside ($\mathbf{r}\left(\mathrm{s}_{\mathrm{d}}^{-}\right)$) and outside ($\mathbf{r}\left(\mathrm{s}_{\mathrm{d}}^{+}\right)$) the guide way is:

$$\begin{aligned}\|\dot{\mathbf{r}}\left(\mathrm{s}_{\mathrm{d}}^{-}\right)\|_2 &= \|-\mathbf{r}'\left(\mathrm{s}_{\mathrm{d}}^{-}\right)\dot{\mathrm{s}}_{\mathrm{d}}\|_2\\ \|\dot{\mathbf{r}}\left(\mathrm{s}_{\mathrm{d}}^{+}\right)\|_2 &= \|-\mathbf{r}'\left(\mathrm{s}_{\mathrm{d}}^{+}\right)\dot{\mathrm{s}}_{\mathrm{d}}\|_2\end{aligned}$$

Inside the guide way, the string is inextensible, meaning $\|\mathbf{r}'\left(\mathrm{s}_{\mathrm{d}}^{-}\right)\|_2 = 1$. Outside the guide way, the string is extensible, $\|\mathbf{r}'\left(\mathrm{s}_{\mathrm{d}}^{+}\right)\|_2 = 1 + \epsilon^+$, where ϵ^+ represents the strain in the string just outside the guide way:

$$\begin{aligned}\|\dot{\mathbf{r}}\left(\mathrm{s}_{\mathrm{d}}^{-}\right)\|_2 &= \|-\mathbf{r}'\left(\mathrm{s}_{\mathrm{d}}^{-}\right)\dot{\mathrm{s}}_{\mathrm{d}}\|_2 = |\dot{\mathrm{s}}_{\mathrm{d}}|\\ \|\dot{\mathbf{r}}\left(\mathrm{s}_{\mathrm{d}}^{+}\right)\|_2 &= \|-\mathbf{r}'\left(\mathrm{s}_{\mathrm{d}}^{+}\right)\dot{\mathrm{s}}_{\mathrm{d}}\|_2 = \left(1+\epsilon^+\right)|\dot{\mathrm{s}}_{\mathrm{d}}|\end{aligned}$$

Therefore, the string speed instantaneously changes by $\epsilon^+|\dot{\mathrm{s}}_{\mathrm{d}}|$ at the guide way. This can be considered a plastic impact, resulting in the following nonconservative virtual work:

$$\begin{aligned}\delta W_{\text{plastic}} = Q\delta \mathrm{s}_{\mathrm{d}} &= -\frac{1}{2}\mu\epsilon^2\dot{\mathrm{s}}_{\mathrm{d}}^2\delta\mathrm{s}_{\mathrm{d}}\\ &= -\frac{1}{2}\mu\left(\|\mathbf{r}'\left(\mathrm{s}_{\mathrm{d}}^{+}\right)\|_2 - 1\right)^2\dot{\mathrm{s}}_{\mathrm{d}}^2\delta\mathrm{s}_{\mathrm{d}}\end{aligned} \tag{C.26}$$

where Q is defined in Eq. C.58, and the derivation based on plastic impact given in Section C.4.

(b) Guide way normal force The nonconservative virtual work from the guide way is defined as the normal force keeping the tether attached to the reel multiplied over the distance of the tether:

$$\delta W_{\text{normal}} = N\delta\mathrm{s}_{\mathrm{d}}$$

where N is defined as the elastic strain force just outside the guide way:

$$
\begin{aligned}
N &= -\frac{1}{2}EA\left(\epsilon^{+}\right)^{2} \\
N &= -\frac{1}{2}EA\left(\left(\|\mathbf{r}'\left(\mathrm{s}_{\mathrm{d}}^{+}\right)\|_{2}-1\right)^{2}\right)
\end{aligned}
$$

Combining gives the virtual work done by the tether normal force at the guidway:

$$\delta W_{\mathrm{normal}} = -\frac{1}{2}EA\left(\left(\|\mathbf{r}'\left(\mathrm{s}_{\mathrm{d}}^{+}\right)\|_{2}-1\right)^{2}\right)\delta \mathrm{s}_{\mathrm{d}} \tag{C.27}$$

(c) Control moment due to the reel motor: The nonconservative virtual work from the reel motor is defined as the force on the tether multiplied over the distance of the tether:

$$\delta W_{\mathrm{motor}} = \frac{\mathrm{u}}{\mathrm{d}}\delta \mathrm{s}_{\mathrm{d}} \tag{C.28}$$

where u is the motor torque, and d the radius of the drum.

Combining the three nonconservative virtual work terms in Eq. C.26, Eq. C.28, and Eq. C.27 yields the final term of Eq. C.11:

$$
\begin{aligned}
\delta W_{\mathrm{NC}} &= \delta W_{\mathrm{plastic}} + \delta W_{\mathrm{normal}} + \delta W_{\mathrm{motor}} \\
&= \left(-\frac{1}{2}\mu\left(\|\mathbf{r}'\left(\mathrm{s}_{\mathrm{d}}^{+}\right)\|_{2}-1\right)^{2}\dot{\mathrm{s}}_{\mathrm{d}}^{2} - \frac{1}{2}EA\left(\left(\|\mathbf{r}'\left(\mathrm{s}_{\mathrm{d}}^{+}\right)\|_{2}-1\right)^{2}\right) + \frac{\mathrm{u}}{\mathrm{d}}\right)\delta \mathrm{s}_{\mathrm{d}}.
\end{aligned}
\tag{C.29}
$$

Inserting Eq. C.12, Eq. C.15 through Eq. C.22, Eq. C.24, Eq. C.25, and Eq. C.29 into Hamilton's Principle from Eq. C.11 yields:

$$
\begin{aligned}
\delta\mathcal{S} = \int_{t_0}^{t_f} \Bigg\{ \Bigg(& -\left(\mu \mathrm{s_d} + \frac{\mathrm{m_d}}{2}\right)\ddot{\mathrm{s}}_\mathrm{d} - \frac{1}{2}\mu\dot{\mathrm{s}}_\mathrm{d}^2 + \frac{1}{2}\mu\dot{\mathrm{s}}_\mathrm{d}^2 \mathbf{r}'\left(\mathrm{s}_\mathrm{d}^+\right)\cdot\mathbf{r}'\left(\mathrm{s}_\mathrm{d}^+\right) \\
& +\mu\left(\mathbf{r}_D\cdot\mathbf{g}\right) - \mu \mathrm{gd}\sin\left(\frac{\mathrm{s_d}-\mathrm{b}}{\mathrm{d}}\right) + \cancel{\frac{1}{2}EA\left(\left(\|\mathbf{r}'\left(\mathrm{s}_\mathrm{d}^+\right)\|_2 - 1\right)^2\right)} - \mu\mathbf{r}\left(\mathrm{s}_\mathrm{d}^+\right)\cdot\mathbf{g} \\
& -\mathbf{f}\left(\mathrm{s}_\mathrm{d}^+\right)\cdot\mathbf{r}'\left(\mathrm{s}_\mathrm{d}^+\right) - \frac{1}{2}\mu\left(\|\mathbf{r}'\left(\mathrm{s}_\mathrm{d}^+\right)\|_2 - 1\right)^2\dot{\mathrm{s}}_\mathrm{d}^2 - \cancel{\frac{1}{2}EA\left(\left(\|\mathbf{r}'\left(\mathrm{s}_\mathrm{d}^+\right)\|_2 - 1\right)^2\right)} + \frac{\mathrm{u}}{\mathrm{d}}\Bigg)\delta\mathrm{s_d} \\
& + \left(\mathrm{m}\mathbf{R}\hat{\boldsymbol{\rho}}_c\dot{\boldsymbol{\Omega}} - \mathrm{m}\ddot{\mathbf{r}}\left(l\right) - \mathrm{m}\mathbf{R}\hat{\boldsymbol{\Omega}}^2\boldsymbol{\rho}_c + \mathrm{m}\mathbf{g} - \mathbf{f}\left(l\right)\right)\cdot\delta\mathbf{r}\left(l\right) \\
& + \left(-\mathrm{m}\hat{\boldsymbol{\rho}}_c\mathbf{R}^T\ddot{\mathbf{r}}\left(l\right) - \boldsymbol{\Pi}\dot{\boldsymbol{\Omega}} - \hat{\boldsymbol{\Omega}}\boldsymbol{\Pi}\boldsymbol{\Omega} + \mathrm{m}\hat{\boldsymbol{\rho}}_c\mathbf{R}^T\mathbf{g}\right)\cdot\boldsymbol{\eta} \\
& + \int_{\mathrm{s_d}}^{l}\left(\frac{\partial}{\partial \mathrm{s}_0}\mathbf{f}\left(\mathrm{s}_0\right) + \mu\mathbf{g} - \mu\ddot{\mathbf{r}}\left(\mathrm{s}_0\right)\right)\cdot\delta\mathbf{r}\left(\mathrm{s}_0\right)d\mathrm{s}_0\Bigg\}\,dt = 0
\end{aligned}
$$

Simplifying the terms multiplied by $\delta\mathrm{s_d}$, inserting the relationship $\mathbf{x}\cdot\mathbf{x} = \left(\|\mathbf{x}\|_2\right)^2$ for $\mathbf{r}'\left(\mathrm{s}_\mathrm{d}^+\right)\cdot\mathbf{r}'\left(\mathrm{s}_\mathrm{d}^+\right)$, and $\mathbf{r}\left(\mathrm{s}_\mathrm{d}^+\right) = \mathbf{r}_G$ yields:

$$
\begin{aligned}
\int_{t_0}^{t_f} \Bigg\{ \Bigg(& -\frac{1}{2}\mu\dot{\mathrm{s}}_\mathrm{d}^2 + \frac{1}{2}\mu\left(\|\mathbf{r}'\left(\mathrm{s}_\mathrm{d}^+\right)\|_2\right)^2\dot{\mathrm{s}}_\mathrm{d}^2 - \frac{1}{2}\mu\left(\|\mathbf{r}'\left(\mathrm{s}_\mathrm{d}^+\right)\|_2 - 1\right)^2\dot{\mathrm{s}}_\mathrm{d}^2 \\
& -\left(\mu\mathrm{s_d} + \frac{\mathrm{m_d}}{2}\right)\ddot{\mathrm{s}}_\mathrm{d} + \mu\left(\mathbf{r}_D - \mathbf{r}_G\right)\cdot\mathbf{g} - \mu\mathrm{gd}\sin\left(\frac{\mathrm{s_d}-\mathrm{b}}{\mathrm{d}}\right) - \mathbf{f}\left(\mathrm{s}_\mathrm{d}^+\right)\cdot\mathbf{r}'\left(\mathrm{s}_\mathrm{d}^+\right) + \frac{\mathrm{u}}{\mathrm{d}}\Bigg)\delta\mathrm{s_d} \\
& + \left(\mathrm{m}\mathbf{R}\hat{\boldsymbol{\rho}}_c\dot{\boldsymbol{\Omega}} - \mathrm{m}\ddot{\mathbf{r}}\left(l\right) - \mathrm{m}\mathbf{R}\hat{\boldsymbol{\Omega}}^2\boldsymbol{\rho}_c + \mathrm{m}\mathbf{g} - \mathbf{f}\left(l\right)\right)\cdot\delta\mathbf{r}\left(l\right) \\
& + \left(-\mathrm{m}\hat{\boldsymbol{\rho}}_c\mathbf{R}^T\ddot{\mathbf{r}}\left(l\right) - \boldsymbol{\Pi}\dot{\boldsymbol{\Omega}} - \hat{\boldsymbol{\Omega}}\boldsymbol{\Pi}\boldsymbol{\Omega} + \mathrm{m}\hat{\boldsymbol{\rho}}_c\mathbf{R}^T\mathbf{g}\right)\cdot\boldsymbol{\eta}\Bigg\}\,dt \\
& + \int_{\mathrm{s_d}}^{l}\left(\frac{\partial}{\partial \mathrm{s}_0}\mathbf{f}\left(\mathrm{s}_0\right) + \mu\mathbf{g} - \mu\ddot{\mathbf{r}}\left(\mathrm{s}_0\right)\right)\cdot\delta\mathbf{r}\left(\mathrm{s}_0\right)d\mathrm{s}_0\Bigg\}\,dt = 0
\end{aligned}
$$

Factoring like terms and expanding $\frac{1}{2}\mu\left(\|\mathbf{r}'\left(\mathrm{s}_\mathrm{d}^+\right)\|_2-1\right)^2\dot{\mathrm{s}}_\mathrm{d}^2$ on the first line yields:

$$\begin{aligned}
&\int_{t_0}^{t_f}\frac{1}{2}\mu\dot{\mathrm{s}}_\mathrm{d}^2\left(-1+\left(\|\mathbf{r}'\left(\mathrm{s}_\mathrm{d}^+\right)\|_2\right)^2-\left(\|\mathbf{r}'\left(\mathrm{s}_\mathrm{d}^+\right)\|_2-1\right)^2\right)\delta\mathrm{s}_\mathrm{d}dt\\
&\qquad=\int_{t_0}^{t_f}\frac{1}{2}\mu\dot{\mathrm{s}}_\mathrm{d}^2\left(-1+\cancel{\left(\|\mathbf{r}'\left(\mathrm{s}_\mathrm{d}^+\right)\|_2\right)^2}-\cancel{\left(\|\mathbf{r}'\left(\mathrm{s}_\mathrm{d}^+\right)\|_2\right)^2}+2\|\mathbf{r}'\left(\mathrm{s}_\mathrm{d}^+\right)\|_2-1\right)\delta\mathrm{s}_\mathrm{d}dt\\
&\qquad=\int_{t_0}^{t_f}\mu\dot{\mathrm{s}}_\mathrm{d}^2\left(\|\mathbf{r}'\left(\mathrm{s}_\mathrm{d}^+\right)\|-1\right)\delta\mathrm{s}_\mathrm{d}dt
\end{aligned}\tag{C.30}$$

The final combined variation for the fixed reel elastic string rigid body pendulum:

$$\begin{aligned}
\int_{t_0}^{t_f}\Bigg\{\Bigg(&-\left(\mu\mathrm{s}_\mathrm{d}+\frac{\mathrm{m}_\mathrm{d}}{2}\right)\ddot{\mathrm{s}}_\mathrm{d}+\mu\left(\mathbf{r}_D-\mathbf{r}_G\right)\cdot\mathbf{g}-\mu\mathrm{g}\mathrm{d}\sin\left(\frac{\mathrm{s}_\mathrm{d}-\mathrm{b}}{\mathrm{d}}\right)\\
&-\mathbf{f}\left(\mathrm{s}_\mathrm{d}^+\right)\cdot\mathbf{r}'\left(\mathrm{s}_\mathrm{d}^+\right)+\mu\dot{\mathrm{s}}_\mathrm{d}^2\left(\|\mathbf{r}'\left(\mathrm{s}_\mathrm{d}^+\right)\|_2-1\right)+\frac{\mathrm{u}}{\mathrm{d}}\Bigg)\delta\mathrm{s}_\mathrm{d}\\
&+\left(\mathrm{m}\mathbf{R}\hat{\boldsymbol{\rho}}_c\dot{\boldsymbol{\Omega}}-\mathrm{m}\ddot{\mathbf{r}}\left(l\right)-\mathrm{m}\mathbf{R}\hat{\boldsymbol{\Omega}}^2\boldsymbol{\rho}_c+\mathrm{m}\mathbf{g}-\mathbf{f}\left(l\right)\right)\cdot\delta\mathbf{r}\left(l\right)\\
&+\left(-\mathrm{m}\hat{\boldsymbol{\rho}}_c\mathbf{R}^T\ddot{\mathbf{r}}\left(l\right)-\boldsymbol{\Pi}\dot{\boldsymbol{\Omega}}-\hat{\boldsymbol{\Omega}}\boldsymbol{\Pi}\boldsymbol{\Omega}+\mathrm{m}\hat{\boldsymbol{\rho}}_c\mathbf{R}^T\mathbf{g}\right)\cdot\boldsymbol{\eta}\Bigg\}dt\\
&+\int_{\mathrm{s}_\mathrm{d}}^{l}\left(\frac{\partial}{\partial\mathrm{s}_0}\mathbf{f}\left(\mathrm{s}_0\right)+\mu\mathbf{g}-\mu\ddot{\mathbf{r}}\left(\mathrm{s}_0\right)\right)\cdot\delta\mathbf{r}\left(\mathrm{s}_0\right)d\mathrm{s}_0\Bigg\}dt=0
\end{aligned}\tag{C.31}$$

C.3 Moving Reel - Elastic String - Rigid Body Pendulum / UAV

Inserting the Lagrangian from Eq. 7.38 into the Extended Hamilton's principle of least action from Eq. 7.24 yields:

$$
\begin{aligned}
\delta\mathcal{S} = \delta\int_{t_0}^{t_f} \bigg(& \frac{1}{2}\left(\mathrm{m_b}+\mathrm{m_d}+\mu \mathrm{s_d}\right)\left(\dot{\mathbf{r}}_{\mathrm{D}}\cdot\dot{\mathbf{r}}_{\mathrm{D}}\right)+\frac{1}{2}\left(\mu \mathrm{s_d}+\frac{\mathrm{m_d}}{2}\right)\dot{\mathrm{s}}_{\mathrm{d}}^2+\frac{1}{2}\boldsymbol{\Omega}_{\mathrm{b}}\cdot\boldsymbol{\Pi}_{\mathrm{b}}\boldsymbol{\Omega}_{\mathrm{b}} \\
& +\frac{1}{2}\mathrm{m_u}\dot{\mathbf{r}}\left(l\right)\cdot\dot{\mathbf{r}}\left(l\right)+\mathrm{m_u}\dot{\mathbf{r}}\left(l\right)\cdot\mathbf{R}_{\mathrm{u}}\hat{\boldsymbol{\Omega}}_{\mathrm{u}}\boldsymbol{\rho}_c+\frac{1}{2}\boldsymbol{\Omega}_{\mathrm{u}}\cdot\boldsymbol{\Pi}_{\mathrm{u}}\boldsymbol{\Omega}_{\mathrm{u}} \\
& +\left(\mathrm{m_b}+\mathrm{m_d}+\mu \mathrm{s_d}\right)\mathbf{r}_{\mathrm{D}}\cdot\mathbf{g}+\mu \mathrm{d}^2\left(1-\cos\frac{\mathrm{s_d}-\mathrm{b}}{\mathrm{d}}\right)\hat{\mathbf{e}}_{\mathrm{b1}}\cdot\mathbf{g}-\mu \mathrm{d}^2\sin\frac{\mathrm{s_d}-\mathrm{b}}{\mathrm{d}}\hat{\mathbf{e}}_{\mathrm{b3}}\cdot\mathbf{g} \\
& +\int_{\mathrm{s_d}}^{l}\left(\frac{1}{2}\mu\dot{\mathbf{r}}\left(\mathrm{s}_0\right)\cdot\dot{\mathbf{r}}\left(\mathrm{s}_0\right)-\frac{1}{2}EA\left(\left\|\mathbf{r}'\left(\mathrm{s}_0\right)\right\|_2-1\right)^2+\mu\mathbf{r}\left(\mathrm{s}_0\right)\cdot\mathbf{g}\right)d\mathrm{s}_0 \\
& \qquad +\mathrm{m_u}\left(\mathbf{r}\left(l\right)+\boldsymbol{\rho}_c\right)\cdot\mathbf{g}+\mathcal{W}_{\mathrm{NC}}\bigg)dt=0.
\end{aligned}
\tag{C.32}
$$

Each term will be evaluated individually:

1. $\delta\int_{t_0}^{t_f}\frac{1}{2}\left(\mathrm{m_b}+\mathrm{m_d}+\mu \mathrm{s_d}\right)\left(\dot{\mathbf{r}}_{\mathrm{D}}\cdot\dot{\mathbf{r}}_{\mathrm{D}}\right)dt$

   Taking the variation yields:

$$
\begin{aligned}
&\delta\int_{t_0}^{t_f}\frac{1}{2}\left(\mathrm{m_b}+\mathrm{m_d}+\mu \mathrm{s_d}\right)\dot{\mathbf{r}}_{\mathrm{D}}\cdot\dot{\mathbf{r}}_{\mathrm{D}}dt \\
&\qquad =\int_{t_0}^{t_f}\left(\mathrm{m_b}+\mathrm{m_d}+\mu \mathrm{s_d}\right)\dot{\mathbf{r}}_{\mathrm{D}}\cdot\delta\dot{\mathbf{r}}_{\mathrm{D}}dt+\int_{t_0}^{t_f}\frac{1}{2}\mu\dot{\mathbf{r}}_{\mathrm{D}}\cdot\dot{\mathbf{r}}_{\mathrm{D}}\delta \mathrm{s_d}dt
\end{aligned}
$$

   This term with $\mathrm{m_b}$ and $\mathrm{m_d}$ need IBP, and follows the derivation in Section C.1, mirroring Eq. C.2:

$$
\int_{t_o}^{t_f}\left(\mathrm{m_b}+\mathrm{m_d}\right)\dot{\mathbf{r}}_{\mathrm{D}}\cdot\delta\dot{\mathbf{r}}_{\mathrm{D}}dt=-\int_{t_o}^{t_f}\left(\mathrm{m_b}+\mathrm{m_d}\right)\ddot{\mathbf{r}}_{\mathrm{D}}\cdot\delta\mathbf{r}_{\mathrm{D}}dt
$$

The part of the first term with $\mathrm{s_d}$ also needs IBP (IBP: $\int_a^b u dv = uv|_a^b - \int_a^b v du$ with $u = \mu \mathrm{s_d} \dot{\mathbf{r}}_\mathrm{D}$ and $dv = \delta \dot{\mathbf{r}}_\mathrm{D}$),

$$\int_{t_o}^{t_f} \mu \mathrm{s_d} \dot{\mathbf{r}}_\mathrm{D} \cdot \delta \dot{\mathbf{r}}_\mathrm{D} dt = \mu \mathrm{s_d} \dot{\mathbf{r}}_\mathrm{D} \cancelto{0}{\delta \mathbf{r}_\mathrm{D}|_{t_0}^{t_f}} - \int_{t_o}^{t_f} \mu \mathrm{s_d} \ddot{\mathbf{r}}_\mathrm{D} \cdot \delta \mathbf{r}_\mathrm{D} dt - \int_{t_o}^{t_f} \mu \dot{\mathrm{s}}_\mathrm{d} \dot{\mathbf{r}}_\mathrm{D} \cdot \delta \mathbf{r}_\mathrm{D} dt$$

Combining results in:

$$\delta \int_{t_o}^{t_f} (\mathrm{m_b} + \mathrm{m_d} + \mu \mathrm{s_d}) \dot{\mathbf{r}}_\mathrm{D} \cdot \dot{\mathbf{r}}_\mathrm{D} dt \tag{C.33}$$

$$= \int_{t_o}^{t_f} - (\mathrm{m_b} + \mathrm{m_d} + \mu \mathrm{s_d}) \ddot{\mathbf{r}}_\mathrm{D} \cdot \delta \mathbf{r}_\mathrm{D} - \mu \dot{\mathrm{s}}_\mathrm{d} \dot{\mathbf{r}}_\mathrm{D} \cdot \delta \mathbf{r}_\mathrm{D} + \frac{1}{2} \mu \dot{\mathbf{r}}_\mathrm{D} \cdot \dot{\mathbf{r}}_\mathrm{D} \delta \mathrm{s_d} dt \tag{C.34}$$

2. $\delta \int_{t_0}^{t_f} \frac{1}{2} \left(\mu \mathrm{s_d} + \frac{\mathrm{m_d}}{2} \right) \dot{\mathrm{s}}_\mathrm{d}^2 dt$:

   This term follows the derivation for the reel given in Section C.2 mirroring Eq. C.12:

$$\delta \int_{t_0}^{t_f} \frac{1}{2} \left(\mu \mathrm{s_d} + \frac{\mathrm{m_d}}{2} \right) \dot{\mathrm{s}}_\mathrm{d}^2 dt = \int_{t_0}^{t_f} \left(- \left(\mu \mathrm{s_d} + \frac{\mathrm{m_d}}{2} \right) \ddot{\mathrm{s}}_\mathrm{d} - \frac{1}{2} \mu \dot{\mathrm{s}}_\mathrm{d}^2 \right) \delta \mathrm{s_d} dt \tag{C.35}$$

3. $\delta \int_{t_0}^{t_f} \frac{1}{2} \mathbf{\Omega}_\mathrm{b} \cdot \mathbf{\Pi}_\mathrm{b} \mathbf{\Omega}_\mathrm{b} dt$:

   This term follows the same derivation as the third term in Section C.1, mirroring Eq. C.4:

$$\delta \int_{t_0}^{t_f} \frac{1}{2} \mathbf{\Omega}_\mathrm{b} \cdot \mathbf{\Pi}_\mathrm{b} \mathbf{\Omega}_\mathrm{b} dt = \int_{t_o}^{t_f} \left(-\mathbf{\Pi}_\mathrm{b} \dot{\mathbf{\Omega}}_\mathrm{b} - \hat{\mathbf{\Omega}}_\mathrm{b} \mathbf{\Pi}_\mathrm{b} \mathbf{\Omega}_\mathrm{b} \right) \cdot \boldsymbol{\eta}_\mathrm{b} dt. \tag{C.36}$$

4. $\delta \int_{t_0}^{t_f} \frac{1}{2} \mathrm{m_u} \dot{\mathbf{r}} (l) \cdot \dot{\mathbf{r}} (l) dt$:

This term follows the derivation in Section C.1 for the first term, mirroring Eq. C.2:

$$\delta \int_{t_0}^{t_f} \frac{1}{2} \mathrm{m}_{\mathrm{u}} \dot{\mathbf{r}}\left(l\right) \cdot \dot{\mathbf{r}}\left(l\right) dt = -\int_{t_o}^{t_f} \mathrm{m}_{\mathrm{u}} \ddot{\mathbf{r}}\left(l\right) \cdot \delta r\left(l\right) dt \tag{C.37}$$

5. $\delta \int_{t_0}^{t_f} \mathrm{m}_{\mathrm{u}} \dot{\mathbf{r}}\left(l\right) \cdot \mathbf{R}_{\mathrm{u}} \hat{\boldsymbol{\Omega}}_{\mathrm{u}} \boldsymbol{\rho}_c dt$:

   This term follows the derivation in Section C.2, mirroring Eq. C.3:

$$\begin{aligned}\delta \int_{t_0}^{t_f} & \mathrm{m}_{\mathrm{u}} \dot{\mathbf{r}}\left(l\right) \cdot \mathbf{R}_{\mathrm{u}} \hat{\boldsymbol{\Omega}}_{\mathrm{u}} \boldsymbol{\rho}_c dt \\ &= \int_{t_0}^{t_f} \left\{ \left(-\mathrm{m}_{\mathrm{u}} \mathbf{R}_{\mathrm{u}} \hat{\boldsymbol{\Omega}}_{\mathrm{u}}^2 \boldsymbol{\rho}_c + \mathrm{m}_{\mathrm{u}} \mathbf{R}_{\mathrm{u}} \hat{\boldsymbol{\rho}}_c \dot{\boldsymbol{\Omega}}_{\mathrm{u}} \right) \cdot \delta \mathbf{r}\left(l\right) - \mathrm{m}_{\mathrm{u}} \hat{\boldsymbol{\rho}}_c \mathbf{R}_{\mathrm{u}}^T \ddot{\mathbf{r}}\left(l\right) \cdot \boldsymbol{\eta}_{\mathrm{u}} \right\} dt.\end{aligned} \tag{C.38}$$

6. $\delta \int_{t_0}^{t_f} \frac{1}{2} \boldsymbol{\Omega}_{\mathrm{u}} \cdot \boldsymbol{\Pi}_{\mathrm{u}} \boldsymbol{\Omega}_{\mathrm{u}} dt$:

   This term follows the same derivation as the third term in Section C.1, mirroring Eq. C.4:

$$\delta \int_{t_0}^{t_f} \frac{1}{2} \boldsymbol{\Omega}_{\mathrm{u}} \cdot \boldsymbol{\Pi}_{\mathrm{u}} \boldsymbol{\Omega}_{\mathrm{u}} dt = \int_{t_o}^{t_f} \left(-\boldsymbol{\Pi}_{\mathrm{u}} \dot{\boldsymbol{\Omega}}_{\mathrm{u}} - \hat{\boldsymbol{\Omega}}_{\mathrm{u}} \boldsymbol{\Pi}_{\mathrm{u}} \boldsymbol{\Omega}_{\mathrm{u}} \right) \cdot \boldsymbol{\eta}_{\mathrm{u}} dt. \tag{C.39}$$

7. $\delta \int_{t_0}^{t_f} -\left(\mathrm{m}_{\mathrm{b}} + \mathrm{m}_{\mathrm{r}} + \mu \mathrm{s}_{\mathrm{d}}\right) \mathbf{r}_{\mathrm{d}} \cdot \mathbf{g} dt$

   Taking the variation via chain rule yields:

$$\delta \int_{t_0}^{t_f} -\left(\mathrm{m}_{\mathrm{b}} + \mathrm{m}_{\mathrm{d}} + \mu \mathrm{s}_{\mathrm{d}}\right) \mathbf{r}_{\mathrm{d}} \cdot \mathbf{g} dt = \int_{t_0}^{t_f} -\left(\mathrm{m}_{\mathrm{b}} + \mathrm{m}_{\mathrm{d}} + \mu \mathrm{s}_{\mathrm{d}}\right) \mathbf{g} \cdot \delta \mathbf{r}_{\mathrm{D}} - \mu \mathbf{r}_{\mathrm{d}} \cdot g \delta \mathrm{s}_{\mathrm{d}} dt \tag{C.40}$$

8. $\delta \int_{t_0}^{t_f} \mu \mathrm{d}^2 \left(1 - \cos \frac{\mathrm{s_d} - \mathrm{b}}{\mathrm{d}}\right) \hat{\mathbf{e}}_{\mathrm{b}1} \cdot \mathbf{g} dt$

   Because $\hat{\mathbf{e}}_{\mathrm{b}1}$ varies in orientation, before taking the variation, it is helpful to convert to global coordinates via $\hat{\mathbf{e}}_{\mathrm{b}1} = \mathbf{R}_\mathrm{b}\hat{\mathbf{e}}_1$. Taking the variation via chain rule yields:

$$\delta \int_{t_0}^{t_f} \mu \mathrm{d}^2 \left(1 - \cos\left(\frac{\mathrm{s_d} - \mathrm{b}}{\mathrm{d}}\right)\right) \mathbf{g} \cdot \mathbf{R}_\mathrm{b}\hat{\mathbf{e}}_1 dt$$
$$= \int_{t_0}^{t_f} \mu \mathrm{d}^2 \left(1 - \cos\left(\frac{\mathrm{s_d} - \mathrm{b}}{\mathrm{d}}\right)\right) \mathbf{g} \cdot \delta\mathbf{R}_\mathrm{b}\hat{\mathbf{e}}_1 + \mu \mathrm{d} \sin\left(\frac{\mathrm{s_d} - \mathrm{b}}{\mathrm{d}}\right) \mathbf{R}_\mathrm{b}\hat{\mathbf{e}}_1 \cdot \mathbf{g} \delta \mathrm{s_d} dt$$

   The first term follows the derivation given in Eq. A.12 ($\int_{t_o}^{t_f} \mathbf{x} \cdot \delta\mathbf{R}\mathbf{y} dt = \int_{t_o}^{t_f} \hat{\mathbf{y}}\mathbf{R}^T\mathbf{x} \cdot \boldsymbol{\eta} dt$):

$$\delta \int_{t_0}^{t_f} \mu \mathrm{d}^2 \left(1 - \cos\left(\frac{\mathrm{s_d} - \mathrm{b}}{\mathrm{d}}\right)\right) \mathbf{g} \cdot \mathbf{R}_\mathrm{b}\hat{\mathbf{e}}_1 dt$$
$$= \int_{t_0}^{t_f} -\mu \mathrm{d}^2 \left(\cos\left(\frac{\mathrm{s_d} - \mathrm{b}}{\mathrm{d}}\right) - 1\right) \hat{\hat{\mathbf{e}}}_1 \mathbf{R}_\mathrm{b}^T \mathbf{g} \cdot \boldsymbol{\eta}_\mathrm{b} + \mu \mathrm{d} \sin\left(\frac{\mathrm{s_d} - \mathrm{b}}{\mathrm{d}}\right) \mathbf{R}_\mathrm{b}\hat{\mathbf{e}}_1 \cdot \mathbf{g} \delta \mathrm{s_d} dt \tag{C.41}$$

   where $\hat{\hat{\mathbf{e}}}_1 = \begin{bmatrix} 0 & 0 & 0 \\ 0 & 0 & -1 \\ 0 & 1 & 0 \end{bmatrix}$ is the skew symmetric mapping of the $\hat{\mathbf{e}}_1$ vector.

9. $\delta \int_{t_0}^{t_f} -\mu \mathrm{d}^2 \sin \frac{\mathrm{s_d} - \mathrm{b}}{\mathrm{d}} \hat{\mathbf{e}}_{\mathrm{b}3} \cdot \mathbf{g} dt$

   Similar to the last term, because $\hat{\mathbf{e}}_{\mathrm{b}3}$ varies in orientation, before taking the variation, it is helpful to convert to global coordinates via $\hat{\mathbf{e}}_{\mathrm{b}3} = \mathbf{R}_\mathrm{b}\hat{\mathbf{e}}_3$. Taking the variation via chain rule yields:

$$\delta\int_{t_0}^{t_f} -\mu \mathrm{d}^2 \sin\left(\frac{\mathrm{s_d}-\mathrm{b}}{\mathrm{d}}\right)\mathbf{g}\cdot\mathbf{R}_\mathrm{b}\hat{\mathbf{e}}_3 dt =$$
$$\int_{t_0}^{t_f} -\mu \mathrm{d}^2 \sin\left(\frac{\mathrm{s_d}-\mathrm{b}}{\mathrm{d}}\right)\mathbf{g}\cdot\delta\mathbf{R}_\mathrm{b}\hat{\mathbf{e}}_3 - \mu\mathrm{d}\cos\left(\frac{\mathrm{s_d}-\mathrm{b}}{\mathrm{d}}\right)\mathbf{R}_\mathrm{b}\hat{\mathbf{e}}_3\cdot\mathbf{g}\delta\mathrm{s_d} dt$$

The first term follows the derivation given in Eq. A.12 ($\int_{t_o}^{t_f}\mathbf{x}\cdot\delta\mathbf{R}\mathbf{y}dt = \int_{t_o}^{t_f}\hat{\mathbf{y}}\mathbf{R}^T\mathbf{x}\cdot\boldsymbol{\eta}dt$):

$$\delta\int_{t_0}^{t_f} - \mu \mathrm{d}^2 \sin\left(\frac{\mathrm{s_d}-\mathrm{b}}{\mathrm{d}}\right)\mathbf{g}\cdot\mathbf{R}_\mathrm{b}\hat{\mathbf{e}}_3 dt$$
$$= \int_{t_0}^{t_f} -\mu \mathrm{d}^2 \sin\left(\frac{\mathrm{s_d}-\mathrm{b}}{\mathrm{d}}\right)\hat{\hat{\mathbf{e}}}_3\mathbf{R}_\mathrm{b}^T\mathbf{g}\cdot\boldsymbol{\eta}_\mathrm{b} - \mu\mathrm{d}\cos\left(\frac{\mathrm{s_d}-\mathrm{b}}{\mathrm{d}}\right)\mathbf{R}_\mathrm{b}\hat{\mathbf{e}}_3\cdot\mathbf{g}\delta\mathrm{s_d}\Bigg\} dt \tag{C.42}$$

where $\hat{\hat{\mathbf{e}}}_3 = \begin{bmatrix} 0 & -1 & 0 \\ 1 & 0 & 0 \\ 0 & 0 & 0 \end{bmatrix}$ is the skew symmetric mapping of the $\hat{\mathbf{e}}_3$ vector.

10. $\delta\int_{t_0}^{t_f}\int_{\mathrm{s_d}}^{l}\frac{1}{2}\mu\dot{\mathbf{r}}(\mathrm{s}_0)\cdot\dot{\mathbf{r}}(\mathrm{s}_0)\,d\mathrm{s}_0 dt$:

This term follows the same derivation, using Leibniz's rule and Green's theorem given in Section C.2 for the second term. However the application of the boundary conditions are different because the reel is not inertially fixed, resulting in Eq. C.15 before applying boundary conditions:

$$\delta\int_{t_0}^{t_f}\int_{\mathrm{s_d}}^{l}\frac{1}{2}\mu\dot{\mathbf{r}}(\mathrm{s}_0)\cdot\dot{\mathbf{r}}(\mathrm{s}_0)\,d\mathrm{s}_0 dt = \int_{t_0}^{t_f}\Bigg\{-\int_{\mathrm{s_d}}^{l}\mu\ddot{\mathbf{r}}(\mathrm{s}_0)\cdot\delta\mathbf{r}(\mathrm{s}_0)\,d\mathrm{s}_0$$
$$-\frac{1}{2}\mu\dot{\mathbf{r}}\left(\mathrm{s_d^+}\right)\cdot\dot{\mathbf{r}}\left(\mathrm{s_d^+}\right)\cdot\delta\mathrm{s_d} + \mu\dot{\mathbf{r}}\left(\mathrm{s_d^+}\right)\cdot\delta\mathbf{r}\left(\mathrm{s_d^+}\right)\dot{\mathrm{s}}_\mathrm{d}\Bigg\} dt$$

The guide way boundary condition can be applied to simplify some terms. However, in this case, the guide way, given by $\mathbf{r}_G = \mathbf{r}\left(\mathrm{s_d}\right) = \left(\mathbf{r}_\mathrm{d} + \mathbf{R}_\mathrm{b}\boldsymbol{\rho}_g\right)$, is no longer inertially fixed. Using the chain rule:

$$\begin{aligned}
\dot{\mathbf{r}}_\mathrm{G} = \dot{\mathbf{r}}\left(\mathrm{s_d^+}\right) + \mathbf{r}'\left(\mathrm{s_d^+}\right)\dot{\mathrm{s}}_\mathrm{d} &= \dot{\mathbf{r}}_\mathrm{D} + \dot{\mathbf{R}}_\mathrm{b}\boldsymbol{\rho}_g \\
&= \dot{\mathbf{r}}_\mathrm{D} + \mathbf{R}_\mathrm{b}\hat{\boldsymbol{\Omega}}_\mathrm{b}\boldsymbol{\rho}_g \\
&= \dot{\mathbf{r}}_\mathrm{D} - \mathbf{R}_\mathrm{b}\hat{\boldsymbol{\rho}}_g\boldsymbol{\Omega}_\mathrm{b}
\end{aligned}$$

where the Kinematic relationship given in Eq. A.5, and the identity from Eq. A.2 was used to swap the hat map. Similarly, using the chain rule for the variation:

$$\delta\mathbf{r}_\mathrm{d} = \delta\mathbf{r}\left(\mathrm{s_d^+}\right) + \mathbf{r}'\left(\mathrm{s_d^+}\right)\delta\mathrm{s_d} = \delta\mathbf{r}_\mathrm{D} + \delta\mathbf{R}_\mathrm{b}\boldsymbol{\rho}_g$$

Solving for $\dot{\mathbf{r}}\left(\mathrm{s_d^+}\right)$ and $\delta\mathbf{r}\left(\mathrm{s_d^+}\right)$ yields the guide way boundary conditions:

$$\begin{aligned}
\dot{\mathbf{r}}\left(\mathrm{s_d^+}\right) &= -\mathbf{r}'\left(\mathrm{s_d^+}\right)\dot{\mathrm{s}}_\mathrm{d} + \dot{\mathbf{r}}_\mathrm{D} - \mathbf{R}_\mathrm{b}\hat{\boldsymbol{\rho}}_g\boldsymbol{\Omega}_\mathrm{b} \\
\delta\mathbf{r}\left(\mathrm{s_d^+}\right) &= -\mathbf{r}'\left(\mathrm{s_d^+}\right)\delta\mathrm{s_d} + \delta\mathbf{r}_\mathrm{D} + \delta\mathbf{R}_\mathrm{b}\boldsymbol{\rho}_g
\end{aligned} \tag{C.43}$$

Plugging the boundary condition in for $\int_{t_0}^{t_f} -\frac{1}{2}\mu\dot{\mathbf{r}}\left(\mathrm{s_d^+}\right)\cdot\dot{\mathbf{r}}\left(\mathrm{s_d^+}\right)\delta\mathrm{s_d}dt$ and $\int_{t_0}^{t_f}\mu\dot{\mathbf{r}}\left(\mathrm{s_d^+}\right)\cdot\delta\mathbf{r}\left(\mathrm{s_d^+}\right)\dot{\mathrm{s}}_\mathrm{d}dt$ yields:

$$\begin{aligned}
&\delta \int_{t_0}^{t_f} \int_{\mathrm{s_d}}^{l} \frac{1}{2}\mu \dot{\mathbf{r}}\left(\mathrm{s}_0\right) \cdot \dot{\mathbf{r}}\left(\mathrm{s}_0\right) d\mathrm{s}_0 dt \\
&= \int_{t_0}^{t_f} \Bigg\{ - \int_{\mathrm{s_d}}^{l} \mu \ddot{\mathbf{r}}\left(\mathrm{s}_0\right) \cdot \delta \mathbf{r}\left(\mathrm{s}_0\right) d\mathrm{s}_0 \\
&- \frac{1}{2}\mu \left(-\mathbf{r}'\left(\mathrm{s}_\mathrm{d}^{+}\right) \dot{\mathrm{s}}_\mathrm{d} + \dot{\mathbf{r}}_\mathrm{D} - \mathbf{R}_\mathrm{b} \hat{\boldsymbol{\rho}}_g \boldsymbol{\Omega}_\mathrm{b}\right) \cdot \left(-\mathbf{r}'\left(\mathrm{s}_\mathrm{d}^{+}\right) \dot{\mathrm{s}}_\mathrm{d} + \dot{\mathbf{r}}_\mathrm{D} - \mathbf{R}_\mathrm{b} \hat{\boldsymbol{\rho}}_g \boldsymbol{\Omega}_\mathrm{b}\right) \cdot \delta \mathrm{s}_\mathrm{d} \\
&+\mu \left(-\mathbf{r}'\left(\mathrm{s}_\mathrm{d}^{+}\right) \dot{\mathrm{s}}_\mathrm{d} + \dot{\mathbf{r}}_\mathrm{D} - \mathbf{R}_\mathrm{b} \hat{\boldsymbol{\rho}}_g \boldsymbol{\Omega}_\mathrm{b}\right) \cdot \left(-\mathbf{r}'\left(\mathrm{s}_\mathrm{d}^{+}\right) \delta \mathrm{s}_\mathrm{d} + \delta \mathbf{r}_\mathrm{D} + \delta \mathbf{R}_\mathrm{b} \boldsymbol{\rho}_g\right) \dot{\mathrm{s}}_\mathrm{d} \Big\} \, dt
\end{aligned}$$

Multiplying only the first term inside the parenthesis for the first set of boundary conditions, all the terms for the second set of boundary conditions and simplifying terms (via swapping the hatmap, and applying the rotation matrix variation identity in Eq. A.12 ($\int_{t_o}^{t_f} \mathbf{x} \cdot \delta \mathbf{R} \mathbf{y} dt = \int_{t_o}^{t_f} \mathbf{x}^T \delta \mathbf{R} \mathbf{y} dt = \int_{t_o}^{t_f} \hat{\mathbf{y}} \mathbf{R}^T \mathbf{x} \cdot \boldsymbol{\eta} dt$) yields:

$$\begin{aligned}
&\delta \int_{t_0}^{t_f} \int_{\mathrm{s_d}}^{l} \frac{1}{2}\mu \dot{\mathbf{r}}\left(\mathrm{s}_0\right) \cdot \dot{\mathbf{r}}\left(\mathrm{s}_0\right) d\mathrm{s}_0 dt \\
&= \int_{t_0}^{t_f} \Bigg\{ - \int_{\mathrm{s_d}}^{l} \mu \ddot{\mathbf{r}}\left(\mathrm{s}_0\right) \cdot \delta \mathbf{r}\left(\mathrm{s}_0\right) d\mathrm{s}_0 \\
&+ \Bigg(-\frac{1}{2}\mu \dot{\mathrm{s}}_\mathrm{d}^2 \mathbf{r}'\left(\mathrm{s}_\mathrm{d}^{+}\right) \cdot \mathbf{r}'\left(\mathrm{s}_\mathrm{d}^{+}\right) + \mu \dot{\mathrm{s}}_\mathrm{d} \dot{\mathbf{r}}_\mathrm{D} \cdot \mathbf{r}'\left(\mathrm{s}_\mathrm{d}^{+}\right) - \mu \dot{\mathrm{s}}_\mathrm{d} \mathbf{R}_\mathrm{b} \hat{\boldsymbol{\rho}}_g \boldsymbol{\Omega}_\mathrm{b} \cdot \mathbf{r}'\left(\mathrm{s}_\mathrm{d}^{+}\right) \\
&- \frac{1}{2}\mu \left(\dot{\mathbf{r}}_\mathrm{D} - \mathbf{R}_\mathrm{b} \hat{\boldsymbol{\rho}}_g \boldsymbol{\Omega}_\mathrm{b}\right) \cdot \left(\dot{\mathbf{r}}_\mathrm{D} - \mathbf{R}_\mathrm{b} \hat{\boldsymbol{\rho}}_g \boldsymbol{\Omega}_\mathrm{b}\right) \Bigg) \delta \mathrm{s}_\mathrm{d} \\
&\left(\mu \dot{\mathrm{s}}_\mathrm{d}^2 \mathbf{r}'\left(\mathrm{s}_\mathrm{d}^{+}\right) \cdot \mathbf{r}'\left(\mathrm{s}_\mathrm{d}^{+}\right) - \mu \dot{\mathrm{s}}_\mathrm{d} \dot{\mathbf{r}}_\mathrm{D} \cdot \mathbf{r}'\left(\mathrm{s}_\mathrm{d}^{+}\right) + \mu \dot{\mathrm{s}}_\mathrm{d} \mathbf{R}_\mathrm{b} \hat{\boldsymbol{\rho}}_g \boldsymbol{\Omega}_\mathrm{b} \cdot \mathbf{r}'\left(\mathrm{s}_\mathrm{d}^{+}\right)\right) \delta \mathrm{s}_\mathrm{d} \\
&+ \left(-\mu \dot{\mathrm{s}}_\mathrm{d}^2 \mathbf{r}'\left(\mathrm{s}_\mathrm{d}^{+}\right) + \mu \dot{\mathrm{s}}_\mathrm{d} \dot{\mathbf{r}}_\mathrm{D} - \mu \dot{\mathrm{s}}_\mathrm{d} \mathbf{R}_\mathrm{b} \hat{\boldsymbol{\rho}}_g \boldsymbol{\Omega}_\mathrm{b} \right) \cdot \delta \mathbf{r}_\mathrm{D} \\
&\left(-\mu \dot{\mathrm{s}}_\mathrm{d}^2 \hat{\boldsymbol{\rho}}_g \mathbf{R}_\mathrm{b}^T \mathbf{r}'\left(\mathrm{s}_\mathrm{d}^{+}\right) + \mu \dot{\mathrm{s}}_\mathrm{d} \hat{\boldsymbol{\rho}}_g \mathbf{R}_\mathrm{b}^T \dot{\mathbf{r}}_\mathrm{D} - \mu \dot{\mathrm{s}}_\mathrm{d} \hat{\boldsymbol{\rho}}_g^2 \boldsymbol{\Omega}_\mathrm{b}\right) \cdot \boldsymbol{\eta}_\mathrm{b} dt
\end{aligned}$$

simplifying terms results in:

$$\begin{aligned}
&\delta \int_{t_0}^{t_f} \int_{\mathrm{s_d}}^{l} \frac{1}{2}\mu \dot{\mathbf{r}}\left(\mathrm{s}_0\right) \cdot \dot{\mathbf{r}}\left(\mathrm{s}_0\right) d\mathrm{s}_0 dt \\
&= \int_{t_0}^{t_f} \left\{ - \int_{\mathrm{s_d}}^{l} \mu \ddot{\mathbf{r}}\left(\mathrm{s}_0\right) \cdot \delta \mathbf{r}\left(\mathrm{s}_0\right) d\mathrm{s}_0 \right. \\
&\quad \left(\frac{1}{2}\mu \dot{\mathrm{s}}_{\mathrm{d}}^2 \mathbf{r}'\left(\mathrm{s}_{\mathrm{d}}^{+}\right) \cdot \mathbf{r}'\left(\mathrm{s}_{\mathrm{d}}^{+}\right) - \frac{1}{2}\mu \left(\dot{\mathbf{r}}_{\mathrm{D}} - \mathbf{R}_{\mathrm{b}} \hat{\boldsymbol{\rho}}_g \boldsymbol{\Omega}_{\mathrm{b}}\right) \cdot \left(\dot{\mathbf{r}}_{\mathrm{D}} - \mathbf{R}_{\mathrm{b}} \hat{\boldsymbol{\rho}}_g \boldsymbol{\Omega}_{\mathrm{b}}\right) \right) \delta \mathrm{s}_{\mathrm{d}} \\
&\quad + \left(-\mu \dot{\mathrm{s}}_{\mathrm{d}}^2 \mathbf{r}'\left(\mathrm{s}_{\mathrm{d}}^{+}\right) + \mu \dot{\mathrm{s}}_{\mathrm{d}} \dot{\mathbf{r}}_{\mathrm{D}} - \mu \dot{\mathrm{s}}_{\mathrm{d}} \mathbf{R}_{\mathrm{b}} \hat{\boldsymbol{\rho}}_g \boldsymbol{\Omega}_{\mathrm{b}} \right) \cdot \delta \mathbf{r}_{\mathrm{D}} \\
&\quad + \left(-\mu \dot{\mathrm{s}}_{\mathrm{d}}^2 \hat{\boldsymbol{\rho}}_g \mathbf{R}_{\mathrm{b}}^T \mathbf{r}'\left(\mathrm{s}_{\mathrm{d}}^{+}\right) + \mu \dot{\mathrm{s}}_{\mathrm{d}} \hat{\boldsymbol{\rho}}_g \mathbf{R}_{\mathrm{b}}^T \dot{\mathbf{r}}_{\mathrm{D}} - \mu \dot{\mathrm{s}}_{\mathrm{d}} \hat{\boldsymbol{\rho}}_g^2 \boldsymbol{\Omega}_{\mathrm{b}} \right) \cdot \boldsymbol{\eta}_{\mathrm{b}} dt
\end{aligned} \tag{C.44}$$

11. $\delta \int_{t_0}^{t_f} \int_{\mathrm{s_d}}^{l} -\frac{1}{2} EA \left(\left\|\mathbf{r}'\left(\mathrm{s}_0\right)\right\|_2 - 1\right)^2 d\mathrm{s}_0 dt$:

This term follows the same derivation given in Section C.2 resulting in Eq. C.24, but also with different boundary condition due to the moving reel. Starting from the result of the Leibniz rule before the boundary conditions are applied yields:

$$\begin{aligned}
&\delta \int_{t_o}^{t_f} \int_{\mathrm{s_d}}^{l} -\frac{1}{2} EA \left(\left\|\mathbf{r}'\left(\mathrm{s}_0\right)\right\|_2 - 1\right)^2 d\mathrm{s}_0 dt \\
&\qquad = \int_{t_o}^{t_f} \left\{ \left(\frac{1}{2} EA \left(\left(\left\|\mathbf{r}'\left(\mathrm{s}_{\mathrm{d}}^{+}\right)\right\|_2 - 1\right)^2 \right) \right) \delta \mathrm{s}_{\mathrm{d}} - \mathbf{f}\left(l\right) \cdot \delta \mathbf{r}\left(l\right) \right. \\
&\qquad\qquad \left. + \mathbf{f}\left(\mathrm{s}_{\mathrm{d}}^{+}\right) \cdot \delta \mathbf{r}\left(\mathrm{s}_{\mathrm{d}}^{+}\right) + \int_{\mathrm{s_d}}^{l} \left(\mathbf{f}'\left(\mathrm{s}_0\right)\right) \cdot \delta \mathbf{r}\left(\mathrm{s}_0\right) d\mathrm{s}_0 \right\} dt
\end{aligned}$$

where again $\mathbf{f}\left(x\right) = EA\left(\frac{\left\|\mathbf{r}'(x)\right\|_2 - 1}{\left\|\mathbf{r}'(x)\right\|} \mathbf{r}'\left(x\right)\right)$ is the tether tension at point x.

Applying the guide way boundary condition from Eq. C.43 yields:

$$
\begin{aligned}
&\delta \int_{t_o}^{t_f} \int_{\mathrm{s_d}}^{l} -\frac{1}{2}EA\left(\|\mathbf{r}'\left(\mathrm{s_0}\right)\|_2 - 1\right)^2 d\mathrm{s_0}dt \\
&\qquad = \int_{t_o}^{t_f} \Bigg\{ \left(\frac{1}{2}EA\left(\left(\|\mathbf{r}'\left(\mathrm{s_d^+}\right)\|_2 - 1\right)^2\right) - \mathbf{f}\left(\mathrm{s_d^+}\right)\cdot\mathbf{r}'\left(\mathrm{s_d^+}\right)\right)\delta\mathrm{s_d} \\
&\qquad\qquad - \mathbf{f}\left(l\right)\cdot\delta\mathbf{r}\left(l\right) + \mathbf{f}\left(\mathrm{s_d^+}\right)\cdot\delta\mathbf{r}_\mathrm{D} + \hat{\boldsymbol{\rho}}_g\mathbf{R}_\mathrm{b}^T\mathbf{f}\left(\mathrm{s_d^+}\right)\cdot\boldsymbol{\eta}_\mathrm{b}dt \\
&\qquad\qquad + \int_{\mathrm{s_d}}^{l}\left(\mathbf{f}'\left(\mathrm{s_0}\right)\right)\cdot\delta\mathbf{r}\left(\mathrm{s_0}\right)d\mathrm{s_0}\Bigg\}dt
\end{aligned}
\tag{C.45}
$$

12. $\delta\int_{t_0}^{t_f}\int_{\mathrm{s_d}}^{l}\mu\mathbf{r}\left(\mathrm{s_0}\right)\cdot\mathbf{g}d\mathrm{s_0}dt$

This term follows the same derivation as in Section C.2, for the eleventh term given in Eq. C.25, repeated here:

$$
\delta\int_{t_o}^{t_f}\int_{\mathrm{s_d}}^{l}\mu\mathbf{r}\left(\mathrm{s_0}\right)\cdot\mathbf{g}d\mathrm{s_0}dt = -\int_{t_o}^{t_f}\mu\mathbf{r}\left(\mathrm{s_d^+}\right)\cdot\mathbf{g}\delta\mathrm{s_d} + \int_{\mathrm{s_d}}^{l}\mu\mathbf{g}\cdot\delta\mathbf{r}\left(\mathrm{s_0}\right)d\mathrm{s_0}dt \tag{C.46}
$$

13. $\delta\int_{t_0}^{t_f}\mathrm{m_u}\mathbf{r}\left(l\right)\cdot\mathbf{g}dt$

This term follows the same derivation as the fifth term in Section C.1, repeating Eq. C.6 here:

$$
\delta\int_{t_0}^{t_f}\mathrm{m_u}\mathbf{r}\left(l\right)\cdot\mathbf{g}dt = \int_{t_0}^{t_f}\mathrm{m_u}\mathbf{g}\cdot\delta\mathbf{r}\left(l\right)dt \tag{C.47}
$$

14. $\delta\int_{t_0}^{t_f}\mathrm{m_u}\mathbf{R}_\mathrm{u}\boldsymbol{\rho}_c\cdot\mathbf{g}dt$

This term follows the same derivation as the sixth term in Section C.1, repeating Eq.

C.7:

$$\delta \int_{t_0}^{t_f} \mathrm{m_u} \mathbf{R}_\mathrm{u} \boldsymbol{\rho}_c \cdot \mathbf{g} dt = \int_{t_0}^{t_f} \mathrm{m_u} \hat{\boldsymbol{\rho}}_c \mathbf{R}_\mathrm{u}^T \mathbf{g} \cdot \boldsymbol{\eta}_\mathrm{u} dt \tag{C.48}$$

15. $\delta \int_{t_0}^{t_f} \mathcal{W}_{\mathrm{NC}} dt$

    There are five nonconservative forces that need to be accounted for: the string velocity discontinuity at the guide way, the guide way normal or restraint force, the control moment on the reel, the UAV overall applied thrust force, and the UAV overall applied moment. The first two follow the same derivation as in Section C.2, and the control moment has an added term due to the rotation of the body.

    (a) String Velocity Discontinuity:

    The string velocity discontinuity can again be considered as a plastic impact, resulting in the following nonconservative virtual work, with the same derivation resulting in Eq. C.26:

$$\delta W_{\mathrm{Plastic}} = Q \delta \mathrm{s_d} = -\frac{1}{2} \mu \left(\| \mathbf{r}' \left(\mathrm{s_d^+} \right) \|_2 - 1 \right)^2 \dot{\mathrm{s}}_\mathrm{d}^2 \delta \mathrm{s_d} \tag{C.49}$$

    where Q is defined in Eq. C.58, and the derivation based on plastic impact given in Section. C.4.

    (b) Guide way normal force:

    The nonconservative virtual work from the guide way is defined as the normal force keeping the tether attached to the reel multiplied over the distance of the tether, with the same derivation given in Eq. C.27, repeated here:

$$\delta W_{\mathrm{Normal}} = -\frac{1}{2} EA \left(\left(\| \mathbf{r}' \left(\mathrm{s_d^+} \right) \|_2 - 1 \right)^2 \right) \delta \mathrm{s_d} \tag{C.50}$$

(c) Control moment due to the reel motor:

The nonconservative virtual work from the reel motor is defined as the force on the tether multiplied over the virtual displacement of the tether plus the dot product of the moment applied to the rigid body rotation with the varitation of the rotation matrix $\boldsymbol{\eta}_{\mathrm{b}}$, similar to the derivation given in Eq. C.28, yielding:

$$\delta W_{\mathrm{motor}} = \frac{\mathrm{u}}{\mathrm{d}} \delta \mathrm{s}_{\mathrm{d}} - u \hat{\mathbf{e}}_{\mathrm{b2}} \cdot \boldsymbol{\eta}_{\mathrm{b}} \tag{C.51}$$

where u is the motor torque, and d the radius of the drum.

(d) UAV normal force and applied moment

The nonconservative virtual work from the UAV normal force is defined as the dot product of the normal force (F_{UAV}) from all the UAV's rotors in the direction of the orientation and the variation of the position vector $\mathbf{r}(l)$. The virtual work from the UAV applied moment is defined as the dot product of the moment on each axis ($\boldsymbol{\tau}_{\mathrm{UAV}} = \begin{bmatrix} \tau_\phi & \tau_\theta & \tau_\psi \end{bmatrix}^T$) with the variation of the rotation matrix, $\boldsymbol{\eta}_{\mathrm{u}}$:

$$\delta W_{\mathrm{UAV}} = -F_{\mathrm{UAV}} \hat{\mathbf{e}}_{\mathrm{u3}} \cdot \delta \mathbf{r}(l) + \boldsymbol{\tau}_{\mathrm{UAV}} \cdot \boldsymbol{\eta}_{\mathrm{u}}$$

Inserting the definition of the body fixed coordinate ($\hat{\mathbf{e}}_{\mathrm{u3}} = \mathbf{R}_{\mathrm{u}} \hat{\mathbf{e}}_3$):

$$\delta W_{\mathrm{UAV}} = -F_{\mathrm{UAV}} \mathbf{R}_{\mathrm{u}} \hat{\mathbf{e}}_3 \cdot \delta \mathbf{r}(l) + \boldsymbol{\tau}_{\mathrm{UAV}} \cdot \boldsymbol{\eta}_{\mathrm{u}} \tag{C.52}$$

Combining the four nonconservative virtual work terms in Eq. C.49, Eq. C.51, Eq. C.50, and Eq. C.52 yields:

$$\begin{aligned}
W_{\mathrm{NC}} &= \delta W_{\mathrm{Plastic}} + \delta W_{\mathrm{Normal}} + \delta W_{\mathrm{motor}} + \delta W_{\mathrm{UAV}} \\
&= \left(-\frac{1}{2}\mu\left(\|\mathbf{r}'\left(\mathrm{s}_{\mathrm{d}}^{+}\right)\|_2 - 1\right)^2 \dot{\mathrm{s}}_{\mathrm{d}}^2 - \frac{1}{2}EA\left(\left(\|\mathbf{r}'\left(\mathrm{s}_{\mathrm{d}}^{+}\right)\|_2 - 1\right)^2\right) + \frac{\mathrm{u}}{\mathrm{d}}\right)\delta \mathrm{s}_{\mathrm{d}} \qquad \text{(C.53)} \\
&- u\hat{\mathbf{e}}_2 \cdot \boldsymbol{\eta}_{\mathrm{b}} - F_{\mathrm{UAV}}\mathbf{R}_{\mathrm{u}}\hat{\mathbf{e}}_3 \cdot \delta\mathbf{r}\left(l\right) + \boldsymbol{\tau}_{\mathrm{UAV}} \cdot \boldsymbol{\eta}_{\mathrm{u}}
\end{aligned}$$

Inserting Eq. C.34 through Eq. C.42, Eq. C.44 through Eq. C.48, and Eq. C.53 into the variation equation from Eq. C.32 yields:

$$\begin{aligned}
\delta\mathcal{S} = \int_{t_0}^{t_f} \Bigg\{ \Bigg(& - \left(\mathrm{m}_{\mathrm{b}} + \mathrm{m}_{\mathrm{d}} + \mu \mathrm{s}_{\mathrm{d}}\right)\ddot{\mathbf{r}}_{\mathrm{D}} - \mu\dot{\mathrm{s}}_{\mathrm{d}}\dot{\mathbf{r}}_{\mathrm{D}} - \mu\dot{\mathrm{s}}_{\mathrm{d}}^2\mathbf{r}'\left(\mathrm{s}_{\mathrm{d}}^{+}\right) + \mu\dot{\mathrm{s}}_{\mathrm{d}}\dot{\mathbf{r}}_{\mathrm{D}} - \mu\dot{\mathrm{s}}_{\mathrm{d}}\mathbf{R}_{\mathrm{b}}\hat{\boldsymbol{\rho}}_g\boldsymbol{\Omega}_{\mathrm{b}} \\
& + \left(\mathrm{m}_{\mathrm{b}} + \mathrm{m}_{\mathrm{d}} + \mu \mathrm{s}_{\mathrm{d}}\right)\mathbf{g} + \mathbf{f}\left(\mathrm{s}_{\mathrm{d}}^{+}\right)\Bigg) \cdot \delta\mathbf{r}_{\mathrm{D}} \\
+ \Bigg(& - \boldsymbol{\Pi}_{\mathrm{b}}\dot{\boldsymbol{\Omega}}_{\mathrm{b}} - \hat{\boldsymbol{\Omega}}_{\mathrm{b}}\boldsymbol{\Pi}_{\mathrm{b}}\boldsymbol{\Omega}_{\mathrm{b}} - \mu\dot{\mathrm{s}}_{\mathrm{d}}^2\hat{\boldsymbol{\rho}}_g\mathbf{R}_{\mathrm{b}}^T\mathbf{r}'\left(\mathrm{s}_{\mathrm{d}}^{+}\right) + \mu\dot{\mathrm{s}}_{\mathrm{d}}\hat{\boldsymbol{\rho}}_g\mathbf{R}_{\mathrm{b}}^T\dot{\mathbf{r}}_{\mathrm{D}} - \mu\dot{\mathrm{s}}_{\mathrm{d}}\hat{\boldsymbol{\rho}}_g^2\boldsymbol{\Omega}_{\mathrm{b}} \\
& - \mu\mathrm{d}^2\sin\left(\frac{\mathrm{s}_{\mathrm{d}} - \mathrm{b}}{\mathrm{d}}\right)\hat{\mathbf{e}}_3\mathbf{R}_{\mathrm{b}}^T\mathbf{g} - \mu\mathrm{d}^2\left(\cos\left(\frac{\mathrm{s}_{\mathrm{d}} - \mathrm{b}}{\mathrm{d}}\right) - 1\right)\hat{\mathbf{e}}_1\mathbf{R}_{\mathrm{b}}^T\mathbf{g} \\
& + \hat{\boldsymbol{\rho}}_g\mathbf{R}_{\mathrm{b}}^T\mathbf{f}\left(\mathrm{s}_{\mathrm{d}}^{+}\right) - \mathrm{u}\hat{\mathbf{e}}_2\Bigg) \cdot \boldsymbol{\eta}_{\mathrm{b}} \\
+ \Bigg(& \frac{1}{2}\mu\dot{\mathbf{r}}_{\mathrm{D}} \cdot \dot{\mathbf{r}}_{\mathrm{D}} - \left(\mu \mathrm{s}_{\mathrm{d}} + \frac{\mathrm{m}_{\mathrm{d}}}{2}\right)\ddot{\mathrm{s}}_{\mathrm{d}} - \frac{1}{2}\mu\dot{\mathrm{s}}_{\mathrm{d}}^2 + \frac{1}{2}\mu\dot{\mathrm{s}}_{\mathrm{d}}^2\mathbf{r}'\left(\mathrm{s}_{\mathrm{d}}^{+}\right) \cdot \mathbf{r}'\left(\mathrm{s}_{\mathrm{d}}^{+}\right) \\
& - \frac{1}{2}\mu\left(\dot{\mathbf{r}}_{\mathrm{D}} - \mathbf{R}_{\mathrm{b}}\hat{\boldsymbol{\rho}}_g\boldsymbol{\Omega}_{\mathrm{b}}\right) \cdot \left(\dot{\mathbf{r}}_{\mathrm{D}} - \mathbf{R}_{\mathrm{b}}\hat{\boldsymbol{\rho}}_g\boldsymbol{\Omega}_{\mathrm{b}}\right) + \mu\mathbf{r}_{\mathrm{d}} \cdot \mathbf{g} \\
& - \mu\mathrm{d}\cos\left(\frac{\mathrm{s}_{\mathrm{d}} - \mathrm{b}}{\mathrm{d}}\right)\mathbf{R}_{\mathrm{b}}\hat{\mathbf{e}}_3 \cdot \mathbf{g} + \mu\mathrm{d}\sin\left(\frac{\mathrm{s}_{\mathrm{d}} - \mathrm{b}}{\mathrm{d}}\right)\mathbf{R}_{\mathrm{b}}\hat{\mathbf{e}}_1 \cdot \mathbf{g} \\
& \cancel{+ \frac{1}{2}EA\left(\left(\|\mathbf{r}'\left(\mathrm{s}_{\mathrm{d}}^{+}\right)\|_2 - 1\right)^2\right)} - \mu\mathbf{r}\left(\mathrm{s}_{\mathrm{d}}^{+}\right) \cdot \mathbf{g} - \mathbf{f}\left(\mathrm{s}_{\mathrm{d}}^{+}\right) \cdot \mathbf{r}'\left(\mathrm{s}_{\mathrm{d}}^{+}\right) \\
& - \frac{1}{2}\mu\left(\|\mathbf{r}'\left(\mathrm{s}_{\mathrm{d}}^{+}\right)\|_2 - 1\right)^2\dot{\mathrm{s}}_{\mathrm{d}}^2 \cancel{- \frac{1}{2}EA\left(\left(\|\mathbf{r}'\left(\mathrm{s}_{\mathrm{d}}^{+}\right)\|_2 - 1\right)^2\right)} + \frac{\mathrm{u}}{\mathrm{d}}\Bigg)\delta \mathrm{s}_{\mathrm{d}} \\
+ \int_{\mathrm{s}_{\mathrm{d}}}^{l} & \left(-\mu\ddot{\mathbf{r}}\left(\mathrm{s}_0\right) + \mathbf{f}'\left(\mathrm{s}_0\right) + \mu\mathbf{g}\right) \cdot \delta\mathbf{r}\left(\mathrm{s}_0\right) d\mathrm{s}_0 \\
+ \Big(& \mathrm{m}_{\mathrm{u}}\mathbf{R}_{\mathrm{u}}\hat{\boldsymbol{\rho}}_c\dot{\boldsymbol{\Omega}}_{\mathrm{u}} - \mathrm{m}_{\mathrm{u}}\ddot{\mathbf{r}}\left(l\right) - \mathrm{m}_{\mathrm{u}}\mathbf{R}_{\mathrm{u}}\hat{\boldsymbol{\Omega}}_{\mathrm{u}}^2\rho_c - \mathbf{f}\left(l\right) + \mathrm{m}_{\mathrm{u}}\mathbf{g} - F_{\mathrm{UAV}}\mathbf{R}_{\mathrm{u}}\hat{\mathbf{e}}_3\Big) \cdot \delta\mathbf{r}\left(l\right) \\
+ \Big(& -\mathrm{m}_{\mathrm{u}}\hat{\boldsymbol{\rho}}_c\mathbf{R}_{\mathrm{u}}^T\ddot{\mathbf{r}}\left(l\right) - \boldsymbol{\Pi}_{\mathrm{u}}\dot{\boldsymbol{\Omega}}_{\mathrm{u}} - \hat{\boldsymbol{\Omega}}_{\mathrm{u}}\boldsymbol{\Pi}_{\mathrm{u}}\boldsymbol{\Omega}_{\mathrm{u}} + \mathrm{m}_{\mathrm{u}}\hat{\boldsymbol{\rho}}_c\mathbf{R}_{\mathrm{u}}^T\mathbf{g} + \boldsymbol{\tau}\Big) \cdot \boldsymbol{\eta}_{\mathrm{u}}\Bigg\} dt
\end{aligned}$$

Applying the same simplification as in Eq. C.30,

$$\begin{aligned}\int_{t_0}^{t_f}\left(-\frac{1}{2}\mu\dot{\mathrm{s}}_{\mathrm{d}}^{2}+\frac{1}{2}\mu\dot{\mathrm{s}}_{\mathrm{d}}^{2}\|\mathbf{r}'\left(\mathrm{s}_{\mathrm{d}}^{+}\right)\|^{2}\ -\frac{1}{2}\mu\left(\|\mathbf{r}'\left(\mathrm{s}_{\mathrm{d}}^{+}\right)\|_{2}-1\right)^{2}\dot{\mathrm{s}}_{\mathrm{d}}^{2}\right)\delta\mathrm{s}_{\mathrm{d}}dt \\ =\int_{t_0}^{t_f}\mu\dot{\mathrm{s}}_{\mathrm{d}}^{2}\left(\|\mathbf{r}'\left(\mathrm{s}_{\mathrm{d}}^{+}\right)\|-1\right)\delta\mathrm{s}_{\mathrm{d}}dt\end{aligned}$$

yields the final variation:

$$\begin{aligned}\delta\mathcal{S}=\int_{t_0}^{t_f}\Bigg\{\Bigg(&-\left(\mathrm{m_b}+\mathrm{m_d}+\mu\mathrm{s_d}\right)\ddot{\mathbf{r}}_{\mathrm{D}}-\mu\dot{\mathrm{s}}_{\mathrm{d}}\dot{\mathbf{r}}_{\mathrm{D}}-\mu\dot{\mathrm{s}}_{\mathrm{d}}^{2}\mathbf{r}'\left(\mathrm{s}_{\mathrm{d}}^{+}\right)+\mu\dot{\mathrm{s}}_{\mathrm{d}}\dot{\mathbf{r}}_{\mathrm{D}}-\mu\dot{\mathrm{s}}_{\mathrm{d}}\mathbf{R}_{\mathrm{b}}\hat{\boldsymbol{\rho}}_{g}\boldsymbol{\Omega}_{\mathrm{b}} \\ &+\left(\mathrm{m_b}+\mathrm{m_d}+\mu\mathrm{s_d}\right)\mathbf{g}+\mathbf{f}\left(\mathrm{s}_{\mathrm{d}}^{+}\right)\Bigg)\cdot\delta\mathbf{r}_{\mathrm{D}} \\ +\Bigg(&-\boldsymbol{\Pi}_{\mathrm{b}}\dot{\boldsymbol{\Omega}}_{\mathrm{b}}-\hat{\boldsymbol{\Omega}}_{\mathrm{b}}\boldsymbol{\Pi}_{\mathrm{b}}\boldsymbol{\Omega}_{\mathrm{b}}-\mu\dot{\mathrm{s}}_{\mathrm{d}}^{2}\hat{\boldsymbol{\rho}}_{g}\mathbf{R}_{\mathrm{b}}^{T}\mathbf{r}'\left(\mathrm{s}_{\mathrm{d}}^{+}\right)+\mu\dot{\mathrm{s}}_{\mathrm{d}}\hat{\boldsymbol{\rho}}_{g}\mathbf{R}_{\mathrm{b}}^{T}\dot{\mathbf{r}}_{\mathrm{D}}-\mu\dot{\mathrm{s}}_{\mathrm{d}}\hat{\boldsymbol{\rho}}_{g}^{2}\boldsymbol{\Omega}_{\mathrm{b}} \\ &-\mu\mathrm{d}^{2}\sin\left(\frac{\mathrm{s_d}-\mathrm{b}}{\mathrm{d}}\right)\hat{\hat{\mathbf{e}}}_{3}\mathbf{R}_{\mathrm{b}}^{T}\mathbf{g}-\mu\mathrm{d}^{2}\left(\cos\left(\frac{\mathrm{s_d}-\mathrm{b}}{\mathrm{d}}\right)-1\right)\hat{\hat{\mathbf{e}}}_{1}\mathbf{R}_{\mathrm{b}}^{T}\mathbf{g} \\ &+\hat{\boldsymbol{\rho}}_{g}\mathbf{R}_{\mathrm{b}}^{T}\mathbf{f}\left(\mathrm{s}_{\mathrm{d}}^{+}\right)-\mathrm{u}\hat{\mathbf{e}}_{2}\Bigg)\cdot\boldsymbol{\eta}_{\mathrm{b}} \\ +\Bigg(&\frac{1}{2}\mu\dot{\mathbf{r}}_{\mathrm{D}}\cdot\dot{\mathbf{r}}_{\mathrm{D}}-\left(\mu\mathrm{s_d}+\frac{\mathrm{m_d}}{2}\right)\ddot{\mathrm{s}}_{\mathrm{d}}+\mu\dot{\mathrm{s}}_{\mathrm{d}}^{2}\left(\|\mathbf{r}'\left(\mathrm{s}_{\mathrm{d}}^{+}\right)\|_{2}-1\right) \\ &-\frac{1}{2}\mu\left(\dot{\mathbf{r}}_{\mathrm{D}}-\mathbf{R}_{\mathrm{b}}\hat{\boldsymbol{\rho}}_{g}\boldsymbol{\Omega}_{\mathrm{b}}\right)\cdot\left(\dot{\mathbf{r}}_{\mathrm{D}}-\mathbf{R}_{\mathrm{b}}\hat{\boldsymbol{\rho}}_{g}\boldsymbol{\Omega}_{\mathrm{b}}\right)+\mu\mathbf{r}_{\mathrm{d}}\cdot\mathbf{g} \\ &-\mu\mathrm{d}\cos\left(\frac{\mathrm{s_d}-\mathrm{b}}{\mathrm{d}}\right)\mathbf{R}_{\mathrm{b}}\hat{\mathbf{e}}_{3}\cdot\mathbf{g}+\mu\mathrm{d}\sin\left(\frac{\mathrm{s_d}-\mathrm{b}}{\mathrm{d}}\right)\mathbf{R}_{\mathrm{b}}\hat{\mathbf{e}}_{1}\cdot\mathbf{g} \\ &-\mu\mathbf{r}\left(\mathrm{s}_{\mathrm{d}}^{+}\right)\cdot\mathbf{g} \\ &-\mathbf{f}\left(\mathrm{s}_{\mathrm{d}}^{+}\right)\cdot\mathbf{r}'\left(\mathrm{s}_{\mathrm{d}}^{+}\right)+\frac{\mathrm{u}}{\mathrm{d}}\Bigg)\delta\mathrm{s}_{\mathrm{d}} \\ +\int_{\mathrm{s_d}}^{l}&\left(-\mu\ddot{\mathbf{r}}\left(\mathrm{s}_{0}\right)+\mathbf{f}'\left(\mathrm{s}_{0}\right)+\mu\mathbf{g}\right)\cdot\delta\mathbf{r}\left(\mathrm{s}_{0}\right)d\mathrm{s}_{0} \\ +\Big(&\mathrm{m_u}\mathbf{R}_{\mathrm{u}}\hat{\boldsymbol{\rho}}_{c}\dot{\boldsymbol{\Omega}}_{\mathrm{u}}-\mathrm{m_u}\ddot{\mathbf{r}}\left(l\right)-\mathrm{m_u}\mathbf{R}_{\mathrm{u}}\hat{\boldsymbol{\Omega}}_{\mathrm{u}}^{2}\rho_{c}-\mathbf{f}\left(l\right)+\mathrm{m_u}\mathbf{g}-F_{\mathrm{UAV}}\mathbf{R}_{\mathrm{u}}\hat{\mathbf{e}}_{3}\Big)\cdot\delta\mathbf{r}\left(l\right) \\ +\Big(&-\mathrm{m_u}\hat{\boldsymbol{\rho}}_{c}\mathbf{R}_{\mathrm{u}}^{T}\ddot{\mathbf{r}}\left(l\right)-\boldsymbol{\Pi}_{\mathrm{u}}\dot{\boldsymbol{\Omega}}_{\mathrm{u}}-\hat{\boldsymbol{\Omega}}_{2}\boldsymbol{\Pi}_{\mathrm{u}}\boldsymbol{\Omega}_{\mathrm{u}}+\mathrm{m_u}\hat{\boldsymbol{\rho}}_{c}\mathbf{R}_{2}^{T}\mathbf{g}+\boldsymbol{\tau}_{\mathrm{UAV}}\Big)\cdot\boldsymbol{\eta}_{\mathrm{u}}\Bigg\}dt\end{aligned} \tag{C.54}$$

C.4 Carnot Energy Loss via Plastic Work at Guide Way

To handle the discontinuity in the string speed at the guide way, a Carnot Energy loss term using a plasticity based derivation can be used [110,130]. Assume the difference in the speed is due to an infinitesimal plastic work, or mass joining together. From conservation of momentum:

$$(\mathrm{M}+\mathrm{dm})\,\mathbf{u}' = \mathrm{M}\mathbf{u} + \mathrm{dm}\mathbf{v}$$

where $\mathbf{u}'$ is the speed of the combined mass, and $\mathbf{u}$ and $\mathbf{v}$ are the initial speeds prior to collision. Lets first show:

$$(\mathrm{M}+\mathrm{dm})\,(\mathrm{M}-\mathrm{dm}) = \mathrm{M}^2 - \mathrm{dm}^2$$

Discard terms $\mathcal{O}\left(\mathrm{dm}^2\right)$ or greater because dm is infinitesimally small:

$$(\mathrm{M}+\mathrm{dm}) \approx \frac{\mathrm{M}^2}{(\mathrm{M}-\mathrm{dm})}$$

Plug in and solve for $\mathbf{u}'$, again discarding terms $\mathcal{O}\left(\mathrm{dm}^2\right)$ or greater:

$$\mathbf{u}' \approx \frac{(\mathrm{M}-\mathrm{dm})}{\mathrm{M}^2}\,(\mathrm{M}\mathbf{u} + \mathrm{dm}\mathbf{v})$$
$$\mathbf{u}' \approx \mathbf{u} - \frac{\mathrm{dm}}{\mathrm{M}}\mathbf{u} + \frac{\mathrm{dm}}{\mathrm{M}}\mathbf{v} + \frac{\cancelto{\approx 0}{\mathrm{dm}^2}}{\mathrm{M}^2}\mathbf{v}$$

$$\mathbf{u}' \approx \mathbf{u} + \frac{\mathrm{dm}}{\mathrm{M}} \left(\mathbf{v} - \mathbf{u} \right) \tag{C.55}$$

The kinetic energy before the collision:

$$T = \frac{1}{2} \mathrm{dm} \mathbf{v}^2 + \frac{1}{2} \mathrm{M} \mathbf{u}^2$$

and after the collision:

$$T' = \frac{1}{2} \left(\mathrm{M} + \mathrm{dm} \right) \mathbf{u}'^2$$

Plugging in $\mathbf{u}'$ from Eq. C.55 and again ignoring terms $\mathcal{O}\left(\mathrm{dm}^2\right)$ or greater:

$$\begin{aligned}
T' &\approx \frac{1}{2} \left(\mathrm{M} + \mathrm{dm} \right) \left(\mathbf{u} + \left(\mathbf{v} - \mathbf{u} \right) \frac{\mathrm{dm}}{\mathrm{M}} \right)^2 \\
&\approx \frac{1}{2} \left(\mathrm{M} + \mathrm{dm} \right) \left(\mathbf{u}^2 + 2 \left(\mathbf{v} - \mathbf{u} \right) \mathbf{u} \frac{\mathrm{dm}}{\mathrm{M}} + \left(\mathbf{v} - \mathbf{u} \right)^2 \frac{\cancelto{\approx 0}{\mathrm{dm}^2}}{\mathrm{M}^2} \right) \\
&\approx \frac{1}{2} \mathrm{M} \mathbf{u}^2 + \frac{1}{2} \mathrm{dm} \mathbf{u}^2 + \left(\mathrm{M} + \mathrm{dm} \right) \frac{\mathrm{dm}}{\mathrm{M}} \left(\mathbf{u}\mathbf{v} - \mathbf{u}^2 \right) \\
&\approx \frac{1}{2} \mathrm{M} \mathbf{u}^2 + \frac{1}{2} \mathrm{dm} \mathbf{u}^2 + \left(\mathrm{dm} + \frac{\cancelto{\approx 0}{\mathrm{dm}^2}}{\mathrm{M}} \right) \left(\mathbf{u}\mathbf{v} - \mathbf{u}^2 \right) \\
&\approx \frac{1}{2} \mathrm{M} \mathbf{u}^2 + \frac{1}{2} \mathrm{dm} \mathbf{u}^2 + \mathrm{dm} \left(\mathbf{u}\mathbf{v} - \mathbf{u}^2 \right) \\
T' &\approx \frac{1}{2} \mathrm{M} \mathbf{u}^2 - \frac{1}{2} \mathrm{dm} \mathbf{u}^2 + \mathrm{dm} \mathbf{u}\mathbf{v}.
\end{aligned}$$

An approximation for the change in kinetic energy is:

$$\begin{aligned}\Delta T \approx T' - T &= \frac{1}{2}\mathrm{M}\mathbf{u}^2 - \frac{1}{2}\mathrm{dm}\mathbf{u}^2 + \mathrm{dm}\mathbf{u}\mathbf{v} - \frac{1}{2}\mathrm{dm}v^2 - \frac{1}{2}\mathrm{M}\mathbf{u}^2 \\ &= -\frac{1}{2}\mathrm{dm}\mathbf{u}^2 + \mathrm{dm}\mathbf{u}\mathbf{v} - \frac{1}{2}\mathrm{dm}\mathbf{v}^2 \\ &= -\frac{1}{2}\mathrm{dm}\left(\mathbf{u}^2 - 2\mathbf{u}\mathbf{v} + \mathbf{v}^2\right) \\ \Delta T \approx T' - T &= -\frac{1}{2}\mathrm{dm}\left(\mathbf{u} - \mathbf{v}\right)^2\end{aligned} \tag{C.56}$$

where $\mathrm{dm} = \mu\dot{\mathrm{s}}_{\mathrm{d}}$ and $(\mathbf{u} - \mathbf{v}) = \epsilon\dot{\mathrm{s}}_{\mathrm{d}}$ is the string speed discontinuity yielding:

$$\Delta T \approx -\frac{1}{2}\mu\epsilon^2\dot{\mathrm{s}}_{\mathrm{d}}^3. \tag{C.57}$$

The power corresponding to the energy dissipation rate is defined as the Carnot energy loss term, Q multiplied by the speed of the tether:

$$\Delta T = Q\dot{\mathrm{s}}_{\mathrm{d}}$$

which yields the Carnot energy loss term:

$$Q = -\frac{1}{2}\mu\epsilon^2\dot{\mathrm{s}}_{\mathrm{d}}^2. \tag{C.58}$$

Appendix D

Shape Functions and Galerkin Method for Three Dimensional Elastic String Pendlulum

In this appendix, the one dimensional linear and quadratic shape functions applied to the three dimensional elastic pendulum will be derived.

D.1 One Dimensional Linear Shape Function

A natural coordinate $\zeta \in [0, 1]$ is defined in each element as a point between two node points as seen in Fig. D.1. The un-stretched length of the string up to that point is equal to the sum of the previous $(i-1)$ elements, along with the fraction of the current element:

$$s_o = l_0 \left(i - 1\right) + l_0 \zeta$$

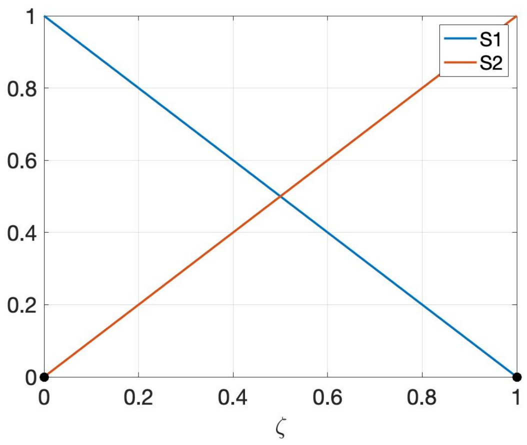

Figure D.1: First order shape function

where l_0 is the nominal element length. Solving for ζ yields:

$$\zeta = \frac{1}{l_0}\left(s_o - l_0\left(i-1\right)\right).$$

Taking the derivative with respect to s_o yields:

$$\begin{aligned}\frac{d\zeta}{ds_o} &= \frac{1}{l_0} \\ ds_o &= l_0 d\zeta.\end{aligned} \tag{D.1}$$

The one dimensional linear shape functions are defined as:

$$\begin{aligned}S_1\left(\zeta\right) &= 1-\zeta \\ S_2\left(\zeta\right) &= \zeta.\end{aligned} \tag{D.2}$$

The position of any point in the element is defined as:

$$\begin{aligned}\mathbf{r}\left(\zeta\right) &= S_1\left(\zeta\right)\mathbf{r}_i + S_2\left(\zeta\right)\mathbf{r}_{i+1} \\ \mathbf{r}\left(\zeta\right) &= \left(1-\zeta\right)\mathbf{r}_i + \zeta\mathbf{r}_{i+1},\end{aligned}$$

and the second time derivative as:

$$\ddot{\mathbf{r}}\left(\zeta\right) = \left(1-\zeta\right)\ddot{\mathbf{r}}_i + \zeta\ddot{\mathbf{r}}_{i+1}.$$

D.2 Linear shape functions as weighting functions

Using the two shape functions as weights, the weighted residual integral in terms of ζ given in Eq. 8.9 can be evaluated analytically.

1. For $w\left(\zeta\right) = S_1\left(\zeta\right) = 1-\zeta$:

$$\begin{aligned}
\mu l_0 \int_0^1 \left(1-\zeta\right)\left(\left(1-\zeta\right)\ddot{\mathbf{r}}_i + \zeta\ddot{\mathbf{r}}_{i+1} - \mathbf{g}\right) d\zeta + q_i\left(\mathbf{r}_{i+1}-\mathbf{r}_i\right)\int_0^1 \left(-1\right) d\zeta - \mathbf{f}\left(\zeta\right)\left(1-\zeta\right)\Big|_0^1 &= 0 \\
\mu l_0 \int_0^1 \left(\left(1-2\zeta+\zeta^2\right)\ddot{\mathbf{r}}_i + \left(\zeta-\zeta^2\right)\ddot{\mathbf{r}}_{i+1} - \left(1-\zeta\right)\mathbf{g}\right) d\zeta - q_i\left(\mathbf{r}_{i+1}-\mathbf{r}_i\right) - \mathbf{f}_{i+1}\cancelto{0}{\left(1-1\right)} + \mathbf{f}_i\left(1-0\right) &= 0 \\
\mu l_0 \left(\left(\zeta - \zeta^2 + \frac{\zeta^3}{3}\right)\ddot{\mathbf{r}}_i + \left(\frac{\zeta^2}{2} - \frac{\zeta^3}{3}\right)\ddot{\mathbf{r}}_{i+1} - \left(\zeta - \frac{\zeta^2}{2}\right)\mathbf{g}\right)\Bigg|_0^1 - q_i\left(\mathbf{r}_{i+1}-\mathbf{r}_i\right) + \mathbf{f}_i &= 0 \\
\mu l_0 \left(\frac{1}{3}\ddot{\mathbf{r}}_i + \frac{1}{6}\ddot{\mathbf{r}}_{i+1} - \frac{1}{2}\mathbf{g}\right) - q_i\left(\mathbf{r}_{i+1}-\mathbf{r}_i\right) + \mathbf{f}_i &= 0
\end{aligned}$$

2. For $w\left(\zeta\right) = S_2\left(\zeta\right) = \zeta$:

$$\begin{aligned}
\mu l_0 \int_0^1 \zeta\left(\left(1-\zeta\right)\ddot{\mathbf{r}}_i + \zeta\ddot{\mathbf{r}}_{i+1} - \mathbf{g}\right) d\zeta + q_i\left(\mathbf{r}_{i+1}-\mathbf{r}_i\right)\int_0^1 \left(1\right) d\zeta - \mathbf{f}\left(\zeta\right)\left(\zeta\right)\Big|_0^1 &= 0 \\
\mu l_0 \int_0^1 \left(\left(\zeta-\zeta^2\right)\ddot{\mathbf{r}}_i + \zeta^2\ddot{\mathbf{r}}_{i+1} - \zeta\mathbf{g}\right) d\zeta + q_i\left(\mathbf{r}_{i+1}-\mathbf{r}_i\right) - \mathbf{f}_{i+1}\left(1\right) + \mathbf{f}_i\cancelto{0}{\left(0\right)} &= 0 \\
\mu l_0 \left(\left(\frac{\zeta^2}{2} - \frac{\zeta^3}{3}\right)\ddot{\mathbf{r}}_i + \frac{\zeta^3}{3}\ddot{\mathbf{r}}_{i+1} - \frac{\zeta^2}{2}\mathbf{g}\right)\Bigg|_0^1 + q_i\left(\mathbf{r}_{i+1}-\mathbf{r}_i\right) - \mathbf{f}_{i+1} &= 0 \\
\mu l_0 \left(\frac{1}{6}\ddot{\mathbf{r}}_i + \frac{1}{3}\ddot{\mathbf{r}}_{i+1} - \frac{1}{2}\mathbf{g}\right) + q_i\left(\mathbf{r}_{i+1}-\mathbf{r}_i\right) - \mathbf{f}_{i+1} &= 0
\end{aligned}$$

Combining yields a system of two equations, one for each node of the element, with the following elemental stencil:

$$\frac{\mu l_0}{6}\begin{bmatrix}2\mathbf{I}_3 & \mathbf{I}_3\\ \mathbf{I}_3 & 2\mathbf{I}_3\end{bmatrix}\begin{bmatrix}\ddot{\mathbf{r}}_i\\ \ddot{\mathbf{r}}_{i+1}\end{bmatrix} = q_i\begin{bmatrix}-\mathbf{I}_3 & \mathbf{I}_3\\ \mathbf{I}_3 & -\mathbf{I}_3\end{bmatrix}\begin{bmatrix}\mathbf{r}_i\\ \mathbf{r}_{i+1}\end{bmatrix} + \frac{\mu l_0}{2} g\begin{bmatrix}\mathbf{I}_3\\ \mathbf{I}_3\end{bmatrix}\hat{\mathbf{e}}_3 + \begin{bmatrix}-\mathbf{f}_i\\ \mathbf{f}_{i+1}\end{bmatrix}. \tag{D.3}$$

D.3 One Dimensional Quadratric Shape Function

A natural coordinate $\zeta \in [-1, 1]$ is defined as a point in one element spanning three nodes as seen in Fig. D.2. The un-stretched length of the string up to any point in the element is equal to the sum of the previous $j-1$ elements, along with the fraction of the current element:

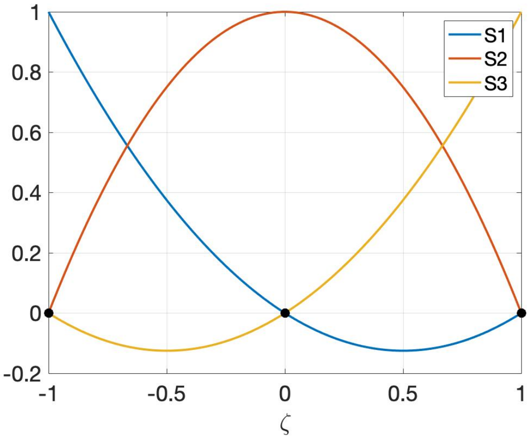

Figure D.2: Second order shape function on [-1 ,1]

$$s_o = l_0\,(j-1) + \frac{l_0}{2}\,(\zeta + 1)$$

where l_0 is the nominal element length. Solving for ζ yields:

$$\zeta = \frac{2}{l_0}\,(s_o - l_0\,(j-1)) - 1.$$

Taking the derivative with respect to s_o yields:

$$\begin{aligned} \frac{d\zeta}{ds_o} &= \frac{2}{l_0} \\ ds_o &= \frac{l_0}{2}d\zeta. \end{aligned} \tag{D.4}$$

The one dimensional quadratic shape functions are defined as:

$$\begin{aligned} S_1(\zeta) &= \frac{\zeta^2 - \zeta}{2} \\ S_2(\zeta) &= 1 - \zeta^2 \\ S_3(\zeta) &= \frac{\zeta^2 + \zeta}{2}. \end{aligned} \tag{D.5}$$

The position of any point in the element is defined as:

$$\begin{aligned} \mathbf{r}(\zeta) &= S_1(\zeta)\,\mathbf{r}_{2j-1} + S_2(\zeta)\,\mathbf{r}_{2j} + S_3(\zeta)\,\mathbf{r}_{2j+1} \\ \mathbf{r}(\zeta) &= \left(\frac{\zeta^2 - \zeta}{2}\right)\mathbf{r}_{2j-1} + \left(1 - \zeta^2\right)\mathbf{r}_{2j} + \left(\frac{\zeta^2 + \zeta}{2}\right)\mathbf{r}_{2j+1}, \end{aligned} \tag{D.6}$$

and the second time derivative as:

$$\ddot{\mathbf{r}}(\zeta) = \left(\frac{\zeta^2 - \zeta}{2}\right)\ddot{\mathbf{r}}_{2j-1} + \left(1 - \zeta^2\right)\ddot{\mathbf{r}}_{2j} + \left(\frac{\zeta^2 + \zeta}{2}\right)\ddot{\mathbf{r}}_{2j+1}. \tag{D.7}$$

D.4 Quadratic shape functions as weights

Unlike the one dimensional linear shape function, the stiffness terms of the quadratic shape function weighted integral can not be solved analytically. Gauss Quadrature, as defined in Eq. 8.4, is applied to the weighted residual integral in terms of ζ, given in Eq.

8.27. For two point Gauss Quadrature, $x_1 = \frac{-1}{\sqrt{3}}$, $x_2 = \frac{1}{\sqrt{3}}$, and $w_i = 1$, yielding:

$$\begin{aligned}
&\frac{EA}{l_0}\int_{-1}^{1}\left(1-\frac{l_0}{\|\mathbf{l}\left(\zeta\right)\|_2}\right)\mathbf{l}\left(\zeta\right)\frac{dw\left(\zeta\right)}{d\zeta}d\zeta\\
&\quad= \left(1\right)\frac{EA}{l_0}\left(1-\frac{l_0}{\|\mathbf{l}\left(\frac{-1}{\sqrt{3}}\right)\|_2}\right)\mathbf{l}\left(\frac{-1}{\sqrt{3}}\right)\left.\frac{dw\left(\zeta\right)}{d\zeta}\right|_{\zeta=\frac{-1}{\sqrt{3}}} + \left(1\right)\frac{EA}{l_0}\left(1-\frac{l_0}{\|\mathbf{l}\left(\frac{1}{\sqrt{3}}\right)\|_2}\right)\mathbf{l}\left(\frac{1}{\sqrt{3}}\right)\left.\frac{dw\left(\zeta\right)}{d\zeta}\right|_{\zeta=\frac{1}{\sqrt{3}}}\\
&\quad= q_j^-\,\mathbf{l}\left(\frac{-1}{\sqrt{3}}\right)\left.\frac{dw\left(\zeta\right)}{d\zeta}\right|_{\zeta=\frac{-1}{\sqrt{3}}} + q_j^+\,\mathbf{l}\left(\frac{1}{\sqrt{3}}\right)\left.\frac{dw\left(\zeta\right)}{d\zeta}\right|_{\zeta=\frac{1}{\sqrt{3}}}
\end{aligned} \tag{D.8}$$

where the two node Gaussian Quadrature biased elemental force density terms, q_j^- and q_j^+ are defined as:

$$q_j^- = \frac{EA}{l_0}\left(1-\frac{l_0}{\|\mathbf{l}\left(\frac{-1}{\sqrt{3}}\right)\|_2}\right),\ q_j^+ = \frac{EA}{l_0}\left(1-\frac{l_0}{\|\mathbf{l}\left(\frac{1}{\sqrt{3}}\right)\|_2}\right) \tag{D.9}$$

Inserting Eq. D.8 back into Eq. 8.27 yields the weighted residual integral for the one dimensional quadratic element in a form that is analytically solvable:

$$\begin{aligned}
\frac{\mu l_0}{2}\int_{-1}^{1} w\left(\zeta\right)\left(\left(\frac{\zeta^2-\zeta}{2}\right)\ddot{\mathbf{r}}_{2j-1} + \left(1-\zeta^2\right)\ddot{\mathbf{r}}_{2j} + \left(\frac{\zeta^2+\zeta}{2}\right)\ddot{\mathbf{r}}_{2j+1} - \mathbf{g}\right)d\zeta\\
+ q_j^-\mathbf{l}\left(\zeta\right)\left.\frac{dw\left(\zeta\right)}{d\zeta}\right|_{\zeta=\frac{-1}{\sqrt{3}}} + q_j^+\mathbf{l}\left(\zeta\right)\left.\frac{dw\left(\zeta\right)}{d\zeta}\right|_{\zeta=\frac{1}{\sqrt{3}}} - \mathbf{f}\left(\zeta\right)w\left(\zeta\right)\Big|_{-1}^{1} = 0
\end{aligned} \tag{D.10}$$

Prior to evaluating, $\mathbf{l}\left(\zeta\right)$ needs to be determined from Eq. 8.26 at both quadrature points:

$$\begin{aligned}
\mathbf{l}\left(\frac{-1}{\sqrt{3}}\right) &= \left(2\frac{-1}{\sqrt{3}}-1\right)\mathbf{r}_{2j-1} + \left(-4\frac{-1}{\sqrt{3}}\right)\mathbf{r}_{2j} + \left(2\frac{-1}{\sqrt{3}}+1\right)\mathbf{r}_{2j+1}\\
&= \frac{1}{3}\left(\left(-3-2\sqrt{3}\right)\mathbf{r}_{2j-1} + 4\sqrt{3}\mathbf{r}_{2j} + \left(3-2\sqrt{3}\right)\mathbf{r}_{2j+1}\right)\\
\mathbf{l}\left(\frac{1}{\sqrt{3}}\right) &= \left(2\frac{1}{\sqrt{3}}-1\right)\mathbf{r}_{2j-1} + \left(-4\frac{1}{\sqrt{3}}\right)\mathbf{r}_{2j} + \left(2\frac{1}{\sqrt{3}}+1\right)\mathbf{r}_{2j+1}\\
&= \frac{1}{3}\left(\left(-3+2\sqrt{3}\right)\mathbf{r}_{2j-1} - 4\sqrt{3}\mathbf{r}_{2j} + \left(3+2\sqrt{3}\right)\mathbf{r}_{2j+1}\right)
\end{aligned} \tag{D.11}$$

Using the three shape functions as weights, evaluating the integral for the mass terms, evaluating the stiffness terms at the Gaussian Quadrature points, and addressing any boundary conditions yields:

1. For $w(\zeta) = S_1(\zeta) = \frac{\zeta^2-\zeta}{2}$:

   - Mass and acceleration terms:

$$
\begin{aligned}
&\frac{\mu l_0}{2}\int_{-1}^{1} w(\zeta)\left(\left(\frac{\zeta^2-\zeta}{2}\right)\ddot{\mathbf{r}}_{2j-1} + \left(1-\zeta^2\right)\ddot{\mathbf{r}}_{2j} + \left(\frac{\zeta^2+\zeta}{2}\right)\ddot{\mathbf{r}}_{2j+1} - \mathbf{g}\right) d\zeta \\
&= \frac{\mu l_0}{2}\int_{-1}^{1}\left(\frac{\zeta^2-\zeta}{2}\right)\left(\left(\frac{\zeta^2-\zeta}{2}\right)\ddot{\mathbf{r}}_{2j-1} + \left(1-\zeta^2\right)\ddot{\mathbf{r}}_{2j} + \left(\frac{\zeta^2+\zeta}{2}\right)\ddot{\mathbf{r}}_{2j+1} - \mathbf{g}\right) d\zeta \\
&= \frac{\mu l_0}{4}\int_{-1}^{1}\left(\left(\frac{\zeta^4-2\zeta^3+\zeta^2}{2}\right)\ddot{\mathbf{r}}_{2j-1} + \left(-\zeta^4+\zeta^3+\zeta^2-\zeta\right)\ddot{\mathbf{r}}_{2j} + \left(\frac{\zeta^4-\zeta^2}{2}\right)\ddot{\mathbf{r}}_{2j+1} - \left(\zeta^2-\zeta\right)\mathbf{g}\right) d\zeta \\
&= \frac{\mu l_0}{4}\left(\left(\frac{\zeta^5}{10}-\frac{2\zeta^4}{8}+\frac{\zeta^3}{6}\right)\ddot{\mathbf{r}}_{2j-1} + \left(-\frac{\zeta^5}{5}+\frac{\zeta^4}{4}+\frac{\zeta^3}{3}-\frac{\zeta^2}{2}\right)\ddot{\mathbf{r}}_{2j} + \left(\frac{\zeta^5}{10}-\frac{\zeta^3}{6}\right)\ddot{\mathbf{r}}_{2j+1} - \left(\frac{\zeta^3}{3}-\frac{\zeta^2}{2}\right)\mathbf{g}\right)\Bigg|_{-1}^{1} \\
&= \mu l_0\left(\frac{2}{15}\ddot{\mathbf{r}}_{2j-1} + \frac{1}{15}\ddot{\mathbf{r}}_{2j} - \frac{1}{30}\ddot{\mathbf{r}}_{2j+1} - \frac{1}{6}\mathbf{g}\right) \\
&= \mu l_0\begin{bmatrix}\frac{2}{15}\mathbf{I}_3 & \frac{1}{15}\mathbf{I}_3 & -\frac{1}{30}\mathbf{I}_3\end{bmatrix}\begin{bmatrix}\ddot{\mathbf{r}}_{2j-1} \\ \ddot{\mathbf{r}}_{2j} \\ \ddot{\mathbf{r}}_{2j+1}\end{bmatrix} - \frac{\mu l_0}{6}\mathbf{g}
\end{aligned}
$$

   - Stiffness terms: $\frac{dw(\zeta)}{d\zeta} = \zeta - \frac{1}{2}$

$$
\begin{aligned}
&q_j^{-}\mathbf{l}(\zeta)\frac{dw(\zeta)}{d\zeta}\Bigg|_{\zeta=\frac{-1}{\sqrt{3}}} + q_j^{+}\mathbf{l}(\zeta)\frac{dw(\zeta)}{d\zeta}\Bigg|_{\zeta=\frac{1}{\sqrt{3}}} \\
&\quad = q_j^{-}\mathbf{l}(\zeta)\left(\zeta-\frac{1}{2}\right)\Bigg|_{\zeta=\frac{-1}{\sqrt{3}}} + q_j^{+}\mathbf{l}(\zeta)\left(\zeta-\frac{1}{2}\right)\Bigg|_{\zeta=\frac{1}{\sqrt{3}}} \\
&\quad = q_j^{-}\mathbf{l}\left(\frac{-1}{\sqrt{3}}\right)\left(\frac{-1}{\sqrt{3}}-\frac{1}{2}\right) + q_j^{+}\mathbf{l}\left(\frac{1}{\sqrt{3}}\right)\left(\frac{1}{\sqrt{3}}-\frac{1}{2}\right) \\
&\quad = q_j^{-}\left(\frac{7+4\sqrt{3}}{6}\mathbf{r}_{2j-1} + \frac{-4-2\sqrt{3}}{3}\mathbf{r}_{2j} + \frac{1}{6}\mathbf{r}_{2j+1}\right) + q_j^{+}\left(\frac{7-4\sqrt{3}}{6}\mathbf{r}_{2j-1} + \frac{-4+2\sqrt{3}}{3}\mathbf{r}_{2j} + \frac{1}{6}\mathbf{r}_{2j+1}\right) \\
&\quad = \left(\frac{q_j^{-}}{6}\begin{bmatrix}\left(7+4\sqrt{3}\right)\mathbf{I}_3 & \left(-8-4\sqrt{3}\right)\mathbf{I}_3 & \mathbf{I}_3\end{bmatrix} + \frac{q_j^{+}}{6}\begin{bmatrix}\left(7-4\sqrt{3}\right)\mathbf{I}_3 & \left(-8+4\sqrt{3}\right)\mathbf{I}_3 & \mathbf{I}_3\end{bmatrix}\right)\begin{bmatrix}\mathbf{r}_{2j-1} \\ \mathbf{r}_{2j} \\ \mathbf{r}_{2j+1}\end{bmatrix}
\end{aligned}
$$

- Elemental boundary conditions:

$$
\begin{aligned}
-\,\mathbf{f}\left(\zeta\right)w\left(\zeta\right)\big|_{-1}^{1} &= -\,\mathbf{f}\left(\zeta\right)\frac{\zeta^2-\zeta}{2}\bigg|_{-1}^{1} \\
&= -\mathbf{f}_{2j-1}\cancelto{}{\frac{1-1}{2}} + \mathbf{f}_{2j-1}\frac{1+1}{2} \\
&= \mathbf{f}_{2j-1}
\end{aligned}
$$

2. For $w\left(\zeta\right) = S_2\left(\zeta\right) = 1-\zeta^2$:

   - Mass and acceleration terms:

$$
\begin{aligned}
&\frac{\mu l_0}{2}\int_{-1}^{1} w\left(\zeta\right)\left(\left(\frac{\zeta^2-\zeta}{2}\right)\ddot{\mathbf{r}}_{2j-1} + \left(1-\zeta^2\right)\ddot{\mathbf{r}}_{2j} + \left(\frac{\zeta^2+\zeta}{2}\right)\ddot{\mathbf{r}}_{2j+1} - \mathbf{g}\right)d\zeta \\
&= \frac{\mu l_0}{2}\int_{-1}^{1}\left(1-\zeta^2\right)\left(\left(\frac{\zeta^2-\zeta}{2}\right)\ddot{\mathbf{r}}_{2j-1} + \left(1-\zeta^2\right)\ddot{\mathbf{r}}_{2j} + \left(\frac{\zeta^2+\zeta}{2}\right)\ddot{\mathbf{r}}_{2j+1} - \mathbf{g}\right)d\zeta \\
&= \frac{\mu l_0}{2}\int_{-1}^{1}\left(\left(\frac{-\zeta^4+\zeta^3+\zeta^2-\zeta}{2}\right)\ddot{\mathbf{r}}_{2j-1} + \left(\zeta^4-2\zeta^2+1\right)\ddot{\mathbf{r}}_{2j}\right. \\
&\qquad\qquad \left. + \left(\frac{-\zeta^4-\zeta^3+\zeta^2+\zeta}{2}\right)\ddot{\mathbf{r}}_{2j+1} - \left(1-\zeta^2\right)\mathbf{g}\right)d\zeta \\
&= \frac{\mu l_0}{2}\left(\left(-\frac{\zeta^5}{10}+\frac{\zeta^4}{8}+\frac{\zeta^3}{6}-\frac{\zeta^2}{4}\right)\ddot{\mathbf{r}}_{2j-1} + \left(\frac{\zeta^5}{5}-\frac{2\zeta^3}{3}+\zeta\right)\ddot{\mathbf{r}}_{2j}\right. \\
&\qquad\qquad \left. + \left(-\frac{\zeta^5}{10}-\frac{\zeta^4}{8}+\frac{\zeta^3}{6}+\frac{\zeta^2}{4}\right)\ddot{\mathbf{r}}_{2j+1} - \left(\zeta-\frac{\zeta^3}{3}\right)\mathbf{g}\right)\bigg|_{-1}^{1} \\
&= \mu l_0\left(\frac{1}{15}\ddot{\mathbf{r}}_{2j-1} + \frac{8}{15}\ddot{\mathbf{r}}_{2j} + \frac{1}{15}\ddot{\mathbf{r}}_{2j+1} - \frac{2}{3}\mathbf{g}\right) \\
&= \mu l_0\begin{bmatrix}\frac{1}{15}\mathbf{I}_3 & \frac{8}{15}\mathbf{I}_3 & \frac{1}{15}\mathbf{I}_3\end{bmatrix}\begin{bmatrix}\ddot{\mathbf{r}}_{2j-1}\\ \ddot{\mathbf{r}}_{2j}\\ \ddot{\mathbf{r}}_{2j+1}\end{bmatrix} - \frac{2\mu l_0}{3}\mathbf{g}
\end{aligned}
$$

- Stiffness terms: $\frac{dw(\zeta)}{d\zeta} = -2\zeta$

$$
\begin{aligned}
& q_j^- \boldsymbol{\mathsf{l}}\left(\zeta\right) \frac{dw\left(\zeta\right)}{d\zeta}\bigg|_{\zeta=\frac{-1}{\sqrt{3}}} + q_j^+ \boldsymbol{\mathsf{l}}\left(\zeta\right) \frac{dw\left(\zeta\right)}{d\zeta}\bigg|_{\zeta=\frac{1}{\sqrt{3}}} \\
&\quad = q_j^- \boldsymbol{\mathsf{l}}\left(\zeta\right)\left(-2\zeta\right)\Big|_{\zeta=\frac{-1}{\sqrt{3}}} + q_j^+ \boldsymbol{\mathsf{l}}\left(\zeta\right)\left(-2\zeta\right)\Big|_{\zeta=\frac{1}{\sqrt{3}}} \\
&\quad = q_j^- \boldsymbol{\mathsf{l}}\left(\frac{-1}{\sqrt{3}}\right)\left(\frac{2}{\sqrt{3}}\right) + q_j^+ \boldsymbol{\mathsf{l}}\left(\frac{1}{\sqrt{3}}\right)\left(\frac{-2}{\sqrt{3}}\right) \\
&\quad = q_j^- \left(\frac{-4-2\sqrt{3}}{3}\boldsymbol{\mathsf{r}}_{2j-1} + \frac{8}{3}\boldsymbol{\mathsf{r}}_{2j} + \frac{-4+2\sqrt{3}}{3}\boldsymbol{\mathsf{r}}_{2j+1}\right) \\
&\qquad + q_j^+ \left(\frac{-4+2\sqrt{3}}{3}\boldsymbol{\mathsf{r}}_{2j-1} + \frac{8}{3}\boldsymbol{\mathsf{r}}_{2j} + \frac{-4-2\sqrt{3}}{3}\boldsymbol{\mathsf{r}}_{2j+1}\right) \\
&\quad = \left(\frac{q_j^-}{3}\begin{bmatrix}\left(-4-2\sqrt{3}\right)\mathbf{I}_3 & 8\mathbf{I}_3 & \left(-4+2\sqrt{3}\right)\mathbf{I}_3\end{bmatrix}\right. \\
&\qquad \left. + \frac{q_j^+}{3}\begin{bmatrix}\left(-4+2\sqrt{3}\right)\mathbf{I}_3 & 8\mathbf{I}_3 & \left(-4-2\sqrt{3}\right)\mathbf{I}_3\end{bmatrix}\right)\begin{bmatrix}\boldsymbol{\mathsf{r}}_{2j-1} \\ \boldsymbol{\mathsf{r}}_{2j} \\ \boldsymbol{\mathsf{r}}_{2j+1}\end{bmatrix}
\end{aligned}
$$

- Elemental boundary conditions:

$$
\begin{aligned}
-\boldsymbol{\mathsf{f}}\left(\zeta\right) w\left(\zeta\right)\big|_{-1}^{1} &= -\boldsymbol{\mathsf{f}}\left(\zeta\right)\left(1-\zeta^2\right)\big|_{-1}^{1} \\
&= -\boldsymbol{\mathsf{f}}_{2j}\cancel{(1-1)} + \boldsymbol{\mathsf{f}}_{2j}\cancel{(1-1)} \\
&= 0
\end{aligned}
$$

3. For $w\left(\zeta\right) = S_1\left(\zeta\right) = \frac{\zeta^2+\zeta}{2}$:

- Mass and acceleration terms:

$$
\begin{aligned}
&\frac{\mu l_0}{2}\int_{-1}^{1} w\left(\zeta\right)\left(\left(\frac{\zeta^2-\zeta}{2}\right)\ddot{\mathbf{r}}_{2j-1}+\left(1-\zeta^2\right)\ddot{\mathbf{r}}_{2j}+\left(\frac{\zeta^2+\zeta}{2}\right)\ddot{\mathbf{r}}_{2j+1}-\mathbf{g}\right)d\zeta\\
&=\frac{\mu l_0}{2}\int_{-1}^{1}\left(\frac{\zeta^2+\zeta}{2}\right)\left(\left(\frac{\zeta^2-\zeta}{2}\right)\ddot{\mathbf{r}}_{2j-1}+\left(1-\zeta^2\right)\ddot{\mathbf{r}}_{2j}+\left(\frac{\zeta^2+\zeta}{2}\right)\ddot{\mathbf{r}}_{2j+1}-\mathbf{g}\right)d\zeta\\
&=\frac{\mu l_0}{4}\int_{-1}^{1}\left(\left(\frac{\zeta^4-\zeta^2}{2}\right)\ddot{\mathbf{r}}_{2j-1}+\left(-\zeta^4-\zeta^3+\zeta^2+\zeta\right)\ddot{\mathbf{r}}_{2j}+\left(\frac{\zeta^4+2\zeta^3+\zeta^2}{2}\right)\ddot{\mathbf{r}}_{2j+1}-\left(\zeta^2+\zeta\right)\mathbf{g}\right)d\zeta\\
&=\frac{\mu l_0}{4}\left(\frac{\zeta^5}{10}-\frac{\zeta^3}{6}\right)\ddot{\mathbf{r}}_{2j-1}+\left(-\frac{\zeta^5}{5}-\frac{\zeta^4}{4}+\frac{\zeta^3}{3}+\frac{\zeta^2}{2}\right)\ddot{\mathbf{r}}_{2j}+\left(\left(\frac{\zeta^5}{10}+\frac{2\zeta^4}{8}+\frac{\zeta^3}{6}\right)\ddot{\mathbf{r}}_{2j+1}-\left(\frac{\zeta^3}{3}+\frac{\zeta^2}{2}\right)\mathbf{g}\right)\Bigg|_{-1}^{1}\\
&=\mu l_0\left(-\frac{1}{30}\ddot{\mathbf{r}}_{2j-1}+\frac{1}{15}\ddot{\mathbf{r}}_{2j}+\frac{2}{15}\ddot{\mathbf{r}}_{2j+1}-\frac{1}{6}\mathbf{g}\right)\\
&=\mu l_0\begin{bmatrix}-\tfrac{1}{30}\mathbf{I}_3 & \tfrac{1}{15}\mathbf{I}_3 & \tfrac{2}{15}\mathbf{I}_3\end{bmatrix}\begin{bmatrix}\ddot{\mathbf{r}}_{2j-1}\\ \ddot{\mathbf{r}}_{2j}\\ \ddot{\mathbf{r}}_{2j+1}\end{bmatrix}-\frac{\mu l_0}{6}\mathbf{g}
\end{aligned}
$$

- Stiffness terms: $\frac{dw(\zeta)}{d\zeta}=\zeta+\frac{1}{2}$

$$
\begin{aligned}
&q_j^-\mathbf{l}\left(\zeta\right)\frac{dw\left(\zeta\right)}{d\zeta}\bigg|_{\zeta=\frac{-1}{\sqrt{3}}}+q_j^+\mathbf{l}\left(\zeta\right)\frac{dw\left(\zeta\right)}{d\zeta}\bigg|_{\zeta=\frac{1}{\sqrt{3}}}\\
&\quad= q_j^-\mathbf{l}\left(\zeta\right)\left(\zeta+\frac{1}{2}\right)\bigg|_{\zeta=\frac{-1}{\sqrt{3}}}+q_j^+\mathbf{l}\left(\zeta\right)\left(\zeta+\frac{1}{2}\right)\bigg|_{\zeta=\frac{1}{\sqrt{3}}}\\
&\quad=q_j^-\mathbf{l}\left(\frac{-1}{\sqrt{3}}\right)\left(\frac{-1}{\sqrt{3}}+\frac{1}{2}\right)+q_j^+\mathbf{l}\left(\frac{1}{\sqrt{3}}\right)\left(\frac{1}{\sqrt{3}}+\frac{1}{2}\right)\\
&\quad=q_j^-\left(\frac{1}{6}\mathbf{r}_{2j-1}+\frac{-4+2\sqrt{3}}{3}\mathbf{r}_{2j}+\frac{7-4\sqrt{3}}{6}\right)\mathbf{r}_{2j+1}+q_j^+\left(\frac{1}{6}\mathbf{r}_{2j-1}+\frac{-4-2\sqrt{3}}{3}\mathbf{r}_{2j}+\frac{7+4\sqrt{3}}{6}\right)\mathbf{r}_{2j+1}\\
&\quad=\left(\frac{q_j^-}{6}\begin{bmatrix}\mathbf{I}_3 & \left(-8+4\sqrt{3}\right)\mathbf{I}_3 & \left(7-4\sqrt{3}\right)\mathbf{I}_3\end{bmatrix}+\frac{q_j^+}{6}\begin{bmatrix}\mathbf{I}_3 & \left(-8-4\sqrt{3}\right)\mathbf{I}_3 & \left(7+4\sqrt{3}\right)\mathbf{I}_3\end{bmatrix}\right)\begin{bmatrix}\mathbf{r}_{2j-1}\\ \mathbf{r}_{2j}\\ \mathbf{r}_{2j+1}\end{bmatrix}
\end{aligned}
$$

- Elemental boundary conditions:

$$
\begin{aligned}
-\mathbf{f}\left(\zeta\right)w\left(\zeta\right)\big|_{-1}^{1}&=-\mathbf{f}\left(\zeta\right)\frac{\zeta^2+\zeta}{2}\bigg|_{-1}^{1}\\
&=-\mathbf{f}_{2j+1}\frac{1+1}{2}+\mathbf{f}_{2j+1}\cancelto{}{\frac{1-1}{2}}\\
&=-\mathbf{f}_{2j+1}
\end{aligned}
$$

Combining these leads to a system of three equations, one for each node of the element:

$$\frac{\mu l_0}{30}\begin{bmatrix} 4\mathbf{I}_3 & 2\mathbf{I}_3 & -\mathbf{I}_3 \\ 2\mathbf{I}_3 & 16\mathbf{I}_3 & 2\mathbf{I}_3 \\ -\mathbf{I}_3 & 2\mathbf{I}_3 & 4\mathbf{I}_3 \end{bmatrix}\begin{bmatrix} \ddot{\mathbf{r}}_{2j-1} \\ \ddot{\mathbf{r}}_{2j} \\ \ddot{\mathbf{r}}_{2j+1} \end{bmatrix} - \frac{\mu l_0}{6} g \begin{bmatrix} \mathbf{I}_3 \\ 4\mathbf{I}_3 \\ \mathbf{I}_3 \end{bmatrix} \hat{\mathbf{e}}_3 + \begin{bmatrix} \mathbf{f}_{2j-1} \\ 0 \\ -\mathbf{f}_{2j+1} \end{bmatrix}$$
$$+ \left(\frac{q_j^-}{6} \begin{bmatrix} \left(7+4\sqrt{3}\right)\mathbf{I}_3 & \left(-8-4\sqrt{3}\right)\mathbf{I}_3 & \mathbf{I}_3 \\ \left(-8-4\sqrt{3}\right)\mathbf{I}_3 & 16\mathbf{I}_3 & \left(-8+4\sqrt{3}\right)\mathbf{I}_3 \\ \mathbf{I}_3 & \left(-8+4\sqrt{3}\right)\mathbf{I}_3 & \left(7-4\sqrt{3}\right)\mathbf{I}_3 \end{bmatrix} \right.$$
$$\left. + \frac{q_j^+}{6} \begin{bmatrix} \left(7-4\sqrt{3}\right)\mathbf{I}_3 & \left(-8+4\sqrt{3}\right)\mathbf{I}_3 & \mathbf{I}_3 \\ \left(-8+4\sqrt{3}\right)\mathbf{I}_3 & 16\mathbf{I}_3 & \left(-8-4\sqrt{3}\right)\mathbf{I}_3 \\ \mathbf{I}_3 & \left(-8-4\sqrt{3}\right)\mathbf{I}_3 & \left(7+4\sqrt{3}\right)\mathbf{I}_3 \end{bmatrix} \right) \begin{bmatrix} \mathbf{r}_{2j-1} \\ \mathbf{r}_{2j} \\ \mathbf{r}_{2j+1} \end{bmatrix} = 0.$$

Rearranging the stiffness terms yields:

$$\frac{\mu l_0}{30}\begin{bmatrix} 4\mathbf{I}_3 & 2\mathbf{I}_3 & -\mathbf{I}_3 \\ 2\mathbf{I}_3 & 16\mathbf{I}_3 & 2\mathbf{I}_3 \\ -\mathbf{I}_3 & 2\mathbf{I}_3 & 4\mathbf{I}_3 \end{bmatrix}\begin{bmatrix} \ddot{\mathbf{r}}_{2j-1} \\ \ddot{\mathbf{r}}_{2j} \\ \ddot{\mathbf{r}}_{2j+1} \end{bmatrix} - \frac{\mu l_0}{6} g \begin{bmatrix} \mathbf{I}_3 \\ 4\mathbf{I}_3 \\ \mathbf{I}_3 \end{bmatrix} \hat{\mathbf{e}}_3 + \begin{bmatrix} \mathbf{f}_{2j-1} \\ 0 \\ -\mathbf{f}_{2j+1} \end{bmatrix}$$
$$+ \left(\frac{q_j^+ + q_j^-}{6} \begin{bmatrix} 7\mathbf{I}_3 & -8\mathbf{I}_3 & \mathbf{I}_3 \\ -8\mathbf{I}_3 & 16\mathbf{I}_3 & -8\mathbf{I}_3 \\ \mathbf{I}_3 & -8\mathbf{I}_3 & 7\mathbf{I}_3 \end{bmatrix} + \frac{4\sqrt{3}\left(q_j^+ - q_j^-\right)}{6} \begin{bmatrix} -\mathbf{I}_3 & \mathbf{I}_3 & 0 \\ \mathbf{I}_3 & 0 & -\mathbf{I}_3 \\ 0 & -\mathbf{I}_3 & \mathbf{I}_3 \end{bmatrix} \right) \begin{bmatrix} \mathbf{r}_{2j-1} \\ \mathbf{r}_{2j} \\ \mathbf{r}_{2j+1} \end{bmatrix} = 0.$$

Define an elemental force density, q_j, and a bias, Δq_j as:

$$q_j = q_j^+ + q_j^-$$
$$\Delta q_j = q_j^+ - q_j^-$$

and the stencil for the j'th element results in:

$$\begin{aligned}\frac{\mu l_0}{30}\begin{bmatrix}4\mathbf{I}_3 & 2\mathbf{I}_3 & -\mathbf{I}_3\\ 2\mathbf{I}_3 & 16\mathbf{I}_3 & 2\mathbf{I}_3\\ -\mathbf{I}_3 & 2\mathbf{I}_3 & 4\mathbf{I}_3\end{bmatrix}\begin{bmatrix}\ddot{\mathbf{r}}_{2j-1}\\ \ddot{\mathbf{r}}_{2j}\\ \ddot{\mathbf{r}}_{2j+1}\end{bmatrix} &= \frac{\mu l_0}{6}g\begin{bmatrix}\mathbf{I}_3\\ 4\mathbf{I}_3\\ \mathbf{I}_3\end{bmatrix}\hat{\mathbf{e}}_3 + \begin{bmatrix}-\mathbf{f}_{2j-1}\\ 0\\ \mathbf{f}_{2j+1}\end{bmatrix}\\ &+ \left(\frac{q_j}{6}\begin{bmatrix}-7\mathbf{I}_3 & 8\mathbf{I}_3 & -\mathbf{I}_3\\ 8\mathbf{I}_3 & -16\mathbf{I}_3 & 8\mathbf{I}_3\\ -\mathbf{I}_3 & 8\mathbf{I}_3 & -7\mathbf{I}_3\end{bmatrix} + \frac{2\sqrt{3}\Delta q_j}{3}\begin{bmatrix}\mathbf{I}_3 & -\mathbf{I}_3 & 0\\ -\mathbf{I}_3 & 0 & \mathbf{I}_3\\ 0 & \mathbf{I}_3 & -\mathbf{I}_3\end{bmatrix}\right)\begin{bmatrix}\mathbf{r}_{2j-1}\\ \mathbf{r}_{2j}\\ \mathbf{r}_{2j+1}\end{bmatrix}.\end{aligned} \tag{D.12}$$

Bibliography

[1] J. Kim, G. F. Dargush, and Y.-K. Ju, “Extended framework of hamilton’s principle for continuum dynamics,” *International Journal of Solids and Structures*, vol. 50, no. 20, pp. 3418–3429, 2013.

[2] G. Schmidt and R. Swik, “Automatic hover control of an unmanned tethered rotor-platform,” *Automatica*, vol. 10, pp. 393–394, Jan. 1974.

[3] S. Y. Choi, B. H. Choi, S. Y. Jeong, B. W. Gu, S. J. Yoo, and C. T. Rim, “Tethered aerial robots using contactless power systems for extended mission time and range,” in *2014 IEEE Energy Conversion Congress and Exposition (ECCE)*, pp. 912–916, Sept 2014.

[4] C. Papachristos and A. Tzes, “The power-tethered uav-ugv team: A collaborative strategy for navigation in partially-mapped environments,” in *22nd Mediterranean Conference on Control and Automation*, pp. 1153–1158, June 2014.

[5] L. Sandino, M. Bejar, K. Kondak, and A. Ollero, “Advances in modeling and control of tethered unmanned helicopters to enhance hovering performance,” *Journal of Intelligent & Robotic Systems*, vol. 73, no. 1, pp. 3–18, 2014.

[6] S. Kiribayashi, K. Yakushigawa, and K. Nagatani, “Position estimation of tethered micro unmanned aerial vehicle by observing the slack tether,” in *2017 IEEE International Symposium on Safety, Security and Rescue Robotics (SSRR)*, pp. 159–165, Oct 2017.

[7] L. A. Sandino, M. Bejar, K. Kondak, and A. Ollero, “On the use of tethered configurations for augmenting hovering stability in small-size autonomous helicopters,” *Journal of Intelligent & Robotic Systems*, vol. 70, no. 1, pp. 509–525, 2013.

[8] M. M. Nicotra, R. Naldi, and E. Garone, “Taut cable control of a tethered UAV,” *IFAC Proceedings Volumes*, vol. 47, no. 3, pp. 3190 – 3195, 2014. 19th IFAC World Congress.

[9] Y. Ouchi, K. Kinoshita, K. Watanabe, and I. Nagai, “Control of position and attitude of the tethered x4-flyer,” in *2014 IEEE/SICE International Symposium on System Integration*, pp. 706–711, Dec 2014.

[10] S. Lupashin and R. D'Andrea, "Stabilization of a flying vehicle on a taut tether using inertial sensing," in *2013 IEEE/RSJ International Conference on Intelligent Robots and Systems*, pp. 2432–2438, Nov 2013.

[11] D. Ferreira de Castro, J. S. Santos, M. Batista, D. Antônio dos Santos, and L. C. Góes, "Modeling and control of tethered unmanned multicopters in hovering flight," in *AIAA Modeling and Simulation Technologies Conference*, American Institute of Aeronautics and Astronautics, June 2015.

[12] S.-R. Oh, K. Pathak, S. K. Agrawal, H. R. Pota, and M. Garratt, "Approaches for a tether-guided landing of an autonomous helicopter," *IEEE Transactions on Robotics*, vol. 22, pp. 536–544, June 2006.

[13] L. A. Sandino, D. Santamaria, M. Bejar, A. Viguria, K. Kondak, and A. Ollero, "Tether-guided landing of unmanned helicopters without gps sensors," in *2014 IEEE International Conference on Robotics and Automation (ICRA)*, pp. 3096–3101, May 2014.

[14] B. Ahmed and H. R. Pota, "Backstepping-based landing control of a ruav using tether incorporating flapping correction dynamics," in *2008 American Control Conference*, pp. 2728–2733, June 2008.

[15] M. M. Nicotra, R. Naldi, and E. Garone, "Nonlinear control of a tethered UAV: the taut cable case," *CoRR*, 2016.

[16] F. M. Briggs IV and T. Stave, "Reactive tether spool," Sept. 14 2017. US Patent App. 15/456,096.

[17] M. Tognon, A. Testa, E. Rossi, and A. Franchi, "Takeoff and landing on slopes via inclined hovering with a tethered aerial robot," in *2016 IEEE/RSJ International Conference on Intelligent Robots and Systems (IROS)*, pp. 1702–1707, Oct 2016.

[18] M. Bernard and K. Kondak, "Generic slung load transportation system using small size helicopters," in *2009 IEEE International Conference on Robotics and Automation*, pp. 3258–3264, May 2009.

[19] F. A. Goodarzi and T. Lee, "Dynamics and control of quadrotor uavs transporting a rigid body connected via flexible cables," in *2015 American Control Conference (ACC)*, pp. 4677–4682, July 2015.

[20] R. Naldi, A. Gasparri, and E. Garone, "Cooperative pose stabilization of an aerial vehicle through physical interaction with a team of ground robots," in *2012 IEEE International Conference on Control Applications*, pp. 415–420, Oct 2012.

[21] L. Zikou, C. Papachristos, and A. Tzes, "The power-over-tether system for powering small uavs: Tethering-line tension control synthesis," in *2015 23rd Mediterranean Conference on Control and Automation (MED)*, pp. 681–687, June 2015.

[22] L. A. Sandino, M. Bejar, K. Kondak, and A. Ollero, "A square-root unscented kalman filter for attitude and relative position estimation of a tethered unmanned helicopter," in *2015 International Conference on Unmanned Aircraft Systems (ICUAS)*, pp. 567–576, June 2015.

[23] A. Al-Radaideh and L. Sun, "Self-localization of a tethered quadcopter using inertial sensors in a gps-denied environment," in *2017 International Conference on Unmanned Aircraft Systems (ICUAS)*, pp. 271–277, June 2017.

[24] B. Galea and P. G. Kry, "Tethered flight control of a small quadrotor robot for stippling," in *2017 IEEE/RSJ International Conference on Intelligent Robots and Systems (IROS)*, pp. 1713–1718, Sept 2017.

[25] M. Tognon, S. S. Dash, and A. Franchi, "Observer-based control of position and tension for an aerial robot tethered to a moving platform," *IEEE Robotics and Automation Letters*, vol. 1, pp. 732–737, July 2016.

[26] S. D. Prior, "Aether - persistent aerial surveillance using a small unmanned aircraft system," in *15th Annual Conference on Unmanned Aerial Systems*, November 2015.

[27] D. Stewart, "A platform with six degrees of freedom," *Proceedings of the Institution of Mechanical Engineers*, vol. 180, no. 1, pp. 371–386, 1965.

[28] V. Gough, "Universal tyre test machine," *Proc. FISITA 9th Int. Technical Congr., London, 1962*, pp. 117–137, 1962.

[29] J. C. Jáuregui, E. E. Hernández, M. Ceccarelli, C. López-Cajún, and A. García, "Kinematic calibration of precise 6-dof stewart platform-type positioning systems for radio telescope applications," *Frontiers of Mechanical Engineering*, vol. 8, pp. 252–260, Sep 2013.

[30] Y. Ting, Y.-S. Chen, and H.-C. Jar, "Modeling and control for a gough-stewart platform cnc machine," *Journal of Robotic Systems*, vol. 21, no. 11, pp. 609–623, 2004.

[31] M. Wapler, V. Urban, T. Weisener, J. Stallkamp, M. DÃŒrr, and A. Hiller, "A stewart platform for precision surgery," *Transactions of the Institute of Measurement and Control*, vol. 25, no. 4, pp. 329–334, 2003.

[32] W. De Zeeuw, "Ship motion compensation platform for high payloads; dynamic analysis and control," *TU Delft*, 2012.

[33] A. L. Madsen, "Design of stewart platform for wave compensation," Master's thesis, Aalborg Universitet, Denmark, 2012.

[34] B. Lotfi and L. Huang, "A novel wave energy converter using the stewart platform," *Journal of Green Engineering*, vol. 4, pp. 33–48, 2014.

[35] A. Campos, J. Quintero, R. Saltaren, M. Ferre, and R. Aracil, "An active helideck testbed for floating structures based on a stewart-gough platform," in *2008 IEEE/RSJ International Conference on Intelligent Robots and Systems*, pp. 3705–3710, Sept 2008.

[36] Y. Ye and W. Chen, "Frequency- and time-domain analysis of a multi-degree-of-freedom point absorber wave energy converter," *Advances in Mechanical Engineering*, vol. 9, p. 168781401772208, 12 2017.

[37] W. Xu, Y. Li, and X. Xiao, "Kinematics and workspace analysis for a novel 6-pss parallel manipulator," *2013 IEEE International Conference on Robotics and Biomimetics, ROBIO 2013*, pp. 1869–1874, 12 2013.

[38] F. Gao, W. Li, X. Zhao, Z. Jin, and H. Zhao, "New kinematic structures for 2-, 3-, 4-, and 5-dof parallel manipulator designs," *Mechanism and Machine Theory*, vol. 37, no. 11, pp. 1395 – 1411, 2002.

[39] J. Jansen, R. Lind, L. Love, P. Lloyd, J. Rowe, and F. G. Pin, "Design and control of a ship motion simulation platform from an energy efficiency perspective," *International Journal of Fluid Power*, vol. 10, no. 2, pp. 19–28, 2009.

[40] S. Fecht, "Inside the wave pool where the navy tests its warships." [Online] https://www.popularmechanics.com/military/navy-ships/a10407/inside-the-wave-pool-where-the-navy-tests-its-warships-16656545/, 2014.

[41] T. C. Smith, "Mask basin b'bank wave survey," tech. rep., Naval Surface Warfare Center Carderock Div Bethesda MD Hydromechanics Directorate, 1999.

[42] K. Slater and A. Fincham, "Surface gravity wave generator and wave pool," Sept. 11 2012. US Patent 8,262,316.

[43] S.-K. Ueng, D. Lin, and C.-H. Liu, "A ship motion simulation system," *Virtual Real.*, vol. 12, pp. 65–76, mar 2008.

[44] Y. Li and Q. Xu, "Kinematic analysis of a 3-prs parallel manipulator," *Robotics and Computer-Integrated Manufacturing*, vol. 23, no. 4, pp. 395 – 408, 2007.

[45] M.-S. Tsai, T.-N. Shiau, Y.-J. Tsai, and T.-H. Chang, "Direct kinematic analysis of a 3-prs parallel mechanism," *Mechanism and Machine Theory*, vol. 38, no. 1, pp. 71 – 83, 2003.

[46] X. Liu, J. Wang, T. Li, and G. Duan, "Parallel mechanisms with two or three degrees of freedom," *Tsinghua Science and Technology*, vol. 8, pp. 105–112, Feb 2003.

[47] Y. Li and Q. Xu, "Kinematics and stiffness analysis for a general 3-prs spatial parallel mechanism," *in Proc. of 15th CISM-IFToMM Symp. on Robot Design, Dynamics and Control*, 02 2019.

[48] K. Balaji and B. S. H. Khan, “Kinematic analysis and performance evaluation of novel PRS parallel mechanism,” *IOP Conference Series: Materials Science and Engineering*, vol. 310, p. 012007, feb 2018.

[49] X. Li, D. Zhu, Z. Mei, and D. Jiang, “Kinematic analysis of 3-rps parallel mechanism,” in *2017 2nd International Conference on Robotics and Automation Engineering (ICRAE)*, pp. 183–187, Dec 2017.

[50] H. Pendar, M. Vakil, and H. Zohoor, “Efficient dynamic equations of 3-rps parallel mechanism through lagrange method,” in *IEEE Conference on Robotics, Automation and Mechatronics, 2004.*, vol. 2, pp. 1152–1157 vol.2, Dec 2004.

[51] J. Gallardo, H. Orozco, and J. M. Rico, “Kinematics of 3-rps parallel manipulators by means of screw theory,” *The International Journal of Advanced Manufacturing Technology*, vol. 36, pp. 598–605, Mar 2008.

[52] X. Liu, T. Zhao, E. Luo, W. Chen, and Q. Pan, “Coupling 3-psr/psu 5-axis compensation mechanism for stabilized platform and its analysis,” *Proceedings of the Institution of Mechanical Engineers, Part C: Journal of Mechanical Engineering Science*, vol. 227, no. 7, pp. 1619–1629, 2013.

[53] L.-W. Tsai, *Marine Observer’s Handbook.* London, England: HMSO, 8th ed., 1995.

[54] T. Bewley, *Numerical Renaissance.* Renaissance Press, 2017.

[55] J. Diebel, “Representing attitude: Euler angles, unit quaternions, and rotation vectors,” *Matrix*, vol. 58, no. 15-16, pp. 1–35, 2006.

[56] E. Darles, B. Crespin, D. Ghazanfarpour, and J.-C. Gonzato, “A survey of ocean simulation and rendering techniques in computer graphics,” in *Computer Graphics Forum*, vol. 30, pp. 43–60, Wiley Online Library, 2011.

[57] A. Newell and V. Zakharov, “The role of the generalized phillips’ spectrum in wave turbulence,” *Physics Letters A*, vol. 372, no. 23, pp. 4230 – 4233, 2008.

[58] O. M. Phillips, “The equilibrium range in the spectrum of wind-generated waves,” *Journal of Fluid Mechanics*, vol. 4, no. 4, p. 426–434, 1958.

[59] O. M. Phillips, “On the generation of waves by turbulent wind,” *Journal of fluid mechanics*, vol. 2, no. 5, pp. 417–445, 1957.

[60] G. Castillo and C. Falcon, “Observation of phillips’ spectrum in faraday waves,” *arXiv preprint arXiv:1608.08961*, 2016.

[61] A. W. Browning, “A mathematical model to simulate small boat behaviour,” *Simulation*, vol. 56, no. 5, pp. 329–336, 1991.

[62] T. Pérez and M. Blanke, "Simulation of ship motion in seaway," Tech. Rep. EE02037, Technical University of Denmark, 2001.

[63] Unity Technologies, "Unity." https://unity3d.com/get-unity/download/archive, https://assetstore.unity.com/packages/3d/vehicles/sea/patrol-boat-46913, https://assetstore.unity.com/packages/tools/particles-effects/uws-ultimate-water-system-100669, 2017. Version 2017.2.0f3.

[64] "World of Earth Science: Douglas Sea Scale," Retreived 9/9/2017. http://www.encyclopedia.com/science/encyclopedias-almanacs-transcripts-and-maps/douglas-sea-scale/.

[65] "Encyclopedia Britannica: Beafort Scale," Retreived 9/9/2017. https://www.britannica.com/science/Beaufort-scale/.

[66] E. Lockwood, "Chapter XIII: The tractrix and catenary," in *A Book of Curves*, pp. 119–124, Cambridge, 1961.

[67] I. Todhunter, "XI flexible strings. inextensible, XII flexible strings. extensible," in *A Treatise on Analytical Statics*, pp. 238–285, Macmillan, 1958.

[68] O. H. Schmitt, "A thermionic trigger," *Journal of Scientific Instruments*, vol. 15, pp. 24–26, jan 1938.

[69] K. Talke, M. Oliveira, and T. Bewley, "Tether shape analysis for a uav - usv team," in *2018 IEEE International Conference on Intelligent Robots (IROS)*, Oct 2018.

[70] H. Carvalho, P. Del Moral, A. Monin, and G. Salut, "Optimal nonlinear filtering in gps/ins integration," *IEEE Transactions on Aerospace and Electronic Systems*, vol. 33, pp. 835–850, July 1997.

[71] Honghui Qi and J. B. Moore, "Direct kalman filtering approach for gps/ins integration," *IEEE Transactions on Aerospace and Electronic Systems*, vol. 38, pp. 687–693, April 2002.

[72] D. Simon, *Optimal state estimation: Kalman, H infinity, and nonlinear approaches.* John Wiley & Sons, 2006.

[73] S. Thrun, W. Burgard, and D. Fox, *Probabilistic robotics.* MIT press, 2005.

[74] J. N. Gross, Y. Gu, and M. B. Rhudy, "Robust uav relative navigation with dgps, ins, and peer-to-peer radio ranging," *IEEE Transactions on Automation Science and Engineering*, vol. 12, pp. 935–944, July 2015.

[75] S. Oh, "Multisensor fusion for autonomous uav navigation based on the unscented kalman filter with sequential measurement updates," in *2010 IEEE Conference on Multisensor Fusion and Integration*, pp. 217–222, Sep. 2010.

[76] G. Schall, D. Wagner, G. Reitmayr, E. Taichmann, M. Wieser, D. Schmalstieg, and B. Hofmann-Wellenhof, “Global pose estimation using multi-sensor fusion for outdoor augmented reality,” in *2009 8th IEEE International Symposium on Mixed and Augmented Reality*, pp. 153–162, Oct 2009.

[77] J. K. Suhr, J. Jang, D. Min, and H. G. Jung, “Sensor fusion-based low-cost vehicle localization system for complex urban environments,” *IEEE Transactions on Intelligent Transportation Systems*, vol. 18, pp. 1078–1086, May 2017.

[78] K. Talke, D. Drotman, N. Stroumtsos, M. Oliveira, and T. Bewley, “Design and parameter optimization of a 3-$\underline{P}SR$ parallel mechanism for replicating wave and boat motion,” in *2019 IEEE International Conference on Robotics and Automation (ICRA)*, May 2019.

[79] P. Abbeel, A. Coates, M. Montemerlo, A. Y. Ng, and S. Thrun, “Discriminative training of kalman filters.,” in *Robotics: Science and systems*, vol. 2, p. 1, 2005.

[80] S. Thrun, “The twiddle algorithm is attributed here to sebastian thrun, in lectures through the udacity programme.” https://www.youtube.com/watch?v=2uQ2BSzDvXs, 2012.

[81] E. Branlard, “Generation of time series from a spectrum,” *TU Denmark*, 2010.

[82] G. Hoffmann, H. Huang, S. Waslander, and C. Tomlin, “Quadrotor helicopter flight dynamics and control: Theory and experiment,” in *AIAA Guidance, Navigation and Control Conference and Exhibit*, p. 6461, 2007.

[83] R. A. Holman, K. L. Brodie, and N. J. Spore, “Surf zone characterization using a small quadcopter: Technical issues and procedures,” *IEEE Transactions on Geoscience and Remote Sensing*, vol. 55, pp. 2017–2027, April 2017.

[84] K. Talke, F. Birchmore, and T. Bewley, “Autonomous hanging tether management and experimentation for an unmanned air - surface vehicle team,” *Field Robotics*, 2021. This publication is in the review process.

[85] J. Winget and R. Huston, “Cable dynamics—a finite segment approach,” *Computers & Structures*, vol. 6, no. 6, pp. 475 – 480, 1976.

[86] E. Dicembrini, M. Scanavino, F. Dabbene, and G. Guglieri, “Modelling and simulation of a tethered uas*,” in *2020 International Conference on Unmanned Aircraft Systems (ICUAS)*, pp. 1801–1808, 2020.

[87] W. Steiner, J. Zemann, A. Steindl, and H. Troger, “Numerical study of large amplitude oscillations of a two-satellite continuous tether system with a varying length,” *Acta Astronautica*, vol. 35, no. 9, pp. 607–621, 1995. Challenges of Space for a Better World.

[88] J. W. Kamman and R. L. Huston, “Multibody dynamics modeling of variable length cable systems,” *Multibody System Dynamics*, vol. 5, no. 3, pp. 211–221, 2001.

[89] F. Muttin, “Umbilical deployment modeling for tethered {UAV} detecting oil pollution from ship,” *Applied Ocean Research*, vol. 33, no. 4, pp. 332 – 343, 2011.

[90] P. Fritzkowski and H. Kaminski, “Dynamics of a rope as a rigid multibody system,” *Journal of mechanics of materials and structures*, vol. 3, no. 6, pp. 1059–1075, 2008.

[91] P. Fritzkowski and H. Kaminski, “A discrete model of a rope with bending stiffness or viscous damping,” *Acta Mechanica Sinica*, vol. 27, no. 1, pp. 108–113, 2011.

[92] P. Fritzkowski and H. Kaminski, “Non-linear dynamics of a hanging rope,” *Latin American Journal of Solids and Structures*, vol. 10, pp. 81 – 90, 01 2013.

[93] T. Lee, M. Leok, and N. H. McClamroch, “Dynamics of a 3d elastic string pendulum,” in *Proceedings of the 48h IEEE Conference on Decision and Control (CDC) held jointly with 2009 28th Chinese Control Conference*, pp. 3347–3352, IEEE, 2009.

[94] M. W. Spong, S. Hutchinson, and M. Vidyasagar, *Robot modeling and control.* Emerald Group Publishing Limited, 2006.

[95] A. C. Ugural and S. K. Fenster, *Advanced strength and applied elasticity.* Pearson education, 2003.

[96] M. S. Triantafyllou, “The Dynamics of Taut Inclined Cables,” *The Quarterly Journal of Mechanics and Applied Mathematics*, vol. 37, pp. 421–440, 08 1984.

[97] A. Bliek, *Dynamic analysis of single span cables.* PhD thesis, Massachusetts Institute of Technology, 1984.

[98] M. Triantafyllou and G. Triantafyllou, “The paradox of the hanging string: an explanation using singular perturbations,” *Journal of Sound and Vibration*, vol. 148, no. 2, pp. 343–351, 1991.

[99] C. T. Howell, “Investigation of the dynamics of low-tension cables,” tech. rep., Woods Hole Oceanographic Institution MA, 1992.

[100] M. Triantafyllou and C. T. Howell, “Nonlinear impulsive motions of low-tension cables,” *Journal of Engineering Mechanics-asce - J ENG MECH-ASCE*, vol. 118, 04 1992.

[101] M. Triantafyllou and C. Howell, “Dynamic response of cables under negative tension: an ill-posed problem,” *Journal of Sound and Vibration*, vol. 173, no. 4, pp. 433 – 447, 1994.

[102] J. Phadikar and S. Pradhan, “Variational formulation and finite element analysis for nonlocal elastic nanobeams and nanoplates,” *Computational Materials Science*, vol. 49, no. 3, pp. 492–499, 2010.

[103] D. H. Hodges, “A mixed variational formulation based on exact intrinsic equations for dynamics of moving beams,” *International Journal of Solids and Structures*, vol. 26, no. 11, pp. 1253–1273, 1990.

[104] L. D. Landau and E. M. Lifshitz, *Theory of Elasticity, Volume 7 (Course of Theoretical Physics).* Butterworth-Heinemann, 3 ed., 1986.

[105] L. D. Landau and E. M. Lifshitz, *Mechanics, Volume 1 (Course of Theoretical Physics).* Butterworth-Heinemann, 3 ed., Jan. 1976.

[106] H. Baruh, *Applied dynamics.* CRC press, 2014.

[107] G. M. Ewing, *Calculus of variations with applications.* Courier Corporation, 1985.

[108] Z. Qi, J. Wang, and G. Wang, “An efficient model for dynamic analysis and simulation of cable-pulley systems with time-varying cable lengths,” *Mechanism and Machine Theory*, vol. 116, pp. 383–403, 2017.

[109] R. F. Zueck, “Modeling the Pay-Out And Reel-In of Cable,” in *International Ocean and Polar Engineering Conference*, 05 1999. ISOPE-I-99-166.

[110] T. Lee, M. Leok, and N. H. McClamroch, “Computational dynamics of a 3d elastic string pendulum attached to a rigid body and an inertially fixed reel mechanism,” *Nonlinear Dynamics*, vol. 64, no. 1-2, pp. 97–115, 2011.

[111] J. Donea, S. Giuliani, and J. Halleux, “An arbitrary lagrangian-eulerian finite element method for transient dynamic fluid-structure interactions,” *Computer Methods in Applied Mechanics and Engineering*, vol. 33, no. 1, pp. 689–723, 1982.

[112] A. M. Bavo, G. Rocatello, F. Iannaccone, J. Degroote, J. Vierendeels, and P. Segers, “Fluid-structure interaction simulation of prosthetic aortic valves: Comparison between immersed boundary and arbitrary lagrangian-eulerian techniques for the mesh representation,” *PLOS ONE*, vol. 11, pp. 1–17, 04 2016.

[113] F. Tveter, “Hamilton’s equations of motion for non-conservative systems,” *Celestial Mechanics & Dynamical Astronomy*, vol. 60, pp. 409–419, 01 1994.

[114] L. Meirovitch, *Methods of analytical dynamics.* Courier Corporation, 2010.

[115] K. K. Mankala and S. K. Agrawal, “Dynamic Modeling and Simulation of Satellite Tethered Systems,” *Journal of Vibration and Acoustics*, vol. 127, pp. 144–156, 06 2004.

[116] M. Krupa, W. Poth, M. Schagerl, A. Steindl, W. Steiner, H. Troger, and G. Wiedermann, "Modelling, dynamics and control of tethered satellite systems," *Nonlinear Dynamics*, vol. 43, no. 1, pp. 73–96, 2006.

[117] T. Lee, M. Leok, and N. H. McClamroch, "High-fidelity numerical simulation of complex dynamics of tethered spacecraft," *Acta Astronautica*, vol. 99, pp. 215–230, 2014.

[118] J. N. Reddy, "An introduction to the finite element method," *New York*, vol. 27, 1993.

[119] R. D. Blevins, "Applied fluid dynamics handbook," *New York*, 1984.

[120] J. D. Anderson and J. Wendt, *Computational fluid dynamics*, vol. 206. Springer, 1995.

[121] S. Bouabdallah, P. Murrieri, and R. Siegwart, "Design and control of an indoor micro quadrotor," in *Robotics and Automation, 2004. Proceedings. ICRA '04. 2004 IEEE International Conference on*, vol. 5, pp. 4393–4398 Vol.5, April 2004.

[122] S. McTavish, A. D'Auteuil, and A. Raeesi, "Effect of cable surface characteristics and flow turbulence on the aerodynamic behaviour of stay cables in dry conditions," *Journal of Wind Engineering and Industrial Aerodynamics*, vol. 207, p. 104414, 2020.

[123] J. C. Doyle, K. Glover, P. P. Khargonekar, and B. A. Francis, "State-space solutions to standard h2 and h infin; control problems," *IEEE Transactions on Automatic Control*, vol. 34, pp. 831–847, Aug 1989.

[124] H. Flanders, "Differentiation under the integral sign," *The American Mathematical Monthly*, vol. 80, no. 6, pp. 615–627, 1973.

[125] E. B. Wilson, *Advanced calculus: a text upon select parts of differential calculus, differential equations, integral calculus, theory of functions; with numerous exercises.* Ginn, 1912.

[126] D. V. Widder, *Advanced calculus.* Courier Corporation, 1989.

[127] K. F. Riley, M. P. Hobson, and S. J. Bence, "Mathematical methods for physics and engineering," 1999.

[128] W. S. Slaughter, *The linearized theory of elasticity.* Springer Science & Business Media, 2012.

[129] A. P. Boresi, R. J. Schmidt, and O. M. Sidebottom, *Advanced mechanics of materials*, vol. 6. Wiley New York, 1985.

[130] E. B. Crellin, F. Janssens, D. Poelaert, W. Steiner, and H. Troger, “On Balance and Variational Formulations of the Equation of Motion of a Body Deploying Along a Cable,” *Journal of Applied Mechanics*, vol. 64, pp. 369–374, 06 1997.